2020

SILICA NANOPOROUS CONFINEMENT EFFECTS ON IONIC LIQUID PROPERTIES FOR BETTER DESIGN OF SMALL MOLECULE SEPARATION, ELECTROCHEMICAL DEVICES AND DRUG DELIVERY

Yuxin He
University of Kentucky, zhangxiaotangnan@gmail.com
Author ORCID Identifier:
https://orcid.org/0000-0002-4436-2623
Digital Object Identifier: https://doi.org/10.13023/etd.2020.171

STUDENT AGREEMENT:

I represent that my thesis or dissertation and abstract are my original work. Proper attribution has been given to all outside sources. I understand that I am solely responsible for obtaining any needed copyright permissions. I have obtained needed written permission statement(s) from the owner(s) of each third-party copyrighted matter to be included in my work, allowing electronic distribution (if such use is not permitted by the fair use doctrine) which will be submitted to UKnowledge as Additional File.

I hereby grant to The University of Kentucky and its agents the irrevocable, non-exclusive, and royalty-free license to archive and make accessible my work in whole or in part in all forms of media, now or hereafter known. I agree that the document mentioned above may be made available immediately for worldwide access unless an embargo applies.

I retain all other ownership rights to the copyright of my work. I also retain the right to use in future works (such as articles or books) all or part of my work. I understand that I am free to register the copyright to my work.

REVIEW, APPROVAL AND ACCEPTANCE

The document mentioned above has been reviewed and accepted by the student's advisor, on behalf of the advisory committee, and by the Director of Graduate Studies (DGS), on behalf of the program; we verify that this is the final, approved version of the student's thesis including all changes required by the advisory committee. The undersigned agree to abide by the statements above.

Yuxin He, Student

Dr. Stephen E. Rankin, Major Professor

Dr. Stephen E. Rankin, Director of Graduate Studies

SILICA NANOPOROUS CONFINEMENT EFFECTS ON IONIC LIQUID PROPERTIES FOR BETTER DESIGN OF SMALL MOLECULE SEPARATION, ELECTROCHEMICAL DEVICES AND DRUG DELIVERY

DISSERTATION

A dissertation submitted in partial fulfillment of the
requirements for the degree of Doctor of Philosophy in the
College of Engineering
at the University of Kentucky

By
Yuxin He
Lexington, Kentucky
Director: Dr. Barbara L. Knutson, Professor of Chemical Engineering
Lexington, Kentucky
2020

https://orcid.org/0000-0002-4436-2623

ABSTRACT OF DISSERTATION

SILICA NANOPOROUS CONFINEMENT EFFECTS ON IONIC LIQUID PROPERTIES FOR BETTER DESIGN OF SMALL MOLECULE SEPARATION, ELECTROCHEMICAL DEVICES AND DRUG DELIVERY

Silica nanoconfinement provides a high level of control of ionic liquids (ILs) in localizing catalysts, creating distinct environment for tuning reactivity and controlling the partition of solvents, reactants and products. Silica thin films with two different pore sizes (2.5 nm and 8 nm) were synthesized to study the effect of nanopore confinement on ionic liquids 1-butyl-3-methylimidazolium hexafluorophosphate ([BMIM][PF_6]), and 1-butyl-3-methylimidazolium chloride ([BMIM][Cl]). Silica thin films with accessible 8 nm pore diameters were synthesized using evaporation-induced self-assembly (EISA) with Pluronic P123 as templating surfactant on a chemically neutral modified substrate. The silica films with similar orthogonal aligned mesostructured but smaller pore size (2.5 nm) were produced through cetyltrimethylammonium bromide (CTAB) templated EISA. The perpendicularly oriented channels were achieved by doping the silica matrix with small amount of titania, which destabilized the nanoporous structure during calcination so that the isolated micelles connect with each other when the films go through thermal contraction during calcination. In situ grazing-incidence small angle X-ray scattering (GISAXS) was performed and it revealed this structure transformation. To broaden the application of this CTAB templated film, a sugar surfactant was added to bind with titania precursor and disperse titania on the pore surface instead of through out the entire matrix.

The absorption of water by ILs is among the most concerning properties when they are utilized in catalysis systems for example, the dehydration of glucose to 5-(hydroxymethyl)furfural (HMF) using [BMIM][Cl] as solvent. Thus, [BMIM][Cl] confined in the 8-nm-pore-diameter silica thin films was investigated and compared to that of bulk ionic liquid. Transmission Fourier transform infrared spectra (FTIR) were collected in situ at room temperature while the relative humidity (RH) of the environment was changed. Pore confinement effects were interpreted from the C-H stretching bands shift and OH stretching band growth. Deconvolution of OH stretching bands shows that weakly coordinated water is promoted in confined [BMIM][Cl], which may affect mechanisms of solubilization and catalysis in confined ILs.

To understand the effect of pore confinement on transport, the two silica thin films were modified with physically absorbed [BMIM][PF_6], chemically tethered 3-methyl-1-[3-(trimethoxysilyl) propyl]-1-imidazolium group ([TMS-MIM]$^+$) and with the presence of both. Electrochemical impedance spectroscopy (EIS) was performed to investigate the permeability of hydrophilic and hydrophobic redox groups through the thin films with different treatments and different pore sizes. Both films with chemically tethered IL possess much higher resistance to hydrophilic molecules than hydrophobic molecules with 14-fold lower permeability through 8-nm tethered films and 30-fold lower for 2.5-nm tethered films. This work successfully produced highly selective silica thin films for selective separation of hydrophilic and hydrophobic species.

Crystallization of ILs is another attractive property of ILs to study but lack of direct characterization results. This dissertation work introduced in situ probing using grazing-incidence wide-angle X-ray scattering (GIWAXS) to characterize the crystallization behavior of [BMIM][PF_6] and [BMIM][Cl] under confinement of the two silica thin films with and without ILs tethering as described above. While certain crystallization behavior can be predicted by the classic Gibbs-Thomson theory, confined ILs in most cases studied do not follow the predictions of Gibbs-Thomson theory. One extreme case is when [BMIM][PF_6] were confined in [TMS-MIM] tethered 2.5-nm porous silica thin films, the composite did not melt at room temperature while [BMIM][PF_6] in bulk melts around -11 °C. This work successfully demonstrates how different confining condition changes the crystallization behavior of the two ILs through the novel in situ GIWAXS characterization, which benefits further studies for drug delivery and battery research.

KEYWORDS: mesoporous silica, nano-confined ionic liquid, imidazole, tethered ionic liquid

Yuxin He

(Name of Student)

03/13/2020

Date

SILICA NANOPOROUS CONFINEMENT EFFECTS ON IONIC LIQUID PROPERTIES FOR BETTER DESIGN OF SMALL MOLECULE SEPARATION, ELECTROCHEMICAL DEVICES AND DRUG DELIVERY

By
Yuxin He

Dr. Barbara L. Knutson
Director of Dissertation

Dr. Stephen E. Rankin
Director of Graduate Studies

03/13/2020
Date

DEDICATION

To my mother, Jianghong Tang. Thank you for giving me the life I get to live today

ACKNOWLEDGEMENTS

Foremost, I want to express my deepest gratitude to my advisers, Dr. Knutson and Dr. Rankin. I could not complete this dissertation work without their patience, caring and guidance. Throughout my PhD study, Dr. Knutson and Dr. Rankin taught me so much about the importance of critical thinking and being meticulous about details, which would benefit me for building my career hereafter. I would also like to thank our collaborator Dr. Folami T Ladipo for providing synthesized chemicals and sharing ideas from a different perspective. My other committee members Dr. Dibakar Bhattacharyya and the outside examiner Dr. David Atwood gave insightful opinions and advices to complete this dissertation work, too.

My appreciation also extends to Nicolas Briot and Dali Qian for the technical support on XPS and maintaining the GISAXS instrument as well as Joseph Strzalka and Qingteng Zhang at Argonne National Laboratory for their assistance for the GIS/WAXS facility. Additionally, I'm fortunate to have a group of kind and supporting lab mates: Syed Islam, Airf Khan, Kwabena Darkwah, Shanshan Zhou, Mahsa Moradipour, Joshua Garay, Aniruddha Shirodkar and Andrew Drake.

I am extremely grateful to always have my parents' encouragement. They believe in me and support me with all they have for my decisions. I would not be where I am now without them. At last, a thank you to the Bertrams and all my friends for making this journey such a special experience.

TABLE OF CONTENTS

List of Figures

List of Tables

Chapter 1: Introduction

Ionic liquids (ILs) are salts with melting points near ambient conditions - usually below 100°C. They are of great and growing interest to researchers because they can be utilized in a wide variety of applications due to good thermal stability, high ion conductivity and tunable properties.[1-3] ILs can also dissolve a large range of inorganic, organic and polymeric materials because of their unusual and tunable combination of molecular interactions.[1, 2] Their extremely low volatility makes them favorable as solvents for some applications since their low vapor pressure means that minimal loss of solvent by evaporation occurs. [4] However, scaling up applications requiring bulk ILs is challenging because of their high cost, debatable toxicity and difficult recovery from non-volatile products.[5-7]

To address these issues, supported IL systems have been developed and studied to significantly cut down the use of ILs, as well as to tailor the properties of ILs for different applications through their interaction with the support. There is evidence in prior reports that confined ILs display different crystallization, thermal, electrochemical and molecular assembly behavior than the corresponding bulk IL.[8-11] The goal of this dissertation work is to better understand and take advantage of the unique properties of IL confined in mesoporous silica films to promote their applications for drug delivery, selective separation, catalytic reactions and electrochemical devices.

Many researchers agree that mesoporous silica materials are good candidates as supporting matrices thanks to their tunable porosity, scalable synthesis approaches, and stable chemical and thermal properties.[12, 13] Therefore, the research presented in this

dissertation will be mainly focused on imidazolium ILs confined in silica mesoporous thin films synthesized by evaporation induced self-assembly (EISA) surfactant templated sol-gel processes. A robust method of producing silica thin films with orthogonally oriented 8 nm diameter pores templated by Pluronic P123 has been developed by Koganti et al. and will used as a platform for understanding nanoconfinement effects on supported ionic liquids.[14, 15] To understand pore size effects, **Chapter 3** presents research directed toward the synthesis of titania-doped silica films with 2.5 nm through EISA using cetyltrimethylammonium bromide (CTAB) as a pore template. Evidence will be provided that incorporation of titanium into the walls of the materials facilitates transformation to a vertically oriented pore architecture during thermal processing of the films. This enables investigation of the impacts of the pore size on the properties of confined ILs. Moreover, this synthesis approach provides an alternative pore size for applications that benefit from size exclusion of smaller molecules than in P123-templated films.

In **Chapter 4**, a unique technique of *in situ* transmission FTIR measurement under varying relative humidity (RH) was developed that takes advantage of thin films with accessible mesopores cast onto thin silicon wafers that are transparent to infrared. This facilitates an *in situ* study of changes in C-H stretching and other infrared bands in nanoconfined IL 1-butyl-3-methylimidaxolium ([BMIM]) chloride in response to humidity. The results are interpreted in terms of terms of changes in inter- and intramolecular interactions of the imidazolium group due to confinement. The amount and degree of intermolecular coordination of water absorbed by the hygroscopic [BMIM][Cl] was compared between confined and unconfined systems because

hygroscopicity is a major concern in catalytic reactions of biomass-derived molecules such as glucose dehydration, both because water is present in the media used for isolation and separation of saccharides and because water is a product of the reaction.[16] This work has been reported in *Industrial and Engineering Chemistry Research* in 2019 and is included as **Chapter 4**.[17]

Other than being used in catalytic reactions and as solvent, ILs are also of intense interest as electrolytes because of their ion dissolution and conductivity properties, and are being studied for applications in electrochemical devices because their wide electrochemical window.[3, 18] The study presented in **Chapter 5** touches upon the electrochemical properties of confined IL incorporated through both physical absorption and covalent tethering. Electrochemical impedance spectroscopy (EIS) is employed to extract resistance values for redox probe transport from aqueous solutions to conductive fluorinated tin oxide (FTO) electrodes in the presence of ILs and nanoconfined ILs. The resistances are used to calculate the permeabilities of hydrophilic and hydrophobic redox species through silica thin films with different treatments of the IL [BMIM] hexafluorophosphate ([$[PF_6]$). Silica thin films with two different pore sizes (8 nm and 2.5 nm) were used as confining materials to study size effects. Nanoconfinement is shown to enhance provide selectivity to ion transport based on the hydrophilicity of the probe investigated.

In **Chapter 6**, the effects of nanoconfinement on crystallization behavior of [BMIM][Cl] and [BMIM][PF_6] in mesoporous silica thin film is explored. Crystallization of ILs is important to researchers investigating their utilization in drug delivery and electrochemical devices because the conductivity, diffusivity and viscosity are directly

affected by their crystallization.[19-22] Thanks to the high-intensity grazing-incidence wide angle X-ray scattering (GIWAXS) with the synchrotron X-ray source at Argonne National Laboratory, *in situ* GIWAXS measurements are reported while varying sample temperature. Different from conventional characterization methods for crystallization such as differential calorimetry scanning (DSC) and X-ray diffraction (XRD), *in situ* GIWAXS allows characterization of crystallization of small amounts of material within thin films deposited on thick substrates. The results show complex effects of nanoconfinement on crystallization, phase transitions and melting of ILs.

Chapter 2: Background

2.1. Applications of Ionic Liquids

A large amount of research has addressed applications of ILs as solvents and reaction media for catalysts. This started with the successful demonstration of the Friedel-Crafts reaction in [EMIM]Cl-$AlCl_3$ in 1986.[23] The first use of IL for homogeneous transition metal catalysis was in 1990 by Chauvin et al. for propene dimerization. [4, 24] After these breakthroughs, research on IL in related fields boomed, partially because of the great potential of IL solvents for bioenergy refinery applications. As an example, good solubility of recalcitrant components of lignocellulosic biomass has drawn the attention of the research groups to the potential of ILs to act as media to control the activity and selectivity of biomass conversion catalysis.[6, 25]

Our interest in ILs was initiated by their applications in the production of 5-(hydroxymethyl)furfural (HMF) as part of the collaborative project with the Ladipo group in the Department of Chemistry at the University of Kentucky.[26, 27] HMF has been of great interest in recent years because as an intermediate for the synthesis of a variety of chemicals from biomass-derived glucose to help improve biofuel economics. [28-30] The dehydration of glucose to HMF can be achieved with a variety of Lewis acid catalysts or Brønsted acids (Fig. 1), but HMF yield is low and there are byproducts from the reactions when using conventional acids such as HCl and H_2SO_4, or in organic media such as dimethyl sulfoxide (DMSO).[5, 31] Other organic solvents suffer from issues of limited biomass solubility and solvent loss through evaporation. In contrast, the extremely low volatility of ILs prevents their loss even at heating or vacuum working

conditions. This also enables their characterization using ultra-high vacuum (UHV) characterization techniques such as X-ray photoelectron spectroscopy (XPS) and grazing-incidence small/wide angle X-ray scattering (GIS/WAXS).[1, 2, 32-34]

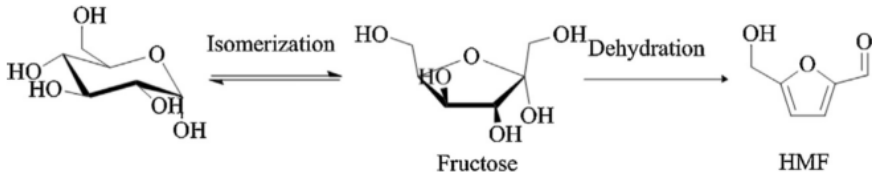

Figure 2-1. Glucose dehydration to HMF reaction pathway [16]

Dialkyl imidazolium cations, which are one of the most common classes of IL cations, have been reported to be a good solvents for saccharides.[35] The chemical and physical properties of imidazolium-based ILs are readily tunable for a given application by altering the length of the alkyl chain and the anion (e.g. chloride, PF_6^-, BF_4^-, etc.). [36-38] Numerous studies have shown that ionic liquid / transition metal catalyst systems provide excellent catalytic performance, giving high HMF yields from glucose dehydration under mild reaction conditions. [28, 29, 39] The following studies will be focusing on imidazolium based ILs. Aluminum-based catalysts are one of the first classes of catalysts to be studied with ILs since 1951 and they are well investigated.[6] Aluminum catalyst will act as Lewis acid for glucose to fructose isomerization and IL will act as Brønsted acid for fructose dehydration to HMF. [5, 16, 38]

In addition to being utilized in catalytic reactions, ILs also have great potential in applications of electrochemical devices because they consist of dissociated ions without the presence of additional solvent, and they have large electrochemical windows.[3, 18, 40] Taking lithium battery as an example, conventional carbonate electrolytes present

challenges due to low lithium ion conductivity, loss of solvent through evaporation and limited temperature range of operation. ILs overcome these concerns by having good thermal stability, good ion conductivity, low inflammability and extremely low vapor pressure.[40-42]

While ILs have many potential advantages, they also have drawbacks that may slow commercial adoption for all applications mentioned above. The high cost of ILs is one of the major problems. In addition, ILs still do not solve the leakage problem in energy storage devices and their high viscosity can lead to slow diffusion.[40] When used as solvent and in catalytic processes, although the low volatility mentioned above is a processing advantage, this property makes it difficult to recover non-volatile products from ILs.[5] Organic solvents have been employed to extract such products from bulk IL-catalyst systems, but it has not been conclusively demonstrated that it is possible to recycle IL catalyst mixtures for most catalytic processes reported.[6] The difficulty of catalyst and product recovery, together with the high cost and potential toxicity of ILs, have delayed their implementation in large scale industrial manufacturing. Supported IL systems are believed to provide a solution where the advantages of ILs can be maintained in a heterogeneous environment while reducing the amount of ILs required and reducing or eliminating their introduction into product streams.[10, 43]

2.2 Silica Mesoporous Material Supported IL Systems (SILS)

For the purpose of more economic and green utilization of ILs as mentioned above, supported ionic liquids (SILS) are believed to allow their solvent and ion transport

properties to be harnessed while facilitating their isolation and recovery.[10, 43] As a support, mesoporous silica is ideal because it provides high contacting area of ILs to catalysts or adsorption sites, and a large pore volume for transport of reactants and products. There is evidence in prior reports that confined ILs display different crystallization, thermal, electrochemical and molecular assembly behavior compared to bulk materials.[8-11] For example, Chen et al. observed similar interesting phenomenon of extreme melting point elevation of the IL [BMIM][PF_6] upon confinement in multiwall carbon nanotubes,[8] which might be a result of the shorter C-H···F bond and a more stable H-bond network that were induced by the carbon nanotube confinement. Moreover, greater charge transport was observed by Iacob et al. for [BMIM][BF_4] confined in nanoporous silica membranes, as measured by broadband dielectric spectroscopy and pulsed field gradient nuclear magnetic resonance (NMR).[9] This was attributed to the change of molecule packing by nanoconfinement, which leads to the higher molecule mobility and electrical conductivity. With more in-depth understanding of the impacts of the silica confinement on ILs as the studies mentioned, SILS can be tailored for different applications.

The heterogeneous composites with solid matrix and confined liquid pose challenges for some conventional characterization techniques such as NMR, x-ray scattering, transmission FTIR, and transmission electron microscopy (TEM). Therefore, new methods that present direct evidence of impacts of nanoconfinement on IL packing and interactions need to be developed to provide fundamental information for further investigations. With more characterization techniques available for confined ILs, the interpretation of studies conducted on bulk ILs can be extended to confined ILs and

compared with the properties observed in the bulk. **Chapter 4 and 6** provide details of modified transmission FTIR and GIWAXS techniques to enable the analysis of nanoporous silica thin film confined ILs and allow the study on hydration and crystallization behavior of confined ILs. Molecular dynamic (MD) simulation has been a popular tool to study the properties of confined ILs [44-48] on the basis of its ability to explore perturbations that that complement existing experiments or examine phenomena in cases in which the experiment is not feasible. However, limited information on ILs without confinement is one of the restrictions to building a robust and accurate model. Moreover, confined IL behavior that cannot be predicted with classic theories for molecule liquid in confined geometry have been observed in this dissertation work. Therefore, further experimental studies are still needed to provide future computational studies with more information.

There are a mainly two primary methods of physically loading of ILs into mesoporous silica materials that have been reported in the literature: *in situ* introduction of IL and post-synthesis impregnation.[49] For the former, ILs are introduced during the synthesis of the nanoporous silica materials. Because of the amphilicity of many ILs, they can be used as structure directing and templating agents in the synthesis of so-called ionogels. However, the synthesis is usually complicated and requires long aging time (a few days to a few weeks), such as in the case of 1-butyl-3-methylimidazolium bis(trifluoromethylsulfonyl)amide ([BMI][TFSI]) templated silica.[49, 50] Also, in the case of [BMI][TFSI] templated ionogel, the pore size is controllable by altering the relative amount of the IL. However, with increasing incorporation of IL, the pore diameter is less uniform, restricting the feasible range of confined IL. This dissertation

work adopts the method of post-impregnation, where the ILs are physically absorbed in the silica nanoporous thin films after synthesis. This extends the investigation to more selections of ILs including those that might not be ideal for synthesizing nanoporous silica materials and also allows more control over the pore size and structure when they are independent from the choice of ILs. It is also easier to reuse the silica supports.[15, 51] Thanks for this, Ivanchikova et al. have used titania oligomer grafted silica porous thin film produced by EISA for catalysis of 2,3,6-trimethylphenol (TMP) oxidization with H_2O_2 and the reaction selectivity remained almost 100% after 7 reuses.[51]

As an example of the study of IL supported by porous silica, Zhang et al. compared CO_2 absorption by the IL [BMIM][BF_4] confined in nanoporous silica gel with an average pore size below 12 nm and the absorption by the silica gel itself after the IL was washed away.[52] They observed much higher CO_2 absorption in the composite with IL confined in the silica gel. They also compared this result with the same IL coated on silica gel and glass particles and the nanoporous silica gel confined [BMIM][BF_4] still possessed the highest CO_2 absorption. This was attributed to the improved contact of IL with CO_2. Carbon dioxide absorption was then compared between the confined IL in nanoporous silica gel with different percentages of IL loading and it was found that the amount of CO_2 absorption per 100 g of IL was about the same. This revealed that there is a portion of the confined IL also displaying bulk IL properties that do not change with IL quantity, implying a complex solvation environment in confined IL with different interfacial and bulk IL properties.

ILs that are only physically confined in nanoporous silica thin films raise concerns about IL leaching especially when placed in flowing systems. Thus, ILs can be covalently

tethered on the silica pore surface to prevent IL leaching. For the existing silica nanoporous thin film in this work, the tethering can be achieved by silylation of the silica surface with an imidazolium-alkyltrialkoxysilane.[53-55] Another approach is to functionalized the silica surface with a linker first, then tether IL-catalyst compounds to the linker. For example, (3-aminopropyl)triethoxylsilane (APS) and n-[3-(trimethoxylsilyl)propyl]ethylenediamine (DA) were employed in Pu et al.'s study as the linker to provide the amine sites on the hydroxylated silicon surface for subsequent immobilization of an imidazolium IL with COOH groups.[56] Liu et al. grafted 1-n-[2-(3,4-dihydroxyphenyl)ethyl]propionamide-3-methylimid-azolium chloride on hydroxylated silicon wafer.[57] In this dissertation, silylated IL tethering is adopted as an easier one-step method to achieve IL tethering, which gives more freedom to attach ligand-promoted catalysts to the IL during the silylation.[27] The procedures were adopted from the study of Vangeli et al. tethering 1-(3-silylpropyl)3-methylimidazolium hexafluorophosphate in nanoporous silica particles for CO_2/CO separation and is described in detail in **Chapter 5**.[58] In **Chapter 5**, post-synthesis IL tethering is extended to nanoporous thin films instead of particles or flat surfaces, as in the studies mentioned above,. XPS depth profiling of the thin film is used to verify the tethering and accessibility of the pores. The functionalization directionally orients the imidazole head groups towards the center of the pores and has been shown to enhance the gas diffusivity compared to physically confined IL by two orders of magnitude in a study of CO_2/CO separation.[59] This tethering also can change the surface properties of hydroxyl-terminated (hydrophilic) silica surfaces, for example with a hydrophobic ionic liquid.[49, 55] This change in surface behavior will be part of the effect explored in Chapter 5 for

redox probes of differing hydrophilicity transported through confined IL in pores with different surface properties.

2.3 Silica Mesoporous Thin Films

Silica thin films with orthogonally aligned nanoporous structure have a wide range of potential applications including for membranes, templated electrodeposition, water purification and biphasic catalysis.[60-63] Nanoporous silica thin films also are excellent model systems that allow the use of advanced charaterization techiques including electrochemical impedance spectroscopy (EIS), Fourier-transform infrared (FTIR) spectroscopy in novel models such as film transmission and attenuated total reflection (ATR), and grazing-incidence wide/small angle X-ray scattering (GIW/SAXS). These powerful tools were employed in past studies in our research group to gain insights into the formation and transformation of nanoporous oxide films, and properties of molecular systems confined within their pores.[14, 15, 64, 65] Synthesis of nanoporous silica films with orthogonally oriented pores is essential to the study of confined ILs, for it provides the confining matrix and supporting material for the research in this dissertation.

Silica thin films utilized in this dissertation are sythesized with sol-gel reactions using the silica precursor tetraethyl orthosilicate (TEOS),[66] where a templating surfactant is dissolved in a solution of hydrolyzed TEOS. The surfactant is expected to co-assemble with the silica precursors into a mesophase analogous to a lyotropic liquid crystal, and the resulting structure are affected by the concentration of the surfactant with respect to silica precursor.[66, 67] The resulting sol will then go through a condensation

reaction where the Si-OH in hydrolyzed TEOS forms -Si-O-Si- bonds and it forms an amorphous silica network.[66] This process is widely used to produce silica nanoporous particles, monolith and thin films.[42, 68] For thin films, the sol is deposited onto support materials (typically glass or silicon wafers) through dip coating or spin coating. Such an evaporation-induced self-assembly (EISA) process accelarates the time-consuming templating procedures in batch operations and can potentially be scaled to roll-to-roll processing.[69, 70] After aging, the condensed film is calcined at high temperature to remove the surfactant and other organics that might be involved in the process. This leaves behind a porous structure (Fig. 2). Pore size under 10 nm can be controlled using different types of templating agents or surfactants.[71, 72] For pore size beyond that, swelling agents can be used to enlarge the pore size for EISA processes. [73, 74]

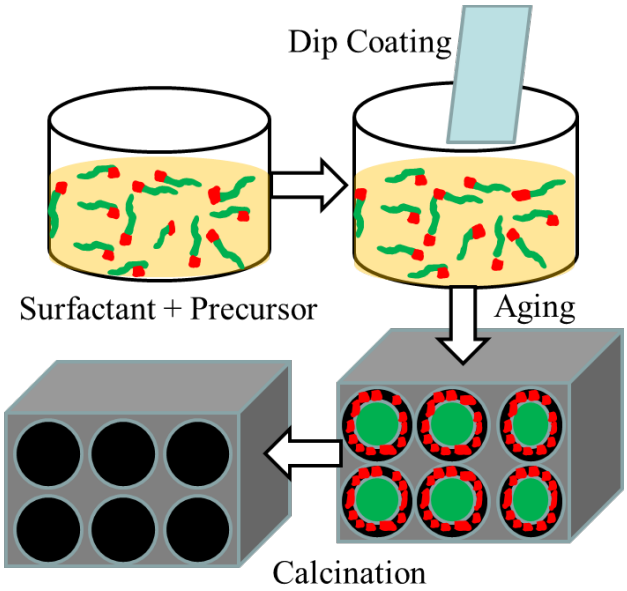

Figure 2-2. Schematic of silica film synthesis by the sol-gel process. Adapted from ref. [65] by Islam, Syed Z.

Surfactants are generally classified into cationic, non-ionic and anionic.[68] Because silica and its precursors are negatively charged above pH 2-4, anionic surfactants usually cannot be used as templates for silicate materials. In this dissertation, the poly(ethylene oxide)-polypropylene oxide (PEO-PPO-PEO) triblock copolymer Pluronic P123 is used as a nonionic pore template. Silica films with vertically oriented mesopore channels have been successfully synthesized using P123 and applied for various studied in our resesarch group.[14, 17, 75] This approach provides silica films with an ordered close-packed array of cylindrical pores with a diameter of about 8-10 nm.[15, 17, 64] To study the impact of pore size on confined ILs, the cationic surfactant cetyltrimethylammonium bromide (CTAB) will also be used as a template to producing silica films with a pore size of 2.5 nm.[76, 77] Other commonly used surfactants include the commercially available non-ionic Brij surfactants (Brij 35 to 56) that provide pores about 3-4 nm and Pluronic F127 (PEO106-PPO70-PEO106) that produces 10 nm cylindrical micelles.[70, 78, 79] For larger pore size, swelling agents are commonly used to enlarge the size of the micelles and push the pore size from the EISA abovee 10 nm. Darren et al.'s study successfully produced Pluronic F127 templated silica with a secondary Pluronic polymer P103 as swelling agent and obtained up to 15 nm porous structure.[74]

Silica surface are common for substrates for silica thin films. Glass slides and Si wafers will be used as supports for silica films and they will be vertically drawn from sols to deposit films by dip-coating. Obtaining vertically aligned pores requires special consideration, however. Surfactant micelles have preferential interactions between their polar headgroups and hydrophilic glass surfaces, resulting in self-assembled as-deposited

films with micelles oriented parallel to the substrate. Perpendicular porous structures can be achieved by creating chemically neutral substrates to eliminate preferential interactions between different parts of the template and the surface.[64, 80-82] Copolymer surfactant templated silica nonporous material was first synthesized using poly(alkylene oxide) block copolymers for Santa Barbara Amorphous type material (SBA) in 1998.[83, 84] For the surfactant under the same cataloge, P123, templated films, the silica surface is modified by crosslinked PEO-PPO random copolymers and P123 to create a chemically neutral surface that is equally attractive to hydrophilic (PEO) and hydrophobic (PPO) blocks of P123 molecule, thus resulting in perpendicularly aligned pores (Fig. 2-3).

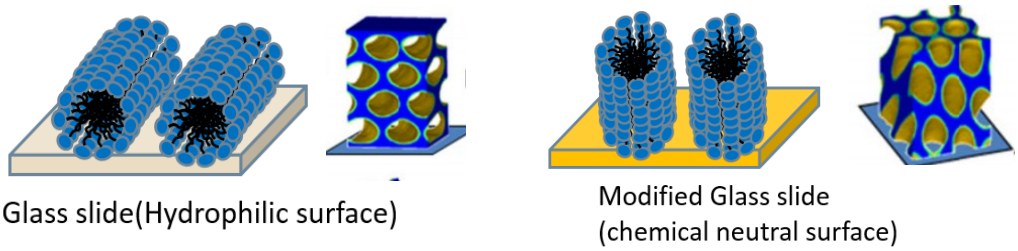

Figure 2-3. Schematics of parallell (left) and perpendicular (right) aligned micelles on unmodified(left) and modified (right) surfaces, and the resulting parallel and perpendicular mesoporous films that they would serve as templates for. Adapted from Zhou et al.,[15] Copyright (2020) with permission from Advanced Materials Interfaces

Attempts have been made to extend this approach by utilizing a surface modifying agent poly(vinyl alcohol-r-ethylene), which is chemically neutral towards CTAB.[76] However, this method is not very effective for CTAB templated silica films. Thus, a novel method of doping the silica matrix with small amount of titania was developed to obtain an alternative pore size. This method takes advantage of the different sizes of Ti and Si in the Si-O-Ti network, which makes the nanoporous structure not as stable as a pure Si-O-Si network during calcination.[85, 86] The mesopores connect with each other vertically when the condensed silica film goes through thermal contraction during calcination and form perpendicularly aligned channels with respect to the substrate. More details will be provided and discussed in **Chapter 3**.

2.4 Characterization Techniques

2.4.1 Fourier Transform Infrared (FTIR) Spectroscopy

FTIR is a characterization technique that provides quantitative measurements of the absorption of infrared energy by solid, liquid or gas samples. It probes vibrational modes of molecules so that researchers can assign absorption bands to functional groups and probe changes in bonding, intermolecular interactions, and quantities of species present in the sample. Multiple single shot spectra are taken then accumulated and averaged to improve the signal-to-noise ratio.[87][88] This technique is widely utilized for qualitative analysis by identifying fingerprint patterns, and tables of absorption bands with associating functional groups are easily accessible from online databases and textbooks. FTIR can also be used for quantitative analysis through Beer's law that establishes a proportional relationship between the intensity of the absorption band and the concentration of the corresponding compound or, in the case of FTIR, bond in a mixture.[87, 89, 90] For example, Hagemann et al. probed the temperature dependent crystalline fraction change in polyethylene by interpreting the increase or decrease in the intensity of the methylene rocking bands near 725 cm^{-1}.[89] Change et al. conducted IR study on the mixture of [BMIM][PF_6] and P123 at different compositions and pressures and revealed that the H-bonding network formed between the imidazole and P123 is more stable at higher pressure, as interpreted from the appearance and greater intensity in the peaks corresponding to the formation of H-bondings.[91] MacMillan et al. also extensively studied hydration of different imidazolium IL droplets with IR and related the hygroscopicity of IL to their carbon side-chain length and counter ions.[36, 92]

More information such as inter-, intra- molecular interactions and different coordination states of functional groups can be interpreted from band position shifts and changes in peak shapes.[93, 94] The study of IR peak shape change is common for the -OH stretching peak from water due to the broad range of frequencies associated with a wide range of strengths of hydrogen bonding interactions among water molecules and with other compounds through hydrogen bonding.[95-97] This -OH stretching peak is usually centered at 3400 cm^{-1} and most commonly seen to be deconvoluted into three peaks with Gaussian peak shapes ranging from 3200 cm^{-1} to 3600 cm^{-1}.[96-98] Higher frequency peaks corresponds to weakly H-bonded water molecules and vice versa.[97, 99] This can be applied in different context and used for interpretation of the solvation environment of water for specific cases. As one example, Oroni et al. used deconvolution of OH stretching bands to identify differently coordinated water molecules entrapped in bis(2-ethylhexyl) sodium sulfosuccinate micelles.[97] They assigned the band at the highest frequency 3603 cm^{-1} to non- or weakly-H-bonded; 3465 cm^{-1} to molecule in distorted structure such as in cyclic form); and the lowest frequency band at 3330 cm^{-1} to regular structured H-bond like in bulk water. Cammarata et al. then observed peak shift and splitting in the OH stretching band from water in the mixture of water and [BMIM] ILs, indicating that water forms H-bonding with ILs.[96] The interpretation of water absorbed by thin films of IL [BMIM][Cl] and the same IL confined in silica nanopores in **Chapter 4** is adapted from the OH band assignment from Fazio et al.'s study.[93] Their study suggested that water aggregates into clusters in the mixture with [BMIM][BF_4]. Fazio et al. also deconvoluted the broad OH stretching band into three components. Within the range of 3200 to 3700 cm^{-1}, they assigned the high frequency component to

relatively weak bonding between anion-water (AW); they assigned the mid frequency band to interface water (IW) at the surface of the aggregated micelles; and the low frequency band was assigned to bulk-like water. This different coordinated water assignment in principle agrees with Oroni et al.'s study mentioned above, and is closer to the system studied in **Chapter 4**. Such analysis of different coordinated water through IR OH stretching band deconvolution is useful for studying dynamics in emulsions, polymers, or upon confinement.[100-102]

The *in situ* transmission FTIR characterization method employed in **Chapter 4** was inspired by a previous study in the group of Koganti et al., where the kinetics of the formation of surfactant templated silica was investigated.[72] Another study of dynamic process of water evaporation followed by crystallization in $NaNO_3$ solution droplets by Zhang et al provided more details to achieve relative humidity control.[103] In their study, the relative humidity (RH) and time are the two controlled variables in their study and the nitrate out-of-plane bending band shifting from 829 cm^{-1} to 837 cm^{-1} was taken as a measurement of crystallization. By comparing the changes in bands of interest with incremental changes in RH (Fig. 2-4), the drying and crystallization process was better understood. Therefore, we believe that the in situ FTIR with varying RH can be used to investigate the CH stretchings and compositions of differently coordinated water molecules and indicate the effects of the silica nanoconfinement on IL properties.

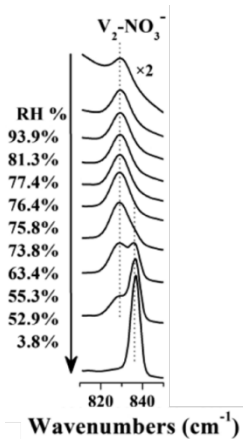

Figure 2-4. *in situ* FTIR spectra of the nitrate out-of-plane bending vibration in $NaNO_3$ droplets during the dehumidifying process. Reprinted from Zhang et al.'s study,[103] Copyright (2014), permission from American Chemical Society

2.4.2 Grazing-incidence Small/wide-angle X-ray Scattering (GIS/WAXS)

GIS/WAXS is a powerful surface-sensitive characterization technique for structure characterization of thin films in organic, inorganic or polymeric materials. The thin film under investigation is usually placed parallel to the x-ray beam line, and then adjusted to allow the x-ray beam to impinge on the film at a very low angle of incidence α_i. This angle is selected to be close to the critical angle of the substrate material, α_c. The two-dimensional x-ray scattering pattern from the sample is projected on a detector placed behind the sample. For a vector from the thin film with the exit angle α_f, out-of-plane angle ψ and in-plane angle 2θ, the reciprocal space vector components q_x, q_z and q_y are shown in the inset of Fig. 2-5.

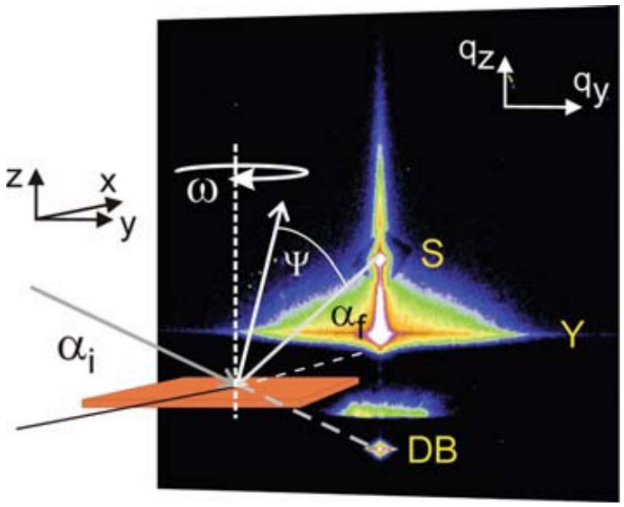

Figure 2-5. Schematic of an example of a 2D GISAXS pattern with DB: direct beam, S: specular peak, and Y: Yoneda horizon. Reprinted from Müller-Buschbaum,[104] Copyright (2009), with permission from Springer Nature

Usually only q_y and q_z are probed using a 2D detector.[104, 105] This 2D pattern arises from regions of contrasting electron density of repetitive structures in the sample – for example, contrast between empty pore space and solid matrix or core-shell structures.[106, 107] The d-spacing can be obtained from the reciprocal vector q by $d = 2\pi/q$. One-dimensional patterns can be reduced by integrating the intensity of the 2D visual representation of the scattering patterns in a color scaled map in vertical, horizontal, azimuthal and angular directions. With the capability of capturing 2D patterns with GIS/WAXS, it is also possible to probe the orientations of non-isotropic structures in the samples. In the case of our study, the perpendicularly oriented HCP structure has been observed to display a GISAXS pattern of two vertical rods asymmetric to $q_z=0$, as discussed in **Chapter 3**.

The sample-to-detector (SD) distance for GISAXS usually ranges from 1 to 10 m to capture features at low angle which correspond to nano- or even micron-scale structures.

Space group, unit cell parameters and angles and other information can be obtained by GISAXS simulation packages such as GIXSGUI [108] and NANOCELL [109]. This is extremely helpful to characterize the pore orientation, structure and dimensions of the orthogonally oriented silica nanoporous thin films because GISAXS is currently the only non-destructive characterization technique providing relevant information. Previously, ethanol flux was employed to characterize properties of channels in P123 templated silica thin film supported by a macroporous membrane.[14] However, the method of solvent flux is limited to silica thin films synthesized on a macroporous membrane support. 1D x-ray diffraction (XRD) characterization have been attempted in the group when P123 templated silica film with perpendicularly oriented pores was first developed. [64] However, XRD only provides indirect proof of the orthogonal pore orientation by observing the absence of the out of plane peak when compared to a parallel porous structure produced with similar method as the control. Microscopic methods such as TEM are also limited to substrates that are thin enough to be electron transparent, which is not applicable for most of the substrates used in this study, such as glass slides and Si wafer. In our previous studies of the pore orientation of silica thin films, successful TEM analysis was only achieved through scraping off the film from the substrate and identifying the pore structure in pieces of the film that are larger than the film thickness obtained through profilometer.[64] However, this method is very inefficient and destructive to the films.

In order to probe atomic level structure such as crystallization in the samples, a small SD distance (100 to 500 mm [110]) is required for GIWAXS to project x-ray patterns onto a wide angle range. GIWAXS has been mentioned in the studies regarding

nanostructured titania thin film for probing titania crystallization under thermal treatment because titania crystallization is a well-known concern for the stability of the nanostructure.[85, 111, 112] It was employed for the similar reason in **Chapter 3**. In **Chapter** 6, GIWAXS was used for probing IL crystallization when confined in silica nanoporous thin films. Li et al. have studied isothermal crystallization of imidazolium chloride ILs with 16 and 18 carbon chains using time-resolved transmission WAXS.[113] Their study observed four polymorphs for both ILs under their melting points and determined the change of crystal phase by tracing the appearance or disappearance of corresponding peaks, which provides us with an initial guideline for interpreting x-ray scattering data of ILs.

For x-ray measurements with grazing-incidence angle feature, the penetration depth Λ can estimated by

$$\Lambda = \frac{\lambda}{4\pi}\sqrt{\frac{2}{\sqrt{(\alpha_i^2-\alpha_c^2)^2+4\beta^2}-(\alpha_i^2-\alpha_c^2)}}$$

,[105] where α_c is the critical angle approximated to be $\sqrt{2\delta}$; and δ is derived from the real part of the complex refractive index, β is obtained from the imaginary part of the complex refractive index:

$$\delta = \frac{\rho N_a r_e \lambda^2}{2\pi}\frac{\sum_{i=1}^{n} c_i f_{1,i}}{\sum_{i=1}^{n} c_i M_i}$$

$$\beta = \frac{\rho N_a r_e \lambda^2}{2\pi}\frac{\sum_{i=1}^{n} c_i f_{2,i}}{\sum_{i=1}^{n} c_i M_i}$$

β and δ are dependent on the fractions of the elements in the sample and the element based parameters f_1, f_2 are available from an online database provided by Berkeley Lab.[114] The composition in our case is determined by the x-ray photoelectron spectroscopy (XPS) depth profile.

In the cases of characterizing crystallizations in the samples, crystallite size D_{hkl} is another quantitative value that can be obtained from peak widths, or the full width at half-maximum (B_{hkl}) of a diffraction spot from the 1D patterns according to Scherrer formula:

$$D_{hkl} = \frac{K\,\lambda}{B_{hkl}\,\cos\theta_{hkl}}$$

where λ is the x-ray wavelength, θ_{hkl} is the Bragg angle and K is the Scherrer's constant that is most observed to be 0.9.[115] With GIWAXS, the non-negligible peak broadening caused by divergence of the scattered beam, radial divergence increased by the energy bandwidth, and geometric smearing due to footprint of the x-ray beam on the samples needs to be taken into account.[116] Smilgies et al. have systematically studied the contributions of each factor to GIWAXS pattern peak broadening and found that the geometric smearing is the most dominant factor.[116] In the study discussed in Chapter 6, the calculation of the crystallite size of unconfined [BMIM][PF_6] at -88 ℃ takes energy bandwidth B_{BW} and geometric smearing B_{geo} into account and obtained B_{res}:

$$B_{res} = \sqrt{B_{BW}^2 + B_{geo}^2}$$

$$B_{BW} = 2\eta \tan\theta_{hkl}$$

$$B_{geo} = w\,(\tan 2\theta_{hkl})/L$$

where η =10^{-4} for Si (111) optics, w is the beam footage on the sample surface estimated to be 8 mm and L is the SD distance of 228 mm in the setup.[116] The real band width B_{hkl} equals $\sqrt{B_{exp}^2 - B_{res}^2}$ and Bexp was obtained from peak analysis using Origin. Then the crystallite size can be calculated from the relation derived from the original Scherrer equation: [116]

$$D_{hkl} = \frac{2\pi K}{\triangle\, q_{hkl}} = \frac{2\pi K}{\frac{4\pi}{\lambda}\cos\theta_{hkl}\frac{B_{hkl}}{2}} = \frac{\lambda\, K}{\cos\theta_{hkl} B_{hkl}}$$

This D_{hkl} was calculated for the three most intensive peaks and the average value was taken for the crystallite size in unconfined [BMIM][PF_6] at -88 ℃.

2.4.3 Electrochemical Impedance Spectroscopy (EIS)

EIS is a non-destructive electrochemical characterization technique that has been applied to corrosion engineering, the development of solid-state electronics and paints.[117] The method is based on measuring how the current of a system responds to a sinusoidal AC potential with small amplitude as a function of frequency.[117-119] The complex impedance measured by EIS can be described by the following relation combining the well-known Ohm's law and Euler's formula,[117, 120]

$$Z(\omega) = \frac{E(\omega)}{I(\omega)} = |Z_0| \exp(j\phi) = |Z_0|(\cos\varphi + j\sin\varphi)$$

$$= |Z_0|\cos\varphi + j|Z_0|\sin\varphi = Z_{Re} + jZ_{Im}$$

where ω is the frequency and φ is the phase shift angle between the potential $E(\omega)$ and responding current $I(\omega)$. There are two common ways to plot the electrochemical impedance data and conduct graphical analysis, Nyquist plots and Bode plots (Fig. 2-6). In Nyquist plot, the Z_{Im} is plotted with respect to Z_{Re} with higher frequency data found close to the origin. Since the frequency is not directly shown on Nyquist plots, some researchers prefer to present data in the form of Bode plots which present the relations of $\log|Z|$ and φ vs. log ω. However, Nyquist plots are more sensitive to changes in the resistance in a system.[121]

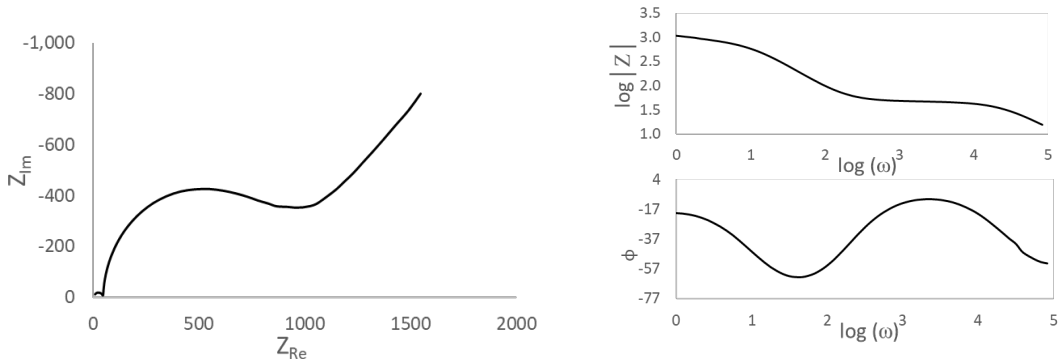

Figure 2-6. Sample experimental Nyquist plot (left) and corresponding Bode plots (right) of a piece of bare fluorine doped tin oxide (FTO) glass tested with a three-electrode cell

For both Nyquist plot and Bode plots, equivalent circuit fitting is required for relating physicochemical parameters to the impedance response and conduct quantitative analysis.[119] Cesiulis et al. have systematically studied EIS data analysis for thin films, summarized optimum equivalent circuits for some representative scenarios and assigned physical meanings to each element in the circuit in the system.[117] The data presented in Fig. 2-6 is fits well with the simple Randles circuit (Fig. 2-7) according to Cesiulis's study, where the resistor R1 represents the electrolyte solution resistance; R2 represents the charge transfer resistance at the surface of the working electrode; Warburg element (Ws1) represents the diffusion of the redox probe in the bulk electrolyte and a constant phase element CPE1 represents the double-layer capacitance attributed to the charge polarization on the working electrode surface.

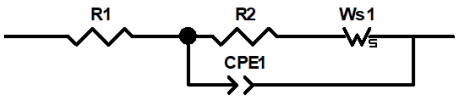

Figure 2-7. Randles equivalent circuit with R1 = electrolyte solution resistance, R2 = charge transfer resistance at the sample surface, Ws1 = Warburg diffusion element, and CPE1 = constant phase element with electric double-layer capacitance.

The system for EIS consists of a piece of glass with a conductive layer of FTO as working electrode, a Pt counter electrode, and a Ag/AgCl reference electrode. The working electrode is submerged in a KCl solution with a redox probe, 1,1'-ferrocenedimethanol (FDM), dissolved in the solution. In the Randles circuit, R1 and R2 are charge transfer resistance corresponding to the small (high-frequency region close to the origin) and big semi-circle (mid-frequency region) on the Nyquist plot (Fig. 2-6); CPE1 represents a double layer capacitor that results from the potential difference between the working electrode and electrolyte and it might contribute to the depression of the big semi-circle of R2 on a Nyquist plot whereas an ideal capacitor yields a non-depressed semi-circle; and following the semi-circle representing R2, is a straight line corresponds to the Warburg diffusion Ws1 in electrolyte solution.[122-124] For silica thin films with different treatments with IL as the material deposited on the conductive FTO surface, R2 is the element that is the most reflective on how easy the redox probes transport through the thin films and get access to the working electrode.[117] Based on this discussion, it should be clear that the advantage of Nyquist plots over Bode plots is that it is easier to compare the charge transfer resistance on the working electrode on Nyquist plots when R2 is the dominant element, which will be the focus of this work. Thus, the EIS data discussed in **Chapter 5** will be in the form of Nyquist plot.

Chapter 3. Formation of Vertically Oriented Channels during Calcination of Surfactant-Templated Titania-doped Mesoporous Silica Thin Films

Yuxin He,[1] M. Arif Khan[1], Joshua Garay[1], Aniruddha Shirodkar[1], Andrew Drake[1], Joseph Strzalka[2], Qingteng Zhang[2], Stephen E. Rankin[1]* and Barbara L. Knutson[1]*

[1] University of Kentucky, Department of Chemical and Materials Engineering, 177 F.P. Anderson Tower, Lexington, KY, USA

[2] X-ray Science Division, Argonne National Laboratory, Argonne, Illinois 60439, USA

3.1 Abstract

The mesoporous structure development during calcination of titania-doped mesoporous silica thin films is characterized by *in situ* grazing-incidence small angle x-ray scattering (GISAXS). A small amount of titania (≤ 6 wt%) was incorporated in cetyltrimethylammonium bromide (CTAB) templated film by two methods in this study: dispersion of titania in the silica matrix, and fixing titania at the pore surface by complexation of the titania precursor with a sugar-based co-surfactant, dodecyl maltoside ($C_{12}G_2$). Before calcination, films templated with only CTAB displayed a mesoporous structure with a mixture of 2D hexagonal and randomly oriented porous structure, while $C_{12}G_2$-complexed film possessed randomly oriented porous structure only. Both methods yield a final structure of hexagonal close-packed pores orthogonally oriented to the substrate after calcination at 500 ℃. This is attributed to weak Si-O-Ti bonds which allow diffusion to occur at 500 ℃, combined with unidirectional thermal contraction of the film in the vertical direction. Thus, the randomly oriented pores merged vertically and formed channels with d-spacing of 3.8 nm (without $C_{12}G_2$) and 4.1 nm (with $C_{12}G_2$).

Titania doping greater than 1% is required for this transformation to happen for films with no $C_{12}G_2$ complexation while the transformation was observed for films with $C_{12}G_2$ complexation even at 0.005% titania doping.

3.2 Introduction

Mesoporous silica materials (with 2 to 50 nm pore diameter[125]) prepared by surfactant templating provide a thermally and chemically stable platform for applications requiring uniform, tunable nanopres.[126] This enables them to stand against possible harsh chemical and thermal environments in applications including electrochemical devices, such as in flow batteries and as solid-state electrolytes.[49, 50, 127] A highly adaptable, scalable approach to preparing thin films of mesoporous silica is evaporation induced self-assembly (EISA) where solvent removal helps to drive the co-assembly of surfactant pore templates and hydrolyzed silica precursors such as tetraethyl orthosilicate (TEOS). The surfactant concentration contributes to different structures of surfactant micelles and the pore size of the silica material can be controlled by the length of the alkyl tail of small molecule surfactants (<10 nm).[67, 68, 70, 126, 128] Taking cetyltrimethylammonium bromide (CTAB) as an example, different ratios of CTAB: Si can result in 2D, 3D hexagonal or bicontinuous cubic mesopore structures.[67, 122, 129]

For many applications requiring fast mass transfer across a mesoporous silica thin film, a desirable architecture to form by EISA would be cylindrical channels oriented perpendicular to the substrate. However, to provide films with small (2-5 nm) mesopores for size exclusion and nanoconfinement enhancement, small molecule surfactant templates need to be used, such as alkyltrimethylammonium salts. Unfortunately, cylindrical micelles of both cationic and non-ionic surfactants in EISA-generated silica

thin films usually align parallel to hydrophilic hydroxyl-terminated oxide substrates due to preferential interactions between hydrophilic headgroups and the substrate. This parallel structure was originally reported in hexagonal close packed (HCP) CTAB-templated mesoporous films by Lu et al.[71] Tolbert et al. developed a method to orient the mesostructure in CTAB-templated silica by applying a magnetic field, but a very high field strength (12 T) is needed, which would limit opportunities for scaling production of films aligned by this approach.[68, 130] Robertson et al. also obtained vertically aligned pores in CTAB templated silica films through electrochemically assisted surfactant assembly but this approach is restricted to conductive substrates.[131] Chemical modification of surfaces such that they interact equally with the head and tail of the surfactant template, possibly combined with confinement between two modified surfaces, has been shown to be a reproducible approach to synthesize Pluronic P123 templated silica films with orthogonally oriented HCP (o-HCP) pores on different substrates including membranes.[14, 17, 64, 75] While effective, this strategy has only been demonstrated with block copolymer templates, which typically give pore diameters in excess of 5 nm.[68] Surface modification has been attempted using the cationic surfactant CTAB in an attempt to produce small, vertically aligned pore channels, but has been found to be challenging.[76]

The present study reports a serendipitous discovery of a method of producing o-HCP films by EISA using CTAB by doping the silica matrix with a small amount of titania to facilitate restructuring during thermal treatment. The original motivation was to observe structure evolution in films with well-dispersed Ti sites expected to be active for catalysis and enediol binding.[132, 133] To promote dispersion, complexation of the sugar-based

dodecyl maltoside surfactant ($C_{12}G_2$) with the titania precursor titanium isopropoxide (TIP) was employed and compared with titanosilica films without $C_{12}G_2$, where CTAB was also used as a majority surfactant in both cases. There are well-known concerns regarding segregation of titania in the silica matrix due to rapid hydrolysis of titania precursors relative to TEOS and subsequent crystallite formation during heating.[85, 112, 133, 134] Hüsing et al. used a complex of Ti with Brij 56 to disperses titania on the micelle surface and prevent titania crystallization.[134] Rahman et al. achieved a similar effect precomplexation of $C_{12}G_2$ with TIP followed by addition of CTAB and TEOS.[85] On the other hand, titania precipitation can be avoided for low Ti loadings by simply handling TIP under a low moisture environment until the formation of Ti-O-Si linkages with TEOS.[132]

In addition to introducing chemical functionality, introduction of transition metals to silica has been shown to change its thermal evolution. Soler-Illia et al. found that introducing Zr to zirconosilicate films increased the degree of unidirectional contraction during aging, suggesting an increase in the mobility of atoms in the walls of the material.[135] This leads us to hypothesize that doping of silica with Ti may facilitate mesophase transformations caused by thermal and solvent-induced stress within the films. Transformations of block copolymer thin films to vertically aligned cylindrical structures have been reported in response to solvent removal,[136] solvent annealing,[137] and thermal treatments (sometimes combined).[138, 139] If Ti doping "softens" the silica matrix to allow similar transformations, vertical cylindrical pores can be formed during aging due to either solvent or thermal effects. In support of this possibility, Oveisi et al. observed that columnar mesopores aligned parallel to the surface

of titania-alumina mixed thin films connect with each other vertically after unidirectional contraction during thermal treatment.[140]

The novelty of this approach is that it takes advantage of unidirectional contraction during aging, surfactant removal and pore wall densification during thermal treatment of titanosilicate films to produce films with vertically aligned, 2.5 nm diameter channels. Variable levels of doping are used to determine the range of titanosilicate composition allowing transformation to vertically aligned pores with retention of long-range order. *In situ* grazing-incidence small-angle x-ray scattering (GISAXS) using a synchrotron x-ray source at Argonne National Laboratory provides insights into the development of the structure during calcination. The mesostructure is probed using *in situ* GISAXS up to 550 °C at a heating rate of 1 °C/min, simulating the calcination process for films prepared with and without $C_{12}G_2$ complexation of TIP. The results of this study will provide evidence of a new strategy for the formation of vertically aligned pore structures based on modification of the mechanical properties of pore walls combined with solvent and thermal annealing methods known in block copolymer literature.

3.3 Experimental Methods and Materials

n-Dodecyl β-D-maltopyranoside ($C_{12}G_2$, HPLC grade, ≥99%) was obtained from BioVision Inc; tetraethyl orthosilicate (TEOS, 99%) from Acros Organics; and cetyltetramethylammonium bromide (CTAB, 99.8%) from MP Biomedicals. Nochromix powder (Godax Labs) and isopropanol (molecular biology grade) were purchased from Fisher Scientific; 200 proof ethanol from Decon Laboratories; and deionized ultra-

filtrated (DIUF) water, acetone (>99.5%) and HCl (36.5-38% in water) from BDH analytical. Titanium (IV) isopropoxide (TIP, ≥97%) and fuming H_2SO_4 (95-98% in water) were obtained from Sigma-Aldrich. All the chemicals were used as received without further purification. Borosilicate glass substrates were purchased from VWR Int.

Non-titania-doped silica sol preparation: Silica thin films with no titania were synthesized by a CTAB-templated sol-gel process according to previously published procedures [141, 142] with minor modifications. Initially, 1.43 mL of TEOS was added to 0.98 mL ethanol under constant stirring and 0.21 mL of DIUF water and 0.27 mL of 0.1 M HCl was added. The mixture was stirred for 1 h to initiate the hydrolysis of silica precursor. Then an additional 0.12 mL of DIUF water and 1.03 mL of ethanol were added. 322 mg of CTAB was added to the reaction mixture before an additional 3.42 mL of ethanol and the final sol for dip coating was made by stirring for another 1 hr.

Titania-doped silica sol preparation with and without sugar surfactant complexation: Silica thin films with 0.005% to 6% titania (complexed) were synthesized by mixed ionic and sugar surfactant complexed with TIP according to our previously published paper.[141] As an example, for 2% titania-doped films, 70 mg of $C_{12}G_2$ was dried under vacuum at 50 °C for 24 hr and dissolved in 2.4 mL of absolutely dry ethanol under nitrogen. 42 µL of TIP was added to this ethanolic solution of $C_{12}G_2$ under dry nitrogen and the resulting solution (Solution 1) was stirred for 3 h in a sealed vial under nitrogen environment to complete complexation of TIP with the sugar head-group of $C_{12}G_2$. Separately, 1.41 mL of TEOS was added to 0.98 mL ethanol under constant stirring and 0.21 mL of DIUF water and 0.27 mL of 0.1 M HCl was added. The mixture was stirred for 1 hr to hydrolyze the silica precursor (Solution 2). Afterwards, Solution 1

was added dropwise to Solution 2 with vigorous mixing in a nitrogen glove bag and the mixture was kept stirring while 0.12 mL of DIUF water and 1.03 mL of ethanol were added. 252 mg of CTAB was added to the reaction mixture before an additional 3.42 mL of ethanol, making the overall molar ratio of TEOS: TIP: EtOH: H_2O: $C_{12}G_2$: CTAB equal to 1: 0.022: 20: 5: 0.004: 0.024: 0.104 and the final sol for dip coating was made by stirring for another 1 h. For silica thin films with different percentages of titania doping, the amount of $C_{12}G_2$ was adjusted based on a 1:1 molar ratio of Ti: $C_{12}G_2$. The amount of CTAB was also adjusted to keep total surfactant mass (CTAB+ $C_{12}G_2$) at 322 mg. For titania doped silica thin films templated only by CTAB, similar amounts of TIP were used without complexing with $C_{12}G_2$, with similar procedure and 322 mg CTAB (no $C_{12}G_2$).

Silica thin film deposition: Borosilicate glass substrates were first cleaned by submerging in Nochromix solution (prepared in fuming H_2SO_4 using the manufacturer's recommended procedure) overnight and multiple repeated rinsing with ethanol and water. After cleaning the glass slides, they were then dried at 90 °C and dip coated with the sol prepared previously (withdrawal speed 6 cm/min) before placing into an oven for aging at 50 °C for 48 hr. Aged films were heated at 120 °C for 6 hr and then calcined in air at 500 °C for 1 hr (heating ramp 1 °C/min). This thermal treatment was intended to promote curing of the silica matrix without loss of mesostructural order.

GISAXS and GIWAXS data acquisition for static samples: The GISAXS and GIWAXS analysis of the silica thin films were performed separately to determine the mesostructure and crystallinity, respectively, at Sector 8-ID-E of the Advanced Photon Source (APS) beamlines at Argonne National Laboratory using X-ray wavelength of 1.14

Å (10.92 keV). Films were attached to the sample holder before placing in a vacuum chamber with mica and Kapton windows (for passage of the incident and scattered beam, respectively). Horizontal beams with sizes 200 μm × 20 μm and 100 μm × 50 μm (H × W) for GISAXS and GIWAXS (respectively) were impinged on the samples (incidence angle, $\alpha_i = 0.16°$). The scattered X-ray was collected using a Pilatus 1M area detector to obtain 2D GISAXS (sample-to-detector distance (SDD) of 2185 mm) and GIWAXS (SDD of 228 mm) profiles. The 2D patterns were reduced along different directions using the GIXSGUI package in MATLAB [108, 143].

In situ GISAXS and GIWAXS measurements: For GIWAXS measurements, samples were heated up to 550 °C in air (heating rate 2 °C/min) in a stainless-steel oven with interior dimensions approximately 2" × 1.875" × 0.75" (Figure 3-1). Resistive cartridge heaters embedded in the plates beneath and above the sample were controlled by means of a PID loop steered by the output of a K-type thermocouple (Omega, part number SCASS-040U-6-SHX) embedded in the base plate. Insulating ceramic plates with openings for the incident and scattered x-ray beams helped maintain the stability of the temperature. *In situ* GISAXS experiments were also carried out separately at Sector 8-ID-E of Advanced Photon Source in Argonne National Laboratory with X-ray wavelength of 1.14 Å. Functionalized films were secured inside the stainless steel oven and the temperature was raised to 250 °C at a heating rate of 2 °C/min to a set temperature, where GISAXS patterns were collected with a X-ray beam size of 100 μm × 50 μm (H × V) after alignment in z and Θ directions. The sample to detector distance for GISAXS measurements was 2185 mm. The procedure was repeated at increasing temperatures (300, 350, 400, 450, 500, and 550 °C) and GIWAXS images were taken at

each temperature 10 min apart. Samples were shifted by 0.1 mm (the width of the beam) before every measurement to prevent any damage caused by beam radiation.

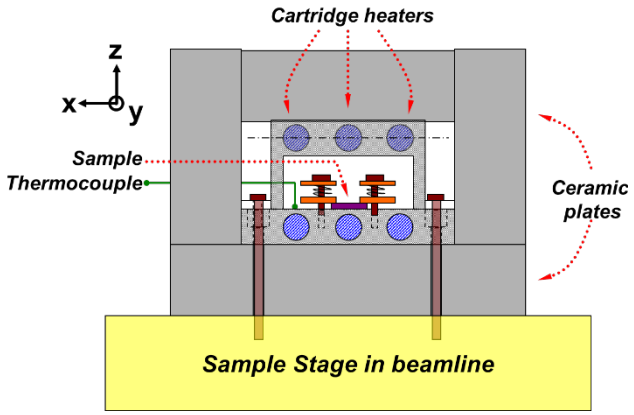

Figure 3-1. Schematic of the stainless-steel thermal cell used for *in situ* GISAXS studies.

3.4 Results and Discussion

As a baseline, pure silica thin films (without Ti doping) templated with only CTAB were synthesized and characterized before and after calcination. As expected, their GISAXS patterns indicate a 2D hexagonal structure with *P6mm* space group (Fig. 3-2(a)) as reported by previous studies.[122, 144] The pattern before calcination fits well with the GIXSGUI peak predictions for a *P6mm* structure with the (0 1 0) direction normal to the substrate. The lattice parameter of a = 5.4 nm were calculated from q_y of the (1 1 0) peak, and b = 7.2 nm was determined to be two times the d-spacing of the (0 2 0) peak.[145] Based on these two parameters, the hexagonal structure obtained after synthesis contracted by about 23% in the (0 1 0) direction compared to an ideal hexagonal structure. After calcination at 500 ℃ for 70 min, the mesostructure remained the same except for vertical elongation in the GISAXS pattern (Fig. 3-2(b)) caused by the unidirectional contraction perpendicular to the substrate due to surfactant removal and pore wall densification during calcination. The most intense spot observe in the q_z direction of the GISAXS patterns in Fig. 3-2 indicates that the d-spacing of the (0 2 0) peak decreases from 3.6 nm to 2.7 nm during calcination, indicating additional contraction normal to the film by about 25%. This is a commonly observed phenomenon for surfactant-templated silica films.[140, 145-147] The CTAB/Si molar ratio adopted for this study is about 0.12, which is close to the intermediate region of the ratios resulting in primitive cubic and 2D hexagonal structures.[129] Therefore, there were also batches possessing a mixed structure with cubic and 2D hexagonal, for which the cubic structure remained after calcination (Fig. A1).

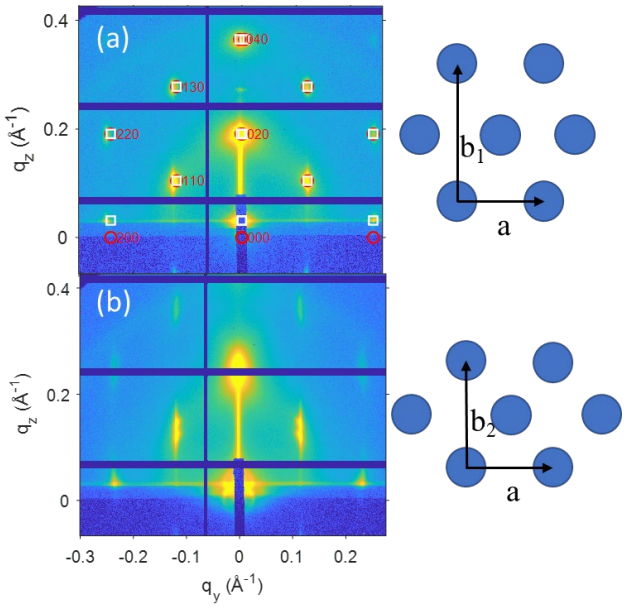

Figure 3-2. GISAXS patterns of CTAB templated silica thin films without titania doping with GIXSGUI overlay of predicted peaks. (a) before calcination (2D hexagonal structure *P6mm*, a = 5.4 nm, b_1 = 7.2 nm, α = β = γ = 90˚); (b) after 70 min calcination at 500 ℃ (*P6mm*, a = 5.4 nm, b_2 = 5.4 nm, α = β = γ = 90˚)

To obtain vertically aligned channels with respect to the substrate, we expect to take advantage of the unidirectional contraction of the film during thermal treatment to drive the fusion of micelles initially disoriented or oriented parallel to the substrate such that vertically aligned channels form. Using GISAXS, Oveisi et al. observed transformation from parallel 2D hexagonal to vertical channels in Pluronic F127 templated titania-alumina films after calcination.[140] This encouraged the idea of doping the silica matrix with titania to facilitate mesostructured transformation. There is also evidence that increasing the amount of titania in titanosilicate films decreases the long-range order of the porous structure.[85, 86] Hüsing et al. reported a lower limit of Si/Ti of about 11 to15 to sustain the mesoporous structure after calcination in mesoporous materials, and the results in Fig. 3-2 suggest that, consistent with this expectation, our pure silica films do not go through mesostructure transformation during calcination.[111] Therefore, different

amounts of titania doping were incorporated starting from a very low content of titania of 0.005%. A very small amount had no effect (as expected), including up to 0.5% TiO_2, such that the films retained most of their starting mesostructure during calcination (Fig. A2). However, at 1% titania doping, the GISAXS pattern of an orthogonally oriented HCP structure was obtained after calcination (Fig. 3-3(b)), which is similar to the o-HCP structure of P123 templated silica films previously obtained by surface modification prior to coating.[17] Moreover, before calcination, the 2D hexagonal structure was accompanied with an isotropic ring with similar d-spacing with lower but uniform intensity (Fig. 3-3(a)), indicating coexistence with a disoriented mesostructure. The d-spacing of the disoriented mesostructure is determined from the intercept of the ring with q_y axis to be about 4.1 nm.

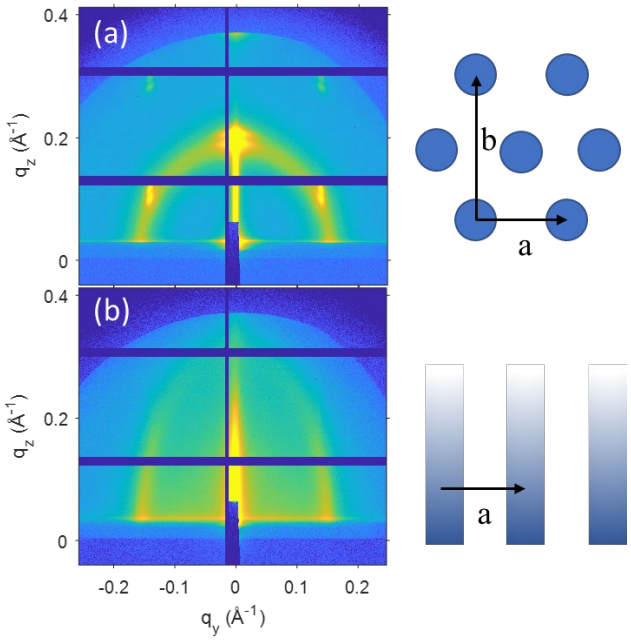

Figure 3-3. 2D GISAXS pattern of CTAB templated silica thin film with 1% titania doping and no sugar surfactant. (a) before calcination, showing similar *P6mm* structure as undoped silica film in Fig. 3-2[122, 144] with a background of an isotropic ring, and (b) after calcination at 500 °C for 70 min.

To better understand the evolution of the mesostructured during heating, *in situ* GISAXS was performed for a CTAB templated film with 1% titania doping. The film was calcined at 450 ℃ for 50 min at first, but the 2D hexagonal structure remained. Then the temperature was raised to 500 ℃ (Fig. 3-4(a)). The (1 1 0) peak (illustrated with the arrow in Fig. 3-4(a)) of the GISAXS pattern started to fade in intensity significantly after only 10 min of calcination at 500 ℃ (Fig. 3-4(b)) and the (0 2 0) peaks normal to the substrate became dominant in intensity. This is an indication of distortion of out-of-plane structure but a sustained in-plane structure.[140] At 40 min of calcination (Fig. 3-4(d)), the (1 1 0) peak from the 2D hexagonal structure was completely gone along with the portion of the isotropic ring in the (0 1 0) direction, which implies that the isolated and randomly oriented micelle units merged in the direction of (0 1 0) and formed vertical channels (Fig. 3-5). After 50 min of calcination (Fig.3- 4(e)), the (0 2 0) peak completely disappeared, leaving behind only the vertical rods from the o-HCP structure. This o-HCP pore structure was sustained after up to 70 min of calcination, and the same in-plane d-spacing as before the calcination was retained as suggested by the static sample in Fig. 3-3(b). The porous structure transformation from randomly oriented pores to vertically aligned channels is due overcoming the activation energy of the Si-O-Ti bond, allowing for increased diffusion during calcination. When the temperature is increased, evidence of reduction in Si-O-Ti bonding (indicating mobility of the metal centers) is found starting at 500 ℃,[148, 149] which agrees with the structural transform temperature in this study. This allows the transformation to happen when there is enough Ti in the films.

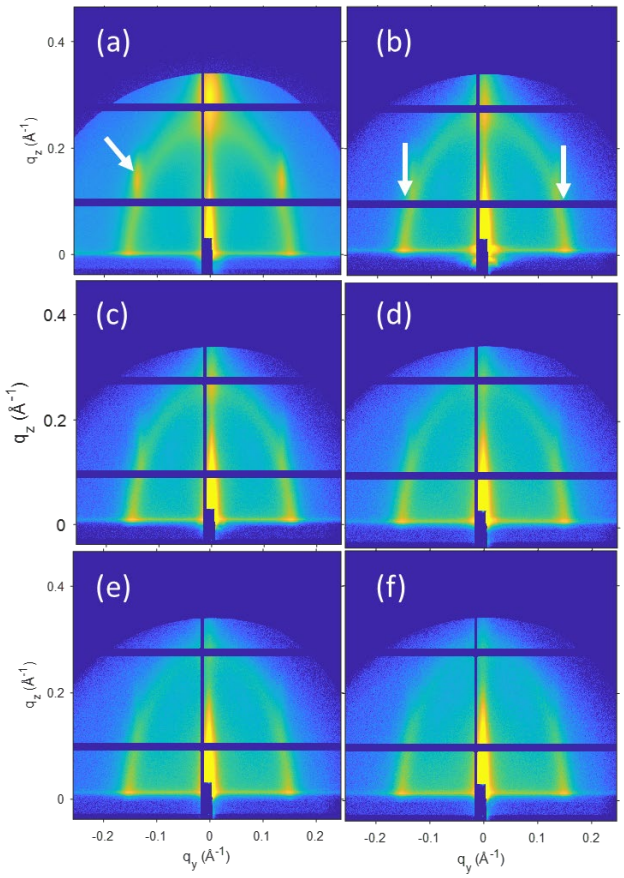

Figure 3-4. GISAXS patterns of the mesostructure development of 1% titania doped silica film at 500 °C calcination for (a) 0 min; (b) 10 min; (c) 20 min; (d) 40 min; (e) 50 min; (f) 70 min. Arrows in (a) and (b) indicate (110) spots from domains of parallel HCP mesophase, which are lost in favor of Bragg rods with highest intensity at the Yoneda band.

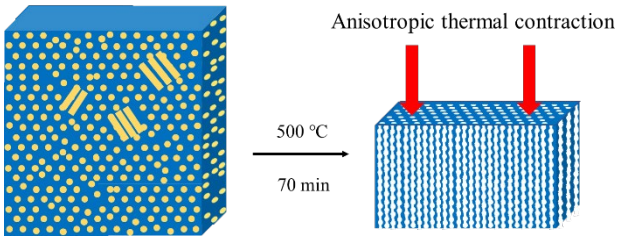

Figure 3-5. Schematics of the mesopore fusion that transforms the porous structure from randomly oriented pores in titania doped silica films with no sugar surfactant

Starting from 2% titania doping without the $C_{12}G_2$: TIP complex, there was only a diffuse isotropic ring in the GISAXS patterns before calculation with no 2D hexagonal structure, and it got more diffuse as the titania doping increased. The ring could only be seen vaguely at 8.5% titania doping, indicating the isotropic structure is losing order with increasing Ti content. The same phenomenon has been observed in other studies of titanosilicate mesoporous materials and it results from the larger size of Ti(IV) tetrahedra (0.68 Å) than Si(IV) tetrahedra (0.41 Å) that distorts the mesoporous structure even before calcination.[85, 86] This explains the disappearance of the 2D hexagonal structure in favor of isotropic pores in films templated with only CTAB and for > 1% Ti.

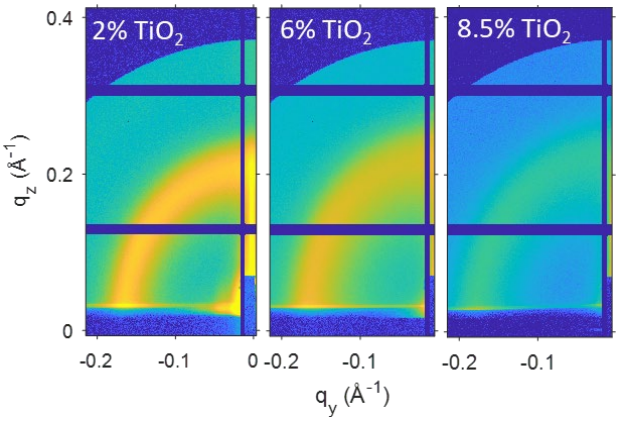

Figure 3-6. GISAXS patterns of silica films templated with only CTAB, with 2%, 6% and 8.5% titania doping before calcination.

According to previous studies in our group, the sugar surfactant $C_{12}G_2$ forms a complex with Ti and prevents titania aggregation or precipitation during hydrolysis, while also acting as a structure directing agent (SDA) together with CTAB. This is expected to disperse titania at the pore surface for applications in catalysis.[85, 150] The investigation of films templated with only CTAB demonstrated that 1% titania doping is the lowest amount for the structure to transform to o-HCP, and that calcination at 500 °C

for a minimum of 40 minutes is required for it to happen. The same conditions were applied to films prepared with CTAB and $C_{12}G_2$ sugar surfactant complexed to Ti as SDAs. The structure before calcination showed randomly oriented micelles (indicated by a ring of uniform intensity) (Fig. 3-7(a)), which is different from the mixed structure from the film templated by CTAB only (Fig. 3-3(a)). This porous structure has a d-spacing of about 3.8 nm, agreeing with the observation in Rahman's study of increased pore size with addition of $C_{12}G_2$ in the surfactant.[142] A former study in our group established the ternary phase diagram of the CTAB-$C_{12}G_2$-water system and its use for predictive synthesis of mesoporous silica.[142] The weight percentages of CTAB+ $C_{12}G_2$ adopted in this study are within the 2D hexagonal region as discussed for non-titania-doped films. However, with the increasing titania doping, the amount of the sugar surfactant also increases in order to maintain a TIP : $C_{12}G_2$ ratio of 1 : 1. This increasing amount of nonionic sugar surfactant may contribute to the loss of the pore orientation of the 2D hexagonal structure as suggested by previous studies.[142, 151]

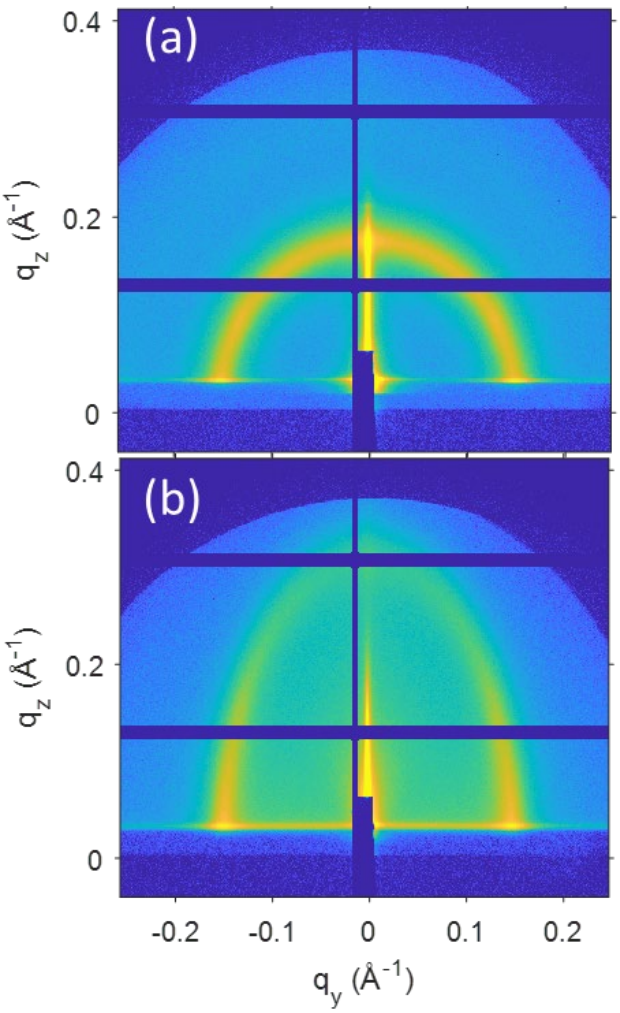

Figure 3-7. GISAXS patterns of 1% titania doped silica film formed with CTAB and $C_{12}G_2$ complexed to the TIP precursor (a) before calcination; (b) after 2 hours of calcination at 500 °C

While possessing less long-range order before calcination, the 1% titania doped film prepared with $C_{12}G_2$ complexation displays the same final structure (Fig. 3-7(b)) as the film without $C_{12}G_2$ complexation (Fig. 3-3(b)) after calcination at 500 °C. Both types of the films have the same in-plane d-spacing of 4.3 nm. The vertical elongation of the isotropic ring on the GISAXS pattern was observed as expected caused by the contraction in the vertical direction to the substrate. The peak in the (0 1 0) direction disappeared,

indicating the deformation of the out-of-plane structure while the in-plane structure was retained.

For the long-term goal of preparing catalytic porous thin films, it is necessary to understand the upper limit of the amount of titania doping that can be incorporated while still maintaining the desired vertical pore structure for the films with $C_{12}G_2$-complexed TIP. The results in Fig. 3-8 show that unlike the CTAB-only templated films, the structure transformation happened even at the lowest amount of titania doping studied (0.005%) when TIP was complexed by the sugar surfactant. After calcination at 500 °C, a $C_{12}G_2$-complexed films show features of the vertical rods at q of about 0.15 $Å^{-1}$ like in the films with 0.005% and 1% titania doping (Fig.3- 8). However, this signal became very faint at 6% titania doping, indicating the loss of the long-range order of the orthogonal HCP structure.

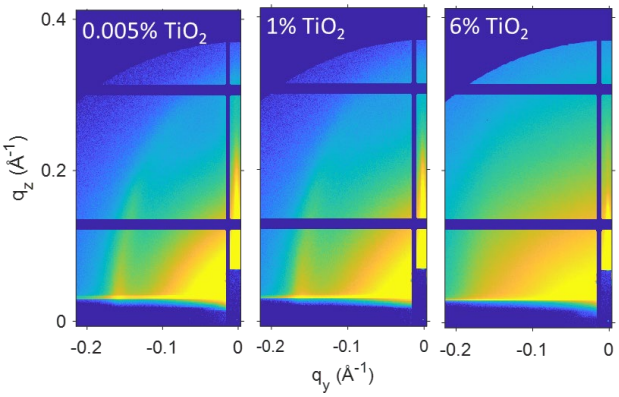

Figure 3-8. GISAXS patterns of titania-doped silica thin films templated with CTAB and $C_{12}G_2$ complexation after calcination.

In fact, a similar trend of losing long-range order with increasing Ti (and $C_{12}G_2$) content was observed even before calcination. The reduced 1D patterns generated by azimuthal integration of the GISAXS patterns are shown in Fig. 3-9 for complexed films

with different levels of Ti doping, all before calcination. Noticeable peak broadening and decrease in peak intensity occurred as the titania doping was raised to 1% and continued to decline to the point of no recognizable peak with 6% Ti doping. These observations are indicative of the decline in mesostructural order with increasing titania doping. In this type of film, the amount of $C_{12}G_2$ added increases when increasing the titania doping in order to keep the $C_{12}G_2$: TIP at 1:1 while the amount of CTAB was decreased to keep the sum of overall surfactant constant across the board. This decreases the CTAB/$C_{12}G_2$ ratio and this has been found to decrease the degree of long-range order in hexagonal lyotrophic mesophases.[142] Therefore, the increasing content of $C_{12}G_2$ in the surfactant mixture is believed to cause the loss of long-range order in films with higher Ti doping even before calcination.

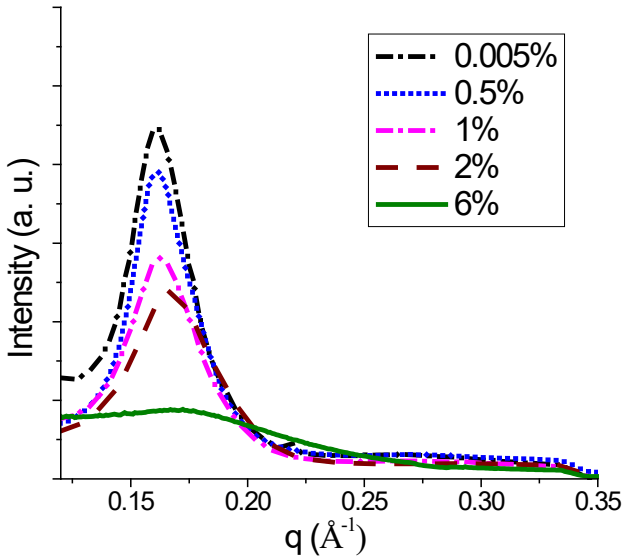

Figure 3-9. Integrated 1D spectra of CTAB / $C_{12}G_2$ complexed silica film with 0.005% to 6% titania doping before calcination.

As mentioned above for titanosilcate films templated with only CTAB, when unidirectional contraction of the films happens during calcination, weakening of Si-O-Ti bonds makes the porous structure unable to withstand stress normal to the film, thus allowing pore fusion to form vertical channels. With added $C_{12}G_2$, the Ti ions were intentionally fixed at the interface, making the concentration of the Si-O-Ti bonds greater at the micelle surface. This causes less order of the porous structure and loss of the 2D hexagonal structure even with low titania doping (below 1%). Thus, for films before calcination, the loss of order in $C_{12}G_2$-complexed films with respect to Ti content is more rapid than the films templated by only CTAB. Comparing films doped with 6% titania, there is still an indication of ordered porous structure in a non-complexed film (Fig. 3-6) while little order was found in a complexed film (Fig. 3-9). This point is also supported by the observation that with CTAB + $C_{12}G_2$-Ti as surfactant, even the lowest composition of Ti studied (0.005%) displayed an isotropic starting structure and possessed structure transformation from disordered porous structure to vertically aligned channels after calcination.

All of the effects of Ti doping observed here can be attributed to mixing of Ti atoms in the silica matrix, and not to effects of strong segregation of the two phases. The precipitation of titania during synthesis is a well-known concern due to the fast hydrolysis rate of TIP,[85, 111, 150, 152] and diffusion and crystallization of TiO_2 during thermal treatment is likely when the Ti atoms are not homogeneously dispersed. However, GIWAXS patterns collected after calcination showed no evidence of titania crystallization in any of the samples, even for a sample containing 6% Ti prepared without $C_{12}G_2$ complexation (Fig. A3).

3.5 Conclusions

Mesoporous titania-doped silica thin films with vertical nanopore channels were synthesized through EISA with CTAB as the primary structure directing agent, followed by calcination at 500 ℃. Two different types of films (with and without maltoside surfactant $C_{12}G_2$ added for Ti complexation) were synthesized and compared, with the goal of understanding mesostructured evolution in titanosilicate films with well-dispersed Ti sites of interest for adsorption and catalysis. The results show that the titania doping provides a route to expanding the range of pore sizes available in oriented mesoporous films for size-exclusion separations and catalysis. The in-plane d-spacing was found to be about 3.8 nm from the GISAXS patterns for films with or without $C_{12}G_2$ complexation, which is significantly smaller than the films synthesized previously with Pluorinc P123 with 9.5 nm d-spacing and 8 nm pores.[14, 17, 64]

The first type of film was templated with only cationic surfactant CTAB and the titania precursor TIP was prehydrolyzed in a low moisture environment to prevent titania precipitation due to rapid hydrolysis of TIP. Instability of mesostructures in titania-silica mixed oxide films after thermal treatment was reported with increasing Ti in previous studies, so titania doping levels of 0.005%, 0.5%, 1%, 2%, and 6% were investigated. The goal was to find a window of Ti content where the desired vertical channel structure could form by merging the initial micelles in the film into orthogonally oriented hexagonal close packed (o-HCP) structures by taking advantage of the unidirectional contraction of the film normal to the substrate. The lowest level of titania doping and calcination temperature found to give such a structural transformation were found to be

1% and 500 ℃ respectively for films templated with only CTAB. The transformation was complete at around 40 minutes of calcination indicated by the disappearance of the (1 1 0) peaks from the original HCP phase oriented parallel to the substrate.

In second type of films, $C_{12}G_2$ was complexed with TIP and acted as a co-surfactant to intentionally fix Ti at the micelle surface and avoid the possibility of titania crystallization. For all Ti contents, this type of film started with an isotropic micelle structure, but because they experienced the same anisotropic stress, the films formed the same o-HCP structure as the other type of films after calcination at 1% Ti doping.

Both types of films lost their long-range ordered structure after calcination when the titania doping was greater than 1%. The loss of order with increasing amount of titania doping occurred even before calcination for both types of films (indicated by isotropic rings of decreasing intensity), suggesting that the thermal treatment is only responsible for the out-of-plane mesostructure deterioration. For films templated with only CTAB, increasing titania doping also increases the precursor/surfactant ratio, which would be expected to lead to less order after condensation. Consequently, the uncalcined films lost the 2D hexagonal structure and displayed an isotropic structure starting from 2% Ti and then further lost long-range order until a very faint structure was observed in 8.5% Ti doped films. On the other hand, the continuous loss of isotropic structure in films templated with CTAB + $C_{12}G_2$-Ti with increasing titania doping is expected to be the result of increasing ratio of $C_{12}G_2$/CTAB because the nonionic sugar surfactant $C_{12}G_2$ is not as good of a structure directing agent as the cationic surfactant CTAB.

This study provides evidence of a new approach to manipulate the orientation of the pores in surfactant-templated silica nanoporous films. Compared to the method of

substrate surface modification developed previously in our group (which requires development of different surface modification procedures for each surfactant) the approach based on Ti doping of silica films is broadly applicable to many surfactants because it takes advantage of the anisotropic stress that arises naturally during processing to induce physical pore transformation. This expands the size range of the vertical channels synthesized using the EISA sol-gel method by enabling the use of surfactants with different lengths. Future studies can be conducted to demonstrate the capability of the titanosilica film for catalytic reactions and providing binding site for enediols. Furthermore, the range of surfactants (length and headgroup type) able to give thin titanosilica films with orthogonally oriented nanopore channels of controlled size can also be investigated.

Chapter 4. In-situ FTIR Study of the Effects of Silica Mesopore Confinement on Hydration of Ionic Liquid 1-Butyl-3-methylimidazolium Chloride ([BMIM][Cl])

Yuxin He[1], Daudi Saang'onyo[2], Folami Ladipo[2], Barbara L. Knutson[1,*] and Stephen E. Rankin[1,*]

[1]*Department of Chemical and Materials Engineering, University of Kentucky, Lexington, KY, 40506, USA*

[2]*Department of Chemistry, University of Kentucky, Lexington, KY, 40506, USA*

**Corresponding author. email: bknut2@uky.edu; stephen.rankin@uky.edu*

4.1 Abstract

The absorption of water by ionic liquid 1-butyl-3-methylimidazolium chloride ([BMIM][Cl]) confined in silica thin films with accessible 8 nm cylindrical mesopores was investigated and compared to bulk ionic liquid. Transmission FTIR spectra were collected *in-situ* at room temperature while changing the relative humidity (RH) of the environment (RH of 0% to 87%). Pore confinement induces binding of imidazolium rings with the silica pore wall under dry conditions, but hydration disrupts hydrogen bonding of imidazolium with both silica and Cl^-, as interpreted from peak shifts corresponding to C-H vibrations on the imidazolium ring. Molecular interactions with water are similar regardless of confinement, but [BMIM][Cl] exhibits significantly reduced water uptake at RH > 15% due to nanopore charge and structuring effects associated with confinement. Deconvolution of OH stretching bands shows that weakly coordinated water is promoted in confined [BMIM][Cl], which may affect mechanisms of solubilization and catalysis in confined ILs.

Keywords: Ionic liquids, mesoporous silica, water uptake, thin films, confined solvents

4.2 Introduction

Ionic liquids (ILs) are salts with melting points close to ambient conditions - usually below 100 °C. Due to their good thermal stability, high ionic conductivity and tunable properties, they are employed for a wide range of applications such as electrolytes, lubricants, separation media, and low-volatility solvents.[2, 153, 154] As reaction media (with or without added catalysts), ILs have been of intense interest due to their ability to dissolve various inorganic, organic and polymeric materials.[2, 5, 6, 153-156] The first breakthrough in homogeneous IL-transition metal catalysis was by Lin and Vasam, who reported the high efficiency Freidel-Crafts reaction in 1-butyl-3-methylimidazolium chloride ([BMIM][Cl]) with dissolved $AlCl_3$.[23] Shortly thereafter, Chauvin et al. reported the catalytic dimerization of alkenes with a nickel complex in organochloroaluminate ILs.[24] ILs continue to be of great interest as reaction media due to their potential in biorefining, in part due to their ability to solvate recalcitrant components of lignocellulosic biomass. One example is the dehydration of glucose to 5-hydroxymethylfurfural (HMF) with Lewis acid catalysts in IL. This pathway of glucose to fructose isomerization followed by dehydration is one of the most developed routes to obtain HMF from glucose.[5, 157, 158]

Despite their promising properties, bulk ILs have been slow to gain widespread use as reaction media for homogeneous catalysis, in part due to the high expense of purified ILs. In addition, while their extremely low vapor pressure can be an advantage for stripping out light components, it is difficult to recover low-volatility products from IL catalyst mixtures, such as the HMF product mentioned above.[6] Residual IL in products can be difficult to

avoid, and its toxicity and effects on product properties are largely unknown.[7] These disadvantages may be overcome with supported IL-catalyst systems. Segregation of the IL and catalyst within the pores of a support not only reduces the amount of IL required, but also keeps the IL separated from the product stream.[59, 159, 160] Furthermore, research has shown evidence of IL properties being strongly influenced by confinement within the pores of supports. For example, Chen et al. found that confinement within multiwalled carbon nanotubes increases the melting point and changes the crystallization behavior of [BMIM][PF_6].[8] In the context of electrochemical materials, Iacob et al. showed that confinement of imidazolium ILs in nanoscale silica pores enhances charge transport.[9, 161] There are also studies showing that nano-confinement induces local ordering of the ions of ILs, leading to locally structured microenvironments.[10, 11] Dispersion of ILs themselves into nanoparticles and thin films has been shown to alter their hydration characteristics by increasing the available IL surface.[36, 92]

Hydration of ILs is of immense importance since many ILs are hygroscopic and the presence of water dramatically changes their properties (*e.g.*, density, viscosity and surface tension).[162, 163] Studies of thermodynamic properties of ILs frequently employ rigorous exclusion of water, but this is not always an operational possibility, especially in systems where water is the natural solvent (such as biorefineries) or where water is a reaction product (such as glucose dehydration). For other applications, understanding the effects of hydration are important for justifying the extent of water removal required for a specific application. Recently Gong, Cheng and coworkers presented evidence that hydration of oxide surfaces (mica in this case) is actually *desirable* because it accentuates the surface charge, leading to better macroscopic wetting and molecular ordering at the

solid/IL interface.[164, 165] Changes in local solvation also have the potential to alter the effectiveness of ILs as solvents for supported catalysts as well as their transport properties. Therefore, investigating the influence of confinement in nanopores on the hydration of ILs and their interaction with the walls of the support is relevant to the broad application of supported ILs in catalysis and separations.

The support materials selected for this study are silica thin films with vertically aligned nanopores. The silica thin films are synthesized by the evaporation-induced self-assembly of Pluronic P123 block copolymer in the presence of hydrolyzed tetraethoxysilane (TEOS) and prepared by dip coating.[69, 70] Koganti et al. showed that vertically aligned arrays of accessible cylindrical pores (9 nm diameter pores) can be formed in these films by first modifying the substrate with a "neutral" crosslinked layer of a random PEO-PPO copolymer or P123 itself.[64, 166] This oriented pore structure forms directly during deposition due to the surface modification [167] and provide an accessible array of uniformly sized channels[14, 168] amenable to *in situ* studies. These silica thin films serve as an ideal model platform for the types of mesoporous oxide supports that have been used previously as IL supports.[10, 161, 169, 170]

Here, [BMIM][Cl] is selected as a representative example of a common IL solvent used for biomass dissolution and reactions.[35] Typical IL cations are based on ammonium, imidazolium, pyridinium and pyrrolidinium groups, and common anions include halides, tetrafluoroborate (BF_4^-) and hexafluorophosphate (PF_6^-).[171] Properties of imidazolium ILs (melting point, viscosity, surface tension, hygroscopic nature, and molecular interactions between ions) are highly tunable by alternating the length of the alkyl chain in

the cation, and the type of anion, [36, 171] making them an ideal system for understanding the combined effects of confinement and hydration.

The effects of confinement within the nanopores of silica thin film supports are investigated here using *in situ* Fourier transform infrared (FTIR) spectroscopy. MacMillan et al. previously showed that attenuated total reflection (ATR) FTIR can be used to monitor vibrational changes in bulk imidazolium ILs caused by changes in relative humidity.[36, 92] More broadly, vibrational spectroscopy has been used to investigate molecule structural changes and interactions in ILs with or without water.[38, 172] Our group has previously demonstrated the use of thin silicon wafers as substrates for *in situ* monitoring of the curing of the silica films themselves.[72] In the present study, we take advantage of the thin silica film platform with accessible pore structure to perform *in situ* transmission FTIR measurements of [BMIM][Cl] as a function of relative humidity (RH) with or without pore confinement.

4.3 Experimental Methods and Materials

Materials: NoChromix® power, glycerol (89%), 1,6-diisocyanatohexane (98%), tetraethoxysilane (99.9%), Pluronic P123 poly(ethylene oxice)-b-poly(propylene oxide)-b-poly(ethylene oxide) copolymer ($M_n \sim 5800$), and 1-butyl-3-methylimidazolium chloride (≥98%) were obtained from Sigma-Aldrich; concentrated sulfric acid (98%), 1 N HCl, and acetone (99.5%) from VWR; and 200 proof ethanol from Decon Labs. The substrates used for sample preparation were borosilicate glass slides (VWR) and 140 ± 10 μm thick, single-side-polished <0 0 1> oriented silicon (Si) wafers (University Wafer, Inc.)

P123 Templated Silica Film Synthesis: Films with orthogonal hexagonal close packed (o-HCP) pores were prepared using the method of Koganti and Rankin.[64] Borosilicate glass slides were first cleaned by submerging them in a solution of NoChromix® in concentrated sulfric acid for more than 2 h. Then, they were rinsed with DI water followed by ethanol and dried with flowing air. For surface modification, three drops of glycerol were added to a 0.696 mM P123 solution in 89 ml acetone, and an equimolar amount of 1,6-diisocyanatohexane was added in a nitrogen-filled glove bag. This modifying solution was dip coated onto glass slides or silicon wafers at a withdrawal speed of 7.6 cm/min. The modified glass slides were cured and dried overnight at 100°C.

The silica film sol was prepared by first mixing TEOS with anhydrous ethanol, DI water and hydrochloride acid (HCl) at an overall molar ratio of 1 : 3.8 : 1 : 5×10^{-5} (TEOS: ethanol: DI water: HCl).[70] The mixture was refluxed in water bath at 70 °C for 90 min, and more DI water and HCl were added to achieve a concentration of 7.34 mM HCl. This solution was then stirred and cooled at room temperature for 15 min and aged at 50 °C for another 15 min. Finally, heating was stopped and a solution of 5.8 g P123 in 83.84 g ethanol was added to give final molar ratios of 1 TEOS: 22 C_2H_5OH: 5 H_2O: 0.004 HCl: 0.01 P123.[168]

The mesoporous silica thin film was formed by sandwiching the final coating between the surfaces of two modified glass slides. First, the sol was dip coated onto a modified substrate (glass or silicon wafer) at a rate of 7.6 cm/min. Another modified glass surface was immediately placed on the sol coating. The sandwiched films were aged and dried first at 45°C for 24 h, and then at 100°C for another 24 h. Finally, the upper modifed glass slide was removed and the silica thin film (still adhered to a modified glass slide) was

calcined at 500 °C for 4 h in air with a heating rate of 1 °C/min. The calcination step removed the pore template agents and the crosslinked polymer modifying layer, while also curing the silica matrix.

Film characterization: The pore spacing and orientation were characterized using grazing-incidence small angle X-ray scattering (GISAXS; Xenocs Xeuss 2.0) in a vacuum chamber (< 1 mbar) with X-ray wavelength of about 1.54 Å. The incidence angle applied was 0.2°. The film thickness was measured using a Dektak 6M Stylus profilometer with a diamond stylus. The surface height difference at the edge of the film on a Si wafer (where the Si wafer was withdrawn from the dip coating) was taken as the film thickness.

Supported Ionic Liquid Sample Preparation: For IL supports, a 140 ± 10 μm thick, single-side-polished <0 0 1> oriented silicon (Si) wafer (University Wafer, Inc.) was trimmed to pieces of about 2×2 cm each. It was important that the wafers be thin (<200 μm by our estimation), and polished on only one side to minimize interference fringes in FTIR spectra. The Si wafer was cleaned by sonication in DI water then in acetone for 20 min each. To compare the same IL supported by bare Si wafer (unconfined) and P123-templated silica films (confined), P123 templated silica films with vertically aligned pores were deposited on Si wafers with the polished side modified as described in the *P123 Templated Silica Film Synthesis* section. The silica film was dried under vacuum at 46 °C overnight, following the full procedure of synthesizing P123-templated films. These dried films were used as supports and loaded with IL solution.

IL loading on Si wafers and P123 templated silica thin films was performed by first dissolving solid 1-butyl-3-methylimidazolium chloride ([BMIM][Cl], ≥ 98.0%, Sigma-

Aldrich) in anhydrous ethanol (200 proof, Koptec) to make a 10 wt% solution. Deposition was carried out in a nitrogen-filled glove bag to prevent moisture absorption by [BMIM][Cl]. A bare Si wafer or silica film on a Si wafer was submerged in the IL solution for two hours. The unpolished side of the wafer was gently wiped with an ethanol-wetted Kimwipe to remove excessive IL that might cause interference. The IL-loaded substrate was quickly transferred to a desiccator with indicating DRIERITE®. The sample was then vacuum dried at room temperature for 30 min, the vacuum was released using ultra-high purity (UHP) N_2, and the supported IL was mounted in the gas cell near the N_2 gas line outlet to minimize contact with moisture in the atmosphere.

Relative Humidity Control: A 5 cm Pyrex gas cell (Pike Technologies Inc.) with zinc selenide (ZnSe) windows (International Crystal Laboratories) was employed to contain the supported IL sample. Nitrogen gas with controlled relative humidity using either deionized water or deuterated water was fed into the gas cell through one port and flowed out through the second gas port (as shown in Fig. B1, Supporting Information). RH was monitored at the gas outlet using a Fisher Scientific™ Certified Traceable™ Digital Hygrometer/Thermometer. This gas cell was mounted in the FTIR sample chamber with the infrared beam passing through the windows and film assembly at the center of the cell. The IL supported on the thin Si wafer (unconfined IL) or the silica thin film-Si wafer (confined IL) was placed on the polished side, sandwiched between two washer-shaped neodymium magnets and Teflon spacers, and monitored by FTIR over time.

In-situ IR Spectra Measurement: FTIR spectra were measured with a Thermo Nicolet Nexus 470 FTIR with KBr beam splitter and liquid N_2-cooled mercury cadmium telluride (MCT) detector. The sample chamber was purged by N_2 gas continuously. Spectra were

taken at a resolution of 1.98 cm^{-1} with 250 scans. Background spectra were obtained for Si wafers (with or without silica films) mounted in the gas cell purged by UHP N_2. After loading of the IL onto the support material, the sample (either IL loaded on mesoporous silica thin film or deposited on Si wafer) was purged with UHP N_2 for three hours to produce the initial "dry" sample for *in situ* FTIR. The sample was loaded back into the film holder so that the exact same region was used to collect the "sample" spectrum. By doing this, contributions from the Si wafer and mesoporous silica film layer were removed from the final spectrum. FTIR spectra of supported IL films were collected at decreasing RH values of 82.5%, 65.5%, 48.5%, 29%,17%, 8% and 0% (±5%) for unconfined [BMIM][Cl] and 78%, 59%, 45%, 28%, 19%, 8.5%, and 0% (±5%) for confined [BMIM][Cl]. The temperature in the chamber, monitored using the RH probe, was 21 °C throughout the experiments. To ensure that the samples reached equilibrium with the water vapor (for the initial "dry" samples and at all subsequent RHs), spectra were collected repeatedly until three spectra collected ten minutes apart were nearly identical at a given RH level. The *in-situ* measurement allows repeated measurements at the same spot on the film to isolate changes due only to hydration of the ionic liquid. To eliminate signal from water vapor in the gas cell, spectra of the vapor-containing gas cell were measured at the set of RH values listed above, and their spectra subtracted from the corresponding supported IL spectra.

Peak deconvolution analysis to determine peak positions and areas was conducted by first using Thermo Scientific™ OMNIC™ software to generate initial guesses of peak positions, areas and widths. Mixed Gaussian/Lorentzian functions and linear baselines were applied for fitting when using OMNIC.[173] For dry samples with CH stretching

bands only, the number of peaks was fixed at 6 in the range of 2800-3200 cm^{-1} and the initial guesses of the peak positions were estimated by inspection of the spectra. For samples exposed to water vapor, three initial OH stretching peak positions were obtained from literature (discussed further below).[92, 93, 96, 97, 100] They were fitted simultaneously with the six CH stretching peaks (9 peaks total). The fitting was refined with Origin Pro 8.5 (OriginLab) to obtain final deconvolution results with detailed statistical analysis. Fitting in Origin used Voigt lineshapes and constant baselines. The peak widths were fit first, with peak positions and peak areas fixed at initial values from OMNIC. This was then repeated for peak areas (with positions and widths fixed), and peak positions (with areas and widths fixed) last. Standard errors of the peak positions and areas, and regression coefficients indicating quality of fit, were obtained from Origin. Distinct peaks at low wavenumbers (<1700 cm^{-1}) did not require deconvolution, and were analyzed individually by batch processing with TQ Analyst™ software (Thermo Fisher Scientific). The results were also taken to Origin for peak fit refinement using the same method as the higher wavenumber peaks.

4.4 Results and Discussion

2D grazing-incidence small angle X-ray scattering (GISAXS) was used to confirm the pore structure for the synthesized thin films, which followed our published procedures.[64] The GISAXS patterns (Fig. B2) verify the o-HCP structure of the silica film with (100) d-spacing of 9.7 nm. This unit cell parameter is close to previous characterization results of the same type of film using ethanol flux.[14] Koganti et al. also confirmed the pore diameter of 9 ± 1.3 nm with TEM images of the same material.[14, 166] Assuming that pore diameter scales approximately with (100) d-spacing, the slight decrease compared to

Wooten et al.[14] suggests a pore diameter of approximately 8 nm. The silica thin film thickness was measured to be 180 nm by profilometry. The FTIR spectrum of the Si wafer support does not contain distinct bands, and the mesoporous silica film is dominated by Si-O stretching bands near 1000-1200 cm^{-1} (Fig. B3).[72] A trace amount of CH stretching peaks (2800-3000 cm^{-1}) can be found in the spectrum from residual ethanol from film cleaning.

FTIR spectra of "dry" IL (exposed to flowing UHP N_2 for 3 h) with and without silica film confinement are compared in Fig. 4-1. Peak deconvolution was necessary to resolve peaks, particularly in the region of 2800-3200 cm^{-1}, as in Fig. 4-1. The procedure in the Methods section was followed for deconvolution, and the graphical results of fitting are shown for the dry [BMIM][Cl] samples in Fig. B4. All reported peak positions (Tables 4-1 and 4-2) are determined from peak deconvolution. A detailed summary of peak positions found by deconvolution can be found in Supporting Information (Tables B1-B4). Since the uncertainties in peak fitting parameters depend not only on data spacing (instrumental resolution) but also on peak width and noise,[174] statistical analysis was performed using Origin to determine the standard errors in peak positions reported here.

The IR bands of the main functional groups for confined and unconfined [BMIM][Cl] were assigned according to literature as summarized in Table 1.[36, 90, 175-177] Most assigned peaks are very close to the literature values. The most significant variation is in the C2-H stretching, which we observed to be shifted from the literature report by about 16 cm^{-1} toward lower wavenumbers in unconfined [BMIM][Cl]. The band is very sensitive to molecular interactions, and may also have been affected by sample preparation and sampling techniques. The feature near 1760 cm-1 for the unconfined ionic liquid is a

background interference fringe that was sometimes observed for uncoated Si wafers. These fringes were minimized by using single-side polished Si wafers, but small features were sometimes found due to the thin native oxide layer on the wafers. The other weak bands at low wavenumber were present in prior studies of [BMIM][Cl],[36] for instance the band near 1000 cm^{-1} due to out-of-plane C2H bending.[178]

Peaks in the wavenumber range 2800-3200 cm^{-1} are assigned to C-H stretching bands in the methyl group and butyl chain attached to the imidazolium ring as well as on C2, C4 and C5 of the ring (Fig. 4-1).[36] The broad C2-H shoulder around 3018-3040 cm^{-1} has been suggested as a probe for investigating hydrogen bonding with the anion and combined effects of its adjacent imidazolium ring.[36, 176, 179, 180] Additionally, the C2H proton plays important roles in many catalytic reactions.[4, 23, 156]

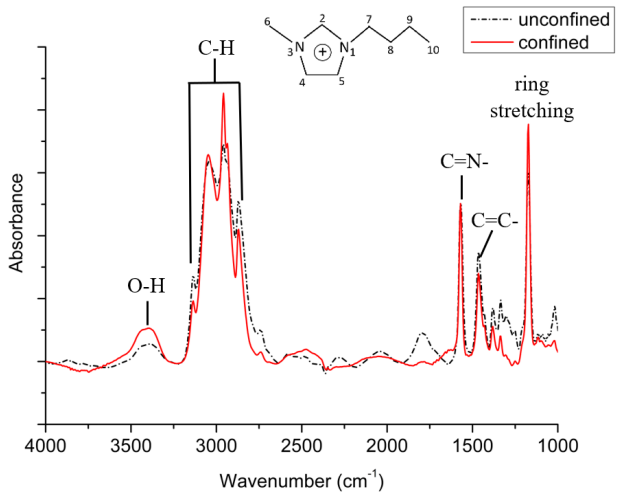

Figure 4-1. Transmission FTIR spectra of "dry" confined and unconfined [BMIM][Cl] that were purged in UHP N_2 for three hours prior to measurement. The inset shows the labeling of carbons in the [BMIM] cation.

Among the peak shifts due to confinement of "dry" [BMIM][Cl] in the pores of the silica support (relative to IL supported on an Si wafer) (Table 1), C2H is the greatest. The

asymmetric CH stretching band on C4C5 (ν_{as} HC4C5H) also shifts to a significant extent compared to the other ionic liquid bands. Shifts of these bands to low wavenumbers upon confinement suggests stronger hydrogen bonds (H-bond) from protons of C2 and C4C5 in confined [BMIM][Cl], causing the CH bond elongation.[172, 175, 176] This interaction exists between Cl^- and the hydrogens of the imidazolium ring in the bulk IL.[92, 176] It may also occur between the ring hydrogen and the negatively charged silica surface in the case of confined [BMIM][Cl] (Fig. 4-2).[181, 182] In contrast, the CH stretches (ν_{ss} CH_3 and ν_{as} CH_3) of the methyl group (C6) do not shift significantly because they are removed from the site of interaction between the anion and imidazolium cation. Similarly, the changes to the three distinctive bands associated with imidazolium ring stretching (C=C-, C=N- and ring stretching) are not significant with confinement relative to the CH stretching bands. The slight shift to higher wavenumbers (higher energy) of the C=N- stretching (~1569 cm^{-1}[36, 90]) observed is consistent with weakening of the C2H bond due to strengthened hydrogen bonding with silica.

Table 4-1. IR peak positions and peak shifts of [BMIM][Cl] upon going from unconfined to confined within o-HCP silica nanopores as determined from peak deconvolution.[a]

CH stretching bonds	Literature (cm^{-1})	Unconfined IL (cm^{-1})	Peak Shift from Unconfined to Confined IL (cm^{-1})
ν_{ss} HC4C5H	3137 [175, 176]	3139.0±0.78	1.2±3.0
ν_{as} HC4C5H	3057 [175, 176]	3060.0±0.46	-6.4±1.2
C2H stretching	3018 [176]	3001.5±0.74	-14.5±2.3
ν_{as} CH_3	2957 [175, 176]	2960.6±0.70	-0.19±2.1
ν_{ss} CH_3	2870 [175, 176]	2861.6±0.48	3.7±1.7
Ring stretching bonds			
C=C- stretching	1465 [172, 177]	1463.2±0.43	-0.17±1.6
C=N- stretching	1569 [36, 90]	1568.1±0.13	1.6±0.34
ring stretching	1172 [36, 90]	1173.2±0.21	0±0.30

[a] *ss* and *as* represents symmetric and asymmetric stretching, respectively

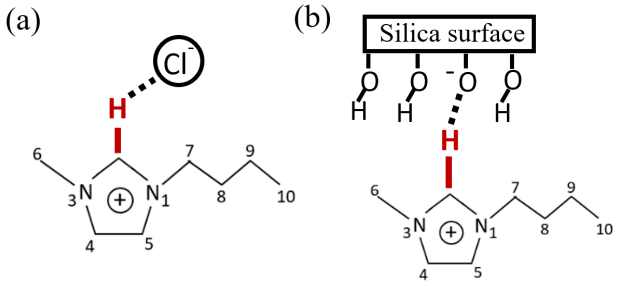

Figure 4-2. Configuration of (a) bulk (unconfined) "dry" [BMIM][Cl] and (b) confined $[BMIM]^+$ near the silica surface.

The effects of pore confinement of "dry" [BMIM][Cl] are consistent with previous interpretations of ILs confined in nanopores in which strong interactions of the imidazolium ring with the pore surface were indicated.[181, 182] The results demonstrate the sensitivity of *in situ* FTIR for the study of the environment of pore confined ILs, which we extend in this study to hydration in confined pores. The overall FTIR spectra of confined and unconfined IL with varying RH are presented in Fig. 4-3. The spectra were first taken for dried supported ILs, which were then exposed to the highest level of RH

and reduced back to a "dry" environment of 0% RH (UHP N_2). The most obvious and expected changes in the spectra upon increasing RH is an increase in the intensity of the OH stretching band around 3400 cm^{-1} and OH bending band around 1635 cm^{-1} for both unconfined and confined IL (Fig. 4-3).[36] Judging from the distinct change in the intensity of this peak with respect to RH and the short time (about 15 minutes) needed to achieve equilibrium after varying RH, [BMIM][Cl] is moisture sensitive and able to take up a significant amount from the vapor phase. Note in Fig. 4-3 that the set of sharp bands associated with the water vapor itself have been subtracted.

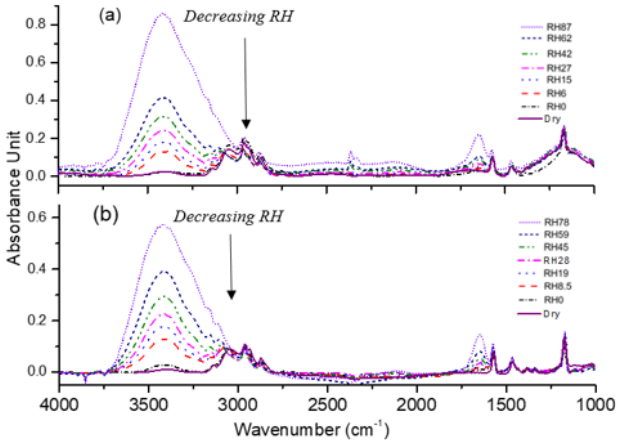

Figure 4-3. FT-IR spectra of (a) unconfined and (b) confined [BMIM][Cl] in contact with N_2 vapor with varying relative humidity (RH) controlled by H_2O. The "dry" samples were measured first, followed by samples in reverse order from highest to lowest RH.

When decreasing RH from 87% back to 0% (UHP N_2), the IR spectrum of unconfined [BMIM][Cl] is almost identical to the "dry" IL in the region of 2800-3200 cm^{-1}. Signature bands of water near 3400 and 1635 cm^{-1} are also present but at very low intensity (Fig. 4-3a). [183] The hydration of bulk IL is observed to be reversible within several minutes. On the other hand, noticable OH bands are still present in going from 78% to 0% (UHP N_2) for confined [BMIM][Cl] (Fig. 4-3b), suggesting that moisture absorbed by the confined

IL is more difficult to remove. This is consistent with the high propensity of hydroxylated silica pore walls to adsorb water by hydrogen bonding. Water uptake properties will be discussed further below.

Reported peak positions in both the C-H / O-H stretching range (2800-3800 cm^{-1}) and the ring band range (1500-1700 cm^{-1}) were determined by deconvolution and peak fitting as described in the Methods. Deconvolution of the high wavenumber peaks consistently provided a good match between the overall model curve and the experimental data, with most R^2 values > 0.99 (the minimum being 0.987). The overall trend is that hydration of confined and unconfined IL results in measurable changes and trends in the both the CH stretching bands and the ring stretching bands (Fig. 4-4). In the case of CH stretching bands, large positive peak shifts are observed for both confined and unconfined [BMIM][Cl] with hydration (Table 4-2). For C2H stretching and ν_{as} HC4C5H, the shifts are approximately 40 cm^{-1} and 37 cm^{-1}, respectively. As a function of RH, the shift occurs most rapidly at low humidity, and then a more gradual increase is observed (Fig. 4-4a). The CH stretching bands of C2H and ν_{as} HC4C5H are both indicators of the interaction of the imidazolium ring with counterions,[175, 184-186] and can be used to interpret the competition between the anion and water in the presence of the silica pore walls. The shift to increasing wavenmumbers is evidence that water molecules compete with C2H and HC4C5H and form H-bonds with Cl^- as they are introduced in the environment of the supported ILs.[93, 100, 184] This competition weakens the H-bonds between C2H or HC4C5H and Cl^-, so large peak shifts of these CH bands with respect to RH implies strong hydration interactions.[172, 176] In the case of confined dry ILs, while stronger H-bonding of CH2 and HC4C5H hydrogens with the wall were indicated by negative wavenumber

shifts, water can also compete for the hydrogen bonding sites on the silica surface. The large positive shifts caused by increasing RH indicate that hydration of both the silica surface and chloride ions weaken hydrogen bonding of the imidazolium ring with counterions.

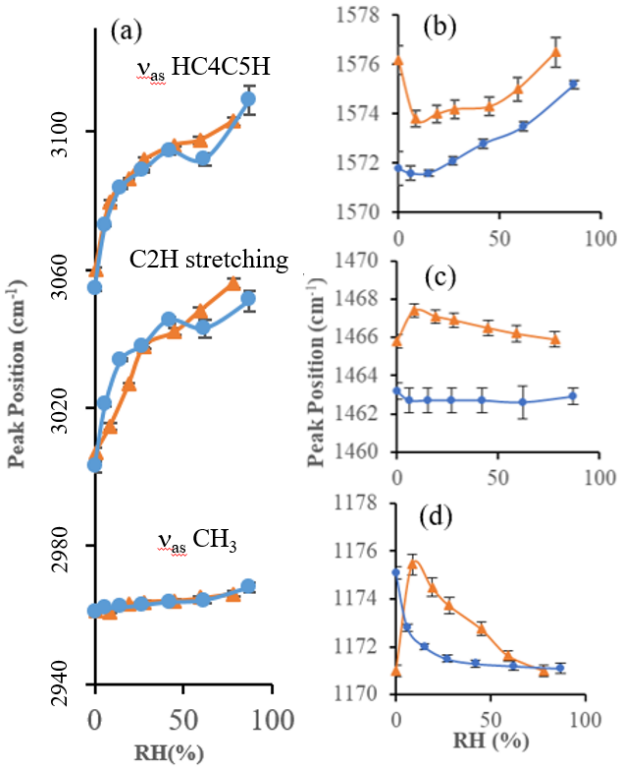

Figure 4-4. Peak positions of CH stretching bands, (a) ν_{as} HC4C5H, C2H stretching and ν_{as} CH_3 and ring stretching bands, (b) C=N-, (c) aromatic C=C- and (d) imidazolium ring stretching in confined (▲) and unconfined (●) [BMIM][Cl] as a function of RH.

Table 4-2. IR peak shifts for a change in relative humidity for unconfined IL (RH 0 to 62%) and confined IL (RH 0 to 59%) as determined from peak deconvolution.

CH stretching bands	**unconfined IL (cm^{-1})**	**confined IL (cm^{-1})**
ν_{ss} HC4C5H	15±2.6	9.8±1.0
ν_{as} HC4C5H	37±2.0	37±1.1
C2H stretching	39±3.2	41±1.9
ν_{as} CH_3	3.5±0.88	3.5±0.63
ν_{ss} CH_3	5.9±1.2	6.7±0.82
Ring stretching bands		
C=C- stretching	-0.6±0.95	0.4±0.55
C=N- stretching	1.7±0.72	-1.2±0.75
ring stretching	-3.9±0.32	0.6±0.45

The hydration-induced peak shifts associated with the imidazolium ring, C=N- and C=C- stretching bands, are not significantly different for confined and unconfined IL when comparing the data taken at endpoints of high and low hydration (Table 2). However, trends in the ring stretching bands are observable (Fig 4b-d) in which the largest change in peak positions usually occurs as H_2O is being introduced (at low RH), with a more gradual change observed as the RH value increases. The C=N- band first decreases with RH and then gradually increases for both the confined and unconfined IL. Fu et al. described a similar effect during [BMIM] halide hydration, and attributed this effect to disrupting hydrogen bonding initially (at low RH) by displacement of hydrated ions, followed by replacement of hydrogen bonding as the population of hydrated ions increases. The C=C- band does not undergo significant shifts because it is removed from the main site of hydrogen bonding, while the less well-defined imidazolium stretching mode follows the opposite trend of the C=N- band. A sharp increase in wavenumber is found in the confined system as RH increases, followed by a gradual decease, while the unconfined system shows

only a monotonic decrease. However, the imidazolium ring itself is much less sensitive to confinement than its hydrogen atoms, as suggested by comparing the magnitude of the peak shifts for the imidazolium ring vibrations and the C-H stretching bands of the imidazolium ring.

Because OH stretching (3400 cm^{-1}) and OH bending (1600 cm^{-1}) [36] bands overlap with some peaks of interest (CH stretching bands and C=N- stretching band), experiments were repeated using D_2O for RH control. The use of D_2O shifts the hydroxyl stretching and bending bands downward to around 2500 cm^{-1} and 1200 cm^{-1} for OD, respectively.[92, 183] The dependence of the peaks for [BMIM][Cl] as a function of RH was the same as H_2O (Supporting Information Tables S3 and S4), with the exception of the C=N- stretching band. Whereas the C=N- stretching band initially drops and gradually increases with RH for the confined system with H_2O, it monotonically increases with D_2O and the difference between confined and unconfined systems is lost (Fig. B5). The C2 proton is the most acidic proton on the imidazolium ring of $[BMIM]^+$ and evidence has been presented for deuterium exchange at the C2 position when D_2O is used as a solvent [90, 176, 187]. Thus, even though the spectra with D_2O are clearer, the H_2O data are used for the remaining analysis of water uptake and water coordination state in ILs. The similarity of the results suggests that deconvolution was adequately able to isolate the shifts of the [BMIM][Cl] bands despite the broad, intense OH stretching band and the interference from OH bending.

As shown in Fig. 4-3, there is a noticeable difference in the shape of the OH stretching bands between confined and unconfined [BMIM][Cl], where the band is slightly broader for confined IL. Previous studies showed that different water coordination states lead to different OH stretching band peaks.[92, 93, 96, 97, 100] To identify the contribution of the

water coordination states to the observed spectra, the broad OH stretching peak was deconvoluted into three peaks associated with different degrees of water coordination: bulk-like water, also known as network water (NW, ~3200 cm^{-1}), interface water (IW, ~3380 cm^{-1}), and anion coordinated water (AW, ~3500 cm^{-1}).[92, 93, 96, 97, 100] Three bands are observed because bulk water has a full hydrogen bonding network and thus low-energy O-H vibrations. Water associated with anions does not have this full hydrogen bond network, and thus has higher energy O-H vibrations. Interfacial water has an intermediate level of hydrogen bonding. One example of the final deconvolution results is shown in Fig. 4-5 for confined [BMIM][Cl] at 78% RH. This is a challenging sample because of the high-intensity OH bands but still is fit with a regression coefficient of R^2 = 0.9994. The peak areas normalized relative to the area of the C=C stretching band (1465 cm^{-1}) are plotted in Fig. 4-6. The C=C band was chosen for normalization because it is unaffected by either confinement or RH changes. [36]

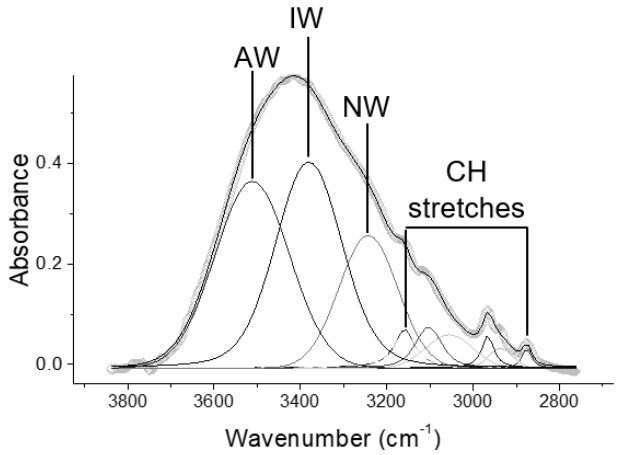

Figure 4-5. Deconvoluted IR spectrum of confined [BMIM][Cl] at RH of 78%. (AW: anion coordinated water; IW: interface water; NW: network water/ bulk-like water). Experimental data are shown as grey unfilled circles, and the overall fit with a black curve. Individual contributions are shown as greyscale curves below the spectrum.

The normalized areas of the water bands increase with RH, indicating water uptake with increasing RH for both confined and unconfined IL (Fig. 4-6). In both cases, anion-coordinated water represents a relatively small contribution to OH stretching that does not change dramatically as RH increases except under very dry conditions (Fig. 4-6). The amount of Cl^- and silica surface (for confined IL) available to interact with water molecules is constant, even as the water content increases with increasing RH. Interface water, also known as "intermediate water" [93, 100], refers to water molecules with distorted H-bonding located at interface of regions with well-defined H-bonding networks [100], which in [BMIM][Cl] is between water associated with Cl^- and the bulk water network.[93, 100] The amount of interface water increases with increasing RH and accounts for the majority of the water taken up by the IL. Bulk-like water accounts for only a small fraction of the overall water content, although it increases with RH. [97, 188] For unconfined [BMIM][Cl], the majority of the water taken up initially is interface water, with bulk-like water added at high RH.

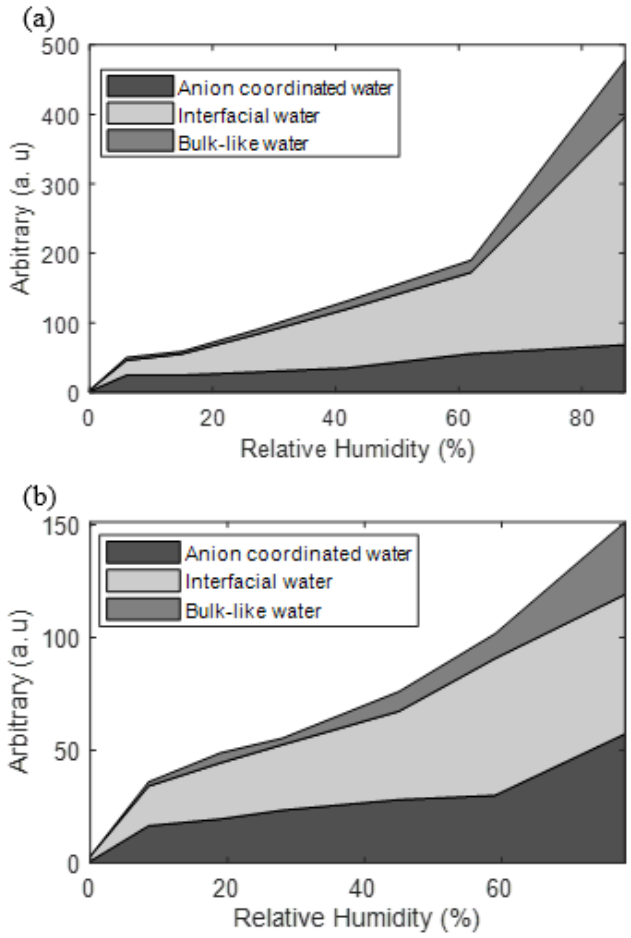

Figure 4-6. Stacked area plots of the OH stretching band area of water in different coordination states based on deconvolution of the O-H stretching band for (a) unconfined and (b) confined [BMIM][Cl]. Intensities are normalized using the C=C- band area.

The biggest difference in the coordination state of water of confined and unconfined IL is found when the RH is decreased to 0%. Because [BMIM][Cl] is extremely hygroscopic, absorbed water is difficult to strip by purging with UHP N_2. Although the OH stretching bands are small at RH 0%, a difference in their relative intensity is measurable from deconvolution. Almost no water exists as bulk-like water in unconfined IL while there is still about 5.3% bulk-like water in confined IL, which might be associated with the hydrophilic silica surface. In confined IL, interface water is a small fraction of the residual

water at RH 0%, whereas the contribution of "anion coordinated" water dominates. This weakly networked water may represent either greater interactions with Cl^- in the ionic liquid, or (more likely) water adsorbed to the surface of the silica support.

In addition to variation in OH stretching peak shape caused by the distribution of water in different hydrogen bonding environments, the growth of the composite OH stretching band with respect to the bands attributed to [BMIM][Cl] indicates a quantitative difference in water uptake caused by nanopore confinement. In Fig. 4-7, the mole fraction of water in the liquid state plotted as a function of RH for confined and unconfined IL. Water content was estimated using the composite OH stretching band area normalized using the area of the C=C- stretching band at around 1465 cm^{-1}. MacMillan et al. reported and modeled the equilibrium water content of [BMIM][Cl] as a function of RH.[36] Here, the water content was estimated using the two-constant Margules model reported by MacMillan et al. at the same RH values at which the normalized OH stretching areas of the bulk (unconfined) [BMIM][Cl] were measured. The resulting data were fit with an exponential function (Fig. B6). Subsequently, this correlation was used to estimate the mole fraction of water in confined [BMIM][Cl] from the normalized OH stretching area, assuming that the extinction coefficients of the bands were not affected by confinement of the ionic liquid and that the IL on the surface of the Si wafer is in equilibrium with the humid nitrogen. The resulting water content for confined and unconfined [BMIM][Cl] as a function of RH is plotted in Fig. 4-7. The water content dependence on increasing RH is similar for confined and unconfined [BMIM][Cl] at RH less than approximately 15%. Above this RH, the IL absorbs significantly less water when confined in silica pores.

Parallel experiment using D_2O as RH control confirm these water uptake results and the details are attached in Supporting Information (Figs. B7 to B9).

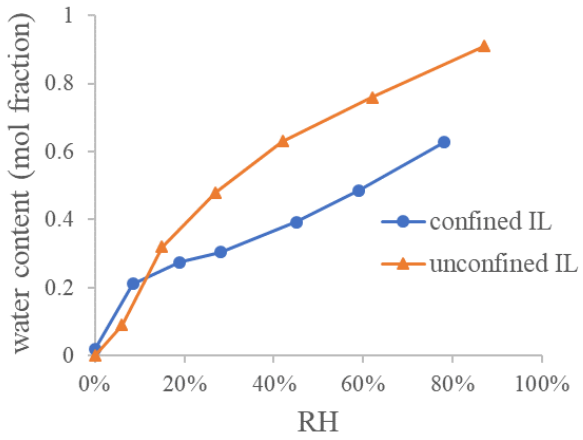

Figure 4-7. Mole fraction of water absorbed as a function of RH for nanopore confined and unconfined [BMIM][Cl] when using H_2O to control humidity. Error bars estimated from the uncertainty in the normalized OH stretching vibration areas are smaller than the data markers.

The differences in water uptake with and without confinement can be explained based on recent molecular simulations of confined ILs. In the dry system (where vacuum treatment was used to eliminate water), the negative wavenumber shift of C2H (Table 4-1) indicates a strong interaction of $[BMIM]^+$ with the negatively charged silica surface, consistent with molecular dynamics simulation of [BMIM][Tf2N] on mica.[189] When water is introduced, it strongly segregates to the silica interface. This disrupts the [BMIM]-silica interaction,[189] which is why the 0% RH sample (which contains residual adsorbed water) loses the C2H band shift relative to unconfined [BMIM][Cl] (Fig. 4-4a). As RH increases, the molecular interactions induced by hydration are very similar, with strong CH stretching effects (Fig. 4-4a) that do not depend on confinement, and weaker but confinement dependent ring stretching effects. The reduced quantity of water taken up in

the confined system (Fig. 4-7) as RH increases can be explained by two effects. The first is comes from the negatively charged pore walls. For a hygroscopic ionic liquid, Docampo-Alvarez et al. showed that confinement in negatively charged graphite nanopores reduces water adsorption in confined ILs because of preferential solvation of anions and the barrier created by the presence of (weakly hydrated) $[BMIM]^+$.[190] While hydrogen bonding is likely to reduce this effect at the immediate silica surface, its charge may produce a barrier to adsorption. The second reason that water uptake is reduced is the increased ordering (layering) of ions near surfaces. Saihara et al. showed based on diffusivity and H/D exchange rates that water is found in heterogeneous clusters within bulk ionic liquids including [BMIM][Cl].[191] It is likely that the layering induced by the silica surface reduces the heterogeneity of the IL, which provides fewer favorable pockets in which water can absorb. Taken together, the *in situ* FTIR results found here show that there is comparable or greater uptake of water at low RH due to strong interaction with the silica surface, continued uptake due to anion hydration that weakens hydrogen bonding to the [BMIM] cations, and a reduction in water uptake at high RH due to surface charge and IL structuring effects within the pores.

4.5 Conclusion

In situ FTIR measurements of supported [BMIM][Cl] were used to probe the effect of confinement on IL structure and water uptake. The ability to use in situ FTIR to characterize the effects of pore confinement was first demonstrated for "dry" [BMIM][Cl]. Deconvoluted vibrational spectra of the CH stretching bands indicate that primary effect of confinement of [BMIM][Cl] in 8 nm pores of silica is the development of interactions

between the silica surface and the imidazolium ring hydrogens, indicated most strongly by shifts of C2-H stretching in “dry” [BMIM][Cl]. The structural changes to the imidazolium ring skeleton are more subtle but consistent with this interaction.

In situ FTIR techniques were extended to study the effect of confinement on water uptake and IL structure as a function of relative humidity (RH). C2H and asymmetric HC4C5H stretching bands experience great peak shifts with increasing RH in [BMIM][Cl] both with and without confinement, suggesting these are the main H-bond forming sites on the imidazolium ring. Hydration of counterions weakens their ability to hydrogen bond with the imidazolium ring hydrogens. Comparable evidence of hydrogen bond disruption by water is observed in the CH stretching bands, but more disruption of hydration is indicated by ring vibrations. Interactions of confined ILs also result in differences in the coordination state of water and the extent of water uptake in [BMIM][Cl], as determined from the deconvoluted OH stretching peaks. Above a threshold RH of approximately 15%, confined [BMIM][Cl] exhibits less hygroscopicity than unconfined ionic liquid, in spite of the hygroscopic nature of the silica support. The interplay of water uptake and confinement is important to the design of supported ILs for separations and catalysis involving water as contaminant, solvent or byproduct.

Acknowledgements

This work was supported by a National Science Foundation grant (CBET-1604491) and the NSF Experimental Program to Stimulate Competitive Research (EPSCoR) grant (award number 1355438)

Supporting Information: Schematic of the *in situ* FTIR set up with humidity control; 2D GISAXS of mesoporous silica thin film; FTIR spectra for the Si wafer and the mesoporous silica thin film; representative IR peak deconvolution for confined and unconfined [BMIM][Cl]; tables of detailed peak IR peak positions for confined and unconfined IL in the presence of H_2O and D_2O; comparison of peak shifts for confined and unconfined ILs as a function of RH; IR spectra and peak shifts for RH control using D_2O; and the empirical correlation of water content as a function of the area ratio of OH stretching.

Chapter 5. Electrochemical Investigation of Nanoconfinement Effects on Redox Probe Transport in Ionic Liquid-Loaded Mesoporous Silica Thin Films

Yuxin He,[1] Arif M. Khan[1], Folami Ladipo,[2] Stephen E. Rankin[1] and Barbara L. Knutson[1,*]

[1] University of Kentucky, Department of Chemical and Materials Engineering, 177 F.P. Anderson Tower, Lexington, KY, USA

[2] University of Kentucky, Department of Chemistry, 125 Chemistry/Physics Building, Lexington, KY, USA

* Corresponding author: bknut2@uky.edu

5.1 Abstract

The permeabilities of two redox probes 1,1'-ferrocenedimethanol (FDM, hydrophilic) and 1,1'-dioctadecyl-4,4'-bipyridinium dibromide (DBD, hydrophobic) through ionic liquid-filled and/or functionalized silica nanoporous thin films with 2.5 and 8 nm diameter pores are compared. The IL treatments include physically confined 1-butyl-3-methylimidazolium hexafluorophosphate ([BMIM][PF_6]), covalently tethered 3-Methyl-1-[3-(trimethoxysilyl)propyl]-1H-imidazol-3-ium ([TMS-MIM]$^+$) group on pore surface, and [BMIM][PF_6] confined in [TMS-MIM] group tethered porous thin films. The permeabilities were obtained from electrochemical impedance spectroscopy (EIS) data in an aqueous system fitted to the Randles equivalent circuit. Functionalization of the nanoporous thin films with an IL-like group provides a barrier to the hydrophilic redox probe (40-fold decrease in permeability relative to bare 2.5 nm porous silica films), with only a 50% corresponding decrease in DBD permeability. The selectivity to hydrophobic solutes suggested by the barrier properties of IL-functionalized silica is less pronounced in the larger pore 8 nm films, with 14-fold decrease in FDM permeability and almost no

change for DBD permeability compared to bare 8 nm porous films. Physically confining the IL in bare and IL-functionalized silica thin films overall results in similar transport properties of the hydrophilic and hydrophobic probes as the non-filled pores. These results suggest that the transport of solutes in IL-confined nanopores is a strong function of the size and surface properties of the nanopores.

5.2 Introduction

Ionic liquids (ILs) are molten salts with melting point near ambit temperature - usually below 100 °C. Unlike conventional liquids and solutions, ILs display good ion conductivity, thermal stability, and extremely low volatility. Therefore, they are widely investigated as solvents, lubricants, and separation media.[2, 3, 154, 192, 193] Supporting ILs on solids or within nanoporous substrates is an attractive alternative to bulk ILs because it reduces the usage of the ILs, thus decreasing the cost of the processes and promoting greener manufacturing.[7, 49, 194] ILs are also potential electrolytes for energy storage and conversion devices, solvating a broad class of solvents for lithium and alkaline salts. [195] More specifically, confining ILs in a nanoporous materials is anticipated for their use in electrodes, solid electrolytes and redox flow batteries. [49, 195, 196] The prediction of transport properties in these highly viscosity fluids is hindered by the complex intra- and inter- molecular interactions in ILs.[197]

Confinement alters crystallization, thermal, electrochemical and spatial behaviors relative to bulk materials. [8-11]. These changes in the physical properties and structure of ILs due to confinement are expected to alter the transport of solutes through confined

ILs. For example, Iacob et al. observed increased charge transport but decreased diffusion coefficients for an IL, [BMIM][BF_4], supported in the pores of silica (average pore size in the range of 7.5 to 10.4 nm), as determined using a combination of broadband dielectric spectroscopy and pulsed field gradient nuclear magnetic resonance. [9, 161] Similarly, the effect of IL confinement has been studied in silica ionogels, in which the IL is confined in the monolithic silica matrix during its synthesis. [50] For as system of confined [Pyr13][NTf_2] with Li salt in a monolithic ionogel with pore diameters ranging from 3.7 nm to 20 nm, the confined network possesses better conductivity than the bulk mixture. [42, 198] A further investigation of the effect of pore size on Li ion mobility in confined IL determined an optimum pore diameter for Li ion ranging from 6 nm to 20 nm. [42] Molecular dynamic (MD) simulations have also been employed to investigate the impact of nanoconfinement on the transport properties of ILs. Coasne et al. concluded that the self-diffusivity of confined [BMIM] [NTf_2] decreases by more than 250% in 4.8 nm silica pores relative to the bulk. Vatamanu et al. also observed a 50% capacitance increase of most ILs studied in carbon-based nanopores relative to unconfined ILs through MD simulations. [48, 49, 199]

Nanoporous silica material have promising advantages as supporting matrices for ILs owing to their tunable porosity and stable chemical and thermal properties, which are important especially to electrochemical applications to withstand high concentration salt solutions and harsh chemicals. [12, 13] In contrast to IL confinement as an ionogel, post-impregnation of ILs in a silica matrix is employed in this study because it provides more flexibility on the form of the supporting matrices (particles, thin films and monoliths) and improved control of pore morphology and surface functionalization.[49] In particular,

synthesis of mesoporous silica thin films using surfactant-templating provides the opportunity to control pore size based on surfactant tail length (< 10 nm) [68, 128] and structure by altering the surfactant choice and concentration.[129] A challenge in developing nanoporous thin films from surfactant templating is the ability to obtain an accessible pore structure. The preferred interaction between the surfactant micelle templates and the substrate surface results pores oriented parallel to the substrate surface and corresponding thin films with inaccessible pores. [14] Methods such as external magnetic fields, surface patterning, and surface modification have been used to obtain vertically aligned pores in silica thin films.[68] We have previously demonstrated the ability to manipulate pore orientation of mesoporous silica thin films templated by Pluronic P123 surfactant using substrate surface functionalization to obtain ordered, accessible pore channels (8-10 nm diameter) [17, 64, 76]. With a goal of comparing the effect of pore size on transport in ionic liquid-filled channels, an alternative synthesis approach to achieve silica thin films with smaller accessible pore channels (2.5 nm) is demonstrated here using a surfactant template with a smaller tail (cetyltrimethylammonium bromide; CTAB) combined with the deposition of a doped silica film sol. Doping the silica matrix with small amount of titania (2%) destabilizes the silica porous structure during calcination, forming accessible pores through vertical thermal contraction of the film.

An alternative approach to confining ionic liquids in silica mesopores is the tethering of IL-like organosilanes directly to the pore walls. The tethering of ILs prevents leaching. The grafting of a hydrophobic IL-like species to the hydrophilic silanol groups on the silica surface also reduces the surface hydrophilicity. [49, 55] Changes in surface hydrophilicity alter IL-pore wall interactions and the structure of ILs confined in these IL-functionalized

thin films. For example, IL molecule rearrangement and reorientation within silica nanoconfinement has been correlated with the interaction between the imidazole or anion of the imidazolium-based ILs and the hydroxyl group (Si-OH) on silica surface.[49, 170, 200, 201] Similarly, covalent attachment of a modified IL as a monolayer on a cobalt (II) oxide surface was demonstrated to change the orientation of free ionic liquid at that surface relative to excess IL deposited on the same surface. [202] These type of surface interactions between IL and tethered IL are hypothesized to alter transport through IL-filled nanoporous channels of silica thin films.

Here, molecular transport of hydrophilic (1,1'-ferrocenedimethanol (FDM)) and hydrophobic (1,1'-dioctadecyl-4,4'-bipyridinium dibromide (DBD)) redox probes through IL-loaded silica thin films (IL filled; tethered IL; and tethered IL + IL filled) was investigated as a function of pore size (2.5 nm and 8 nm diameter) and compared to bulk IL using electrochemical impedance spectroscopy (EIS). EIS is non-destructive method to study charge transfer resistance at interfaces including ion transport in thin films. [117, 123, 124, 203] EIS has the advantage of characterizing both the accessibility of the nanopores [122] and the permeability of probe molecules through porous substrates. [122-124] The IL 1-butyl-3-methylimidazolium hexafluorophosphate ([BMIM][PF_6]) was selected because it is a common hydrophobic IL, where hydrophobicity is required because the supported ionic liquid is submerged in aqueous electrolytes. The role of hydrophobicity and hydrophilicity in transport through pore-confined IL is interpreted from the permeabilities of the redox probe molecules and highlights the potential selectivity of IL-confined silica thin films.

5.3 Experimental Methods and Materials

Materials. Titanium (IV) isopropoxide (TIP, ⩾97%), glycerol (89%), 1,6-diisocyanatohexane (98%), tetraethoxysilane (99.9%), Pluronic P123 poly(ethylene oxice)-b-poly(propylene oxide)-b-poly-(ethylene oxide) copolymer (Mn ~ 5800), 1,1'-ferrocenedimethanol (FDM, 97%), 1,1'-dioctadecyl-4,4'-bipyridinium dibromide (DBD, 97%), NOCHROMIX® powder, n-methylimidazole (99%), (3-chloropropyl)trimethoxysilane (⩾97%) and the ionic lqiuid 1-butyl-3-methylimidazolium hexafluorophosphate ([BMIM][PF_6], ⩾98%) were obtained from Sigma-Aldrich; concentrated sulfric acid (98%), 1 N HCl, and acetone (99.5%) from VWR; cetyltrimethylammonium bromide (CTAB, 99.8% was purchased from MP Biomedicals; tetraethyl orthosilicate (TEOS, 99%) was purchased from Acros Organics; sugar surfactant n-Dodecyl β-D-maltopyranoside ($C_{12}G_2$, HPLC grade, ⩾99%) was purchased from BioVision Inc; and 200 proof ethanol from Decon Laboratories. The substrates used for sample preparation were borosilicate glass slides (VWR), fluorine doped tin oxide (FTO) glass (Sigma-Aldrich) and 600 μm thick silicon (Si) wafers (University Wafer, Inc.). Toluene and Diethyl ether (both ACS grade) were purchased from Pharmco-Aaper.

Cetyltrimethylammonium bromide (CTAB) templated silica thin film synthesis: Cetyltrimethylammonium bromide (CTAB) was used to template Ti-doped silica films with oriented 2-3 nm diameter pores. Silica thin films with 2% titania were synthesized by mixed templating using CTAB and a sugar-based surfactant (n-Dodecyl β -D-maltopyranoside; $C_{12}G_2$) which complexes with the Ti-precursor, following a modified

procedure of Rahman et al. [141] Initially, 70 mg of $C_{12}G_2$, was dried in a vacuum oven at 50 °C for 24 h and then dissolved in 2.4 mL of dry ethanol under dry nitrogen. 42 µL of TIP was added to this ethanolic solution (resulting in a Ti:$C_{12}G_2$ molar ratio of = 1:1) and the solution was stirred for 3 h in a sealed vial under dry nitrogen to allow for the complexation of TIP with the sugar headgroup of $C_{12}G_2$. Separately, 1.41 mL of TEOS was added to 0.98 mL ethanol under constant stirring and 0.21 mL of DIUF water and 0.27 mL of 0.1 M HCl was added to this solution. The TEOS mixture was stirred for an hour to allow for the hydrolysis of silica precursor. The TEOS solution was then added dropwise to the TIP:$C_{12}G_2$ mixture with vigorous mixing in a nitrogen glove bag. The mixture was then stirred while 0.12 mL of DIUF water and 1.03 mL of ethanol were added. Finally, 252 mg of CTAB was added to the reaction mixture followed by 3.42 mL ethanol. The final sol for dip coating was made by stirring for another hour.

Two different substrates were employed for the silica thin films: silicon wafers for thin film characterization and FTO glass for EIS. The silicon wafer was cut into approximately 1cm × 3 cm pieces, which were cleaned with NOCHROMIX® in concentrated sulfric acid solution. The FTO glass was sliced into 1.5 cm × 3 cm pieces and the pieces were sonicated in deionized ultra-filtered (DIUF) water and then acetone for 20 minutes, followed by UV-ozone treatment in a Bioforce Nanoscience UV.TC.110 instrument for 20 minutes. The cleaned silicon wafer and FTO slides were coated with the sol prepared (withdrawal speed 6 cm/min) and then placed into an oven to age at 50 °C for 48 h. Aged films were heated at 120 °C for 6 h and then calcined in air at 500 °C for 1 h (heating ramp 1 °C/min).

Pluronic P123 templated silica thin film synthesis: Silica films with larger oriented mesopore channels (8-10 nm) were synthesized by depositing the silica film sol on a

chemically modified substrate, which was used to achieve an accessible pore orientation. Following a method adapted from Koganti and Rankin,[14, 64] cleaned glass slides and FTO slides were first modified with cross-linked copolymer P123 prepared using glycerol, acetone, DCH and P123. The silica film sol initially consisted of 1 : 3.8 : 1 : 5×10^{-5} molar ratios of TEOS: ethanol: DI water: HCl. After allowing for hydrolysis at 70 °C for 1.5 hr, more DI water and HCl were added to reach 7.34 mM HCl in the solution, following by a 15-min aging at 50 °C. Then P123 in ethanol solution was added to make a final molar ratio of TEOS: ethanol: DI water: HCl: P123 equal to 1: 22: 5: 0.004: 0.01. The final sol was dip-coated on the modified glass slides or FTO slides. The films were then aged at 45 °C then 100 °C for 24 hours each. Finally, they were calcined at 500 °C for four hours in air with heating rate of 1 °C/min.

Characterization of silica thin films: The d-spacings and orientations of the pores for the CTAB- and P123-templated silica thin films on Si wafers were determined with grazing incidence small angle x-ray scattering (GISAXS) using a Xeuss 2.0 instrument (Xenocs U.S. Inc.) with X-ray wavelength of 1.54 Å and exposure time of 10 min. The 2D GISAXS pattern imaging and data reduction were performed using FOXTROT (Synchrotron SOLEIL). The film thickness was determined using a Dektak 6M Stylus profilometer; the height difference at the drawback line from dip coating was considered to be the film thickness.

3-Methyl-1-[3-(trimethoxysilyl)propyl]-1H-imidazol-3-ium chloride ([TMS-MIM][Cl]) synthesis and tethering to silica thin films: The organosilane with an imidazole head group was synthesized in Dr. Ladipo's lab. A mixture of N-methylimidazole (2.00 ml, 25 mmol) and (3-chloropropyl)trimethoxysilane (4.59 ml, 25 mmol) was refluxed in toluene (40 ml)

for 36 h. The mixture was allowed to cool to room temperature and the supernatant solution was removed with a pipette. The resultant oil was washed with diethyl ether (10 ml for three times) to remove unreacted materials, and then dried under reduced pressure at room temperature. The product was obtained as a colorless oil (6.80 g, 97%). The identity of the prepared ionic liquid was established by comparing its 1 H and 13C NMR spectra with the reported literature.[204, 205] Both solvents, toluene and diethyl ether dried and distilled by standard methods prior to use.[206]

To functionalize mesoporous films, synthesized [TMS-MIM][Cl] (about 15 mg) was dissolved in 10 mL of chloroform. The silica films were submerged in the solution and heated in a water bath at 60 °C under reflux for 26 hours. [207] Before reflux, the procedures were carried out under nitrogen environment to prevent [TMS-MIM][Cl] from being hydrolyzed. After reflux, the silica films were removed from the solution and rinsed with DI water and ethanol then dried with compressed air.

X-ray photoelectron spectroscopy (XPS) depth profile of tethered silica films: Silica films deposited on Si wafers with [TMS-MIM][Cl] tethering were characterized by XPS depth profiling under ultra-high vacuum. A K-Alpha XPS instrument (Thermo Scientific) was employed to measure the elemental composition of C, N, Si, and O in each layer before ion gun etching. During etching, an electron flood gun was turned on for charge compensation. A survey scan was first performed, then Si and O were analyzed with 10 scans while C and N were analyzed with 15 scans assuming a small relative amount of these two elements. The Ar^+ ion gun power was set at 500 eV for 12 increments of etching in total between the readings. The etching time was 10 seconds for the first 4 intervals and 200 seconds for the remaining 8 intervals. Avantage software (Thermo Scientific) was used

for both data acquisition and analysis. The atomic percentage of the elements were calculated based on the electron density verses binding energy peak areas by Avantage, and then plotted with respect to the etching time.

Supported IL on FTO substrates. [BMIM][PF_6] was deposited on five different substrates: bare FTO glass (unconfined IL), P123 templated silica films with and without tethering, and CTAB templated silica films with and without tethering. A very small drop of IL was placed on the silica films and bare FTO glass, then covered by a piece of cover glass (VWR). The cover glass was gently pressed from the top to spread out and squeeze out the excessive IL from the edge of the cover glass. This was to minimize the IL sitting in between the cover glass and silica film, also to obtain an even thin layer of IL when supported by a flat surface.

Measurement of redox probe transport by EIS. EIS was performed using the redox probes 1,1'-ferrocenedimethanol (FDM) and 1,1'-dioctadecyl-4,4'-bipyridinium dibromide (DBD) (Scheme. 5-1). In addition to the five types of supported IL substrates described previously, EIS was also performed on bare FTO slides and bare CTAB-templated and P123-templated silica thin films.

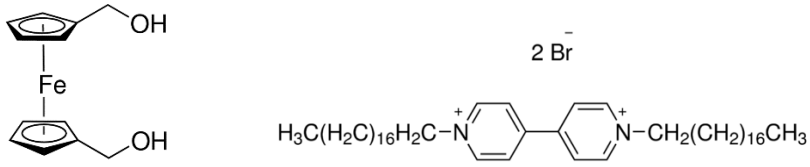

Scheme 5-1. Molecular structure of FDM (left) and DBD (right)

EIS was conducted in a three-electrode cell shown in Fig. 5-1, where the Pt counter electrode, working electrode (FTO slides deposited with different silica thin film

samples) and Ag/AgCl reference electrode were submerged in 25 ml electrolyte containing 1 M KCl and either 1 mM FDM hydrophilic redox couple or 0.3 mM DBD hydrophobic redox couple. The three electrodes were connected to a potentiostat (CHI 660D CH Instruments Inc.). The EIS was measured over a frequency range (ω) of 0.1 Hz to 100 kHz at room temperature. An AC sinusoidal potential (E) with amplitude of 0.01V was applied to the working electrode along with a DC potential triggering the redox reaction of the electroactive species in the electrolyte. The DC potential was 0.21V for FDM and -0.6V for DBD, as determined by cyclic voltammetry. [15, 122]

The resulting complex impedance is measured over a range of frequencies, ω. The response signal I is shifted in phase ϕ. The response can be described by the following equation, which combines Ohm's law combining with Euler's relation [117].

$$Z(\omega) = \frac{E}{I} = |\mathrm{Z}_0| \exp(\mathrm{j}\phi) = |\mathrm{Z}_0|(\cos\varphi + j\sin\varphi)$$

$$= |\mathrm{Z}_0|\cos\varphi + j|\mathrm{Z}_0|\sin\varphi = Z_{Re} + jZ_{Im} \quad (1)$$

The complex impedance data were exported to ZView (Scribner Associates, Inc.) to fit a Randles equivalent circuit shown in Fig. 5-1. [122] The circuit consist of four elements, which are R1, the resistance of the electrolyte solution; R2, the charge transfer resistance between the redox species and the electrode at the interface; Ws1, Warburg impedance corresponding to 1D semi-infinite mass transfer of electrolyte in the bulk phase representing diffusion in the porous film; and a constant phase element, CPE1, in parallel to R2 and Ws1, representing the electrical double layer capacitance at the electrolyte-sample interface. [122, 124, 208]

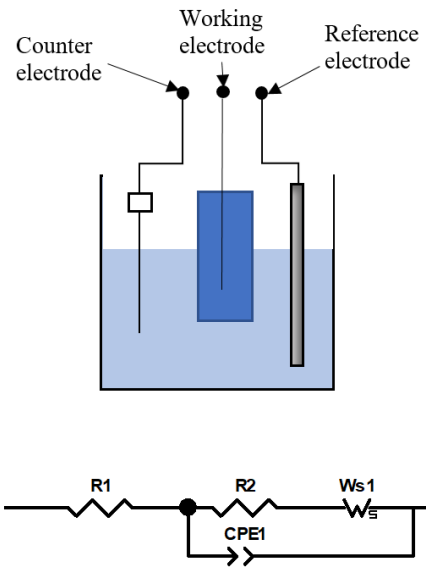

Figure 5-1. Schematics of a three-electrode cell for impedance measurement and equivalent circuit with R1 = electrolyte solution resistance, R2 = charge transfer resistance at the sample surface, Ws1 = Warburg diffusion element, and CPE1 = constant phase element with electric double-layer capacitance.

FTIR characterization of IL deposition on bare FTO slide: [BMIM][PF_6] was deposited on a piece of clean Si wafer with thickness of 150 µm using the same method as described above. The FTIR spectrum of the film was taken (100 scans) using a Thermo Nicolet Nexus 470 FTIR with a KBr beam splitter and a liquid N_2-cooled mercury cadmium telluride (MCT) detector. The Si wafer with IL was then soaked in DI water for two minutes and removed from the water. This was to simulate the EIS measurement in an aqueous solution. After that, the wafer was air dried and the FTIR spectrum measured again.

Water contact angle measurements: Non-porous silica films with and without TIP were synthesized on glass slides following the procedures described for the synthesis of CTAB template silica thin films, but in the absence of CTAB or sugar surfactants. The mean contact angle of the water droplets (10 µl) on the non-porous silica surfaces synthesized with and without TIP were measured using a Krűss GmbH instrument.

5.4 Results and Discussion

The effect of nanoconfinement on transport in ILs was compared at two pore diameters (approximately 2.5 nm and 8 nm) by first synthesizing the corresponding silica thin films with accessible pore structure. Pore dimensions and orientation are verified by grazing-incidence small-angle X-ray scattering (GISAXS). The GISAXS pattern in Fig. 5-2(a) for P123 templated silica films shows a portion of an elongated ring with absence of the part at (010) direction (normal to the substrate). The elongation of the ring in the GISAXS pattern reflects the unidirectional contraction of the thin film perpendicular to the substrate due to the removal of the surfactant.[140] The remaining portion of the pattern consists of two vertical rods in the plane of (100) and ($\bar{1}$00) with d-spacing calculated as 9.6 nm. This is consistent with the orthogonally oriented hexagonal close-packed (o-HCP) structure obtained from our previous studies using the same film synthesis method.[166, 209] The d-spacing of 9.6 nm in a hexagon geometry yields a pore center-to-center distance of 11.2 nm. According to Coquil et al.'s study, the wall thickness of P123 templated 2D hexagonal porous structure in silica was determined to be 3 to 5 nm.[210] This wall thickness gives an estimation of 7.2 ± 1 nm for the pore size. The corresponding pore diameter was estimated in a previous study in the group to be 9 ± 1.3 nm, as determined from TEM of films scraped from the substrate.[14, 15, 17] Given the uncertainties associated with both approaches, it is reasonable to approximate the pore diameter of the P123 templated films produced in this study as 8 nm. The thickness of the film was determined by profilometer to be about 180 nm.

In extending the synthesis of silica thin film with accessible pores to a smaller pore size, we first selected a smaller surfactant template (CTAB). While CTAB templated

silica films have smaller pores than P123 templated silica films, the pores are oriented parallel to the substrate and are therefore inaccessible (Chapter 2). Our rationale for doping the thin film with titania (which was complexed to a sugar surfactant when introduced in the sol gel) was based on previous attempts to synthesize titanosilicate thin films for epoxidation catalysis. [141, 150] As suggested by these previous studies, the order of the pore structure decreased with titania incorporation. We hypothesized that doping the silica with a small amount of titania would destabilize the porous structure and that the degree of instability would be related to the concentration of titania. Further, this instability could be exploited during the subsequent calcination of the silica thin films to remove the template, leading to an alternate morphology. In this study, doping the films with 2% titania (introduced complexed with $C_{12}G_2$) results in a disordered porous structure prior to calcination, as interpreted from the isotropic ring (d-spacing approximately 3.5 nm) of the high resolution GISAXS pattern obtained from Argonne National Laboratory of 1% titania doped film with complexation as a representation (Fig. 5-2(b)). During calcination, the film went through a thermal contraction in the vertical direction (Chapter 2), causing the micelles to connect and form vertically oriented channels with respect to the substrate (Fig. 5-2(c)). The final structure was a similar o-HCP structure as P123 templated film (Fig. 5-2(a)). The d-spacing determined from the position of the vertical rods from the GISAXS pattern (Fig. C2) of CTAB templated film is 3.5 nm. This d-spacing represents the distance between the planes of the HCP structure and this allows us to calculate the distance between the centers of two neighboring pores to be $2/\sqrt{3} \times$ d-spacing, which is about 4 nm. The pore wall is estimated to be about 1 to 2 nm thick from other CTAB templated silica materials, [74, 146, 211, 212] so the pore

diameter in this study is estimated to be about 2.5 nm. The CTAB templated silica thin films are about 100 nm thick, as measured using a profilometer measurement after calcination to remove surfactants. Titanosilicate films with different dosages of titania were compared in **Chapter 2** and 2% titania doping provided the most stable and reproducible thin films. Water contact angle measurements on non-porous silica film with and without the 2% titania are similar (43.0 ± 4.7˚ vs. 44.2 ± 4.2˚, respectively), which supports the assumption that the titania doping does not change the properties of the silica surface. Thus, we expect primarily structural differences between CTAB and P123 templated thin films.

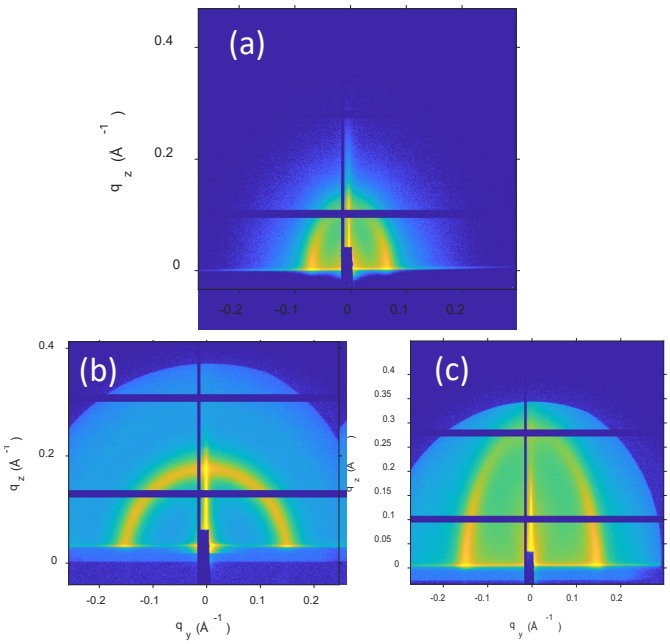

Figure 5-2. GISAXS 2D patterns of (a) P123 templated silica film with o-HCP structure; CTAB templated silica film (b) before calcination showing disordered porous structure and (c) after calcination showing o-HCP structure

After the synthesis of the silica thin film supports, an IL-like molecule ([TMS-MIM][Cl]) was covalently tethered to the thin films. Similar attachment methods have been used to functionalize silica particles with ILs for the design of electrorheological fluids, catalysts, and adsorbents [54, 55, 58] Under some conditions, [TMS-MIM][Cl] has been reported to self-polymerize during surface silanization. [58] This might block the pathway of silica nanopores, thus preventing uniform tethering of [TMS-MIM][Cl] in the pores, limiting subsequent physical sorption of [BMIM][PF_6], and hindering the diffusion-limited electrochemical reaction of the probe molecules in the EIS experiments. Therefore, XPS depth profiles were obtained for the films with tethered [TMS-MIM][Cl] to investigate the uniformity of the tethering at the surface and within the nanopores of the film. The atomic percentages of C, N, Si, and O with respect to ion etching time are presented in Fig. 5-3 and the tabulated values are presented in Appendix C (Table C1, C2). The etching time is assumed to be proportional to the distance of the current layer from the original top surface in a uniform substance, so it represents the relative depth of the layer from the top. For both types of the films (2.5 nm and 8 nm), the portion of the film where the Si: O atomic ratio is about 1: 2 corresponds to the silica film. As the etching goes deeper, it reaches the silicon substrate where there is almost pure Si. In both tethered porous films, the atomic ratio of C: N prior to reaching the Si wafer is about 3.5, which is consistent with the tethering compound ($C_7H_{12}N_2SiO_3$-). In addition, the composition with respect to C and N from the top surface (etching time=0) through the silica layer is approximately is constant, suggesting the top surface of the silica films are not blocked by self-polymerized [TMS-MIM][Cl] and that the tethered IL is distributed across the entire thickness of the silica films.

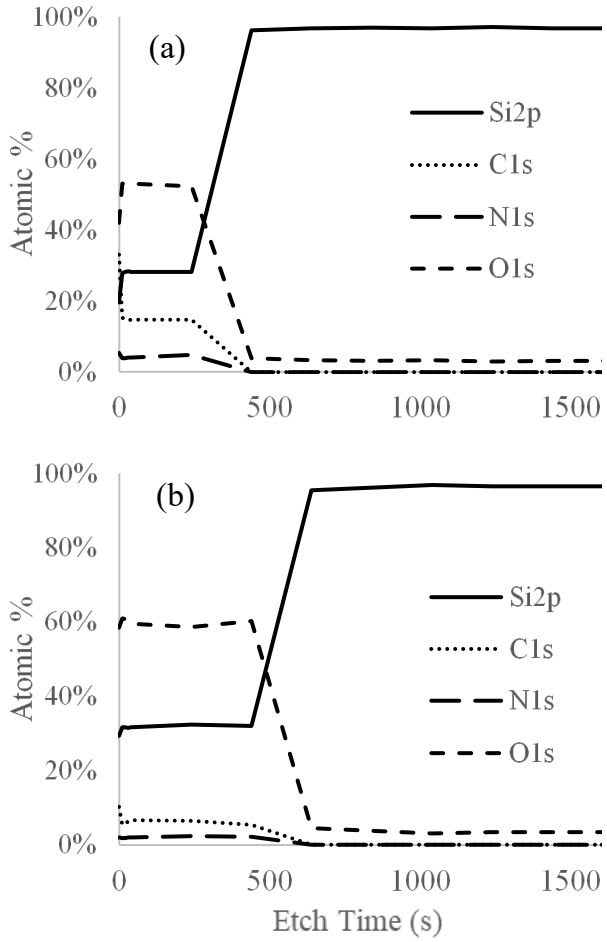

Figure 5-3. XPS depth profiles of (a) CTAB templated (2.5 nm pores) and (b) P123 templated (8 nm pores) silica films with [TMS-MIM][Cl] tethering. Increased etching time corresponds to deeper layer from the top surface (etching time = 0 s)

The effect of confinement on supported ILs on redox probe transport was quantified using EIS measurements. Positively charged and/or neutral redox species FDM^+/FDM and DBD redox couples were selected as probe molecules. Because the silica surface is negatively charged, electrostatic repulsion would dominate transport if an anionic redox species was used and hinder the interpretation of the EIS data. FDM and DBD represent hydrophilic and hydrophobic probes, respectively. A small amplitude sinusoidal AC

bias was applied in the presence of a DC potential to trigger the redox reaction of the redox probe molecules (0.21V for FDM) to measure the complex impedance ($Z(\omega) = Z_{RE} + j\, Z_{IM}$) over a range of frequency. The complex impedance, which can be presented in a Nyquist plot, is used to fit the elements of a Randles equivalent circuit (Fig. 5-1).

As an example of the interpretation of EIS data, Fig. 5-4 presents the Nyquist plot for the redox probes FDM and DBD probes interacting with bare FTO slides and [BMIM][PF_6] supported directly on an FTO slide (unconfined IL). Three of the four equivalent circuit elements can be roughly estimated from the Nyquist plot. R1 represents the resistance posed by the electrolyte solution, corresponding to the intercept with the low frequency region on the x axis of the Nyquist plot. R2 represents the charge transfer resistance on the working electrode surface. For thin films and membranes deposited on the working electrode, additional resistance of the transport of the redox species in these layers is interpreted using R2.[117, 123, 213] R2 corresponds to the larger semi-circle in the Nyquist plot and the value can be estimated from the diameter of the semi-circle. The straight line following this semi-circle corresponds to Ws1, the Warburg impedance, representing the 1D semi-infinite diffusion of the redox probe in the bulk electrolyte phase.[117, 122, 209]

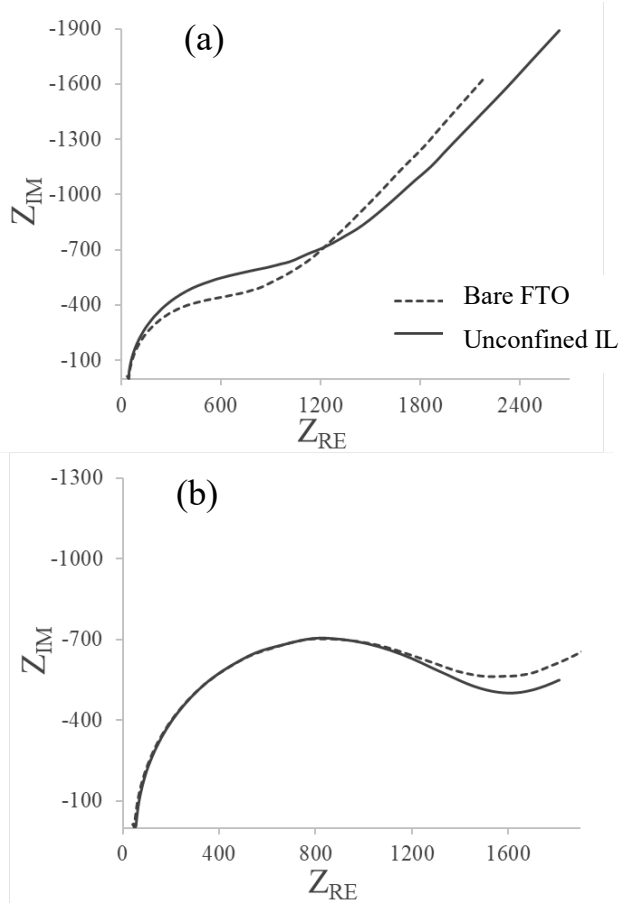

Figure 5-4. Nyquist plot of bare FTO slides (solid line) and [BMIM][PF_6] deposited on FTO slides (representing unconfined IL, dashed line) with (a) FDM and (b)DBD as redox species

The resistance to surface charge transfer, R2, is the element most relevant to interpreting the impact of thin film structure, functionalization, and confined ionic liquid on the resistance for the charge carriers to travel through the thin films and reach to the working electrode underneath. The Nyquist plot in Figure 4 provides a comparison of the resistance to surface charge of the redox probes at the interface of working electrode for bare FTO and unconfined IL (IL deposited on bare FTO). In the case of the hydrophobic (DBD) redox probe, the unconfined IL does not significantly alter the charge transfer resistance relative to the bare FTO (Figure 4(b)). This is evident from the similar diameter

of the semi-circle and confirmed from fitting the impedance data to the equivalent circuit model (Table S3). The flat surface supported IL did increase the resistance to hydrophilic (FDM) slightly (Fig. 5-4(a)), which is consistent with the hydrophobic nature of the IL. The FTIR tests confirmed that [BMIM][PF_6] remained on the surface after submerging in aqueous solution to further validate the conclusion. (Fig. C2) The contribution to diffusion of the redox probe in the electrolyte represented by the Warburg impedance will not be the focus of this study; the straight line corresponding to the Warburg impedance becomes shorter as the surface charge resistance becomes greater in the restricted frequency range of the EIS experiments.[209] For this reason, the uncertainty associated with the calculated Warburg impedance values are significant (Table C3) when the surface resistance is the dominant element. The double layer capacitance of the bare FTO surface calculated from the equivalent circuit fitting is about 19.8 μF (Table C3), which is close to the value of 21.1 μF in Wei et al.'s study under comparable conditions [122] and there is no great variation for the same film with different treatments with the same redox probe. The double layer capacitor represented by CPE1 arises from the potential difference between the electrode surface and the electrolyte.[214] The capacitance can provide information regarding the thickness of the materials deposited on the electrode. Since the thickness of the two types of the silica thin film is fixed in this study, it is not surprising that the double layer capacitances are similar for the same type of film. R2 will be the focus of this study since it provides values with relatively high confidence for interpretation of the effects of pore size, functionalization and IL confinement on the transport of the redox probes through silica thin films. The purpose of the equivalent circuit fitting is to extract the value of R2 more accurately for further analysis.

Transport of the redox probe FDM through of the bare silica thin films (in the absence of IL) as a function of pore size was first measured and was compared to bare FTO. The goal was to quantify the contribution of charge transfer resistance on the electrode surface due to partial surface coverage by the nonconductive porous silica and determine the working electrode accessibility, (1-θ). Following the method of Wei et al, (1-θ) is equal to the ratio of the charge transfer resistance of bare FTO slides to silica films supported on the FTO substrate. [122]. Wei et al. conducted a systematic study using EIS to characterize the working electrode accessibility under self-assembled nanoporous silica thin films with pore structures and orientations verified by grazing-incident small angle X-ray scattering (GISAXS). The working electrode accessibility for a 2D hexagonal structure aligned parallel to the substrate surface (p-HCP), as determined by Wei et al., [122] is much smaller than that of o-HCP films synthesized here with the same templating surfactant (Table 1). This is consistent with the alignment of pore channels to obtain accessible pores in o_HCP films. The 1- θ values of the o-HCP films obtained from this study are comparable with that of body-centered cubic (0.55) and double gyroid (0.33) structures, [122], which are connective porous structures with accessible pores. As shown in Table 1, the silica film with 2.5 nm pores has greater working electrode accessibility to the FDM redox probe than 8 nm porous films, possibly due to the thinner pore wall of the CTAB templated silica films as mentioned earlier (1 to 2 nm for CTAB templated silica and 3 to 5 nm for P123 templated silica [74, 146, 210-212]).

Table 5-1. Surface charge resistances from Randles equivalent circuit fitting and working electrode surface accessibilities to FDM/FDM^+

	R_2 surface charge transfer resistance (Ω)	1-θ (o-HCP)	1-θ (p-HCP)[122]
bare FTO	1262 ± 36	1	1
2.5 nm porous film (CTAB)	2302 ± 84	0.55	<0.001
8 nm porous film (P123)	3397 ± 119	0.37	0.09

Figure 5 summarizes the redox transport studies conducted for the supported IL. These include unconfined supported IL (directly on FTO), IL-tethered mesoporous silica, and IL confined on mesoporous silica and IL-tethered mesoporous silica. Impedance studies of supported ILs examined transport of both a hydrophilic (FDM) and hydrophobic (DBD) redox probe and considered both pore sizes (2.5 nm and 8 nm) of the mesoporous silica thin films. The impedance data were processed and fit to a Randles equivalent circuit model, as described previously. The fit of the models for each substrate/probe combination is summarized in the Supplemental Information (Table. S3).

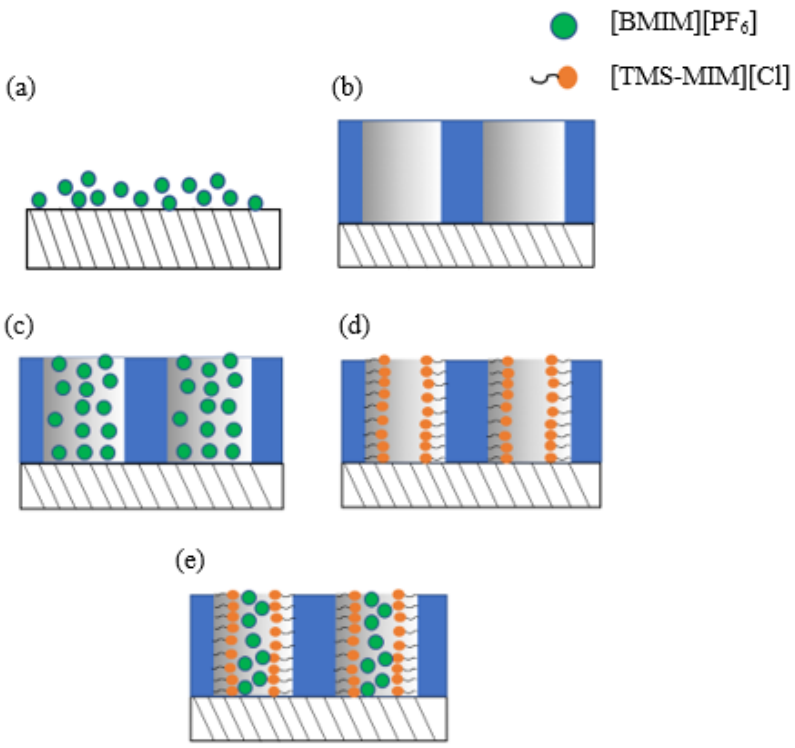

Figure 5-5. Schematic summary of measurements of probe transport through supported ILs (a) unconfined IL supported by a flat surface; (b) bare silica film; (c) confined IL (silica film + IL); (d) silica film with [TMS-MIM][Cl] tethering; (e) confined IL in silica film with tethering (tethered silica film + IL), with 2.5 or 8 nm pores

Surface charge resistances obtained from the EIS experiment can be translated to redox probe permeability through the films by the following equation: [122-124]

$$R2 = \frac{4RT}{n^2F^2A\,C_{R2}\,\omega_{R2}\,(1-\theta)} \quad (2)$$

where R2 is the surface charge resistance (in Ω) and ω_{R2} (m/s) is the corresponding permeability of the redox group at the interface of the silica film and electrolyte. R and F are gas constant and Faraday constants, respectively; n is the number of charges transferred in the redox reaction (1 in this case); and all other parameters (operating temperature T, working electrode submerging area A (1.8 cm^2 for 2.5 nm porous film and 3.4 cm^2 for 8 nm porous film), and concentration of the redox species in the electrolyte

C) are well defined in the experiment. The difference of electrode surface accessibility between the films with two different pore sizes are normalized in the equation with (1- θ) to allow comparison across different surface coverages, where (1- θ) is equal to 1 for bare FTO. The permeabilities for the supported IL samples are tabulated in Table 2.

Table 5-2. Permeability of redox probes, $\omega_{R2,}$ through mesoporous supports with and without nanoconfinement of [BMIM][PF_6]

	2.5 nm pores ω_{R2} ($\times 10^{-7}$ m/s)		8 nm pores ω_{R2} ($\times 10^{-7}$ m/s)	
	FDM (hydrophilic)	DBD (hydrophobic)	FDM (hydrophilic)	DBD (hydrophobic)
IL (unconfined)	8.50 ± 0.66	19.20 ± 1.17	8.50 ± 0.66	19.20 ± 1.17
Silica film (no IL)	11.59 ± 1.25	19.35 ± 2.60	6.26 ± 0.81	10.88 ± 1.11
Silica film + IL	9.21 ± 0.89	37.27 ± 2.39	4.06 ± 0.46	10.16 ± 1.02
Tethered silica film (no IL)	0.30 ± 0.05	29.54 ± 3.25	0.44 ± 0.03	9.94 ± 0.87
Tethered silica film + IL	1.79 ± 0.21	24.41 ± 1.59	0.51 ± 0.01	10.19 ± 0.70

In interpreting the permeabilities in Table 2, the most direct comparison of values can be made for the same pore size films. This is due the effect of film thickness on permeability (ω) through a membrane, [123]:

$$\omega = \frac{D \times K}{\delta}$$

where δ is the film thickness, D is the diffusion coefficient, and K the partition coefficient. The thickness of the two films is 90 nm and 180 nm for the CTAB and P123 templated films, respectively. This is consistent the observation that the 8 nm pore silica thin films are less permeable to both probes than the 2.5 nm pore silica thin films ((silica film (no IL)). Overall, the permeability of both redox probes is approximately half the value in the 8 nm porous film relative to the 2.5 nm pores for nonfunctionalized silica

films (with and without IL loading). The thickness of the unconfined IL deposited on the FTO is unknown, and therefore the permeability of this IL treatment is not directly compared to transport in the silica thin films.

The effect of confinement and IL-tethering on the transport of redox probes though IL-loaded pores is dramatically different for the hydrophilic and hydrophobic probe molecules (Table. 2). In the absence of IL for bare silica films and tethered films, a tremendous decrease in permeability of the hydrophilic FDM probe is observed through 2.5 nm pores with tethering (tethered silica film (no IL)) relative to bare 2.5 nm porous silica films. The almost 40-fold decrease in permeability in the IL-functionalized silica thin films is attributed to the change in surface properties (from hydrophilic to hydrophobic) with the tethering of the hydrophobic imidazolium head group. [49, 55] The hydrophobic surface of these channels possesses much greater resistance for the hydrophilic redox probe than bare silica. A significant decrease in hydrophilic probe permeability was also observed in 8 nm pores with tethering (also in the absence of IL). The decrease in permeability (14-fold for 8 nm pores) is not as severe as in 2.5 nm pores, but the absolute value of the permeability is similar for the transport of the hydrophilic probe in IL-functionalized 2.5 nm and 8 nm pores in the absence of IL. XPS depth profiles (Fig. 5-4) show that the amount of [TMS-MIM][Cl] tethered on the pore surface is greater in CTAB templated films. As a result, the more hydrophobic pore surface in the tethered film gives even greater resistance for the transport of hydrophilic probes. In addition, smaller channels may make the tethering on the inner surface more effective to the solvation environment across the entire pore diameter.

While functionalizing the pore walls with a hydrophobic moiety provides an effective barrier to the transport of the hydrophilic probe, physically loading a hydrophobic IL in the bare silica pores only slightly decreases the permeability through the bare silica films with both pore sizes (silica film without IL versus silica film + IL). In addition, the physically loaded IL does not substantially reduce the resistance to the transport of the hydrophilic redox probe introduced by tethering. Thus, the nature of transport of the hydrophilic probe is different through a confined ionic liquid in a hydrophilic pore (silica film +IL) and a hydrophobic pore (tethered silica film +IL). These results suggest that tailoring pore size and pore surface properties are the key to exploiting the selectivity that is suggested by tremendous barrier properties of IL-functionalized silica to hydrophilic solutes in IL-confined pores.

This barrier properties of IL-functionalized silica pores may be due to a combination of orientation and mobility of ILs in nanoconfinement. In addition to surface hydrophobicity, the covalent tethering of the IL provides directionality and potential orientation to the physically absorbed IL. A previous study shows that [$BMIM^+$] interacts with the negatively charged, hydrophilic silica pore surface [17], thus decreasing the hydrophilicity in the channel and resulting in lower permeability of the hydrophilic probe. Confined IL slightly increases hydrophilic probe permeability through tethered silica film (tethered film without IL versus tethered film with IL). This increase is subtle but might indicate that the physically absorbed [BMIM][PF_6] mitigates the hydrophobic effect from pore surface tethering.

In the case of the hydrophobic redox probe (DBD) permeability through the 2.5 nm channels, physically confinement of the IL doubles the permeability through the silica

film relative to the bare film (silica film + IL versus silica film). The DBD redox probe is estimated to be larger than FDM according to their molecular structures showed in Scheme 5-1. The higher permeability through all treatments of 2.5 nm pore film relative to the 8 nm confined IL suggests that size exclusion does not dominate transport resistance. In the case of 2.5 nm pores, we hypothesize that IL confinement alters the packing of the IL molecules in the pores, providing a structure that enhances the permeability of the DBD species. A pair of neutral IL cation and anion for [BMIM][PF_6] is estimated to have a length of about 0.7 nm from density and assuming cubic packing.[215] With this estimation, the 2.5 nm pore channel can accommodate three pairs of [BMIM][PF_6] ions.[216] Both computational and experimental studies have shown that the molecule packing of IL under this circumstance results in decrease in the mass density, which leads to faster ion or molecule transport in confined IL.[9, 217] In the absence of IL, the increased permeability of DBD species through [TMS-MIM][Cl] tethered 2.5 nm silica films relative to bare silica film can be attributed to the increased surface hydrophobicity with functionalization. When [BMIM][PF_6] is confined in the tethered IL film, the permeability decreases slightly, which is also consistent with previous conclusion that confinement decreases the effect of pore hydrophobicity in tethered films. With the same method of estimation as above, 8 nm channels can accommodate approximately 10 layers of [BMIM][PF_6]. For this reason, the hydrophobic probe permeability is similar regardless of the different treatments of the 8 nm porous thin film.

Transport of the hydrophilic redox probe through nanoconfined IL was demonstrated to be sensitive to surface functionalization and pore size and these variables can be used

to create barrier properties. In contrast, transport of the hydrophobic probe was fairly robust. These differences can be exploited to design of selective separation processes. Understanding of the transport of solutes through confined ionic liquids can guide the design of supported IL membranes in separations and electrochemical devices and the optimization of IL-based heterogenous catalysis.

5.5 Conclusion

Silica nanoporous thin film with orthogonally aligned 2.5-nm-diameter pores was synthesized using CTAB as surfactant. The orthogonal pore orientation is formed by destabilizing the porous structure with 2% TiO_2 impurity in the silica matrix, which allows the micelles to vertically connect with each other when the thin film goes through thermal contraction during calcination. Combining with the silica thin films with 8 nm in pore diameter, size effects on molecule transport properties can be studied.

The EIS study shows that bulk [BMIM][PF_6] did not change the permeability of the hydrophobic probe on a flat surface and it did not significant effect the permeability of the hydrophilic probe, either. Physically absorbed [BMIM][PF_6] in 8 nm silica confinement exhibits similar effects as the addition of unconfined [BMIM][PF_6] to a flat surface: confined [BMIM][PF_6] decreases permeability of hydrophilic redox probes by 35% and almost no effect on hydrophobic group comparing to bare silica films. While these differences are not very pronounced, [BMIM][PF_6] confined in [TMS-MIM][Cl] tethered silica nanoporous thin films has a tremendously decreased permeability of the hydrophilic probe by about 10-fold. This difference is caused by the changing of the pore

surface from a negatively charged bare silica surface to a positively charged hydrophobic tethered surface. When both covalently tethered [TMS-MIM][Cl] and physically absorbed [BMIM][PF_6] are present in the nanopore, the permeabilities of hydrophilic and hydrophobic are similar to the [TMS-MIM][Cl] tethered films in the absence of the IL.

In 2.5 nm pores, similar trend of changing between different film treatments was observed, where the [TMS-MIM][Cl] tethering made the greatest change to permeability of hydrophilic redox probe, but it did not possess as dramatic changes on hydrophobic redox probe permeability. The influence of tethering on hydrophilic redox group is exaggerated with almost 40-fold of increase in permeability because more [TMS-MIM][Cl] is tethered. Interestingly, the hydrophobic redox group permeabilities are enhanced overall by about 25% to 90% in smaller pores, which might because of the combination effects of the smaller film thickness and different IL molecule orientation This is associated with lower [BMIM][PF_6] density due to the different molecular packing within smaller pores. These results suggest that smaller pores give even higher selectivity of hydrophobic probes over hydrophilic probes. These findings suggest that the heterogenous system with [BMIM][PF_6] incorporated in nanoporous silica thin films with and without imidazolium organosilane tethering can be a superior material for design of selective separation, heterogenous catalysis and electrochemical devices.

Chapter 6. Crystallization of Nanopore Confined Imidazolium Ionic Liquids Probed by Temperature-resolved *In Situ* Grazing-incidence Wide Angle X-ray Scattering (GIWAXS)

Yuxin He,[1] Arif M. Khan[1], Joshua Garay[1], Aniruddha Shirodkar[1], Andrew Drake[1], Stephen Goodlett[1], Joseph Strzalka[2], Folami Ladipo[3], Stephen E. Rankin[1]* and Barbara L. Knutson[1]*

[1] University of Kentucky, Department of Chemical and Materials Engineering, 177 F.P. Anderson Tower, Lexington, KY, USA

[2] X-ray Science Division, Argonne National Laboratory, Argonne, Illinois 60439, USA

[3] University of Kentucky, Department of Chemistry, 125 Chemistry/Physics Building, Lexington, KY, USA

6.1 Abstract

The crystallization behavior of 1-butyl-3-methylimidazolium hexafluorophosphate ([BMIM][PF_6]) and 1-butyl-3-methylimidazolium chloride ([BMIM][Cl]) were observed when they were confined in 2.5 nm and 8 nm silica nanoporous thin films and the thin films with 1-(3-trimethoxysilylpropyl)3-methylimidazolium [TMS-MIM]$^+$ group covalently tethered on the pore wall. With the *in situ* grazing-incidence wide angle x-ray scattering (GIWAXS) probing, these confined ionic liquids (ILs) were found to display different crystallization behavior than unconfined ILs with different polymorphs and melting temperatures when heating slowly from as low as -140 °C to room temperature. "Nanodomains" were observed in both ILs at melting state, but they were disturbed by the nanoconfinement. After comparing the melting points of all samples, it is concluded that larger pore size (8 nm) gives more space for the IL to self-organize. Therefore, 8 nm porous thin film with and without tethering gives higher melting points to [BMIM][PF_6] and crystallization was observed only in 8 nm confined [BMIM][Cl]. The IL-like

organosilane [TMS-MIM] tethering also promotes the crystallization of [BMIM][PF_6] and results in higher melting points. The combination effects of a larger pore size and pore surface tethering on [BMIM][PF_6] result in a single stable and symmetric crystal phase that sustained from -140 °C to room temperature. Better understanding of the effects of different nanoconfinement on the crystallization behavior of ILs is important for better designs of drug delivery vehicles, electrochemical devices and supports for catalysis.

6.2 Introduction

Ionic liquids (ILs) are salts with melting points near ambient conditions - usually below 100 °C. They are of interest for a wide range of applications because of their low volatility, good thermal stability, high ion conductivity and versatile properties. ILs are also known as tunable solvents for a variety of inorganic, organic and polymeric materials [1, 2] and as media for catalytic reactions [23, 218]. Although catalysis and separations using bulk ILs are intensively studied and well established [6, 157, 160, 219], many applications benefit from using nanopore-confined ("nanoconfined") ILs, either to reduce cost and quantity of IL required, to prevent contamination of contacting phases with ILs, and to ease separation. A further benefit of nanoconfinement is using interfacial effects to further tune structure, solvation, transport, and catalytic properties.

Supported IL (SIL) catalysts are among the most-studied nanoconfined systems, in which ILs are chemically or physically immobilized in solid porous matrices, such as polymers, silicas, and carbon materials [11, 49, 55, 58, 220]. Studies of successful

hydroformylation, hydrogenation, and other reactions using supported ILs have been reported [160, 221-223]. Confined ionic liquids also play important roles in emerging applications such as electrochemical energy storage[224, 225] and supported IL membranes.[226, 227] Numerous experimental and computational studies show evidence that nanoconfinement of ILs causes significant changes in thermal, electrochemical, and molecular assembly behavior [8-11].

Crystal phase transition behavior is among the properties of ILs that are affected by confinement [8, 170, 228]. Crystallization is an important aspect of IL physical chemistry because as complex, self-assembling fluids, they are prone to exhibit unusual solidification and melting behavior [33, 216, 229]. Moreover, crystallization of ILs directly affects ion conductivity, molecular transport and catalyst effectiveness, which may dictate operating temperatures for SILs [19-22]. Early observations of crystal structures of imidazolium salts, a commonly used family of ILs, revealed polymorphism in the crystal structures of 1-butyl-3-methylimidazolium chloride ([BMIM][Cl]) [229-232]. Subsequently, polymorphs was reported for 1-butyl-3-methylimidazolium hexafluorophosphate ([BMIM][PF_6]) [19, 233]. Because the crystallographic behavior of these two ILs have been investigated in bulk, [BMIM][Cl] and [BMIM][PF_6] will be the two ILs of choice for this study.

Two competing effects are anticipated for nanoconfined ILs. On on hand, classic Gibbs-Thomson theory predicts that conventional molecular liquid experience melting temperature (T_m) depression under confinement, and that the degree of T_m depression is inversely related to pore diameter.[234] This effect has been reported for ILs confined in nanoporous silica "ionogels" prepared by gelation in the presence of the IL.[235] In

small pores (<5 nm), evidence for crystallization has been found to be lost, suggesting that strong interactions with the pore wall may prevent formation of an ordered solid.[235, 236] However, researchers have observed the opposite for ILs confined in other materials. Chen et al. confined [BMIM][PF_6] in carbon nanotubes and obtained a composite with extreme T_m elevation of about 200 °C compared to unconfined [BMIM][PF_6].[8] Another study of the same IL confined in mesoporous silica particles also showed significant T_m elevation after treatment with compressed gas.[237] Within the same nanoporous silica support, T_m elevation or depression has been shown to depend on the type of IL being confined.[238] All of these observations show that nanoconfinement effects on crystallization are complex, and more study is needed of the effects of variables such as pore size and surface chemistry.

Mesoporous silica materials are selected as support matrices in the study because of their tunable porosity and stable chemical and thermal properties [12, 13]. The films are synthesized using a surfactant templated sol-gel method, specifically evaporation-induced self-assembly by dip coating onto silicon wafer substrates.[14, 17, 64] This creates ideal structures for investigating confinement effects by grazing incidence x-ray scattering techniques. Nanoporous thin films with two different pore diameters, 2.5 nm and 8 nm, will be prepared using cetyltrimethylammonium bromide (CTAB)[239] and Pluronic P123 triblock copolymer[240] as structure directing agents, respectively. These supports also provide the opportunity to observe the effects of surface modification with tethered ionic liquid-like functional groups. These grafting groups can be used to stabilize IL in the pores,[241, 242] similar to what have been studied for CO_2/CO separation and catalysis.[55, 58, 59] Romanos and coworkers previously showed evidence that grafted

imidazolium ionic liquid crystallizes in mesoporous silica pores whereas physically entrapped IL does not.[58, 59] This inspired us to further investigate the impacts of tethering on nanoconfined ILs, specifically using the organosilane IL1-(3-trimethoxysilylpropyl)-3-methylimidazolium chloride ([TMS-MIM][Cl]) to graft onto surface silanol groups.

Here, the effects of nanoconfinement in silica and [TMS-MIM][Cl]-modified silica are investigated using *in situ* grazing incidence wide angle x-ray scattering (GIWAXS). When investigating crystallization of imidazolium ILs, it is common to use DSC to determine overall phase transition temperatures and a combination of XRD, Raman or other techniques for structural information.[8, 45, 170, 243, 244] However, the crystallization of imidazolium ILs is complicated due to the large ion sizes, asymmery, and the possibility of multiple carbon chain conformations.[245] Because ILs are complex fluids, cold crystallization and polymorphism are common. Temperatures for the onset of crystallization and transitions between polymorphs have been found to be history dependent, as well as the final solid-to-liquid transition temperature. [BMIM][PF_6] for example, has been reported to display different melting points when prepared and measured under different conditions in previous studies (Table. 1) so our own studies of unconfined ILs were conducted to set a baseline for the current series of experiment. The high intensity synchotron source used here provides the temporal resolution needed to get a comprehensive picture regarding both transition temperatures and crystal structures by temperature-resolved *in situ* GIWAXS . It also helps to distinguish single and co-existing crystal phases as a function of temperature. This study takes advantage of our ability to create silica films with accessible, vertically oriented

mesopore channels of varying size to provide novel insights into how nanoconfinement affects crystallization behavior of [BMIM][Cl] and [BMIM][PF_6] by *in situ* x-ray scattering.

Table 6-1. T_m of [BMIM][PF_6] from previous studies.

Method	Melting Point	Reference
Cooled at > 0.02 K/s below 210 K then slow heating	11 ℃	[246]
Heated from -100 ℃	10 ℃	[247]
Cooled to -150 ℃ at 6 ℃/min then heating at 10 ℃/min	1.9 ℃	[19]
Cooled below -100 ℃ then heating at 10 ℃/min	6.6 ℃	[228]
Heating from -90 ℃ to 40 ℃ at 0.3 ℃/min	11 ℃	[248]
Not specified	4 ℃	[249]
Cooled to -30 ℃ followed by shock-induced crystallization	11 ℃	[233]

6.3 Experimental Methods and Materials

Materials. NoChromix power, titanium (IV) isopropoxide (TIP, ⩾97%), glycerol (89%), 1,6-diisocyanatohexane (98%), tetraethoxysilane (99.9%), Pluronic P123 poly(ethylene oxice)-b-poly(propylene oxide)-b-poly-(ethylene oxide) copolymer (Mn ~ 5800), acetonitrile (anhydrous, 99.8%), toluene (anhydrous, 99.8%), the ionic lqiuid 1-butyl-3-methylimidazolium hexafluorophosphate ([BMIM][PF_6], ⩾98%), and 1-butyl-3-methylimidazolium chloride ([BMIM][Cl], ⩾98%) were obtained from Sigma-Aldrich; concentrated sulfuric acid (98%), 1 N HCl, and acetone (99.5%) from VWR; cetyltrimethylammonium bromide (CTAB, 99.8%) from MP Biomedicals; tetraethyl orthosilicate (TEOS, 99%) from Acros Organics; sugar surfactant n-dodecyl β-D-

maltopyranoside ($C_{12}G_2$, HPLC grade, ⩾99%) from BioVision Inc; and 200 proof ethanol from Decon Laboratories. The substrates used for sample preparation were borosilicate glass slides (VWR) and 600 μm thick silicon (Si) wafers (University Wafer, Inc.). Kapton film (125 μm) was purchased from The McCrone Group, Inc.

Pluronic P123 templated silica film preparation: Silica films with hexagonal close packed pores that are oriented orthogonally to the substrates are prepared by using the sol-gel method of Koganti and Rankin[64]. The silicon (Si) wafers were first cleaned with Nochromix, and then modified with Pluronic surfactant P123 crosslinked using 1,6-diisocyanatohexane (0.696 mM of each reagent in acetone with a drop of glycerol for crosslinking). The Si wafers were then dip coated with silica precursor solution with a final molar ratio of tetraethoxysilane (TEOS): ethanol: DI water: HCl: P123 of 1: 22: 5: 0.0004: 0.01. Finally, the silica films were cured, and the modifying layer and templating surfactant were removed by calcinating at 500 °C for hour hours in air. More details can be found in He et al. [17]

Cetyltrimethylammonium bromide (CTAB) templated silica thin film preparation: CTAB was used as surfactant to synthesize silica thin films with nanochannels perpendicular to the substrate with diameter of about 2.5 nm. Silica thin films with 2% titania were synthesized by mixed templating using CTAB and a sugar-based surfactant ($C_{12}G_2$) which complexes with the Ti-precursor, following a modified procedure of Rahman et al. [141] Initially, 70 mg of $C_{12}G_2$, was dried in a vacuum oven at 50 °C for 24 h and then dissolved in 2.4 mL of dry ethanol. 42 μL of TIP was added to this ethanolic solution (resulting in a Ti:$C_{12}G_2$ molar ratio of = 1:1) and the solution was stirred for 3 h in a sealed vial to allow for the complexation of TIP with the sugar headgroup of $C_{12}G_2$.

To prevent contact with moisture in the air, the procedures above were conducted in a glove bag filled with dry nitrogen. Separately, 1.41 mL of TEOS was added to 0.98 mL ethanol under constant stirring and 0.21 mL of DIUF water and 0.27 mL of 0.1 M HCl was added to this solution. The TEOS mixture was stirred for an hour to allow for the hydrolysis of silica precursor. The TEOS solution was then added dropwise to the TIP:$C_{12}G_2$ mixture with vigorous mixing in a nitrogen glove bag. The mixture was then stirred while an additional 0.12 mL of DIUF water and 1.03 mL of ethanol were added. Finally, 252 mg of CTAB was added to the reaction mixture followed by 3.42 mL ethanol. This solution was stirred for an hour before dip coating onto the glass slides.

Two different substrates were employed for the silica thin films: silicon wafers and glass slides. The silicon wafer was cut into approximately 1cm × 3 cm pieces, which were cleaned with NOCHROMIX® in concentrated sulfric acid solution then rinsed with DIUF water and blow dried. The same cleaning procedures were also applied to the glass sides. The cleaned silicon wafer and glass slides were coated with the titanium-doped silica sol (withdrawal speed 6 cm/min) and then placed into an oven to age at 50 °C for 48 h. Aged films were heated at 120 °C for 6 h and then calcined in air at 500 °C for 1 h with a heating rate of 1 °C/min.

1-(3-trimethoxysilylpropyl)3-methylimidazolium chloride [TMS-MIM][Cl] tethering: The synthesis of [TMS-MIM][Cl] was synthesized by reacting n-methylimidazole with (3-chloropropyl)trimethoxysilane according to the detailed procedures described in **Chapter 5**. For IL tethering, silica films obtained after calcination were submerged in a solution of 0.05 mol/L [TMS-MIM][Cl] in chloroform. This step was carried out in a nitrogen glove bag to prevent [TMS-MIM][Cl] from being hydrolyzed by moisture. The

submerged film was heated at 60 °C for 24 hours under reflux. After that, the silica films were removed from the solution and rinsed thoroughly with ethanol and DI water.

X-ray photoelectron spectroscopy (XPS) depth profile of [TMS-MIM][Cl] tethered silica film: A Kα XPS instrument (Thermo Scientific) was employed to measure compositions of the elements of C, N, Si, and O using ion gun etching with an electron flood gun on for charge compensation. A survey scan was first performed, then Si and O were analyzed with 10 high resolution scans while C and N were analyzed with 15 scans presuming small amounts relative to the other two elements. The Ar^+ ion gun power was set at 500 eV for 12 increments of etching in total between the readings. The etching time was 10 seconds for the first 4 intervals and 200 seconds for the remaining 8 intervals. Avantage software (Thermo Scientific) was used for both data acquisition and analysis. The atomic percentage of the elements were calculated based on the electron density verses binding energy peak areas using Avantage, then it was plotted with respect to the etching time.

[BMIM][Cl] recrystallization and drying: [BMIM][Cl] was purified by recrystallization in a nitrogen purged glove bag to eliminate ambient humidity.[250] About 5 g of [BMIM][Cl] was mixed with a just enough acetonitrile to dissolve the IL after 30 min of stirring. Then about 10 drops of toluene was added to the solution. The final solution was cooled in a freezer at -18 °C overnight. After that, white crystals of [BMIM][Cl] formed. They were washed with cold toluene after filtration. Finally, the crystals were heated at 100 °C in a vacuum oven overnight to eliminate toluene residue and moisture taken up during brief exposure to ambient air. The vacuum was released with high-purity nitrogen gas right before deposition of the IL.

[BMIM][PF_6] drying: Approximately 2 ml of the purchased IL was transferred to a glass vial and vacuum dried at 100 °C overnight to remove residual moisture. Then the vacuum was released with high-purity nitrogen gas and kept at a nitrogen purged environment until deposition.

IL deposition: Both ILs were deposited on five different substrates for comparison: bare flat silicon (Si) wafer (unconfined IL), P123-templated silica films on Si wafers (confined IL), P123-templated silica films tethered with [TMS-MIM][Cl] (Tconfined IL) and CTAB-templated silica films with and without the same tethering on glass slides. For unconfined ILs, an 8 mm diameter and 0.5 mm depth silicone isolator (Grace Bio-Labs) was placed on a Si wafer and 50 µL of IL was placed in the isolator to form a "pool" of IL. For confined ILs, a small drop of each IL was placed on the silica films, then covered by a piece of 125 µm thick Kapton film. The Kapton film was gently scraped with a ruler wrapped by a Kimwipe® to spread and squeeze out excess IL from the edge of the Kapton film. This was to minimize the IL sitting between the Kapton film and silica film. Since [BMIM][Cl] is moisture sensitive, this step was carried out in a nitrogen bag. [BMIM][PF_6] is not as hygroscopic as [BMIM][Cl], so it was quickly deposited under ambient air.

In situ GIWAXS measurement with varying temperature: GIWAXS measurements were taken using Beamline 8-ID-E at the Advanced Photon Source at Argonne National Laboratory. The synchrotron X-ray wavelength was 0.114 nm with beam size of 800 µm × 4 µm. The *in situ* cold crystallization was carried out in a vacuumed chamber with pressure of 0.01 torr and the temperature was controlled using a Linkam HFSX350 stage (Linkam Scientific). The samples went through two cooling cycles and one heating cycle

between temperatures of 25 °C to -140 °C (-120 °C for unconfined [BMIM][PF_6] and -130 °C for confined [BMIM][PF_6]) and 25 °C with temperature ramp of 10 °C/min and remained for 10 minutes at the end of each cycle. After the second cooling cycle, the samples were slowly heated at 0.3 °C/min for GIWAXS measurements. Two seconds of beam exposures were used for measurements about every five minutes.

Sample temperature vs. Linkam HFSX350 stage temperature: The temperature on the surface of the silica films deposited on both Si wafers and glass slides were measured as the "real" sample temperature with an external resistance temperature detector (RTD Pt-111, Lake Shore Cryotronics) and compared to the temperature read from the Linkam stage. This sample temperature on a Si wafer was measured with the RTD epoxied to the top surface of a mesoporous silica film while lowering the temperature of the Linkam stage from room temperature to -150 °C at 10 °C/min, then raising it to 280 °C at 10 °C/min. The temperature curves with time does not show significant differences over the temperature range of -140 °C to 200 °C (Fig. S1). For silica films deposited on glass slides, the temperature was lowered from room temperature to -140 °C, maintained for 10 minutes then raised back to room temperature at a same ramp rate as above. The lowest sample surface temperature only went down to about -105 °C when the Linkam temperature reading was -140 °C and there was about a three-minute temperature response delay below -65 °C when cooling but a much smaller offset during heating at 10 °C/min (Fig. S2). The temperature ramp rate during GIWAXS measurement is much lower (0.3 °C/min heating compared to 10 °C/min), so it is reasonable to also assume the Linkam stage temperature reading is true to the sample surface temperature when it was above -105 °C and that -105 °C represents the minimum known temperature even though

the Linkam stage reached lower temperatures for glass slides. A caveat regarding this comparison is that thermal contraction may have affected the measurement. During the measurement, the RTD sensor on the sample surface slightly lifted the glass slide, causing loss of contact of the glass slide with the Linkam temperature stage. Thus, the lowest temperature of -105 °C is the worst-case scenario and is used to represent a conservative upper bound on the range of temperatures investigated for glass substrates.

Crystallography analysis: the 2D GIWAXS pattern was integrated radially and reduced to intensity with respect to scattering vector q ($Å^{-1}$) using MATBLAB based software, GIXSGUI [108]. Q in reciprocal space was then converted to 2θ (°) with the wavelength of 1.54 Å (Cu Kα as x-ray source) for easier comparison with literature. A background spectrum of the Kapton film was subtracted from the confined and Tconfined samples. The crystal structures of the samples were determined using TOPAS software (Bruker) by fitting lattice parameters starting from IL crystal structures of Dibrov et al. [233] for [BMIM][PF_6] (COD# 2014366) and Holbrey et al. [230] for [BMIM][Cl] (COD# 7103776). Atom occupancy and coordinates as well as temperature factors were fixed during Pearson VII peak shape function fitting.

6.4 Results and Discussion

The mesopore structures of the two types of silica films (with 2.5 nm and 8 nm pores) were verified by grazing-incidence small angle scattering (GISAXS) to be vertically oriented hexagonal close packed nanopore channels. The orthogonal pore orientation in P123-templated films was achieved by confining the silica film between two surfaces

modified with crosslinked P123, giving a film about 180 nm thick after curing and calcination.[14, 17, 64] The vertically aligned channels in CTAB-templated films were obtained by doping the silica matrix with 2 wt% titania to soften the matrix and allow merging of pores in the vertical direction due to thermal contraction of the films during calcination according to the observations in **Chapter 3**. These films were 90 nm thick as determined by profilometry that was discussed in **Chapter 3**. To examine the accessibility of the pore pathway and confirm successful [TMS-MIM][Cl] tethering in the pores of the films, Tconfined films were analyzed by XPS depth profiling. The composition profiles of films with both 2.5 nm and 8 nm pores are presented in the Supplementary Material (Table S1 and Table S2) as a function of cumulative ion etching time. Because the length of the etching steps varied, the absolute depth is not known, but it is clear from the atomic percentages of C and N that a uniform layer of [TMS-MIM][Cl] was tethered onto the pore wall throughout the entire thickness of both types of silica films. A constant composition of both C and N is found from the top surface until the point that the silicon signal dominates (when the Si substrate is reached).

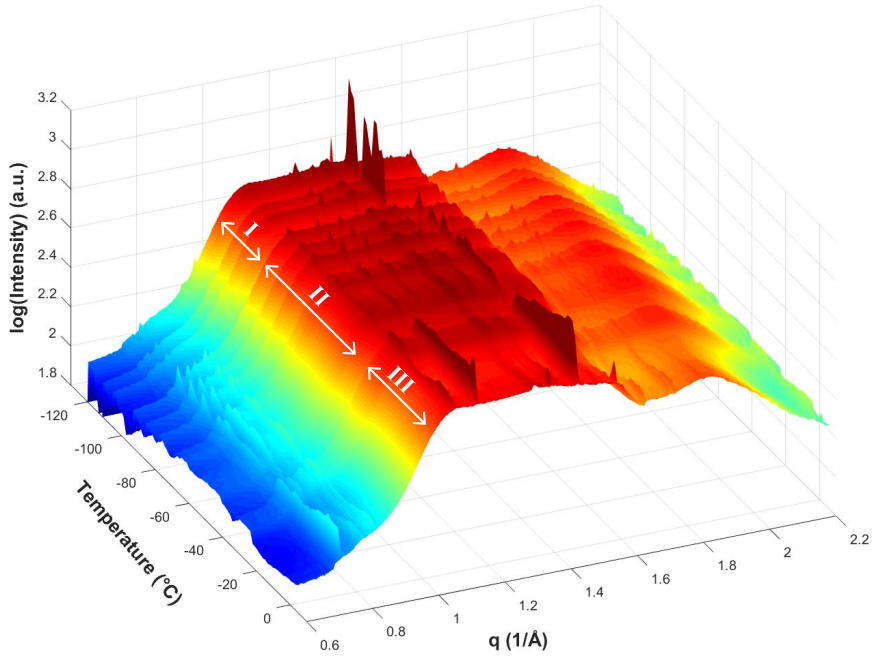

Figure 6-1. 3D plot of integrated GIWAXS data as a function of temperature prior to background subtraction for [BMIM][PF_6] confined in 8 nm nanopores.

Having established that the films have the expected vertical nanopore structure, we now discuss the results of temperature-resolved GIWAXS for confined and unconfined ILs. Representative 2D GIWAXS patterns and their analysis are presented in the Supplementary Materials but only integrated 1D patterns are shown in the main text. Figure 6-1 shows an example of the full series of 1D GIWAXS patterns for confined [BMIM][PF_6] from *in situ* measurement during the slow heating from -130 °C. The ridges in the direction of increasing temperature are caused by sample alignment issues, which are resolved by background subtraction. Three regions of sharp peaks from crystalline ionic liquid can be identified, labeled as I, II and III corresponding to three polymorphs of confined [BMIM][PF_6] (discussed further below). Background subtraction was performed for data presentation and analysis from this point forward to eliminate the

interference from the Kapton film and reflection from the substrate. A sample GIWAXS background is presented in the Supplementary Materials (Fig. D3).

Before diving into more complicated confined systems, GIWAXS of bulk [BMIM][PF_6] supported only by a bare Si wafer is discussed. This unconfined [BMIM][PF_6] did not crystallize during cooling down to -120 °C, but crystallization began when the temperature was raised to -106 °C (Fig. 6-2). This cold crystallization behavior has been noted previously in DSC studies of [BMIM][PF_6],[19, 251] and the lack of a crystal pattern at -107.5 C in Fig. 6-2 is representative of this behavior. However, before crystallization is observed, the GIWAXS pattern shows indications of short range local structure, or "nanodomains", with small d-spacings (Fig. 6-3a & 6-3c). The pair of reflections corresponding to the nanodomains are low in intenstiy, most likely because of their small size and concentration. These nanodomains are also present in the liquid state; above the melting temperature, the same short-range nanodomains were observed as in supercooled [BMIM][PF_6] and maintainted at the end of measurement at 25 °C (Fig. 6-3b, 6-3d). This agrees with numerous molecular dynamic simulation studies showing heterogeneous ordered domains in ILs [245, 252, 253], as well as XRD results of Triolo et al. for other 1-alkyl-3-methyl-imidazolium-based salts [254]. However, these GIWAXS results are the first experimental evidence of nanodomains in amorphous [BMIM][PF_6] to the best of our knowledge.

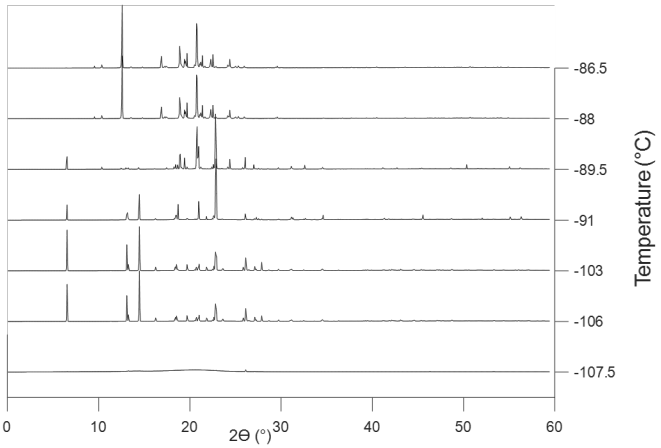

Figure 6-2. Crystal phase transition of unconfined [BMIM][PF_6] from the amorphous subcooled state to phase I at -106 °C then transformation to phase II starting at -91 °C. The GIWAXS pattern at 25 °C is subtracted as background.

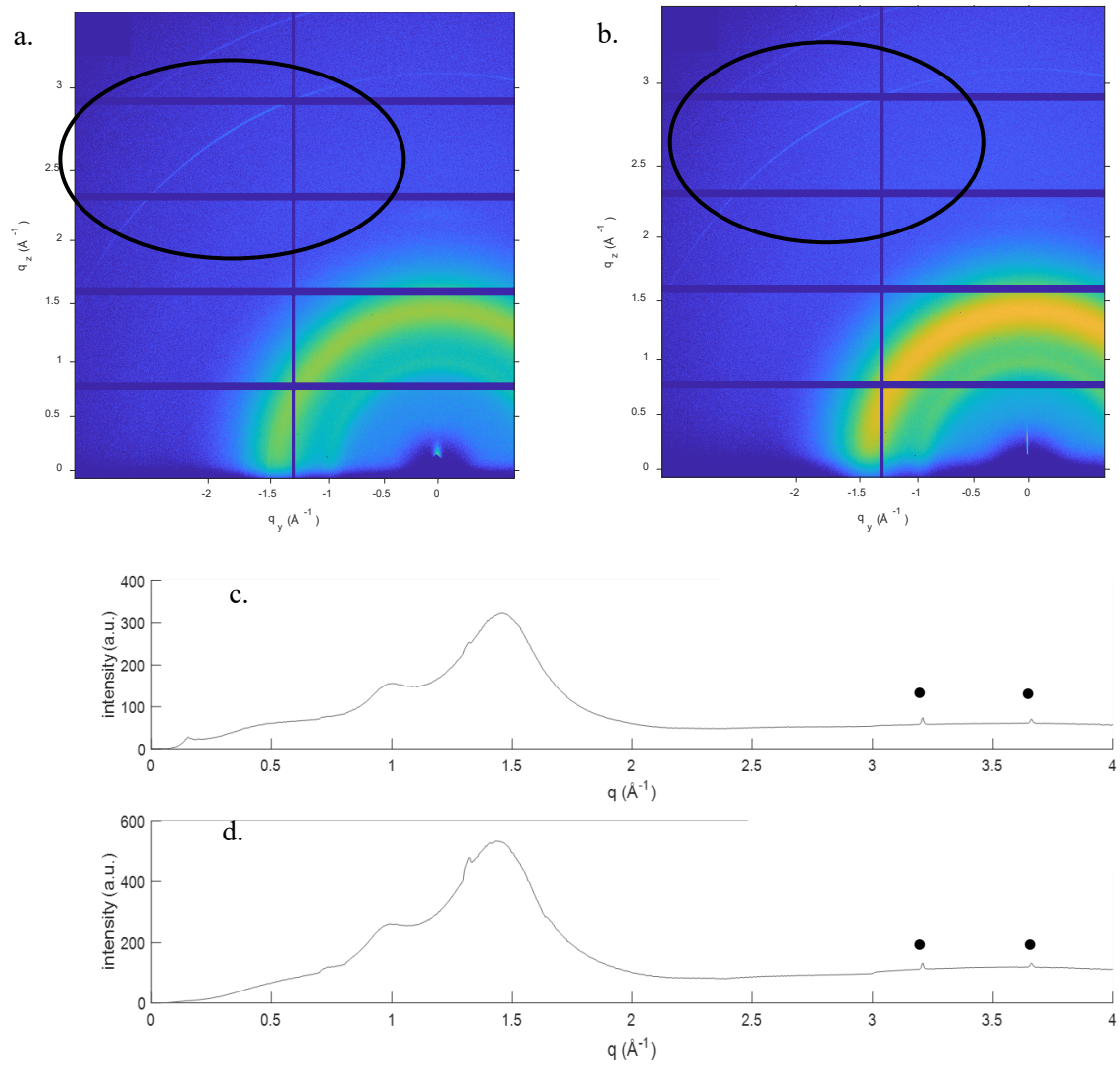

Figure 6-3. GIWAXS pattern of unconfined [BMIM][PF_6] at -115 °C (2D: a.; 1D: c.) and 25 °C (2D: b.; 1D: d.)) indicating the existence of nanodomains (marked with filled circles) before and after forming solid crystal phases.

Unconfined [BMIM][PF_6] is found to form two stable polymorphs and the phase transition temperature between the two is at -91 °C (Fig. 6-2). The second polymorph has a similar diffraction pattern to that reported by Triolo [246] and Choudhury [19] at around -90 °C, but with minor differences in unit cell parameters. The melting points is -11 °C, which is lower than reported values ranging from 1.9 °C to 11 °C (Table. 1) with 11 °C being the most observed melting temperature with different measurement

conditions.[19, 228, 233, 247, 251] Different thermal histories (including heating and cooling rates) can result in observation of different polymorphs and phase transition temperatures, which is common among studies of ILs [246, 251] For example, Triolo et al. observed two polymorphs noted as cry.I and cry.II. Cry.I occurred when [BMIM][PF_6] was kept at -13 °C for a few hours and after quenching then heating cry.I to -27 °C, it transformed to cry.II. However, this behavior changed with a different heating procedure. Cry.II appeared first at -53 °C when heating from -113 °C and transformed to cry.I when the heating continued to -21 °C.[246] The current study was not designed to produce [BMIM][PF_6] single crystals, so the small crystallite size can contribute to melting point depression according to the Gibbs-Thompson effect (discussed below).[234, 255] For example, the crystallite size of [BMIM][PF_6] was calculated to be only 5.3 nm at -88 ˚C using the Scherrer equation.[116] Another common cause for melting point depression is the presence of impurities. In the cases of ILs, water is usually the most common and inevitable impurity. According to Huddleston et al., T_m was found to be 4 ℃ and 10 ℃ for [BMIM][PF_6] containing 11700 ppm and 590 ppm of water,[247] indicating that a trace of water in [BMIM][PF_6] are probably not responsible for reducing the melting temperature by more than 20 ℃. Because [BMIM][PF_6] is not highly hygroscopic and was vacuum dried at elevated temperature prior to analysis, it can be concluded that this melting temperature depression was not caused by water impurity.

In confined systems, a sandwiched sample geometry was used for GIWAXS measurements consisting of the Si substrate, silica nanoporous thin film loaded with IL, and high x-ray transmittance Kapton film covering the sample. Therefore, it was necessary to ensure that patterns were obtained from the silica nanoporous thin film layer.

To do so, a GIWAXS pattern of a confined sample without IL crystallinity was taken and the low q value region was expanded. The beam stop is prominent in the resulting image, but the pattern is consistent with the perpendicular HCP structure from the nanoporous silica thin film that was observed by GISAXS (Fig. D4 shows this for a 2.5 nm, CTAB-templated film). Since we are able to see the pattern from the ordered silica support at low angles, the current setup is confirmed to give GIWAXS signal from confined IL in the silica nanoporous film layer. For the films with 8 nm pores, the GIWAXS signal from the nanoporous film was too close to the beamstop to be observed. The x-ray penetration depth of the tethered film was estimated to be about 10.9 nm based on the incidence angle of 0.16 ° and the atomic percentages from XPS depth profile of the films (Table. D1)[105, 256].

With the confirmation that the x-ray scattering is probing the structure of the nanoporous layer, we begin to address the effects of confinement of [BMIM][PF_6] in bare silica supports with 2.5 nm and 8 nm pores. Confined [BMIM][PF_6] in both types of films exhibits three polymorphs in the temperature range measured that all have different peak positions and relative intensities compared to the unconfined IL (Fig. 6-4 and Fig. 6-5). As anticipated, [BMIM][PF_6] displays very complicated crystalization behavior and it changes with pore size. In 2.5 nm pores, the IL crystallizes by the start of the heating ramp into polymorph I, and undergoes a transition to polymorph II at -88 °C, close to the transition temperature of the unconfined system. However, in the 2.5 nm pores, [BMIM][PF_6] melts at -20 °C, which is 9 °C lower than the unconfined IL. This T_m depression is described by the Gibbs-Thomson equation for confined molecular liquids (eq. 2).

$$\Delta T_m = \frac{k_{GT}}{r} \quad (2)$$

where ΔT_m is the melting temperature depression ($T_{bulk} - T_{confined}$) and r is the pore radius.[234] k_{GT} is a constant depending on liquid properties, pore geometry and pore wall wetting, and is usually greater than 0. The second type of silica film templated with P123 has the same type of pore geometry and pore chemistry, so it should have the same wetting characteristics with [BMIM][PF_6], as discussed in **Chapter 5**. Eq. 2 can then be used to predict that T_m of [BMIM][PF_6] confined in 8 nm pore is expected to be higher than when confined in 2.5 nm pores but still lower than unconfined [BMIM][PF_6].

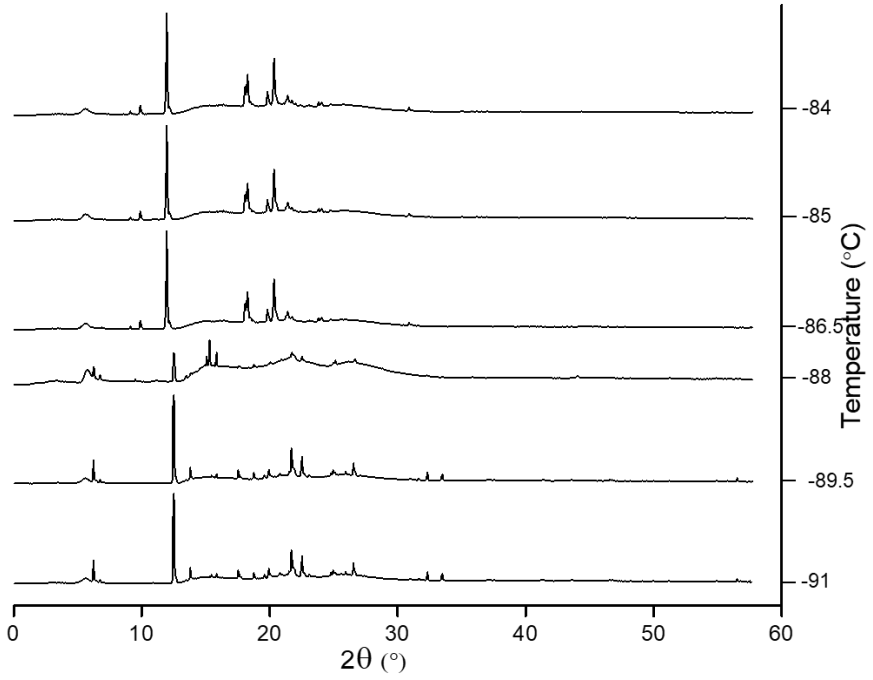

Figure 6-4. Representative GIWAXS patterns showing the primary crystal phase transition of confined [BMIM][PF_6] in 2.5 nm pores from crystal phase I to phase II starting from -88 °C. Below this temperature, phase I is observed, and phase II is observed above -84 °C until T_m is reached at -20 °C.

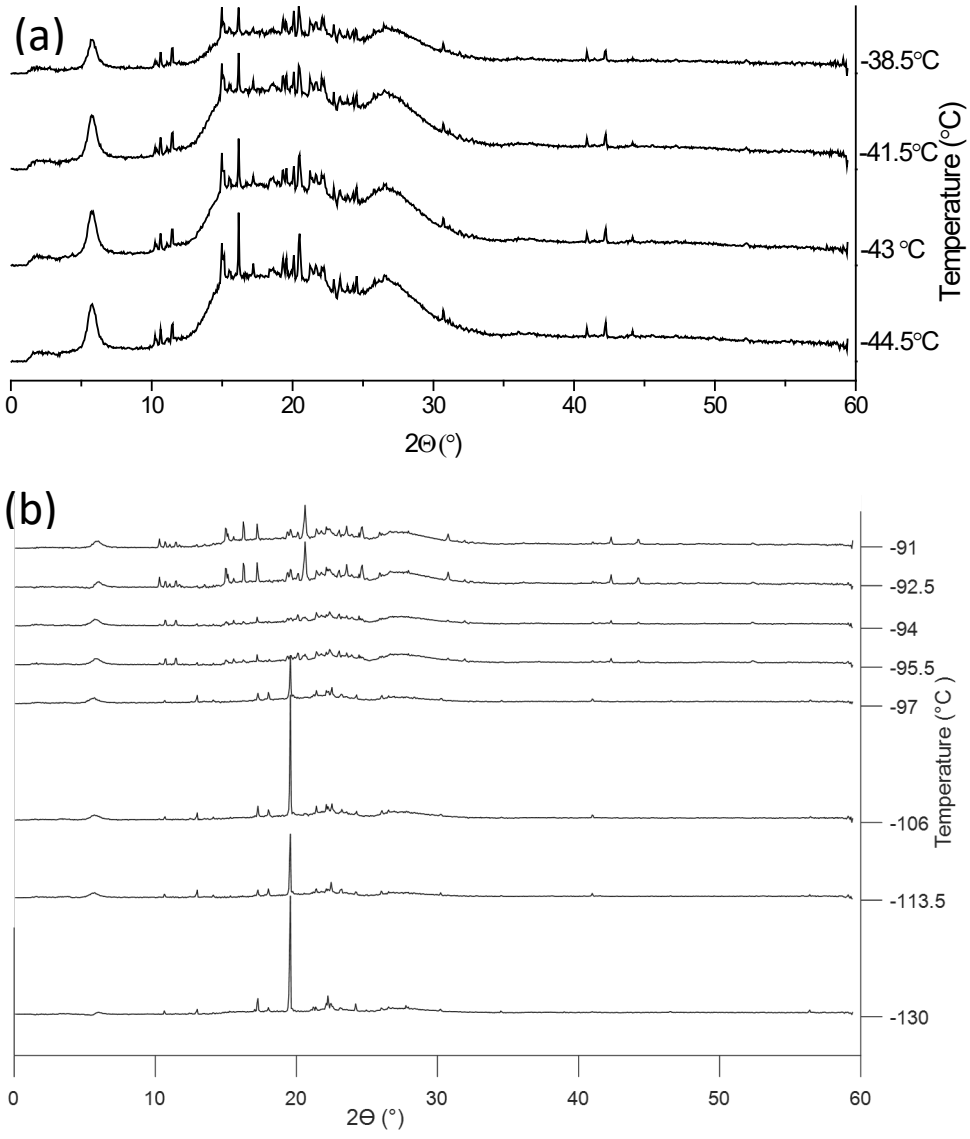

Figure 6-5. GIWAXS patterns showing the crystal phase transition of confined [BMIM][PF_6] in 8 nm pore (a) from crystal phase II to phase III with disappearing of the peak around 17° starting from -41.5 °C; and (b) from crystal phase I to phase II starting from -97 °C.

When confined in 8 nm silica pores, [BMIM][PF_6] also crystallizes by the start of the heating ramp into a first polymorph. Fig. 6-5 shows that the first phase transition to the second polymorph happened at -97 °C, a lower temperature than in 2.5 nm pores. This second polymorph then transformed to a third crystal phase at around -40 °C (Fig. 6-1).

While having a lower first cystsal phase transition temperature, the last polymorph of [BMIM][PF_6] confined in 8 nm pores melts at 6.5 °C, experiencing a T_m elevation by 17.5 °C compared to unconfined [BMIM][PF_6]. The Gibbs-Thomson equation apparently does not apply to this observation, which calls for an alternative explanation for this behavior. Previously, T_m elevations were observed when [BMIM][PF_6] was confined in carbon nanotubes and 2D nano graphene sheets [8, 257]. The confined [BMIM][PF_6] went through enormous T_m elevation in both cases, which was attributed to promotion of molecular order by nanoconfinement. The Gibbs-Thomson model assumes that the molecular structure of the solid and liquid phases are unaffected by confinement, so it does not capture the possibility that confinement induces greater ordering in the liquid phase, and therefore stabilizes the solid against melting. In the case of SiO_2 nanopores, the simulation study of Sha et al. suggests that 4 layers of [BMIM][PF_6] liquid can fit a 2.5 nm channel, and 10 to 12 layers in 8 nm channels.[216] As a result, the 8 nm pores give more space for [BMIM][PF_6] to reorient themselves, thus showing a stronger nanoconfinement-induced ordering effect (leading to T_m elevation).

As noted above, unlike unconfined [BMIM][PF_6], nanoconfined [BMIM][PF_6] in both 2.5 nm and 8 nm pores already crystallizes by the time the system reaches the minimum temperature (-140 °C or ≤-105 °C). This may be because the nanodomains found in bulk [BMIM][PF_6] are disrupted by silica nanoconfinement since no GISAXS features indicating ordered domains are observed in confined [BMIM][PF_6] after melting. This leaves molten [BMIM][PF_6] with disordered molecule distances and orientations, which is at a higher free energy state than [BMIM][PF_6] with ordered nanodomains as shown in the schematic in Fig. 6-6. Therefore, the free energy barrier to crystallization is

smaller for confined [BMIM][PF_6]. This explains the absence of a supercooled liquid state for confined [BMIM][PF_6]. It also is possible that one or more layers of ions near the pore wall promote heterogeneous nucleation of crystallites and contribute to the depletion of nanodomains from the rest of the fluid.

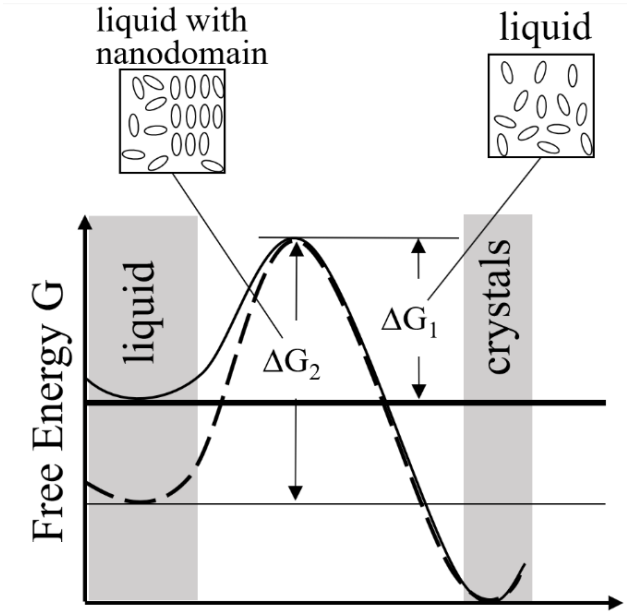

Figure 6-6. Schematic of crystallization of regular liquid with random molecule position and orientation with free energy barrier of ΔG_1 (solid curve), and liquid with short range nanodomain such as [BMIM][PF_6] with relatively higher free energy barrier of ΔG_2 (dash curve). Inspired by [258, 259]

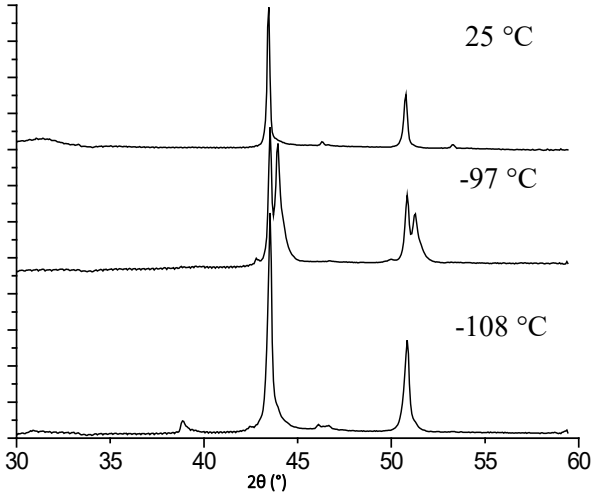

Figure 6-7. Three representative spectra of Tconfined [BMIM][PF_6] in the mesoporous silica film with 8 nm channels throughout the temperature range showing one metastable crystal phase.

In addition to investigating pore size effects on IL crystallization, the effects of functionalizing the surface with IL-like groups were studied. IL grafting has been used for the purpose of preventing IL leaching, and we have observed that attachment of [TMS-MIM][Cl] to the silica pore surface dramatically changed the permeability of redox probes through nanoporous silica films according to **Chapter 5**. By changing the interactions of the free IL with the surface, tethering is also expected to have significant impacts on the crystallization behavior of ILs because they are in contact with imidazolium groups rather than surface silanol groups.[55] When [BMIM][PF_6] was confined in a [TMS-MIM][Cl] tethered silica film with 2.5 pores, it went through similar "cold crystallization" as for unconfined [BMIM][PF_6], where it did not show crystallinity until heated slowly to -99 °C. This did not happen to the IL confined in bare silica films of either pore size, indicating that the tethering with imidazolium groups provides a more

bulk-IL-like environment to the confined [BMIM][PF_6]. As the temperature kept increasing, a second polymorph appeared at -57 °C and coexisted with the first one until there was only the second polymorph remaining at -43.5 °C (Fig. D5 and D6). It completely melted at 1 °C (Fig. D7), which is a 12 °C increase compared to the T_m of unconfined [BMIM][PF_6] and a 21 °C increase compared to the T_m of [BMIM][PF_6] confined in the same type of film but without tethering. This suggests that the [TMS-MIM][Cl] tethering promotes the ordering of [BMIM][PF_6] in the 2.5 nm pores.

The promotion of ordering was observed to be extraordinarily amplified in the tethered 8 nm pores. When [BMIM][PF_6] was confined in the 8 nm nanoporous silica film with tethering, it did not show much crystallization after two cycles of cooling at 10 ℃/min followed by a slow heating at 0.3 ℃/min, but exhibited a stable crystal phase after aging for 4 days under nitrogen at room temperature. The crystal phase experienced some d-spacing change during the heating process but showed a single stable crystal phase (Fig. 6-7). The crystal phase did not melt or show indication of reduced diffraction intensity at room temperature and the crystal structure is very symmetric. It is not uncommon that it takes a few hours to a few days to obtain stable crystal phases in the case of ILs [229, 232, 254, 258]. From the crystal phases presented so far, it is clear that [BMIM][PF_6] demonstrates very complicated crystallization behavior due to cold crystallization, nanosize effects, and confinement-induced ordering. However, 8 nm nanopores tethered with [TMS-MIM][Cl] stabilize the confined [BMIM][PF_6] to only one crystal phase due to the combined molecule ordering promotion effects of both nanoconfinement and surface modification. This can be extremely beneficial for the design of stable supported ionic salt systems such as electrochemical devices, but should

be viewed as a warning for systems requiring liquid phase behavior such as catalysis and drug delivery systems – a nominal ionic liquid may in fact become a crystalline solid due to nanopore confinement.

When considering nanoconfinement effects, it is important to recognize that IL properties can be largely influenced by the type of counterion employed.[22, 38, 180, 247, 260] Thus, a hygroscopic IL with the same cation but an anion smaller in size, [BMIM][Cl], was also investigated to expand our understanding of nanoconfinement effects. It is believed that the interaction between cation and anion in [BMIM][Cl] is stronger than [BMIM][PF_6] and this results in [BMIM][Cl] being in solid form at room temperature.[38, 229] This can make [BMIM][Cl] less attractive since it needs to be melted before being utilized as an ionic "liquid". GIWAXS of unconfined [BMIM][Cl] (Fig. 6-8) give T_m close to reported values at around 70 °C [232, 233, 261, 262]. In Hayashi et al.'s study, two polymorphs of [BMIM][Cl] were observed with XRD.[232] It was found that one of the polymorphs is a metastable form that was more frequently obtained when cooling [BMIM][Cl] at -18 °C for two days and the other is stable at dry-ice temperature. The unconfined [BMIM][Cl] in this study also exhibits two polymorphs. The first one appeared when the measurement started at -120 °C without having to go through a cold crystallization step, and melted at around -84 °C (Fig. 6-8). The second polymorph emerged at -48 °C and completely melted at around 70 °C (Fig. 6-8). Short range nanodomains are also observed in molten [BMIM][Cl] and during the tempearature gap between the two polymorphs. The high-angle reflections associated with the nanodomains were sustained until the end of measurement at 165 °C (Fig. 6-9). These

two polymorphs act similarly as what was observed by Hayashi et al.[232], where the two appears in different temprature ranges and do not have overlapping peaks.

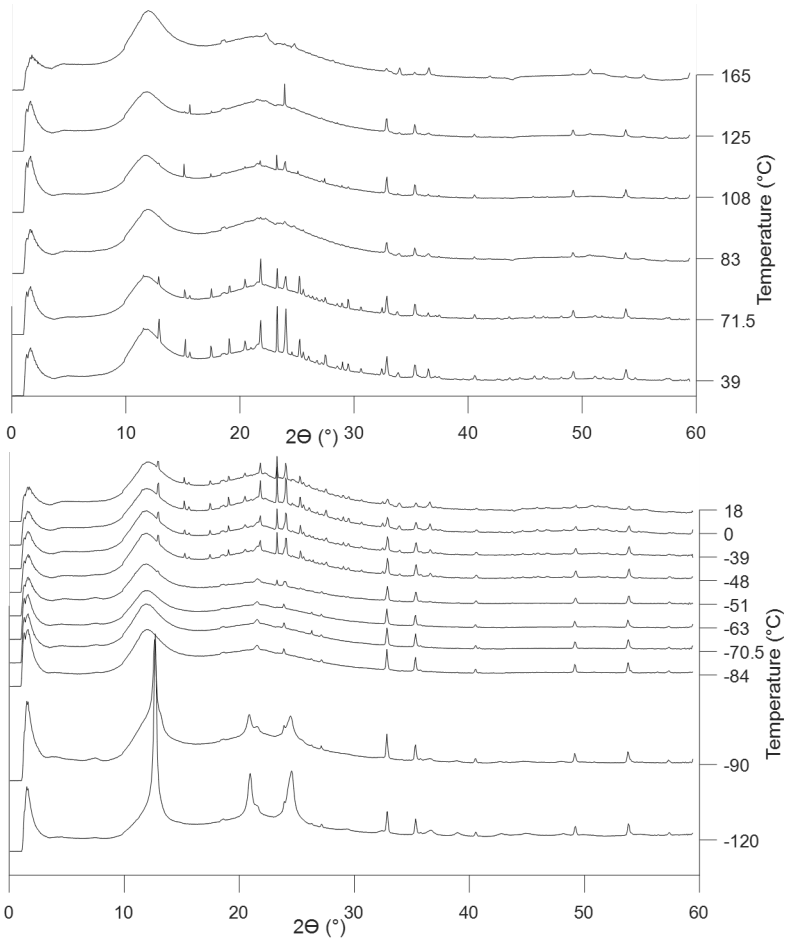

Figure 6-8. Crystal phase transition of unconfined [BMIM][Cl] from phase I to amorphous state at around -90 °C, then from amorphous state to phase II at around -51 °C (bottom); crystal phase transition of unconfined [BMIM][Cl] from phase II to amorphous state at around 71.5 °C (top). The pattern almost remains the same between -48 °C and 71.5 °C.

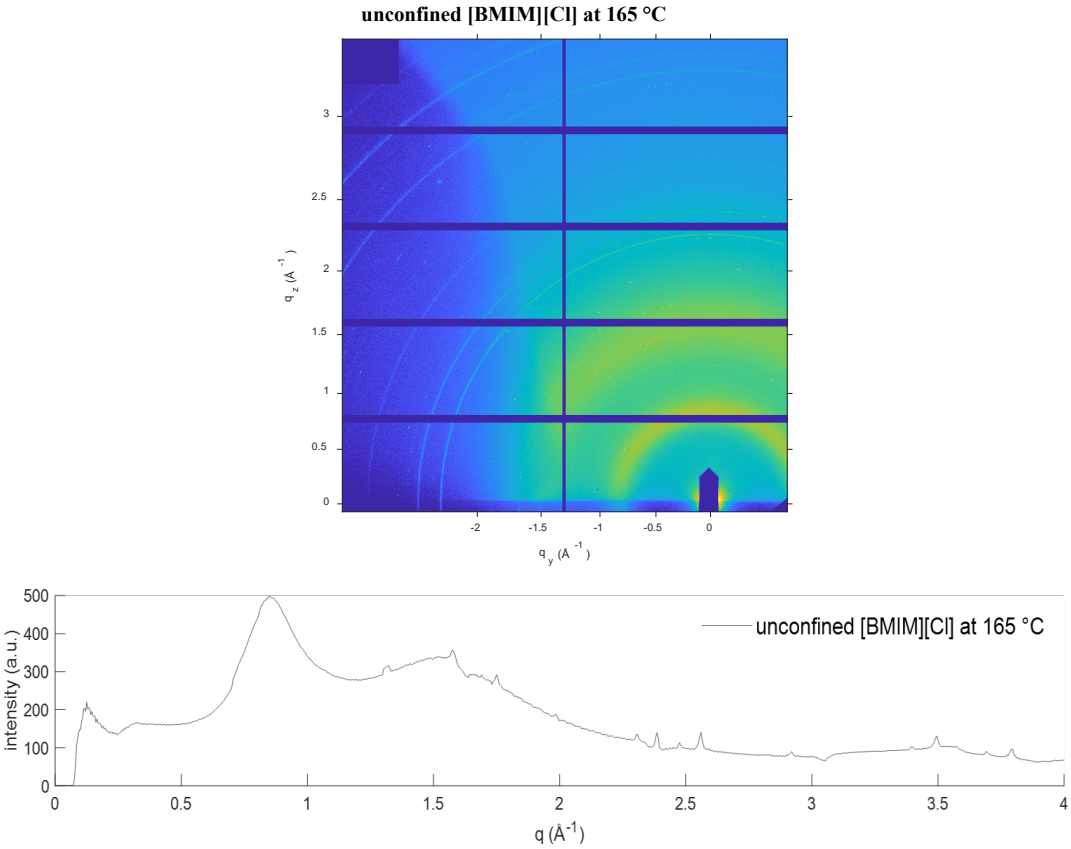

Figure 6-9. 2D and 1D GIWAXS patterns of unconfined [BMIM][Cl] at 165 °C indicating existence of nanodomains after the crystal phase melts.

After characterizing the crystallization behavior of unconfined [BMIM][Cl], phase behavior was examined for [BMIM][Cl] confined in silica nanoporous films with both 2.5 and 8 nm diameter pores, with and without pore surface tethering. Surprisingly, for [BMIM][Cl], crystallization was only observed when confined in bare (non-tethered) 8 nm silica channels. For 2.5 nm bare pores and either pore size with IL tethering, no crystallization was observed during cooling or heating, or upon aging at room temperature, suggesting that the crystalline phases of [BMIM][Cl] were destabilized by the presence of pores, even if layering of ionc near the pore surface is expected due to nanoconfinement. The GIWAXS results for 8 nm silica pores (Fig. 6-10) show a mixture

of two crystal phases at the lowest temperature, -140 °C. Upon heating, one of the crystal phases melted around -128 °C. The remaining polymorph, crystal II, melted completely at -119 °C, which is much lower than for unconfined [BMIM][Cl]. The quantitative analysis combined with crystal structure fitting with the literature[230] from TOPAS software gives a composition of about 68.6% of crystal I and 34.4% of crystal II at -140 °C. The descending fraction of crystal I is apparent in Fig. 6-10 and the structure is determined to be monoclinic like crystal II. This is a perfect example of identifying coexisting crystal phase with *in situ* temperature-resolving GIWAXS using synchrotron X-rays. No nanodomains were observed in molten confined [BMIM][Cl] in any of the four cases, showing the same response as the nanodomain in [BMIM][PF_6].

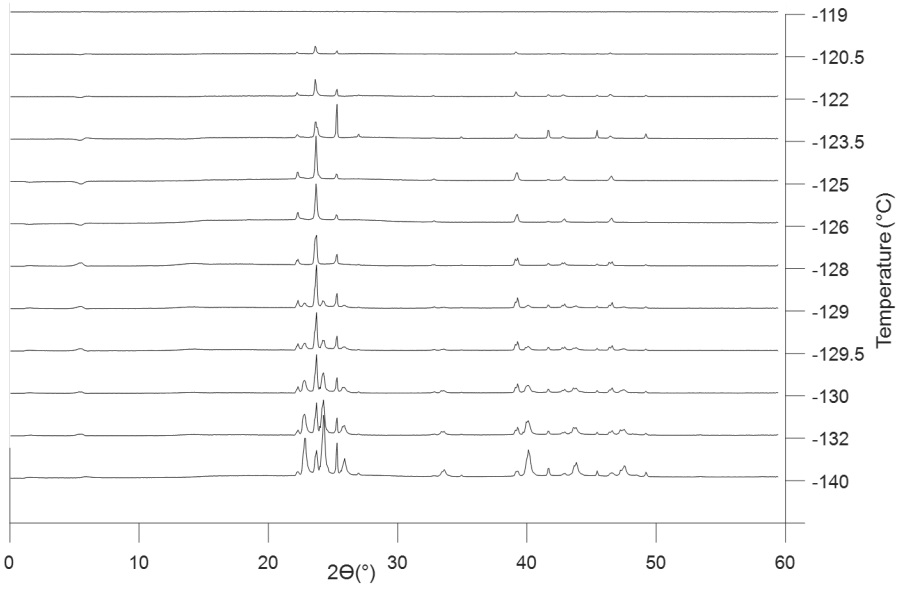

Figure 6-10. Crystal phase transition of confined [BMIM][Cl] and completely molten at -119 °C. Spectrum of confined [BMIM][Cl] at 25 ℃ is subtracted as background.

The different crystal phases observed in this study are most likely attributed to the different conformations of the butyl chain under different environments and

temperatures, which is a popular explanation that is supported by numerous studies about both [BMIM][PF_6] and [BMIM][Cl].[230, 243, 248, 263] The crystal phase transition temperatures of all samples showing crystallization are summarized and compared in Figure 6-11. The corresponding unit cell parameters from TOPAS fitting are tabulated in Table 6-2. Details of the fitting are provided in the Supplementary Material. All of the patterns were fitted well using crystal structures with refined unit cell parameters and space groups for bulk [BMIM][PF_6] and [BMIM][Cl] from literature [19]. The crystal densities are in general smaller for the crystal phases at a higher temperature in the same sample. This is most likely due to thermal expansion.

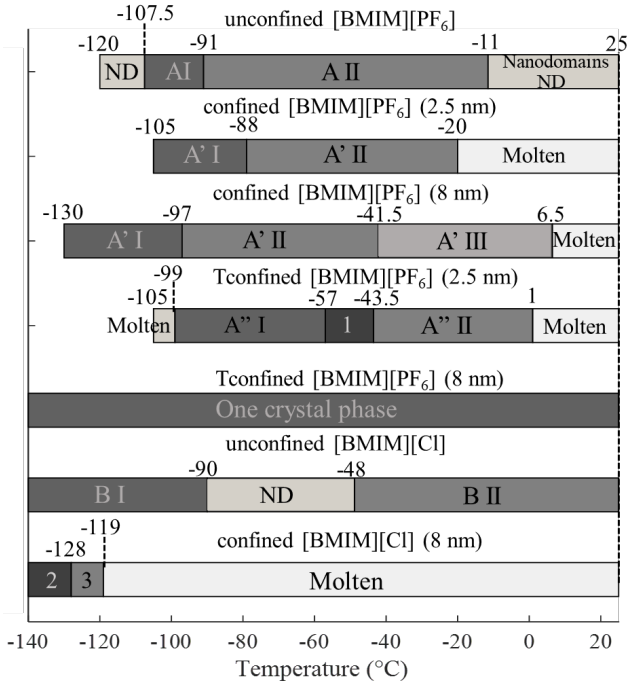

Figure 6-11. Crystal phase transition temperatures of A: unconfined [BMIM][PF_6], B: unconfined [BMIM][Cl], A': confined [BMIM][PF_6], B': confined [BMIM][Cl], A": confined [BMIM][PF_6] in [TMS-MIM][Cl] tethered pores. I and II represent the first and second crystal phase appeared in corresponding samples. The notations 1 = A''I + A''II; 2 = B'I+B'II; 3 = B'II'

The first general trend found in Fig. 6-11 is, that GIWAXS indicates that nanodomains found in the molten state for both [BMIM][PF_6] and [BMIM][Cl] are eliminated by nanoconfinement. These nanodomains represent ordered small clusters of IL at equilibrium with disordered liquid, so it is likely that liquid layering at the pore surface lowers the driving force for formation of separate nanodomains in the fluid inside the pore. The nanodomains are associated with cold crystallization – that is, crystallization during heating under severe subcooling. Since the nanodomains are not present to stabilize the liquid phase, cold crystallization is not found in fluids confined in bare silica pores. Also, the observation of melting point elevation in some cases for [BMIM][PF_6] suggests that nanoconfinement-induced layering plays an important role for ILs, and either contributes to or completely opposes the melting point depression usually expected according to the Gibbs-Thomson effect. This is most exaggerated for [BMIM][PF_6] in 8 nm IL-tethered pores, where nucleation is slow but a single crystalline phase forms that is stable all the way to room temperature. In contrast to these effects, strong and specific interactions between $BMIM^+$ and Cl^-, which are responsible for the high melting temperature of pure [BMIM][Cl], are disrupted by layering in the liquid state. This leads to severe melting point depression (observed only in 8 nm bare silica pores) or suppression (observed in smaller silica pores and with IL tethering).

Table 6-2. Unit cell parameters refinement results of crystal phases identified in Fig. 6-11

	space group	a (Å)	b (Å)	c (Å)	α (°)	β (°)	γ (°)	Density (g/cm^3)
[BMIM][PF_6]								
unconfined								
A I -103 °C	P-1	9.08	7.67	5.90	102.51	115.23	109.23	2.96
A II -88 °C	P-1	8.21	8.96	8.89	95.76	118.51	103.24	1.74
bare 2.5 nm silica confinement								
A'I -91 °C	P-1	8.00	11.81	8.89	86.48	94.67	92.55	1.13
A'II -84 °C	P-1	7.11	8.85	13.37	91.67	114.80	106.15	1.31
bare 8 nm silica confinement								
A' I -130 °C	P-1	7.77	8.89	8.49	96.84	114.38	102.27	1.86
A' II -61 °C	P-1	7.56	9.22	9.00	97.12	114.85	102.61	1.75
A' III 0.5 °C	P-1	8.63	8.79	9.03	95.67	114.38	103.24	1.59
Tethered 2.5 nm silica confinement								
A"I -49.5 °C	P-1	9.02	9.48	9.05	94.64	113.68	101.83	1.38
A"II -9.5 °C	P-1	8.73	8.97	8.94	95.77	115.30	102.95	1.57
Tethered 8 nm silica confinement								
A" 25 °C	P-1	8.61	9.13	9.02	94.60	116.39	102.85	1.56
[BMIM][Cl]								
unconfined								
B I -120 °C	P121/c1	11.44	10.05	8.87	90.00	115.21	90.00	1.26
B II 39 °C	P121/c1	9.87	11.95	9.73	90.00	119.89	90.00	1.17
bare 8 nm silica confinement								
B' I -140 °C (68.55%)	C2	9.39	16.62	8.51	90.00	124.63	90.00	1.06
B' II -140 °C (31.45%)	P121/c1	9.85	12.22	9.76	90.00	120.07	90.00	1.14

**crystallography information from Choudhury et. al [19, 230] ([BMIM][PF_6]) and Holbrey et al.[230] ([BMIM][Cl]). A/B: unconfined IL. A'/B': confined IL. A": Tconfined IL.*

The tremendous depression or even supression of melting of [BMIM][Cl] in silica nanopores found in this study suggest that the impacts of confinement on crystallization of [BMIM][Cl] are much greater than for [BMIM][PF_6]. The different melting point changes of [BMIM][Cl] and [BMIM][PF_6] in response to bare and tethered silica nanoconfinement are most likely due to the stronger H-bonding between $BMIM^+$ and Cl^-

[38, 230]. A previous FTIR study by He et al. shows evidence for an interaction between silica pore walls and $[BMIM]^+$ in [BMIM][Cl].[17] When the relatively strong interaction between $[BMIM]^+$ and Cl^- is disturbed, the lack of driving force for specific molecular orientation in a crystal might cause the great depression and suppression of T_m of confined [BMIM][Cl] compared to bulk. With most of the confined [BMIM][Cl] displaying T_m suppression, it is difficult to compare and reason about the impacts of different confinements on [BMIM][Cl]. Nevertheless, the confinements employed in this study all result in [BMIM][Cl] with much lower T_m, which suggests when nanoconfined, it can be used over a wide temperature range as a true ionic liquid.

6.5 Conclusion

Temperature-resolved *in situ* GIWAXS was successfully performed to probe the crystallization of unconfined [BMIM][PF_6] and [BMIM][Cl], as well as the two ILs in 2.5 nm and 8 nm-pore-diameter nanoporous silica films with and without [TMS-MIM][Cl] tethering. Short-range nanodomains were observed in both unconfined ILs even when they were in the amorphous state. This experimental evidence agrees with computational studies suggesting the presence of heterogeneous ordered clusters coexisting with disordered liquid in bulk ILs. When [BMIM][PF_6] is confined in 2.5 nm silica nanopores, it experienced T_m depression by 9 °C as predicted by the Gibbs-Thomson equation. However, the Gibbs-Thomson effect is not applicable when it comes to [BMIM][PF_6] confined in 8 nm pores where T_m is *elevated* by 17.5 °C. This unconventional behavior is due to more space in the 8 nm pores allowing [BMIM][PF_6] to layer more extensively, which stabilized the crystalline IL. When the silica pore

surface was tethered with [TMS-MIM][Cl], confined [BMIM][PF_6] in both sizes of pore show higer T_m because the pore surface is more similar to the IL itself and no effects due to hydrogen bonding with SiOH groups are seen. These effects are expressed most strongly in 8 nm pores where layering and tethering favor crystallization. [BMIM][PF_6] presented only one stable crystal phase under this condition that did not melt at room temperature. This provides a new method of stablizing the complicated crystallization behavior of [BMIM][PF_6] and suppressing polymorph, which gives better control of crystal phases of [BMIM][PF_6] over a wider temperature range.

For the IL with a smaller anion that has stronger and more specific interactions with the cations, [BMIM][Cl], crystallization under nanoconfinement was found only for 8 nm bare silica pore confinement, but with great T_m depression of -119 °C. This is suspected to result from the disturbance of the cation-anion interaction in the crystalline state, which is the major driving force for stable ordering of [BMIM][Cl]. Simulations suggest that alternating ion layering still happens over a large distance in the liquid state, but in this case that lowers the ability of the system to assemble into crystalline solids. Because [BMIM][Cl] is found in liquid form over a much wider temperature range, nanoconfinemt should enhance its properties for uses requiring a liquid form at low temperature. The findings from this study give some guidance to the range of crystallization behaviors that can be found for ionic liquids by tayloring the pore size and surface properties depending on the behavior of the bulk IL. By varying the crystal phase transition temperatures, nanoconfinement creates new opportunities for applications of ILs in fields including drug delivery, separations, electrochemical devices and catalyst supports.

Chapter 7. Conclusions and Future Directions

Chapter 3 describes the principles and processes of a novel method of producing titanosilicate mesoporous thin film with orthogonally oriented nano-sized channels through EISA with CTAB templating. As indicated by GISAXS patterns, after template removal with calcination, the film showed a vertically aligned nanostructure with respect to the substrate and the diameter is estimated to be about 2.5 nm. This provides the supporting materials with a smaller pore size comparing to the existing P123 templated films with about 8 nm pores for the studies in **Chapter 5&6**. Unlike manipulating pore orientation with substrate surface modification in producing vertically oriented pores with P123 templating, the micelles in CTAB templated titanosilicate films were destabilized during calcination because of the breakage of the Ti-O-Si bonds and merged in vertical direction. This not only enables comparisons between confined and unconfined IL system, but also allows comparisons between different sizes of confinement. The catalysis capability can be tested by comparing the titanosilicate thin films with and without sugar surfactant complexation (titania dispersed on the pore surface verses in silica matrix) to further the original goal of the study, which was to produce mesoporous thin films with catalytic pore surface with titania.

Chapter 4 presents a *in situ* transmission FTIR technique with varying RH to investigate the bond changing in [BMIM][Cl] and its hydration with and without confinement. The results suggest interaction formed between the [$BMIM^+$] and the silica pore surface and unexpectedly, the confined [BMIM][Cl] in the hygroscopic silica nanoporous material expressed less hygroscopicity comparing to unconfined [BMIM][Cl]. This characterization technique can be employed for studies of hydration of

various ILs. Furthermore, catalysts or catalytic reaction systems can be introduced to the confined IL and being investigated regarding their response to moisture. Glucose dehydration with ligand-promoted Al catalyst studied by Dr. Ladipo's group is a candidate subject.[26] The RH control method and setup can also be converted to adapt wide varieties of gas control for studies, such as gas absorption and separation.

Chapter 5 compared how easy the hydrophilic redox probe (FDM) and the hydrophobic redox probe (DBD) can get access to the substrate surface through the silica thin films with two different pore sizes (2.5 nm and 8 nm) and with different treatments (physically confined [BMIM][PF_6], tethered [TMS-MIM^+] group and both). The results indicate that the tethered thin films pose tremendously increased resistance for FDM redox couples to pass through in terms of the low permeability comparing to non-tethered films with or without physically confined IL with about 14-fold decrease. However, the different treatments do not affect permeability of DBD redox couples. Such difference between the permeability of FDM and DBD redox probes is even greater (more than 30-fold) in the smaller channels with diameter of 2.5 nm. This finding suggests that [TMS-MIM] group tethering on the silica pore wall can be advantageous for small molecule separation based on the hydrophobicity of the molecules.

In **Chapter 6**, direct physical evidences were obtained by temperature-resolved *in situ* GIWAXS measurement of impacts of different silica nanoconfinements on crystallization behavior of the two ILs studied, [BMIM][PF_6] and [BMIM][Cl]. The crystal phase changes and polymorphs observed in the samples were identified and analyzed from the GIWAXS patterns. It was concluded that the larger pore confinement of 8 nm provides more space for [BMIM][PF_6] to self-organize, thus promoting the

ordering and expressing elevations in melting point. The IL-like pore surface functionalization was also proven to results in higher melting point than unconfined [BMIM][PF_6]. An extreme case with [BMIM][PF_6] confined in 8 nm pores with tethering stood out by displaying only one crystal phase throughout the entire temperature range of measurement (-140 ℃ to 25 ℃). The IL [BMIM][Cl] with stronger interaction between the cations and anions has higher melting point than [BMIM][PF_6] without nanoconfinement. Nevertheless, this interaction that helps [BMIM][Cl] for easier crystallization is disturbed by the silica surface and the confinement as illustrated in **Chapter 4**. Therefore, crystallization was only observed in 8 nm bare mesoporous silica film confined [BMIM][Cl] at low temperature below -119 ℃. This characterization technique can be modified for IL confined silica mesoporous particles in both dry conditions and suspended in liquid to observe how the results in silica mesoporous thin films translate to mesoporous particles. It can also investigate how the crystallization behavior of confined ILs respond to the surrounding liquid environment, which broadens the applications of SIL for compounds delivery vehicles.

Furthering from the development of the titanosilicate thin films, the effects of the titania dispersed on the pore surface can be studied as originally proposed, such as the previous study in our group regarding adsorption and recovery of polyphenolic flavonoids with titania functionalized silica mesoporous particles.[264] If differences in the adsorption, catalytic efficiency, or other properties of interest are observed, it can be further proved that titania is successfully dispersed at the pore surface with sugar surfactant complexation and more applications can be advanced from here.

With the highly selective film produced through treatment of silica mesoporous thin film with [TMS-MIM] group tethering, future studies with the discoveries of this investigation can be conducted by depositing the highly selective thin films on the anodic aluminum oxide (AAO) membranes that have been employed in the group for previous studies.[14] Thus, a free-standing composite membrane can be tested for separation and selectivity through solvent flux and solute diffusion with respect to the hydrophobicity of the molecules in a static system to begin with.

Appendix

Appendix A

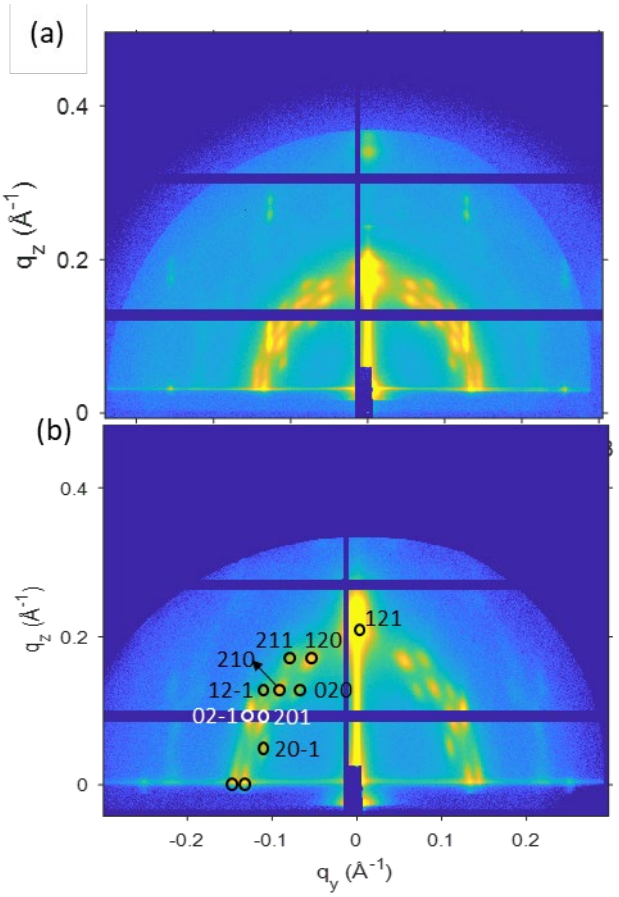

Figure A1. GISAXS patterns of CTAB templated silica thin films without titania doping with peak indexing (a) before calcination (mixture of 2D hexagonal and primitive cubic structure $Pm\bar{3}n$); (b) after 40 min calcination at 500 °C (primitive cubic structure $Pm\bar{3}n$)

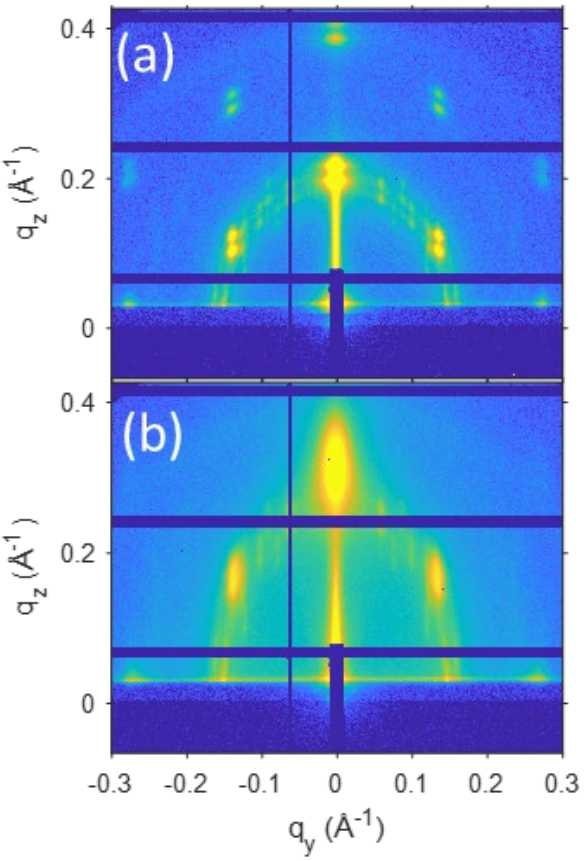

Figure A2. GISAXS patterns of 2D GISAXS pattern of CTAB templated silica thin film with 0.5% titania doping and no sugar surfactant (a) before calcination and (b) after calcination at 500 °C for 30 min.

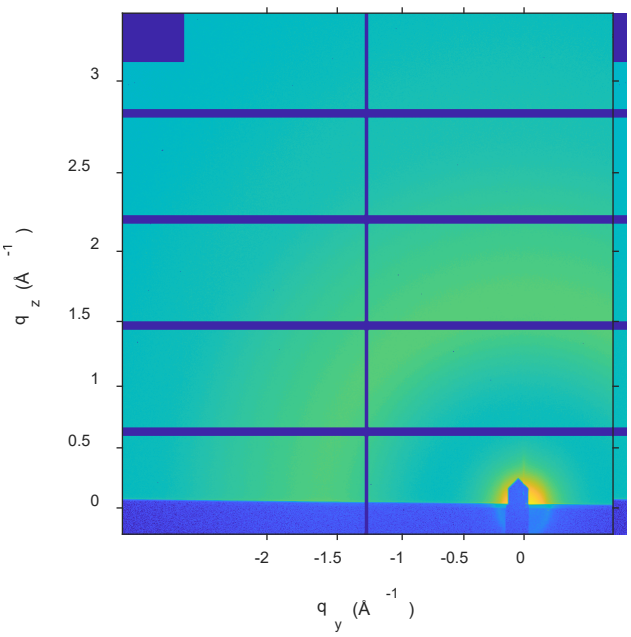

Figure A3. GIWAXS pattern of silica thin films with 6% titania doping and no sugar surfactant complexation after calcination

Appendix B

Table B1. Peak positions (wavenumber (cm^{-1})) determined by deconvolution at different RH values for unconfined [BMIM][Cl] when the RH is controlled by H_2O.

Bonds \ RH	87.0%	62.0%	42.0%	27.0%	15.0%	6.0%	0.0%	Dry IL
v_{ss} HC4C5H	3158 ± 3.7	3154 ± 2.1	3150.9 ± 0.74	3148.1 ± 0.50	3145.9 ± 0.42	3144.9 ± 0.76	3138 ± 1.6	3138.9 ± 0.78
v_{as} HC4C5H	3109 ± 4.2	3092 ± 1.9	3094.2 ± 0.83	3088.7 ± 0.46	3083.9 ± 0.36	3072.8 ± 0.35	3054.6 ± 0.68	3060± 0.46
C2H stretching	3051 ± 3.0	3043 ± 2.7	3045.4 ± 0.87	3038.1 ± 0.50	3033.9 ± 0.33	3021.0 ± 0.65	3003 ± 1.6	3001.5 ± 0.74
v_{as} CH_3	2968 ± 1.4	2964.2 ± 0.68	2963.7 ± 0.30	2962.8 ± 0.22	2961.8 ± 0.29	2961.8 ± 0.29	2960.8 ± 0.56	2960.6 ± 0.7
v_{ss} CH_3	2874 ± 2.3	2871.2 ± 0.83	2872.0 ± 0.55	2869.5 ± 0.33	2862.1 ± 0.17	2866.2 ± 0.45	2865.3 ± 0.79	2861.6 ± 0.48
anion coordinated water	3515.5 ± 0.82	3486.2 ± 0.99	3481.1 ± 0.74	3471.4 ± 0.42	3458.2 ± 0.38	3454.1 ± 0.54	3420 ± 22	N/A
interface water	3393.6 ± 0.43	3380.8 ± 0.56	3382.0 ± 0.47	3372.5 ± 0.35	3367.5 ± 0.42	3367.4 ± 0.60	3360 ± 24	N/A
bulk-like water	3235.6 ± 0.88	3232.0 ± 1.0	3240.0 ± 0.87	3238.8 ± 0.77	3242.1 ± 0.82	3251 ± 1.6	3250	N/A
R^2 (CH and OH)	0.9978	0.9985	0.9987	0.9990	0.9989	0.9962	0.9879	0.9971
C=N- stretching	1575.2 ± 0.16	1573.5 ± 0.20	1572.8 ± 0.18	1572.1 ± 0.16	1571.6 ± 0.14	1571.6 ± 0.29	1571.8 ± 0.69	1568.1 ± 0.17
R^2 (C=N- stretching)	0.9971	0.9918	0.9923	0.9939	0.9952	0.9795	0.8979	0.9959
aromatic C=C- stretching	1462.9 ± 0.43	1462.6 ± 0.85	1462.7 ± 0.66	1462.7 ± 0.66	1462.7 ± 0.66	1462.7 ± 0.66	1463.2 ± 0.43	1463.7 ± 0.66
R^2 (aromatic C=C- stretching)	0.9438	0.9031	0.8255	0.8197	0.8201	0.8741	0.9518	0.9959
IM stretching	1171.1 ± 0.21	1171.2 ± 0.18	1171.3 ± 0.16	1171.5 ± 0.14	1172.0 ± 0.14	1172.8 ± 0.16	1175.1 ± 0.26	1173.2 ± 0.21
R^2 (IM stretching)	0.9844	0.9885	0.9917	0.9936	0.9944	0.993	0.9833	0.9915

Table B2. Peak positions (wavenumber (cm^{-1})) determined by deconvolution at different RH values in confined [BMIM][Cl] when the RH is controlled by H_2O.

Bonds \ RH	78.0%	59.0%	45.0%	28.0%	19.0%	8.5%	0.0%	Dry IL
ν_{ss} HC4C5H	3158.8 ± 0.74	3154.3 ± 0.86	3152.9 ± 0.52	3152.1 ± 0.61	3149.8 ± 0.61	3149.4 ± 0.72	3144.6 ± 0.51	3140.2 ± 2.2
ν_{as} HC4C5H	3103 ± 1.3	3097.5 ± 0.87	3096.1 ± 0.54	3091.8 ± 0.67	3086.4 ± 0.36	3079.5 ± 0.74	3059.8 ± 0.68	3053.6 ± 0.77
C2H stretching	3056 ± 1.3	3048 ± 1.3	3042.0 ± 0.91	3038 ± 1.0	3026.7 ± 0.70	3014.7 ± 0.91	3007 ± 1.3	2987 ± 1.6
ν_{as} CH_3	2966.2 ± 0.63	2964.9 ± 0.56	2964.2 ± 0.31	2963.9 ± 0.27	2963.1 ± 0.25	2961.2 ± 0.52	2961.4 ± 0.24	2960.4 ± 1.4
ν_{ss} CH_3	2875 ± 1.0	2873.9 ± 0.78	2873.4 ± 0.47	2872.9 ± 0.48	2872.1 ± 0.49	2869.9 ± 0.53	2867.2 ± 0.26	2865.3 ± 1.2
anion coordinated water	3511.5 ± 0.27	3505.5 ± 0.45	3482.7 ± 0.43	3465.7 ± 0.97	3464.2 ± 0.51	3449.1 ± 0.47	3454 ± 1.0	N/A
interface water	3380.6 ± 0.27	3380.8 ± 0.32	3379.6 ± 0.42	3376 ± 1.1	3377.8 ± 0.63	3368.2 ± 0.90	3379.6 ± 0.78	N/A
bulk-like water	3242.9 ± 0.35	3237.5 ± 0.59	3240.0 ± 0.46	3241.1 ± 0.71	3241 ± 1.1	3223 ± 1.6	N/A	N/A
R^2 (OH and CH)	0.9994	0.9991	0.9994	0.9991	0.9985	0.9972	0.9983	0.9886
C=N- stretching	1576.5 ± 0.61	1575.0 ± 0.46	1574.3 ± 0.38	1574.2 ± 0.38	1574.0 ± 0.35	1573.8 ± 0.34	1576.2 ± 0.59	1570 ± 0.17
R^2 (C=N-stretching)	0.9149	0.943	0.9578	0.9606	0.9634	0.9655	0.9885	0.9959
aromatic C=C-stretching	1465.9 ± 0.41	1466.2 ± 0.43	1466.5 ± 0.41	1466.9 ± 0.38	1467.1 ± 0.35	1467.4 ± 0.36	1465.8 ± 0.34	1463.5 ± 0.59
R^2 (aromatic C=C-stretching)	0.9524	0.9528	0.9571	0.9637	0.9685	0.9691	0.9696	0.9947
IM stretching	1171.0 ± 0.19	1171.6 ± 0.19	1172.7 ± 0.25	1170.9 ± 0.33	1174.4 ± 0.32	1175.4 ± 0.50	1171.0 ± 0.23	1173.2 ± 0.10
R^2 (IM stretching)	0.9668	0.9722	0.9591	0.9337	0.9278	0.9128	0.9668	0.9981

Table B3. Peak positions determined by deconvolution at different RH values in unconfined [BMIM][Cl] when the RH is controlled by D_2O

Bonds \ RH	0.0%	9.5%	17.5%	31.0%	53.0%	62.0%	85.0%
ν_{ss} HC4C5H	3141 ± 1.0	3146.4 ± 0.80	3150.6 ± 0.75	3150.5 ± 0.63	3152.9 ± 0.35	3155.1 ± 0.60	3158.3 ± 0.37
ν_{as} HC4C5H	3071 ± 1.4	3085 ± 1.1	3091 ± 1.2	3094.3 ± 0.95	3100.9 ± 0.59	3104 ± 1.1	3110.5 ± 0.97
C2H stretching	3041.7 ± 0.37	3041.8 ± 0.68	3046.9 ± 0.74	3048.5 ± 0.71	3058.9 ± 0.48	3062.2 ± 0.96	3078.7 ± 0.67
ν_{as} CH_3	2961.2 ± 0.32	2961.7 ± 0.48	2962.2 ± 0.38	2962.9 ± 0.38	2964.4 ± 0.19	2965.0 ± 0.45	2967.0 ± 0.20
ν_{ss} CH_3	2865.2 ± 0.43	2869.5 ± 0.58	2870.2 ± 0.52	2871.3 ± 0.47	2872.5 ± 0.35	2872.9 ± 0.59	2874.7 ± 0.4
R^2 (OH and CH)	0.9961	0.9896	0.9869	0.9880	0.9945	0.9808	0.9928
aromatic C=C- stretching	1459.9 ± 0.68	1461.0 ± 0.60	1461.4 ± 0.77	1462.2 ± 0.72	1463.0 ± 0.64	1463.4 ± 0.57	1463.7 ± 0.31
R^2 (aromatic C=C- stretching, global)	0.9893	0.9893	0.9893	0.9893	0.9893	0.9893	0.9893
C=N- stretching	1570.7 ± 0.22	1570.9 ± 0.15	1571.1 ± 0.16	1571.4 ± 0.16	1571.9 ± 0.20	1572.0 ± 0.20	1572.6 ± 0.24
R^2 (C=N- stretching)	0.9816	0.98642	0.9868	0.9906	0.9918	0.9926	0.986
IM stretching	1173.6 ± 0.18	1171.5 ± 0.16	1171.1 ± 0.19	1170.9 ± 0.25	1170.9 ± 0.38	1171.2 ± 0.48	1170.4 ± 0.22
R^2 (IM stretching)	0.9887	0.9392	0.9593	0.9818	0.9894	0.992	0.9903

Table B4. Peak positions determined by deconvolution at different RH values in confined [BMIM][Cl] when the RH is controlled by D_2O.

Bonds \ RH	0.0%	9.5%	19.5%	29.0%	49.0%	59.5%	78.0%
ν_{ss} HC4C5H	3141 ± 1.1	3146.6 ± 0.86	3148.6 ± 0.55	3149.0 ± 0.64	3152.1 ± 0.52	3153.0 ± 0.46	3155.5 ± 0.46
ν_{as} HC4C5H	3065 ± 2.7	3083 ± 1.2	3089.3 ± 0.70	3093.2 ± 0.52	3099.4 ± 0.71	3101.7 ± 0.49	3105.0 ± 0.95
C2H stretching	3035 ± 1.1	3039.8 ± 0.86	3045.2 ± 0.59	3048.9 ± 0.73	3058.0 ± 0.72	3063.2 ± 0.73	3070.1 ± 0.84
ν_{as} CH_3	2960.7 ± 0.23	2961.8 ± 0.34	2962.5 ± 0.23	2963.1 ± 0.36	2964.0 ± 0.24	2964.8 ± 0.27	2966.0 ± 0.30
ν_{ss} CH_3	2866.8 ± 0.45	2870.2 ± 0.51	2870.6 ± 0.45	2871.2 ± 0.49	2872.3 ± 0.47	2872.8 ± 0.45	2873.9 ± 0.46
R^2 (OH and CH)	0.9959	0.9903	0.9946	0.9909	0.9914	0.9920	0.9906
aromatic C=C- stretching	1461.6 ± 0.78	1462.8 ± 0.89	1462.7 ± 0.64	1463.5 ± 0.51	1464.2 ± 0.44	1464.9 ± 0.36	1465.0 ± 0.40
R^2 (C=C- stretching)	0.8559	0.8069	0.895	0.9318	0.9535	0.9667	0.9608
C=N- stretching	1570.8 ± 0.21	1571.0 ± 0.30	1571.2 ± 0.14	1571.7 ± 0.14	1572.4 ± 0.15	1572.6 ± 0.16	1572.8 ± 0.17
R^2 (C=N- stretching)	0.9885	0.9737	0.9939	0.994	0.9929	0.9907	0.9898
IM stretching	1173.9 ± 0.15	1171.9 ± 0.29	1171.6 ± 0.19	1171.4 ± 0.22	1171.3 ± 0.26	1171.6 ± 0.28	1172.5 ± 0.35
R^2 (IM stretching)	0.9944	0.9775	0.9904	0.9876	0.9824	0.9803	0.9687

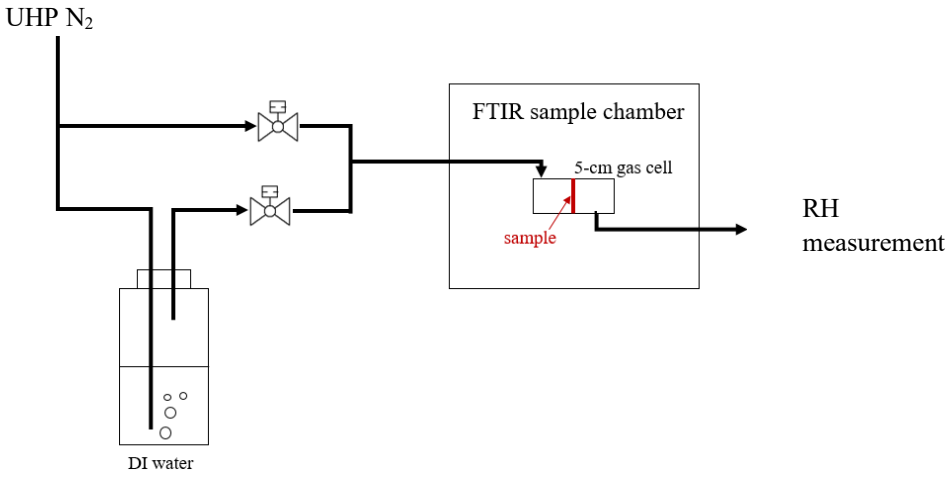

Figure B1. Illustration of the setup for transmission sampling of thin films on silicon wafers under controlled vapor conditions in a 5 cm Pyrex gas cell with ZnSe windows. Relative humidity is controlled by mixing dry UHP N2 with N2 saturated with H_2O or D_2O by bubbling through a gas wash bottle. The mixed gas passes over the ionic liquid sample, either as a free film or supported in mesoporous silica, on a thin silicon wafer. Relative humidity is measured as the gas mixture passes out of the glass cell.

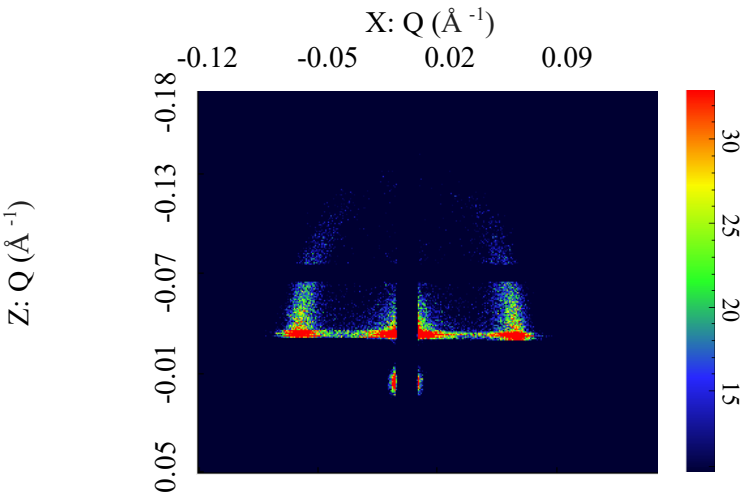

Figure B2. 2D GISAXS patterns of o-HCP silica film.

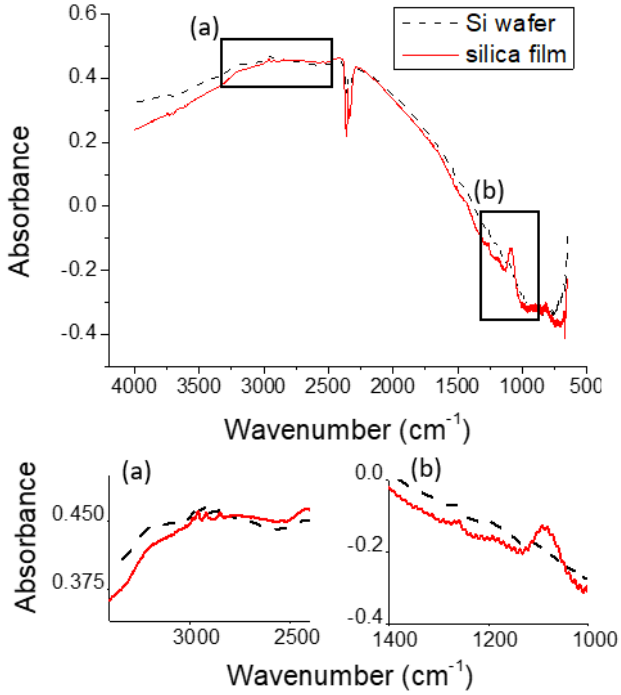

Figure B3. FTIR spectra without ionic liquid of the Si wafer and mesoporous silica film. The regions labeled (a) and (b) are magnified views of the indicated regions of the whole spectrum. The Si wafer has too little SiO_2 to give distinct bands, but the mesoporous film gives mainly features from Si-O stretching near 1000-1200 cm^{-1}. The small CH stretching bands near 3000 cm^{-1} are due to trace ethanol from cleaning.

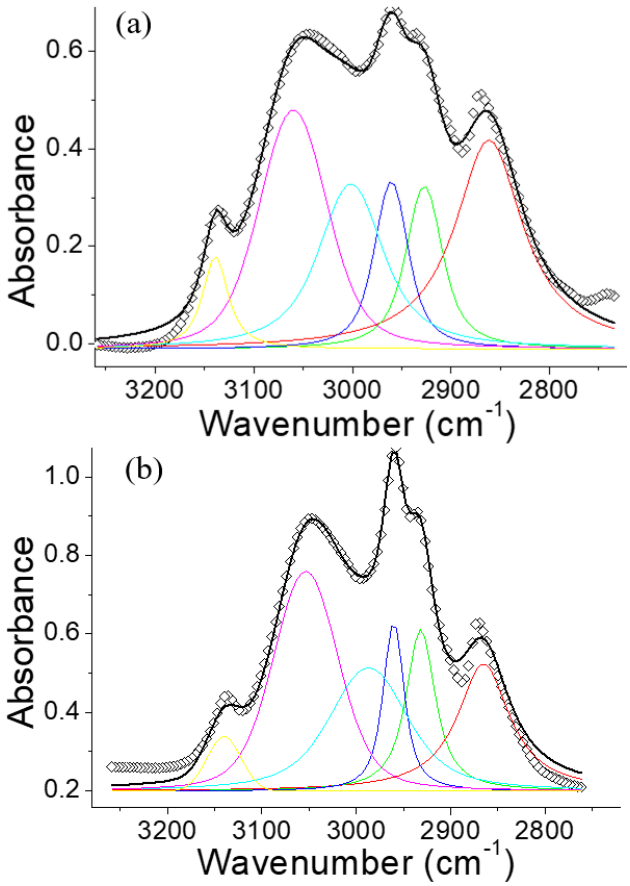

Figure B4. IR peak deconvolution of dry [BMIM][Cl] either (a) unconfined as a film on the Si wafer support, or (b) confined in mesoporous silica. Colored curves represent individual contributions to the spectrum. The points are the original data, and the black curve is the overall fit.

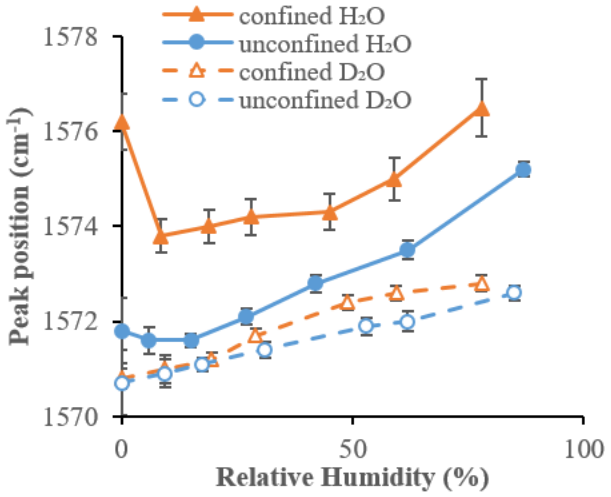

Figure B5. Peak positions of C=N- stretching in confined (▲) and unconfined (●) [BMIM][Cl] at different RHs when RH is controlled by H_2O, and in confined (△) and unconfined (○) when RH is controlled by D_2O.

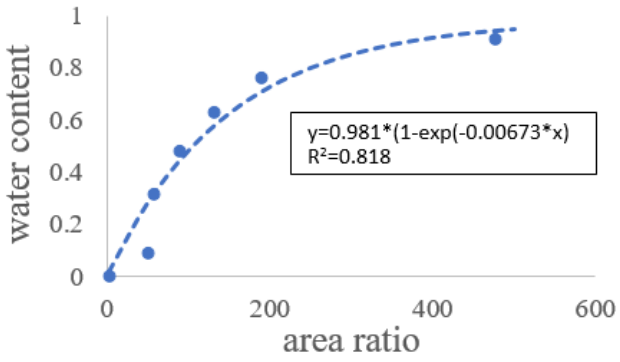

Figure B6. Water content as a function of the area ratio of OH stretching bands to C=C- stretching bands in unconfined [BMIM][Cl] when using H_2O to control humidity. The water content of the unconfined IL is set equal to be the value reported by MacMillan et al.[36] at the same water activity (RH) at which the area ratio was measured.

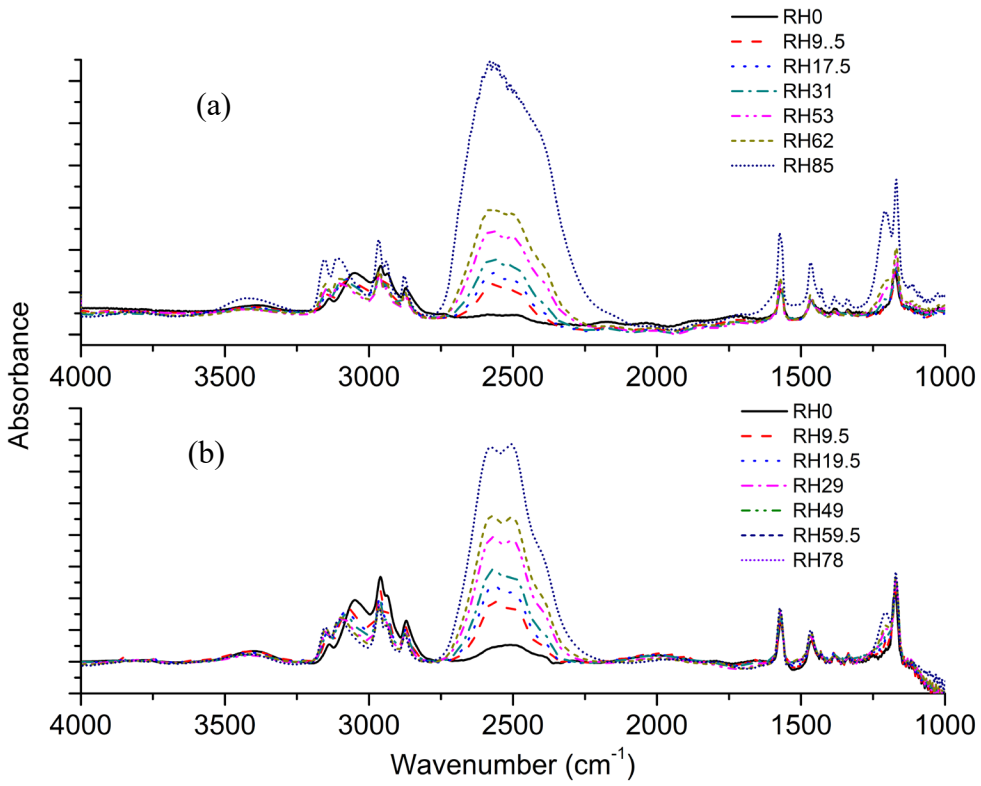

Figure B7. FT-IR spectra of (a) unconfined and (b) confined IL with decreasing relative humidity (RH), where RH is controlled by D_2O.

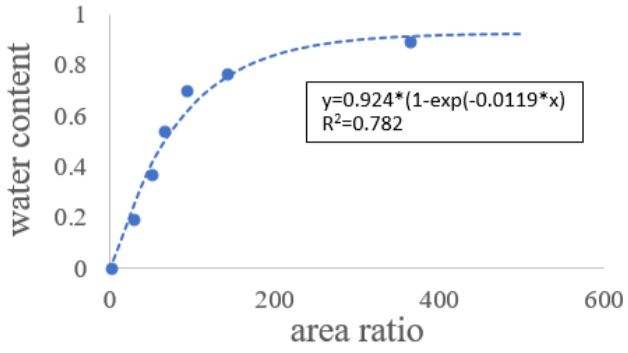

Figure B8. Water content as a function of the area ratio of OH stretching bands to C=C-stretching bands in [BMIM][Cl] when using D_2O to control humidity. The water content of the unconfined IL is set equal to be the value reported by MacMillan et al.[36] at the same water activity (relative humidity) at which the area ratio was measured.

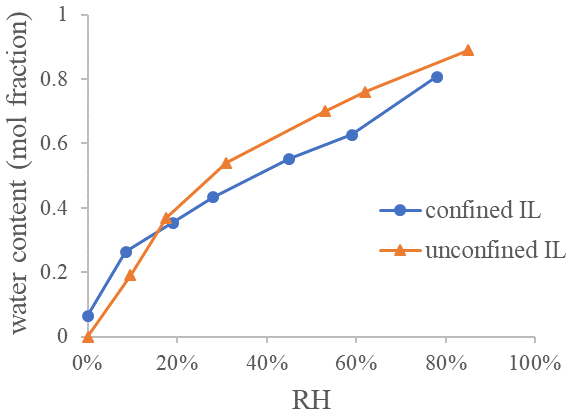

Figure B9. Mole fraction of water absorbed as a function of RH for nanopore confined and unconfined [BMIM][Cl] when using D_2O to control humidity. Error bars estimated from the uncertainty in the normalized OH stretching vibration areas are smaller than the data markers.

Appendix C

TiO_2 + SiO_2 film

Table C1. Water contact angles (CA)

Results	Value	Stdev
Mean CA(M) [°]	42.80	4.85
Mean CA(L) [°]	41.37	6.62
Mean CA(R) [°]	44.24	4.24

SiO_2 film

Results	Value	Stdev
Mean CA(M) [°]	43.33	3.49
Mean CA(L) [°]	43.63	3.03
Mean CA(R) [°]	43.02	4.72

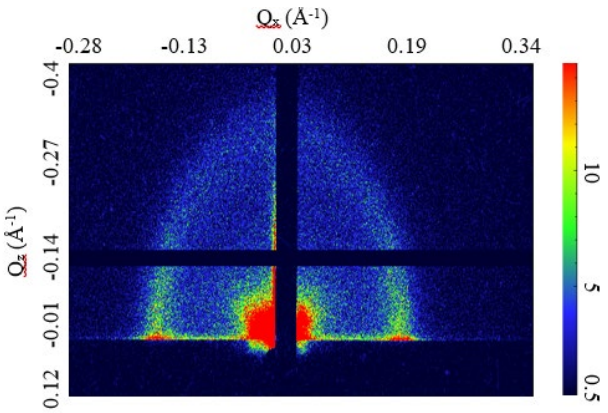

Figure C1. GISAXS 2D pattern of the CTAB templated silica film used for the EIS study with d-spacing of 3.5 nm and orthogonal orientation with respect to the substrate

Table C1. Atomic percentage of selected elements in [TMS][Cl] tethered CTAB templated silica thin film (2.5 nm) from XPS depth profile with ion gun etching

Etch Time (sec)	Si2p	C1s	N1s	O1s
		Atomic %		
0.00	19.56%	33.07%	5.29%	42.08%
10.00	27.71%	15.32%	3.91%	53.05%
20.00	28.13%	14.90%	3.78%	53.18%
30.00	28.27%	14.58%	4.13%	53.01%
40.00	28.26%	14.63%	4.04%	53.08%
240.02	28.19%	14.72%	4.73%	52.36%
440.05	96.21%	0.00%	0.00%	3.79%
640.07	96.76%	0.00%	0.00%	3.24%
840.10	96.91%	0.00%	0.00%	3.09%
1040.12	96.77%	0.00%	0.00%	3.23%
1240.17	97.16%	0.00%	0.00%	2.84%
1440.18	96.89%	0.00%	0.00%	3.11%
1640.20	96.86%	0.00%	0.00%	3.14%

Table C2. Atomic percentage of selected elements in [TMS][Cl] tethered P123 templated silica thin film (8 nm) from XPS depth profile with ion gun etching

Etch Time (sec)	Si2p	C1s	N1s	O1s
	Atomic %			
0.00	29.33%	10.17%	2.03%	58.46%
10.00	31.66%	5.43%	1.89%	61.02%
20.00	31.65%	5.83%	1.79%	60.74%
30.00	31.47%	6.27%	2.07%	60.19%
40.00	31.67%	6.71%	2.13%	59.50%
240.02	32.43%	6.53%	2.37%	58.66%
440.03	32.13%	5.51%	2.16%	60.20%
640.06	95.47%	0.00%	0.00%	4.53%
840.08	96.11%	0.00%	0.00%	3.89%
1040.10	96.97%	0.00%	0.00%	3.03%
1240.12	96.50%	0.00%	0.00%	3.50%
1440.15	96.59%	0.00%	0.00%	3.42%
1640.16	96.58%	0.00%	0.00%	3.42%

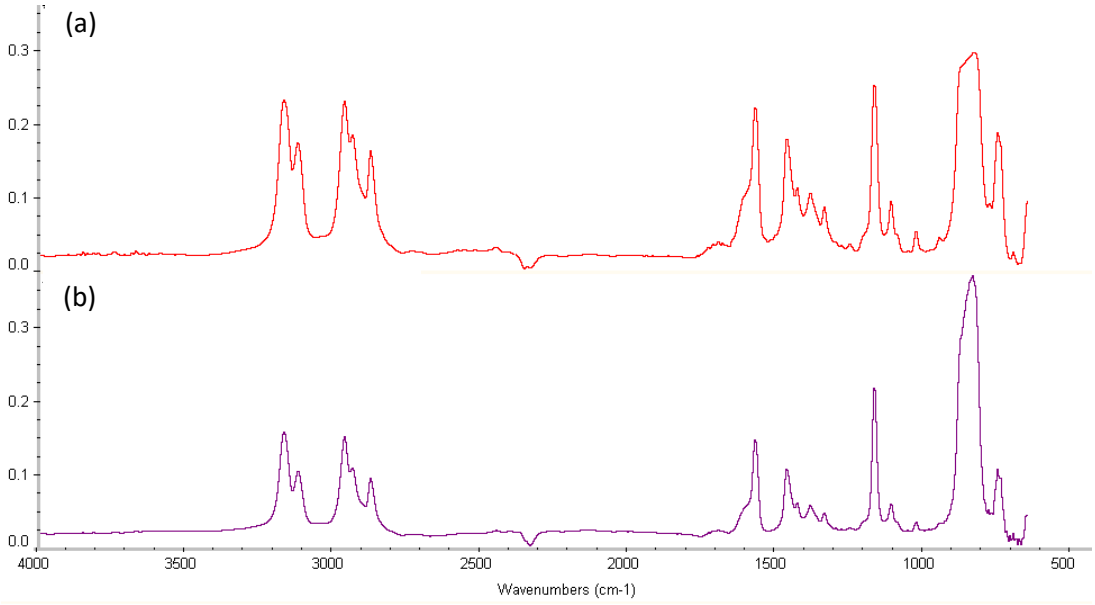

Figure C2. Transmission FTIR spectra of [BMIM][PF_6] on Si wafer (a) before and (b) after one-minute submerging in DI water

Table C3. Equivalent circuit fitting results of all samples analyzed

	Chi-Sqr	Sum-Sqr	R1(Ω/cm^2)	R1(Error)	R1(Error%)
FTO FDM	0.00779	1.075	41.99	0.30208	0.71941
unconfined FDM	0.014099	1.9457	42.73	0.43193	1.0108
FTO DBD	0.022293	3.0765	45.71	0.37932	0.82984
unconfined DBD	0.02851	3.9343	51.24	0.46729	0.91196
CTAB FDM	0.013878	1.9152	57.92	0.50337	0.86908
CTAB DBD	0.027613	3.8106	68.97	0.59218	0.85861
CTAB confined FDM	0.013135	1.8127	51.48	0.45019	0.87449
CTAB confined DBD	0.024071	3.2978	58.44	0.50405	0.86251
CTAB tethered DBD	0.022618	3.1213	43.95	0.35542	0.80869
CTAB tethered FDM	0.013883	1.9158	47.28	0.32909	0.69604
CTAB Tconfined DBD	0.029303	4.0439	59.29	0.49826	0.84038
CTAB Tconfined FDM	0.020539	2.8344	51.26	0.47763	0.93178
P123 FDM	0.010755	1.4841	42.16	0.33431	0.79296
P123 confined FDM	0.010759	1.4848	41.06	0.31469	0.76642
P123 tethered FDM	0.01482	2.0748	45.98	0.33191	0.72186
P123 Tconfined FDM	0.002095	0.25559	38.41	0.16796	0.43728
P123 DBD	0.024975	3.4466	58.98	0.44084	0.74744
P123 confined DBD	0.024768	3.4179	46.18	0.37011	0.80145

R1 and R2 both have units of Ω/cm^2 and the surface charge transfer resistance obtained for Table. 1 and 2 are obtained from multiplying R1 and R2 by the corresponding submerging area provided in the main text.

Ws1-R (Ω/cm^2), Ws1-T (sec) and Ws1-P are the parameters required to obtain the impedance of the Warburg element: Z = R* tanh ((ì T * ω) ^ P) / (ì T * ω) ^ P. ω is the angular frequency of the AC potential and ì equals sqrt (-1). Ws1-P is fixed at 0.5 during fitting to represent the high frequency behavior.

Table C3. (continued)

	R2 (Ω/cm^2)	R2(Error)	R2(Error%)	Ws1-R (Ω/cm^2)	Ws1-R (Error)	Ws1-R (Error%)
FTO FDM	693.4	19.814	2.8575	2.23E+06	6.57E+11	2.94E+07
unconfined FDM	944.9	37.05	3.921	1.84E+06	7.63E+11	4.14E+07
FTO DBD	1384	40.487	2.9254	7102	3.46E+07	4.87E+05
unconfined DBD	1395	42.259	3.0293	5935	4.93E+07	8.31E+05
CTAB FDM	1265	46.026	3.6384	9649	4339.8	44.977
CTAB DBD	8801	295.18	3.3539	770.2	2.65E+05	34346
CTAB confined FDM	1591	52.21	3.2816	51209	1.77E+10	3.46E+07
CTAB confined DBD	4476	111	2.4799	0.071868	2.04E+05	2.84E+08
CTAB tethered DBD	6716	263.99	3.9308	0.002337	407.65	1.74E+07
CTAB tethered FDM	33857	1759.7	5.1974	16239	32461	199.9
CTAB Tconfined DBD	7266	235.87	3.2462	0.000118	159.84	1.35E+08
CTAB Tconfined FDM	5739	224.43	3.9106	7772	5306.3	68.275
P123 FDM	1008	35.211	3.4932	7377	8428.9	114.26
P123 confined FDM	1555	47.779	3.0726	5980	4015.5	67.149
P123 tethered FDM	14348	253.12	1.7641	NA	NA	NA
P123 Tconfined FDM	12362	95.584	0.77321	NA	NA	NA
P123 DBD	1520	42.272	2.7811	2542	47436	1866.1
P123 confined DBD	1628	44.367	2.7252	4527	3.50E+07	7.74E+05

For the constant phase element 1 (CPE1), the impedance consists of two parameters: T (F/cm^2-s ^ (P - 1), CPE1-T in Tab. S3) and P (CPE1-P in Tab. S3) whose values are presented in the two tables below with a relation of $Z = \frac{1}{T \times (i\,\omega)^P}$. T is the capacitance of the double layer capacitor CPE1 if it were an ideal capacitor and P is a factor parameter that equals 1 if this element were an ideal capacitor. The P values between 0.9 and 1 in our case are typical for a porous surface.

Table C3. (continued)

	Ws1-T (sec)	Ws1-T (Error)	Ws1-T (Error%)	Ws1-P	CPE1-T	CPE1-T (Error)
FTO FDM	1.56E+06	9.16E+11	5.89E+07	0.5	2.29E-05	1.06E-06
unconfined FDM	7.93E+05	6.57E+11	8.28E+07	0.5	2.33E-05	1.38E-06
FTO DBD	158.6	1.54E+06	9.73E+05	0.5	6.87E-05	2.49E-06
unconfined DBD	166.1	2.76E+06	1.66E+06	0.5	6.71E-05	2.69E-06
CTAB FDM	17.73	15.618	88.088	0.5	2.26E-05	1.12E-06
CTAB DBD	46.59	32161	69030	0.5	3.64E-05	9.25E-07
CTAB confined FDM	477.3	3.31E+08	6.93E+07	0.5	2.30E-05	1.00E-06
CTAB confined DBD	2.58E+06	7.94E+12	3.08E+08	0.5	3.34E-05	8.86E-07
CTAB tethered DBD	3.125	1.19E+06	3.82E+07	0.5	5.51E-05	1.27E-06
CTAB tethered FDM	10.59	34.304	323.93	0.5	3.00E-05	4.94E-07
CTAB Tconfined DBD	0.40171	6.39E+05	1.59E+08	0.5	5.60E-05	1.23E-06
CTAB Tconfined FDM	10.57	12.289	116.26	0.5	3.03E-05	9.34E-07
P123 FDM	26.97	62.017	229.95	0.5	5.14E-05	2.24E-06
P123 confined FDM	19.61	25.846	131.8	0.5	4.89E-05	1.70E-06
P123 tethered FDM	NA	NA	NA	NA	3.78E-05	5.33E-07
P123 Tconfined FDM	NA	NA	NA	NA	3.14E-05	2.33E-07
P123 DBD	46.7	1749.1	3745.4	0.5	7.90E-05	2.63E-06
P123 confined DBD	158.8	2.46E+06	1.55E+06	0.5	7.63E-05	2.47E-06

C1 (μF) is the real capacitance of CPE1 calculated by $C1 = \frac{(T \times R2 \times area)^{1/q}}{R}$ [119]

Table C3. (continued)

	CPE1-T (Error%)	CPE1-P	CPE1-P (Error)	CPE1-P (Error%)	C1 (μF)
FTO FDM	4.6549	0.96152	0.007405	0.77009	19.84
unconfined FDM	5.9231	0.94266	0.009407	0.99788	19.18
FTO DBD	3.6292	0.95565	0.007496	0.78439	63.31
unconfined DBD	4.0154	0.95473	0.008392	0.87896	61.65
CTAB FDM	4.9823	0.96087	0.008501	0.88469	19.99
CTAB DBD	2.5391	0.979	0.005698	0.58202	36.01
CTAB confined FDM	4.3392	0.95316	0.007451	0.78173	20.17
CTAB confined DBD	2.651	0.97553	0.005626	0.57669	32.35
CTAB tethered DBD	2.3009	0.96972	0.005178	0.53401	54.38
CTAB tethered FDM	1.6448	0.9646	0.003503	0.36313	30.73
CTAB Tconfined DBD	2.1931	0.97038	0.005155	0.53125	55.53
CTAB Tconfined FDM	3.0772	0.95978	0.006073	0.63274	28.92
P123 FDM	4.3614	0.90148	0.007676	0.85144	42.47
P123 confined FDM	3.4791	0.91183	0.006363	0.69782	42.82
P123 tethered FDM	1.4102	0.95901	0.003267	0.34065	38.78
P123 Tconfined FDM	0.74253	0.96194	0.001613	0.16764	31.71
P123 DBD	3.332	0.96642	0.00741	0.76678	76.51
P123 confined DBD	3.2321	0.9671	0.007012	0.72502	74.09

Appendix D

Table D1. Atomic percentages of N, O, Si, and O in P123 templated (8 nm pore) silica nanoporous film with [TMS-MIM][Cl] tethering from XPS depth profile. Si wafer used as the substrate.

Etch Time (s)	Etch Level	Elements Atomic %			
		N1s	O1s	Si2p	C1s
0	0	2.03	58.5	29.3	10.2
10	1	1.89	61.0	31.7	5.43
20	2	1.79	60.7	31.7	5.83
30	3	2.07	60.2	31.5	6.27
40	4	2.13	59.5	31.7	6.71
240	5	2.37	58.7	32.4	6.53
440	6	2.16	60.2	32.1	5.51
640	7	0.00	4.53	95.5	0.00
840	8	0.00	3.89	96.1	0.00
1040	9	0.00	3.03	97.0	0.00
1240	10	0.00	3.50	96.5	0.00
1440	11	0.00	3.42	96.6	0.00
1640	12	0.00	3.42	96.6	0.00

Table D2. Atomic percentages of N, O, Si, and O in CTAB templated (2.5 nm pore) silica nanoporous film with [TMS-MIM][Cl] tethering from XPS depth profile. A glass slide was used as the substrate.

Etch Time (s)	Etch Level	Elements Atomic %			
		N1s	O1s	Si2p	C1s
0	0	4.38	50.4	24.6	20.6
10	1	3.00	56.6	29.6	10.8
20	2	3.22	56.1	29.6	11.1
30	3	3.36	56.0	29.4	11.2
40	4	3.45	56.1	29.4	11.1
240	5	3.58	55.1	29.5	11.8
440	6	0.00	67.4	31.9	0.69
640	7	0.00	67.5	32.0	0.53
840	8	0.00	67.7	31.9	0.47
1040	9	0.00	67.6	32.4	0.00
1240	10	0.00	67.3	32.3	0.48
1440	11	0.00	67.2	32.3	0.46
1640	12	0.00	67.2	32.3	0.43

Temperature Calibration for GIWAXS Stage

For *in situ* temperature-controlled GIWAXS measurements, temperature was measured using a thermocouple (Scheme. 1). However, the temperature at the surface of the substrate (where the silica films and ionic liquid were located) needed to be calibrated due to the limited thermal conductivity of glass and silicon wafers. The procedures of measuring the heating and cooling curves on the sample surface with an external thermostat were described in the experiment section.

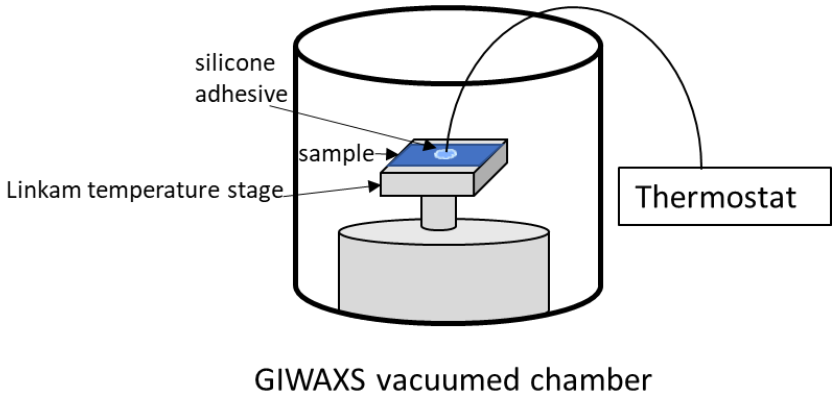

Schematic D1. Sample surface temperature measurement with an external thermostat

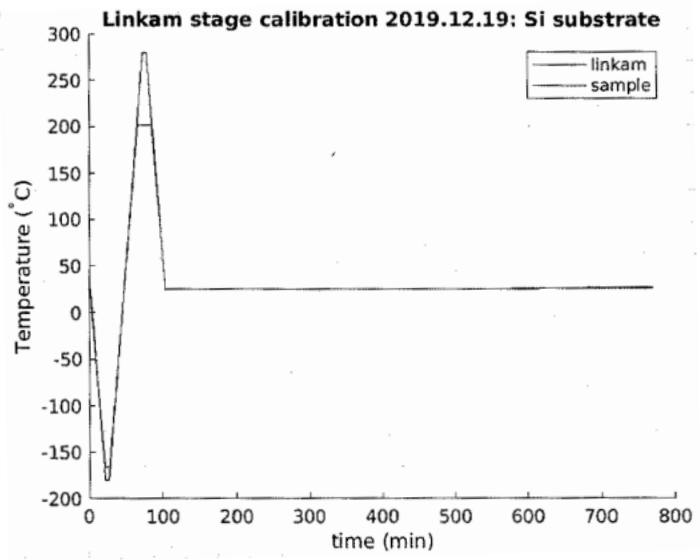

Figure D1. Temperature curves with respect to time from Linkam stage and external thermostat (sample) temperature reading of a silica film deposited onto a Si wafer. The temperature at the top of the film follows the base plate temperature closely except at the maximum temperature.

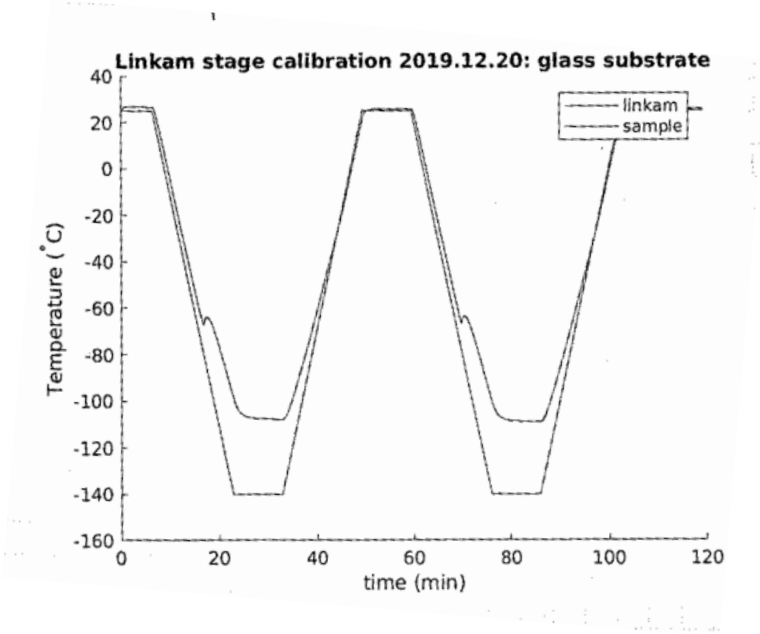

Figure D2. Temperature curves with respect to time from Linkam stage and external thermostat (sample) temperature reading of silica film deposited onto a glass slide. Note the offset at low temperature.

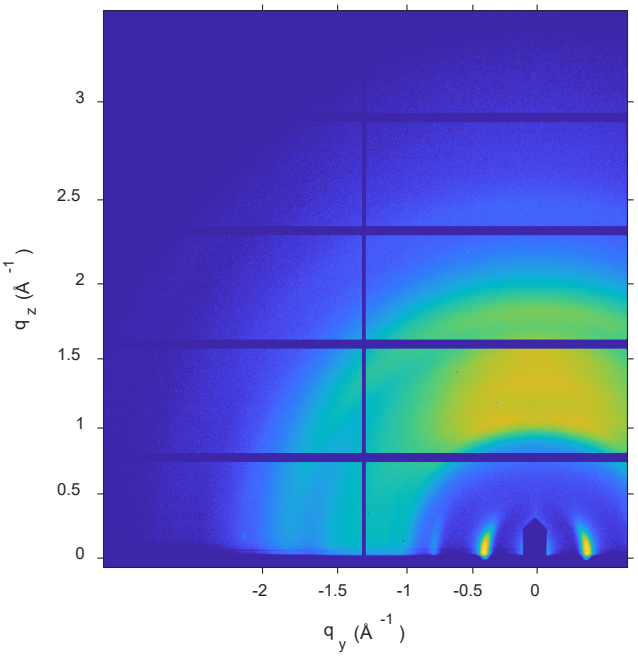

Figure D3. GIWAXS pattern of Si wafer and Kapton film background.

X-ray Scattering Background Patterns

Figure D3 shows the GIWAXS background from the Si wafer and Kapton film. This pattern was used for background subtraction during processing of confined IL films. The GIWAXS pattern at low scattering vector of IL confined in mesoporous films were also be used to confirm the presence of the vertical pore structure with IL loading at low temperature. While the focus in the main text is the evolution of crystal structure, the expansion of the GIWAXS pattern (Figure D4a) at low q values (Figure D4b) yields a pattern that matches what is observed at better resolution and without an interfering beam stop by GISAXS (Figure D4c). The vertical rods found to the left and right of the beam stop confirm a vertically aligned channel pore structure.

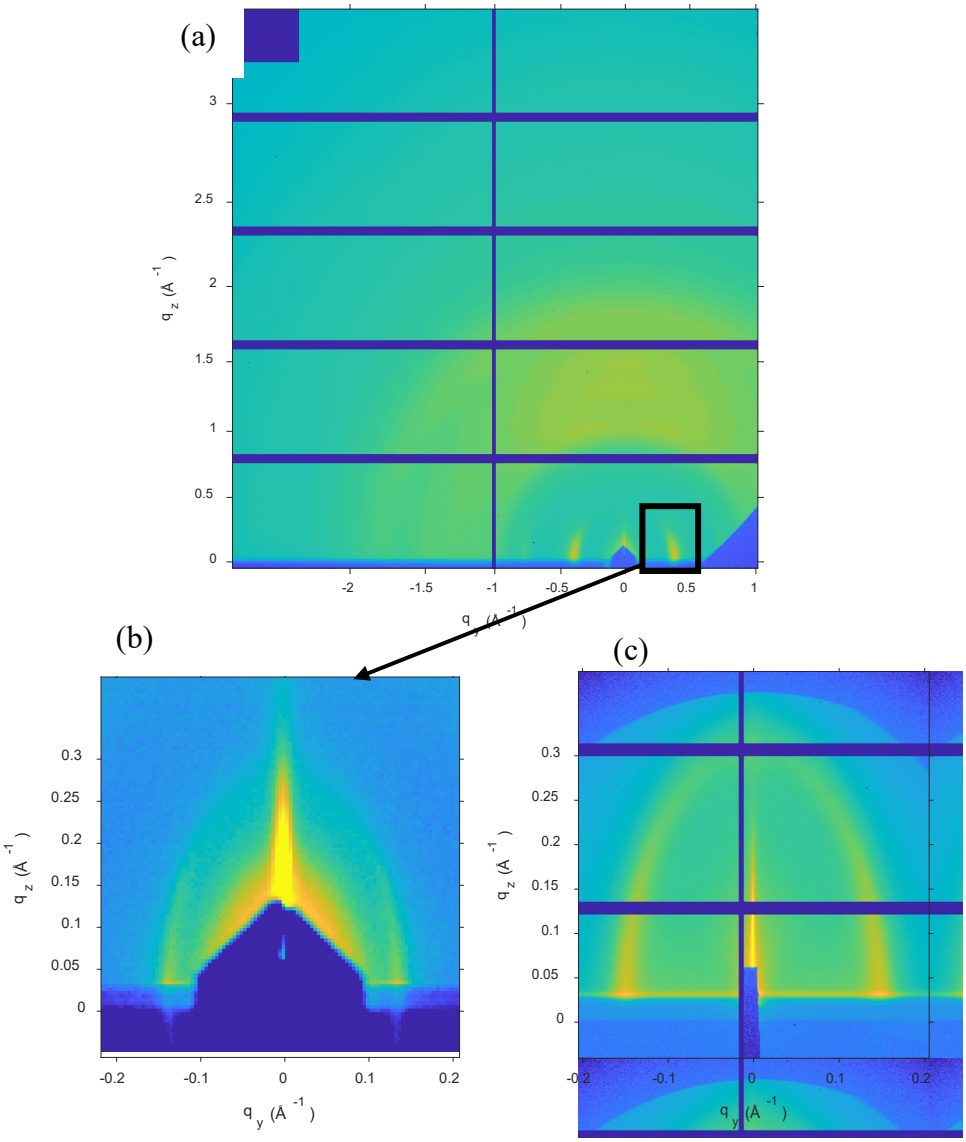

Figure D4. GIWAXS patterns of (a) [BMIM][PF_6] confined in 2.5 nm porous silica film at -103.5 °C; (b) low q region of pattern (a); and (c) GISAXS patterns of CTAB templated silica film with 2.5 nm pores

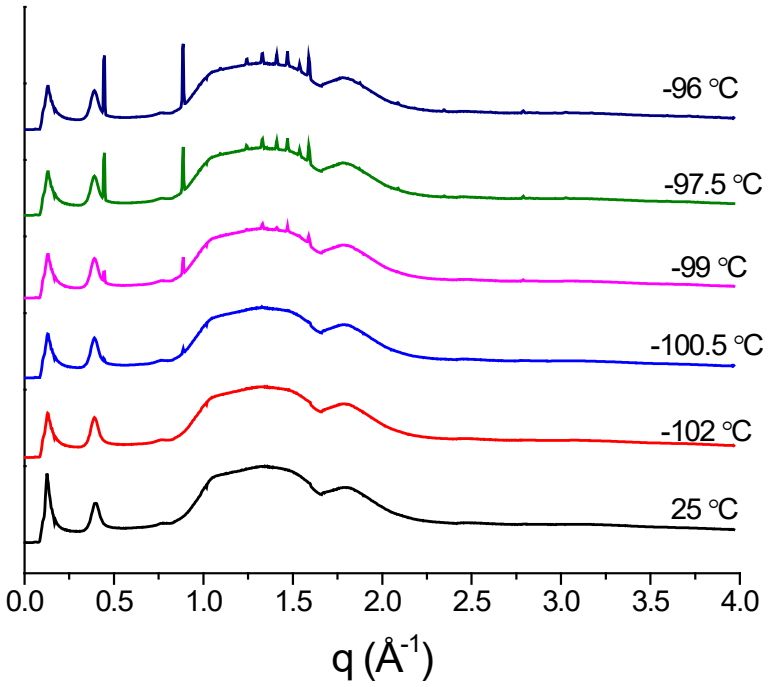

Figure D5. GIWAXS patterns of [BMIM][PF_6] confined in tethered 2.5 nm porous silica thin films from -102 °C to -96 °C with the pattern at 25 °C (melted) at the bottom showing the background with no crystallization

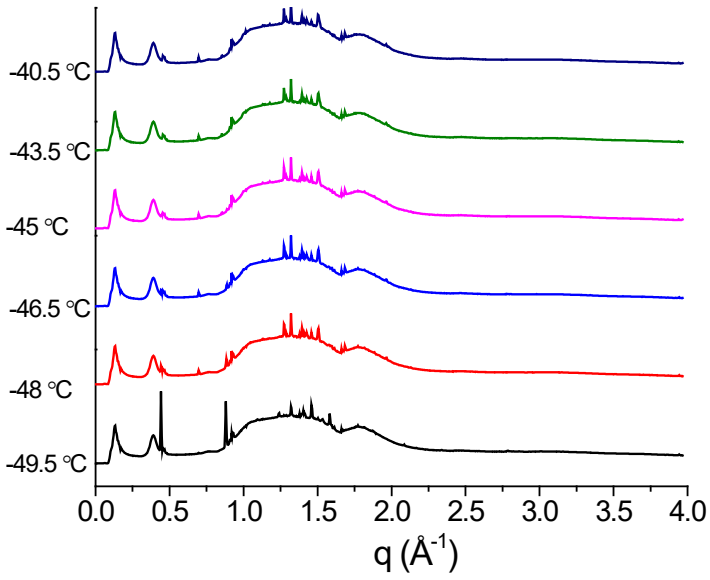

Figure D6. GIWAXS patterns of [BMIM][PF_6] confined in tethered 2.5 nm porous silica thin films from -49.5 °C to -40.5 °C showing the complete disappearance of the phase I with the two intense peaks around 0.4 and 0.8 $Å^{-1}$ at -43.5 °C

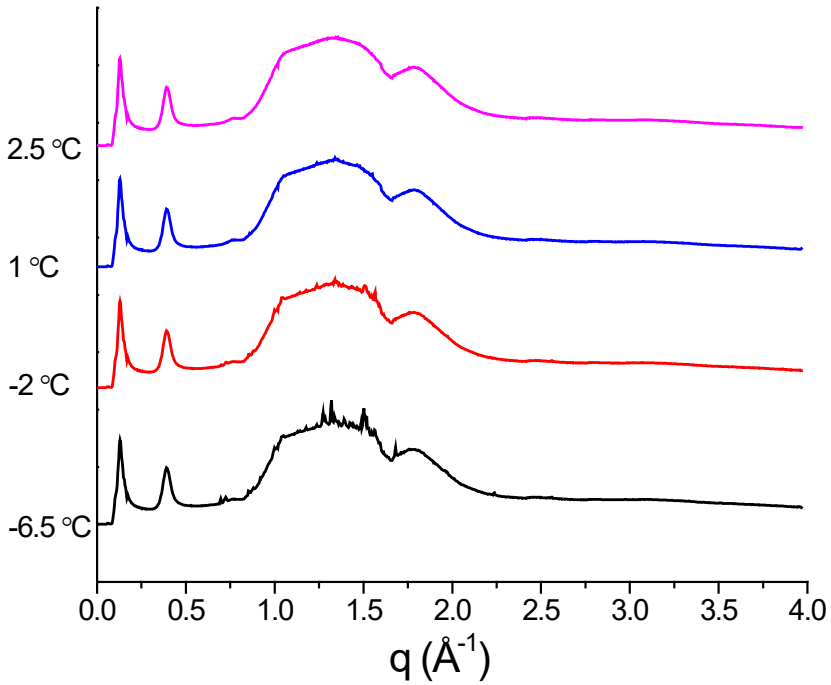

Figure D7. GIWAXS patterns of [BMIM][PF_6] confined in tethered 2.5 nm porous silica thin films from -6.5 ℃ to 2.5 ℃ showing the complete melting of phase II at 1 ℃

Crystal Structure Analysis

2D GIWAXS patterns of each samples are shown below followed by TOPAS crystallography structure refinement output files. The atomic coordinates, atom occupancy and equivalent temperature factor (B_{eq}) are fixed, so they are only listed once for both ILs.

Because of the unconventional thin film form of sample for GIWAXS measurements of nanoconfined ILs, which involve heterogeneous soft and hard materials, there are greater variations in peak intensities compared to powder patterns since some of the rings from GIWAXS patterns are not complete. Thus, during crystal refinement, greater R-values (about 30) are allowed compared to the common suggested value of 20. The 2θ values are converted from q ($Å^{-1}$) using a wavelength of 1.54 Å (Cu Kα) for easier refinement from literature crystal structure information in terms of angle. The unit cell parameters resulting from this analysis are summarized in the main text.

Unconfined [BMIM][PF_6] at -103 °C

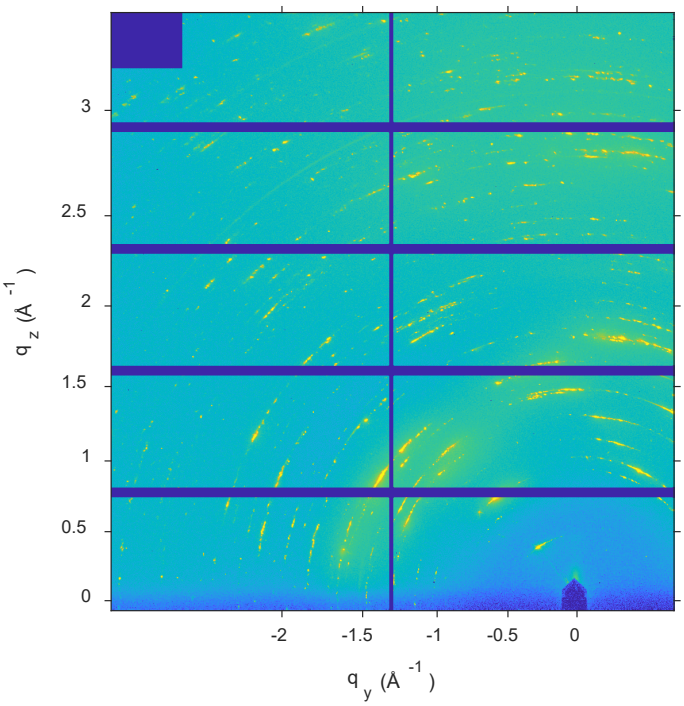

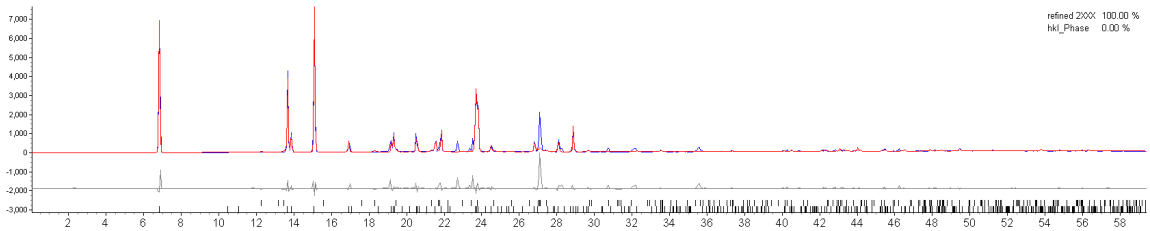

R-Values

```
Rexp : 7.19     Rwp : 29.69     Rp  : 18.68   GOF : 4.13
Rexp`: 10.36    Rwp`: 42.78     Rp` : 33.04   DW  : 1.03
```

Quantitative Analysis - Rietveld

```
   Phase 1  : "refined 2XXX"                  100.000 %
   Phase 2  : hkl_Phase                       0.000 %
```

Background

```
   Chebychev polynomial, Coefficient  0       54.00018
                                      1       49.34894
                                      2       -3.995787
                                      3       -0.568013
                                      4       -3.262048
                                      5       -3.763277
```

Instrument

```
   Primary radius (mm)                        217.5
```

Secondary radius (mm)	217.5

Corrections

Zero error	0.01670187
LP Factor	0

Structure 1

Phase name	refined 2XXX
R-Bragg	45.930
Spacegroup	P-1
Scale	3.69059398e-005
Cell Mass	568.372
Cell Volume (Å^3)	318.63200
Wt% - Rietveld	100.000
Crystallite Size	
Cry size Lorentzian (nm)	58.9
Crystal Linear Absorption Coeff. (1/cm)	50.036
Crystal Density (g/cm^3)	2.962
PVII peak type	
FWHM = a + b/Cos(Th) + c Tan(Th)	
a	0.01417506
b	0.007878899
c	0.0001
Exponent m = 0.6+ma+mb/Cos(Th)+mc/Tan(Th)	
ma	19.99996
mb	4.999994
mc	4.999981
Lattice parameters	
a (Å)	9.0784892
b (Å)	7.6703595
c (Å)	5.8971551
alpha (°)	102.5097
beta (°)	115.2332
gamma (°)	109.2292

Site	Np	x	y	z	Atom	Occ	Beq
P1	2	0.18444	0.79488	0.44901	P	1	2.199
F1	2	0.35521	0.93965	0.57091	F	1	3.237
F2	2	0.29779	0.67516	0.50853	F	1	3.869
F3	2	0.12957	0.78229	0.59432	F	1	4.256
F4	2	0.07314	0.91488	0.38757	F	1	3.664
F5	2	0.24066	0.81036	0.30242	F	1	4.295
F6	2	0.01489	0.65083	0.32406	F	1	4.035
N1	2	0.75199	0.72952	0.65019	N	1	2.132
N2	2	0.78894	0.83706	0.89274	N	1	2.187
C1	2	0.69310	0.69370	0.46853	C	1	3.182
H1A	2	0.58390	0.72160	0.41060	H	1	4.816
H1B	2	0.67150	0.58060	0.42940	H	1	4.816
H1C	2	0.78460	0.75510	0.44440	H	1	4.816
C2	2	0.70855	0.83227	0.72967	C	1	2.227
H2	2	0.63220	0.89270	0.67830	H	1	2.685
C3	2	0.86449	0.66566	0.76617	C	1	2.503
H3	2	0.91630	0.58900	0.74360	H	1	3
C4	2	0.88720	0.73249	0.91775	C	1	2.55
H4	2	0.95780	0.71150	1.02240	H	1	3.079
C5	2	0.76590	0.92927	1.02293	C	1	2.779

H5A	2	0.71160	1.01120	0.97740	H	1	3.316
H5B	2	0.88280	0.98340	1.11980	H	1	3.316
C6	2	0.65000	0.82430	1.08181	C	1	2.424
H6A	2	0.70700	0.74480	1.13030	H	1	2.921
H6B	2	0.64200	0.89010	1.17210	H	1	2.921
C7	2	0.46470	0.73904	0.94394	C	1	2.645
H7A	2	0.47170	0.66970	0.85540	H	1	3.158
H7B	2	0.40830	0.81790	0.89270	H	1	3.158
C8	2	0.35100	0.63970	1.00890	C	1	3.3
H8A	2	0.40610	0.56120	1.05940	H	1	4.974
H8B	2	0.23360	0.58560	0.91560	H	1	4.974
H8C	2	0.34000	0.70840	1.09360	H	1	4.974

Unconfined [BMIM][PF_6] at -88 °C

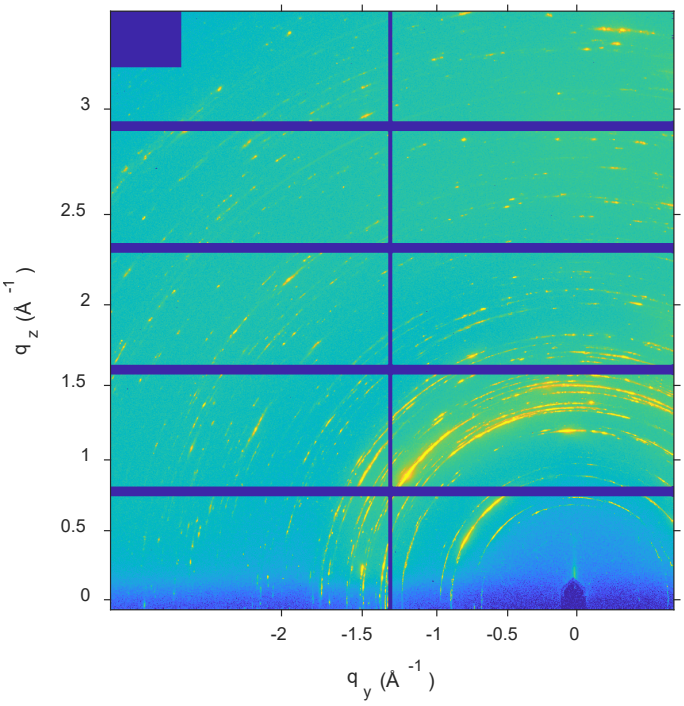

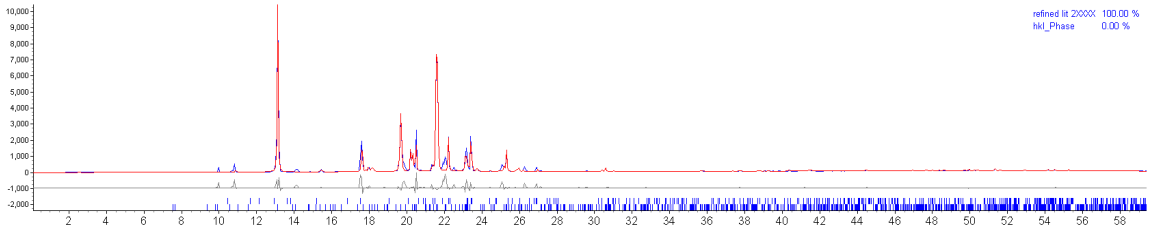

R-Values

Rexp : 3.23	Rwp : 25.19	Rp : 14.10	GOF : 7.80
Rexp`: 4.40	Rwp`: 34.37	Rp` : 23.30	DW : 1.34

Quantitative Analysis - Rietveld

Phase 1 : "refined lit 2XXXX"	100.000 %
Phase 2 : hkl_Phase	0.000 %

Background

Chebychev polynomial, Coefficient	0	56.69783
	1	56.44368
	2	-5.832474
	3	-10.62477
	4	-7.487998
	5	-3.686097

Instrument

Primary radius (mm)	217.5
Secondary radius (mm)	217.5

Corrections

Zero error	0.100127
Specimen displacement	9.842157
LP Factor	0

Structure 1

Phase name	refined lit 2XXXX
R-Bragg	21.148
Spacegroup	P-1
Scale	2.33069156e-006
Cell Mass	568.372
Cell Volume (Å^3)	543.06831
Wt% - Rietveld	100.000
Crystallite Size	
Cry size Lorentzian (nm)	9999.9
Crystal Linear Absorption Coeff. (1/cm)	29.357
Crystal Density (g/cm^3)	1.738
PVII peak type	
FWHM = a + b/Cos(Th) + c Tan(Th)	
a	0.3785677
b	0.0006103156
c	0.0001009526
Exponent m = 0.6+ma+mb/Cos(Th)+mc/Tan(Th)	
ma	19.99992
mb	4.999981
mc	4.999991
Lattice parameters	
a (Å)	8.2137512
b (Å)	8.9633556
c (Å)	8.8948718
alpha (°)	95.75617
beta (°)	118.5138
gamma (°)	103.2361

Confined [BMIM][PF_6] in 2.5 nm pores at -91 °C

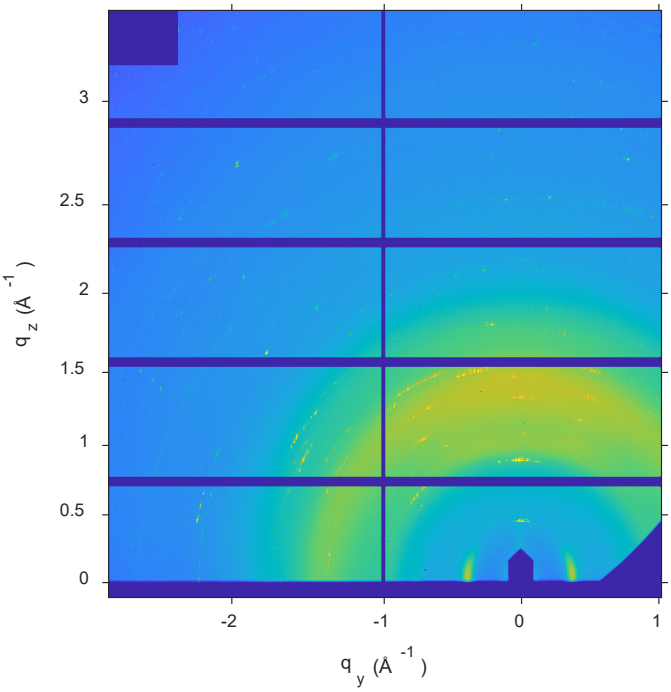

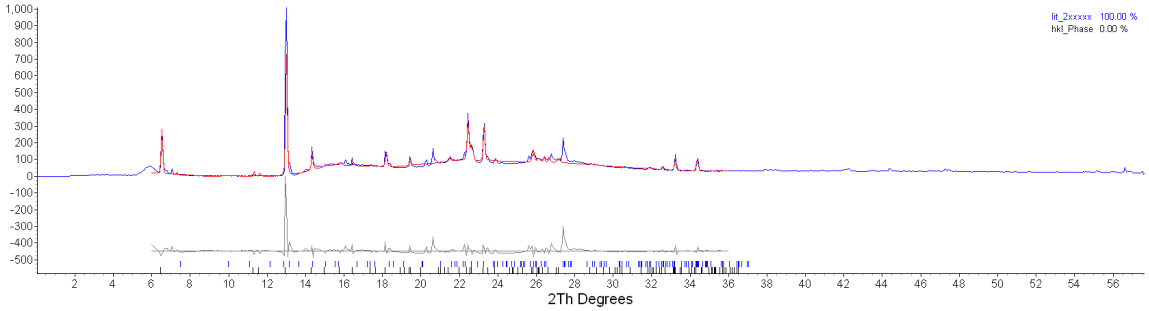

R-Values

```
Rexp : 11.03    Rwp : 23.08     Rp  : 15.21  GOF : 2.09
Rexp`: 11.38    Rwp`: 23.82     Rp` : 26.04  DW  : 1.02
```

Quantitative Analysis - Rietveld

```
   Phase 1  : lit_2xxxxx                    100.000 %
   Phase 2  : hkl_Phase                     0.000 %
```

Background

```
   Chebychev polynomial, Coefficient  0      20.15245
                                      1      22.74066
                                      2      -18.89273
                                      3      -21.22206
                                      4      12.59577
                                      5      1.905042
```

Instrument

Primary radius (mm)	217.5
Secondary radius (mm)	217.5

Corrections

Zero error	0.05894278
Specimen displacement	-0.02481741
LP Factor	0

Miscellaneous

Start X	6
Finish X	36

Structure 1

Phase name	lit_2xxxxx
R-Bragg	99.993
Spacegroup	P-1
Scale	5.68882887e-006
Cell Mass	568.372
Cell Volume (Å^3)	834.63842
Wt% - Rietveld	100.000
Crystallite Size	
Cry size Lorentzian (nm)	3.6
Crystal Linear Absorption Coeff. (1/cm)	19.102
Crystal Density (g/cm^3)	1.131
PVII peak type	
FWHM = a + b/Cos(Th) + c Tan(Th)	
a	0.001135905
b	0.0008336294
c	0.0001
Exponent m = 0.6+ma+mb/Cos(Th)+mc/Tan(Th)	
ma	0.1015895
mb	0.1029966
mc	0.002438917
Lattice parameters	
a (Å)	8.0010524
b (Å)	11.8101211
c (Å)	8.8859681
alpha (°)	86.47793
beta (°)	94.669
gamma (°)	92.55243

Confined [BMIM][PF_6] in 2.5 nm pores at -84 °C

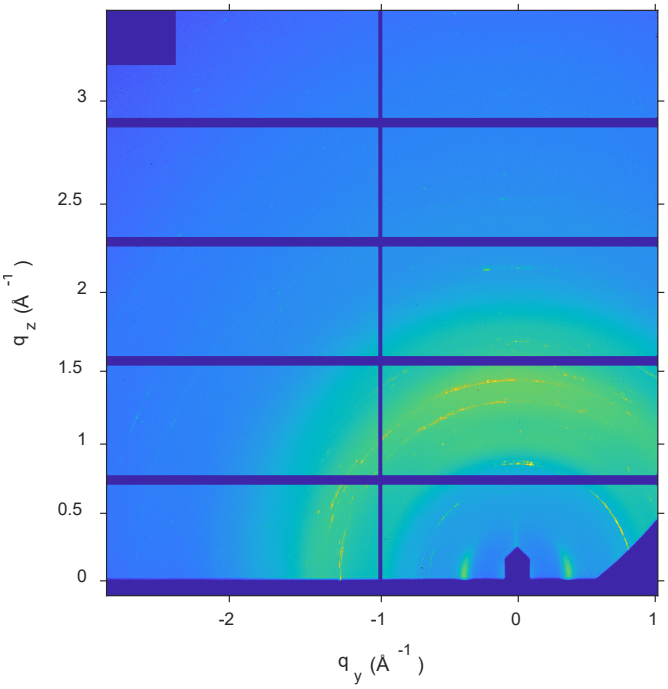

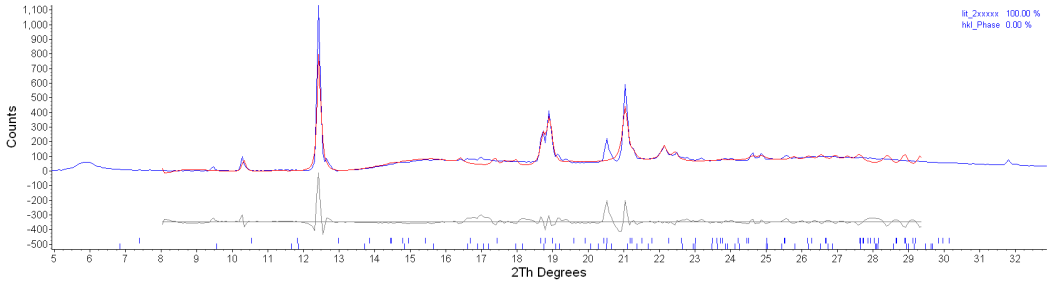

R-Values

Rexp : 10.05	Rwp : 27.05	Rp : 16.83	GOF : 2.69
Rexp`: 2.14	Rwp`: 5.75	Rp` : 7.02	DW : 0.76

Quantitative Analysis - Rietveld

Phase 1 : hkl_Phase	0.000 %
Phase 2 : lit_2xxxxx	100.000 %

Background

Chebychev polynomial, Coefficient	0	-108.6482
	1	62.89484
	2	-2.236589
	3	4.033432
	4	-38.1332
	5	1.047605

Instrument

Primary radius (mm)	217.5
Secondary radius (mm)	217.5

Corrections

Zero error	0.3497134
Specimen displacement	-0.7898925
LP Factor	0

Miscellaneous

Start X	8

Structure 2

Phase name	lit_2xxxxx
R-Bragg	99.997
Spacegroup	P-1
Scale	0.00031627151
Cell Mass	568.372
Cell Volume (Å^3)	723.43157
Wt% - Rietveld	100.000
Crystallite Size	
Cry size Lorentzian (nm)	7.8
Crystal Linear Absorption Coeff. (1/cm)	22.038
Crystal Density (g/cm^3)	1.305
PVII peak type	
FWHM = a + b/Cos(Th) + c Tan(Th)	
a	0.575721
b	0.5656161
c	0.9999999
Exponent m = 0.6+ma+mb/Cos(Th)+mc/Tan(Th)	
ma	0.0001
mb	0.0001
mc	0.06907023
Lattice parameters	
a (Å)	7.1088386
b (Å)	8.8532715
c (Å)	13.3699974
alpha (°)	91.67198
beta (°)	114.7952
gamma (°)	106.1454

Confined [BMIM][PF_6] in 8 nm pores at -130 °C

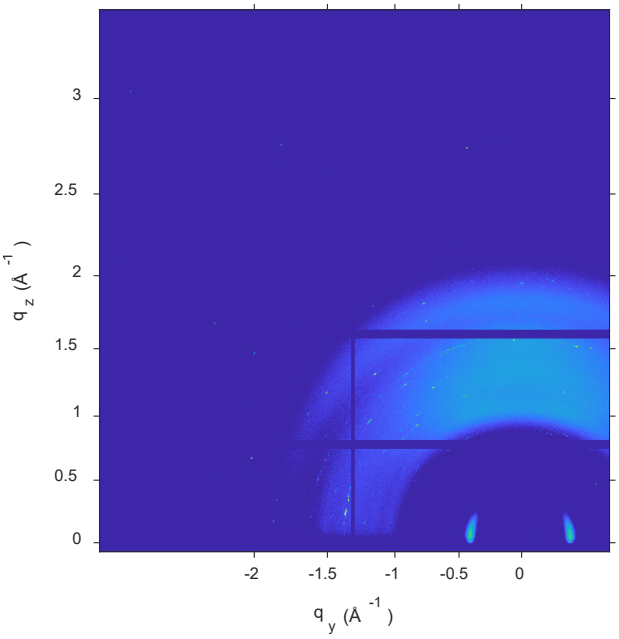

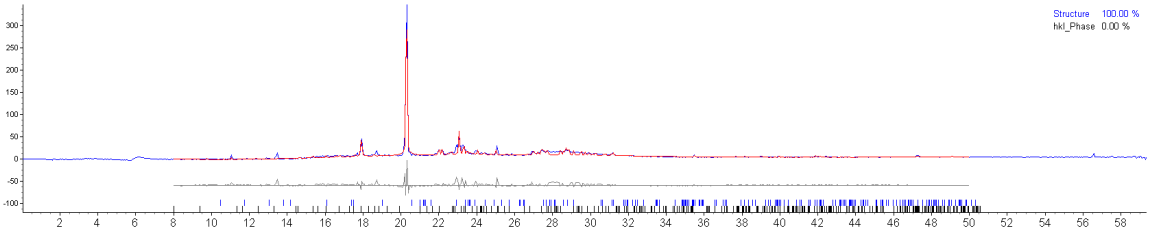

R-Values

Rexp : 26.10	Rwp : 25.31	Rp : 17.65	GOF : 0.97
Rexp`: 53.89	Rwp`: 52.24	Rp` : 45.77	DW : 1.26

Quantitative Analysis - Rietveld

Phase 1 : hkl_Phase	0.000 %
Phase 2 : Structure	100.000 %

Background

Chebychev polynomial, Coefficient	0	4.300214
	1	1.907978
	2	-2.885172
	3	1.461686
	4	1.470159
	5	-1.30142

Instrument

Primary radius (mm)	217.5
Secondary radius (mm)	217.5

Corrections

Zero error	-0.6966527

LP Factor	0

Miscellaneous

Start X	8
Finish X	50

Structure 2

Phase name	Structure
R-Bragg	99.872
Spacegroup	P-1
Scale	5.54053237e-008
Cell Mass	568.372
Cell Volume (Å^3)	507.90148
Wt% - Rietveld	100.000
Crystallite Size	
Cry size Lorentzian (nm)	2959.2
Crystal Linear Absorption Coeff. (1/cm)	31.390
Crystal Density (g/cm^3)	1.858
Lattice parameters	
a (Å)	7.7730522
b (Å)	8.8879274
c (Å)	8.4929573
alpha (°)	96.83687
beta (°)	114.3848
gamma (°)	102.2719

Confined [BMIM][PF_6] in 8 nm pores at -61 °C

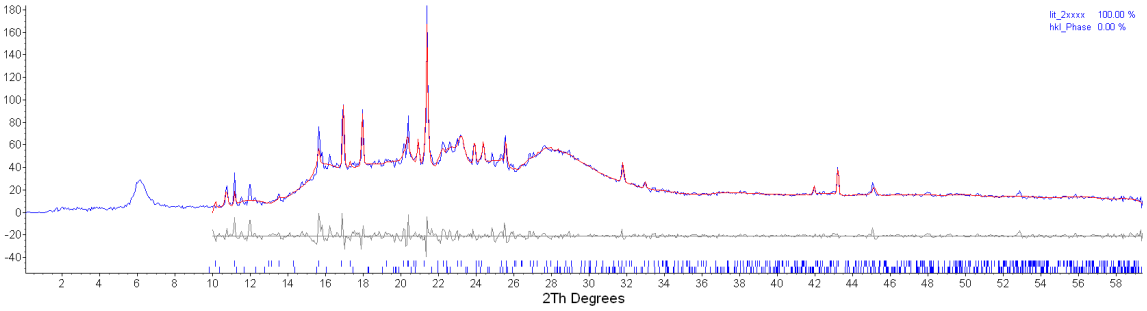

R-Values

Rexp : 11.30	Rwp : 8.89	Rp : 5.51	GOF : 0.79
Rexp`: 6.48	Rwp`: 5.10	Rp` : 4.55	DW : 1.46

Quantitative Analysis - Rietveld

Phase 1 : hkl_Phase	0.000 %
Phase 2 : lit_2xxxx	100.000 %

Background

One on X		98.00818
Chebychev polynomial, Coefficient	0	-12.84894
	1	30.66952
	2	-20.87548
	3	11.76158
	4	-4.900315
	5	-4.516647

Instrument

Primary radius (mm)	217.5
Secondary radius (mm)	217.5

Corrections

Zero error	0.3000172
Specimen displacement	0.5639539
LP Factor	0

Miscellaneous

Start X	10

Structure 2

Phase name	lit_2xxxx
R-Bragg	99.940
Spacegroup	P-1
Scale	5.16027343e-007
Cell Mass	568.372
Cell Volume (Å^3)	538.55715
Wt% - Rietveld	100.000

Crystallite Size	
Cry size Lorentzian (nm)	166.7
Crystal Linear Absorption Coeff. (1/cm)	29.603
Crystal Density (g/cm^3)	1.752
PVII peak type	
FWHM = a + b/Cos(Th) + c Tan(Th)	
a	0.004504127
b	0.004481975
c	0.0004105741
Exponent m = 0.6+ma+mb/Cos(Th)+mc/Tan(Th)	
ma	0.0001
mb	0.0001
mc	1.289897
Lattice parameters	
a (Å)	7.5570020
b (Å)	9.2197380
c (Å)	9.0001039
alpha (°)	97.12184
beta (°)	114.8494
gamma (°)	102.6104

Site	Np	x	y	z	Atom	Occ	Beq
P1	2	0.18444	0.79488	0.44901	P	1	2.199
F1	2	0.35521	0.93965	0.57091	F	1	3.237
F2	2	0.29779	0.67516	0.50853	F	1	3.869
F3	2	0.12957	0.78229	0.59432	F	1	4.256
F4	2	0.07314	0.91488	0.38757	F	1	3.664
F5	2	0.24066	0.81036	0.30242	F	1	4.295
F6	2	0.01489	0.65083	0.32406	F	1	4.035
N1	2	0.75199	0.72952	0.65019	N	1	2.132
N2	2	0.78894	0.83706	0.89274	N	1	2.187
C1	2	0.69310	0.69370	0.46853	C	1	3.182
H1A	2	0.58390	0.72160	0.41060	H	1	4.816
H1B	2	0.67150	0.58060	0.42940	H	1	4.816
H1C	2	0.78460	0.75510	0.44440	H	1	4.816
C2	2	0.70855	0.83227	0.72967	C	1	2.227
H2	2	0.63220	0.89270	0.67830	H	1	2.685
C3	2	0.86449	0.66566	0.76617	C	1	2.503
H3	2	0.91630	0.58900	0.74360	H	1	3
C4	2	0.88720	0.73249	0.91775	C	1	2.55
H4	2	0.95780	0.71150	1.02240	H	1	3.079
C5	2	0.76590	0.92927	1.02293	C	1	2.779
H5A	2	0.71160	1.01120	0.97740	H	1	3.316
H5B	2	0.88280	0.98340	1.11980	H	1	3.316
C6	2	0.65000	0.82430	1.08181	C	1	2.424
H6A	2	0.70700	0.74480	1.13030	H	1	2.921
H6B	2	0.64200	0.89010	1.17210	H	1	2.921
C7	2	0.46470	0.73904	0.94394	C	1	2.645
H7A	2	0.47170	0.66970	0.85540	H	1	3.158
H7B	2	0.40830	0.81790	0.89270	H	1	3.158
C8	2	0.35100	0.63970	1.00890	C	1	3.3
H8A	2	0.40610	0.56120	1.05940	H	1	4.974
H8B	2	0.23360	0.58560	0.91560	H	1	4.974
H8C	2	0.34000	0.70840	1.09360	H	1	4.974

Confined [BMIM][PF_6] in 8 nm pores at 0.5 °C

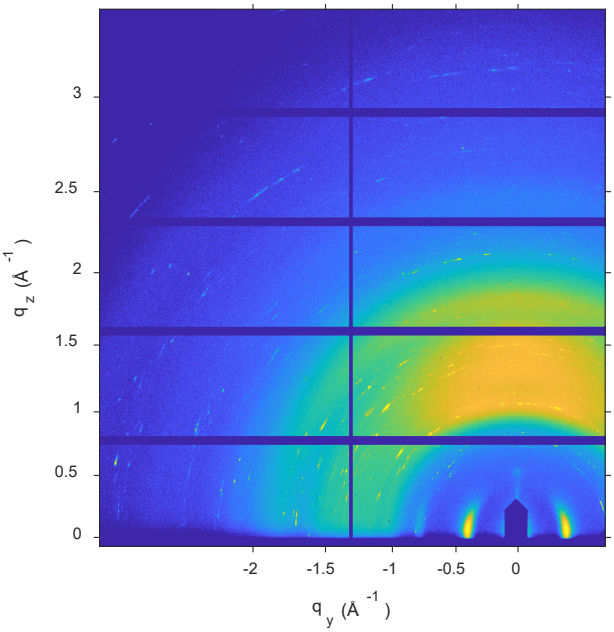

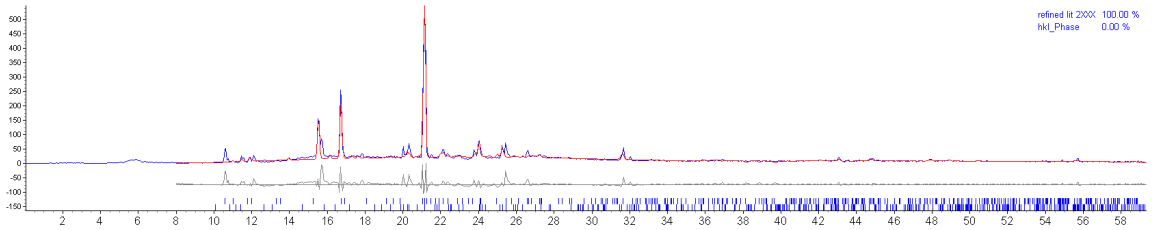

R-Values

Rexp : 17.77	Rwp : 25.05	Rp : 17.59	GOF : 1.41
Rexp`: 30.85	Rwp`: 43.49	Rp` : 37.88	DW : 1.05

Quantitative Analysis - Rietveld

Phase 1 : hkl_Phase	0.000 %
Phase 2 : "refined lit 2XXX"	100.000 %

Background

Chebychev polynomial, Coefficient	0	8.245037
	1	-3.276262
	2	-4.213524
	3	7.762794
	4	-1.826303
	5	-3.068859

Instrument

Primary radius (mm)	217.5
Secondary radius (mm)	217.5

Corrections

Zero error	0.8810527
LP Factor	0

Miscellaneous

Start X	8

Structure 2

Phase name	refined lit 2XXX
R-Bragg	17.724
Spacegroup	P-1
Scale	1.78411767e-006
Cell Mass	568.372
Cell Volume (Å^3)	592.27633
Wt% - Rietveld	100.000
Crystallite Size	
Cry size Lorentzian (nm)	10000.0
Crystal Linear Absorption Coeff. (1/cm)	26.918
Crystal Density (g/cm^3)	1.594
PVII peak type	
FWHM = a + b/Cos(Th) + c Tan(Th)	
a	0.0298965
b	0.01624297
c	0.02230486
Exponent m = 0.6+ma+mb/Cos(Th)+mc/Tan(Th)	
ma	20
mb	5
mc	5
Lattice parameters	
a (Å)	8.6283531
b (Å)	8.7861253
c (Å)	9.0291505
alpha (°)	95.67048
beta (°)	114.379
gamma (°)	103.2429

Confined [BMIM][PF_6] in 2.5 nm pores with [TMS-MIM][Cl] tethering at -49.5 °C

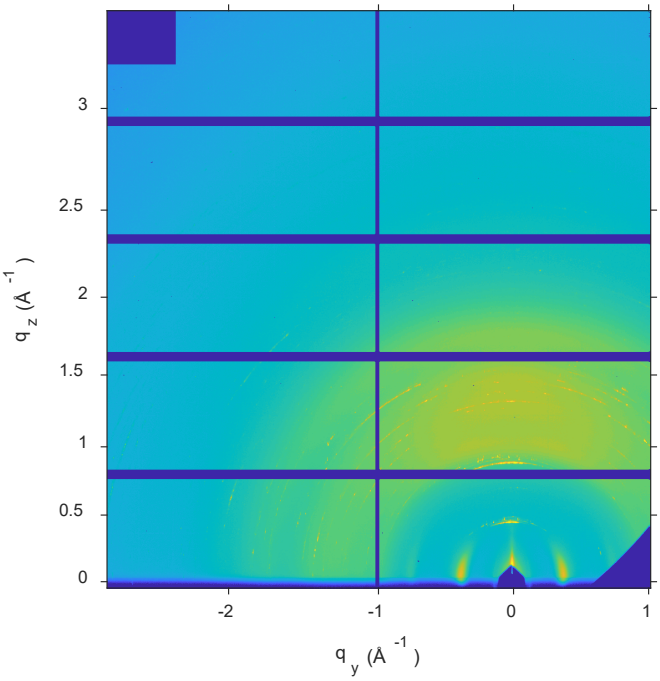

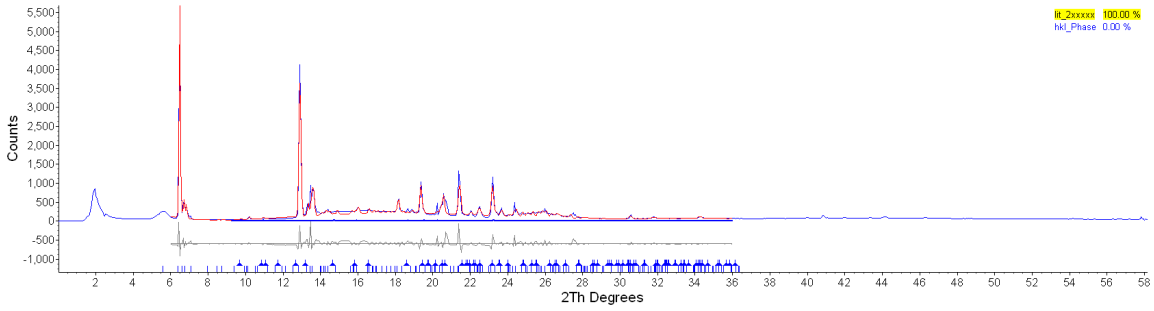

R-Values

```
Rexp : 5.36     Rwp : 19.90     Rp  : 14.44   GOF : 3.71
Rexp`: 9.29     Rwp`: 34.51     Rp` : 29.61   DW  : 1.34
```

Quantitative Analysis - Rietveld

```
   Phase 1  : lit_2xxxxx                      100.000 %
   Phase 2  : hkl_Phase                       0.000 %
```

Background

```
   Chebychev polynomial, Coefficient  0       98.57399
                                      1       -11.32461
                                      2       -47.71616
                                      3       16.83724
                                      4       36.52009
                                      5       -38.94331
```

Instrument

```
   Primary radius (mm)                        217.5
```

Secondary radius (mm)	217.5

Corrections

Zero error	0.03551109
Specimen displacement	-0.1071728
LP Factor	0

Miscellaneous

Start X	6
Finish X	36

Structure 1

Phase name	lit_2xxxxx
R-Bragg	17.463
Spacegroup	P-1
Scale	2.12492909e-006
Cell Mass	568.372
Cell Volume (Å^3)	682.16180
Wt% - Rietveld	100.000
Crystallite Size	
Cry size Lorentzian (nm)	10000.0
Crystal Linear Absorption Coeff. (1/cm)	23.371
Crystal Density (g/cm^3)	1.384
PVII peak type	
FWHM = a + b/Cos(Th) + c Tan(Th)	
a	0.01222944
b	0.01039967
c	0.0001000001
Exponent m = 0.6+ma+mb/Cos(Th)+mc/Tan(Th)	
ma	20
mb	5
mc	5
Lattice parameters	
a (Å)	9.0242117
b (Å)	9.4764987
c (Å)	9.0506408
alpha (°)	94.63928
beta (°)	113.6794
gamma (°)	101.8333

Confined [BMIM][PF_6] in 2.5 nm pores with [TMS-MIM][Cl] tethering at -28.5 °C

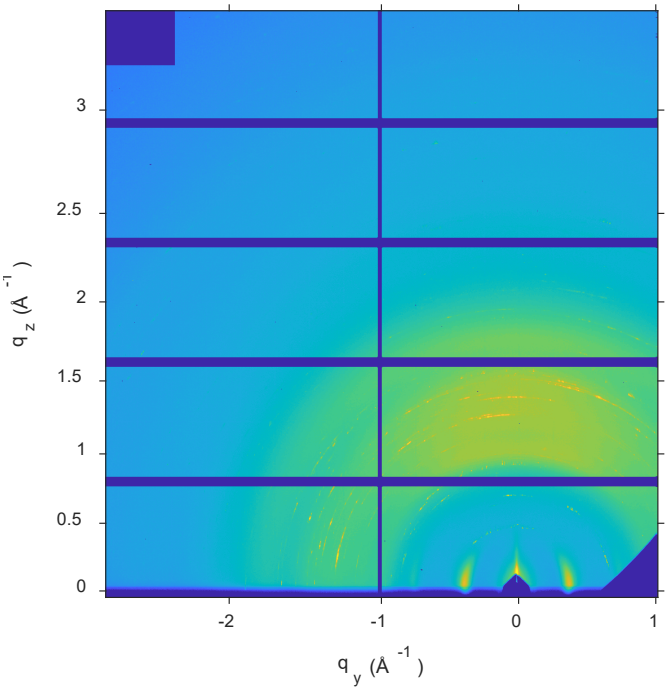

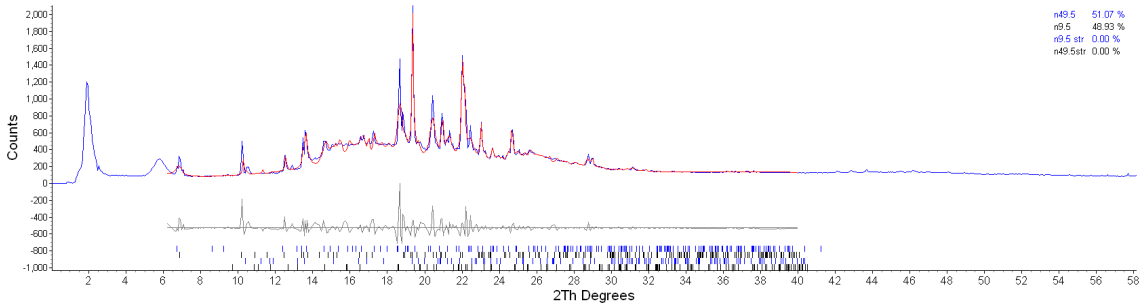

R-Values

```
Rexp : 3.43     Rwp : 11.69     Rp  : 7.67    GOF : 3.41
Rexp`: 6.64     Rwp`: 22.65     Rp` : 16.73   DW  : 1.43
```

Quantitative Analysis - Rietveld

```
   Phase 1  : n49.5                          51.069 %
   Phase 2  : n9.5                           48.931 %
   Phase 3  : "n9.5 str"                     0.000 %
   Phase 4  : n49.5str                       0.000 %
```

Background

```
   Chebychev polynomial, Coefficient  0      140.9702
                                      1      14.24338
                                      2      -42.52262
                                      3      15.19745
                                      4      20.63974
                                      5      -19.61057
```

Instrument

Primary radius (mm)	217.5
Secondary radius (mm)	217.5

Corrections

Zero error	0.06335782
Specimen displacement	-0.07219221
LP Factor	0

Miscellaneous

Start X	6.2
Finish X	40

hkl Phase - 1 Pawley method

Phase name	n49.5
R-Bragg	1.458
Spacegroup	P-1
Cell Mass	568.372
Cell Volume (Å^3)	952.30732
Wt% - Rietveld	51.069
Crystallite Size	
Cry size Lorentzian (nm)	27.9
PVII peak type	
FWHM = a + b/Cos(Th) + c Tan(Th)	
a	0.01135947
b	0.01157184
c	0.009452699
Exponent m = 0.6+ma+mb/Cos(Th)+mc/Tan(Th)	
ma	20
mb	5
mc	5
Lattice parameters	
a (Å)	6.7339958
b (Å)	10.7386826
c (Å)	15.2708756
alpha (°)	106.548
beta (°)	115.4356
gamma (°)	87.31875

hkl Phase - 2 Pawley method

Phase name	n9.5
R-Bragg	1.355
Spacegroup	P-1
Cell Mass	568.372
Cell Volume (Å^3)	914.12259
Wt% - Rietveld	48.931
Crystallite Size	
Cry size Lorentzian (nm)	10000.0
PVII peak type	
FWHM = a + b/Cos(Th) + c Tan(Th)	
a	0.02343934
b	0.001744159
c	0.1141426
Exponent m = 0.6+ma+mb/Cos(Th)+mc/Tan(Th)	
ma	0.03117285
mb	0.02913543
mc	0.0001

Lattice parameters	
a (Å)	9.1328053
b (Å)	7.9551910
c (Å)	13.3192964
alpha (°)	83.71658
beta (°)	78.62794
gamma (°)	102.5739

Confined [BMIM][PF_6] in 2.5 nm pores with [TSMIM][Cl] tethering at -9.5 °C

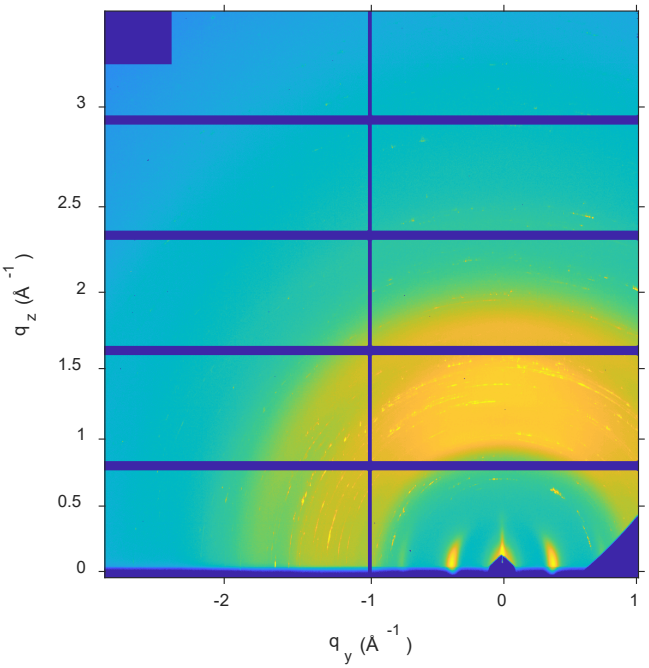

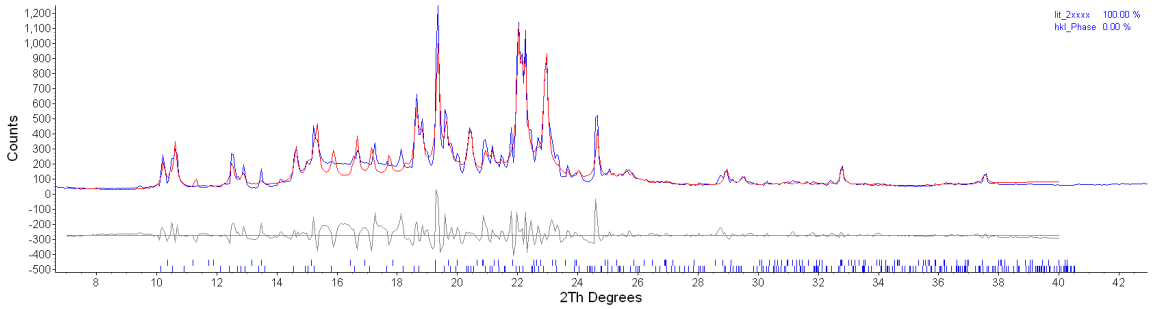

R-Values

Rexp : 6.14	Rwp : 19.71	Rp : 15.30	GOF : 3.21
Rexp` : 8.13	Rwp` : 26.12	Rp` : 21.27	DW : 1.15

Quantitative Analysis - Rietveld

Phase 1 : hkl_Phase	0.000 %
Phase 2 : lit_2xxxx	100.000 %

Background

Chebychev polynomial, Coefficient	0	44.70588
	1	22.50044
	2	6.337499
	3	7.557339
	4	10.46497
	5	-9.069654

Instrument

Primary radius (mm)	217.5
Secondary radius (mm)	217.5

Corrections

Zero error	0.0514826
Specimen displacement	-0.06454349
LP Factor	0

Miscellaneous

Start X	7
Finish X	40

Structure 2

Phase name	lit_2xxxx
R-Bragg	14.973
Spacegroup	P-1
Scale	5.63425085e-006
Cell Mass	568.372
Cell Volume (Å^3)	602.09058
Wt% - Rietveld	100.000
Crystallite Size	
Cry size Lorentzian (nm)	10000.0
Crystal Linear Absorption Coeff. (1/cm)	26.479
Crystal Density (g/cm^3)	1.568
PVII peak type	
FWHM = a + b/Cos(Th) + c Tan(Th)	
a	0.01894677
b	0.01380774
c	0.0001001927
Exponent m = 0.6+ma+mb/Cos(Th)+mc/Tan(Th)	
ma	19.99852
mb	4.99998
mc	0.0001173348
Lattice parameters	
a (Å)	8.7345916
b (Å)	8.9725120
c (Å)	8.9445080
alpha (°)	95.77493
beta (°)	115.3017
gamma (°)	102.9492

Confined [BMIM][PF_6] in 8 nm pores with [TSMIM][Cl] tethering at 25 °C

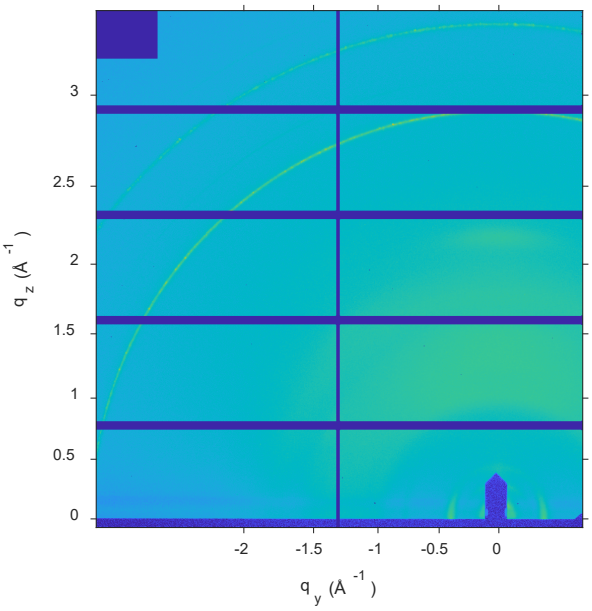

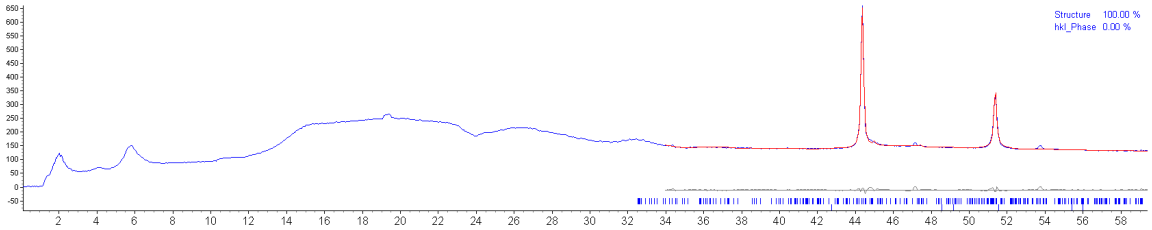

R-Values

Rexp : 7.79	Rwp : 1.42	Rp : 0.94	GOF : 0.18
Rexp`: 43.18	Rwp`: 7.87	Rp` : 8.41	DW : 0.82

Quantitative Analysis - Rietveld

Phase 1 : hkl_Phase	0.000 %
Phase 2 : Structure	100.000 %

Background

Chebychev polynomial, Coefficient	0	132.8134
	1	-1.5377
	2	1.456767
	3	-3.316805
	4	3.711253
	5	-2.715081

Instrument

Primary radius (mm)	217.5
Secondary radius (mm)	217.5

Corrections

Zero error	0.5587051

Specimen displacement	9.864444
LP Factor	0

Miscellaneous

Start X	34

Structure 2

Phase name	Structure
R-Bragg	0.178
Spacegroup	P-1
Scale	0.000146075982
Cell Mass	568.372
Cell Volume (Å^3)	606.12720
Wt% - Rietveld	100.000
Crystallite Size	
Cry size Lorentzian (nm)	10000.0
Crystal Linear Absorption Coeff. (1/cm)	26.303
Crystal Density (g/cm^3)	1.557
Preferred Orientation (Dir 1 : 0 1 0)	4.474878
(Dir 2 : 0 0 1)	0.8740383
Fraction of Dir 1	0.2149738
PVII peak type	
FWHM = a + b/Cos(Th) + c Tan(Th)	
a	0.6849915
b	0.0001
c	0.0001
Exponent m = 0.6+ma+mb/Cos(Th)+mc/Tan(Th)	
ma	0.5428876
mb	0.04136159
mc	0.1143809
Lattice parameters	
a (Å)	8.6076528
b (Å)	9.1331851
c (Å)	9.0189785
alpha (°)	94.59697
beta (°)	116.3858
gamma (°)	102.8464

Unconfined [BMIM][Cl] at -120 °C

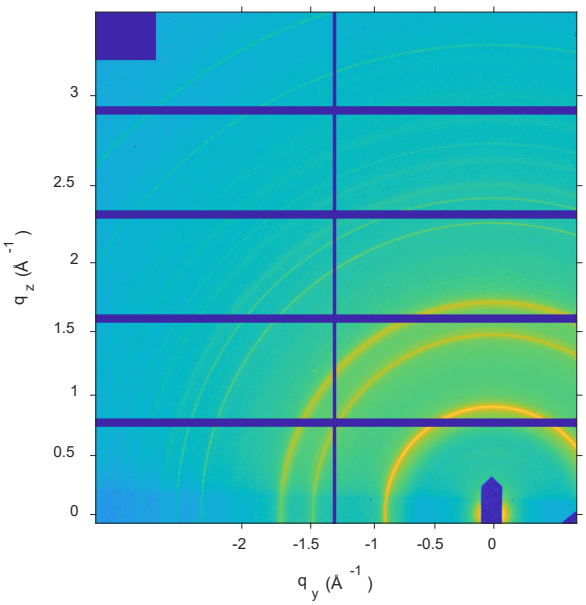

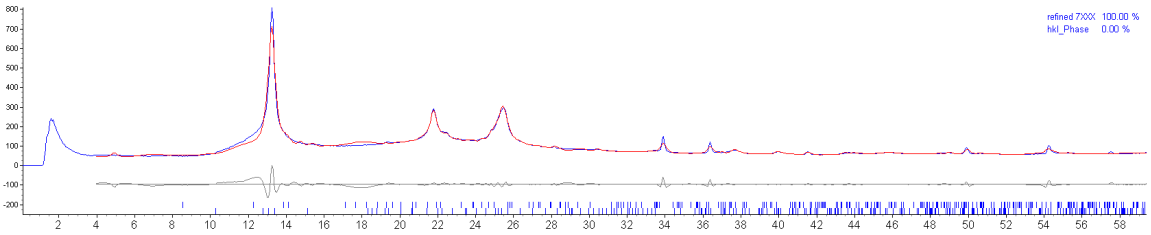

R-Values

Rexp : 8.65	Rwp : 6.93	Rp : 4.55	GOF : 0.80
Rexp`: 17.86	Rwp`: 14.31	Rp` : 10.43	DW : 0.25

Quantitative Analysis - Rietveld

Phase 1 : "refined 7XXX"	100.000 %
Phase 2 : hkl_Phase	0.000 %

Background

Chebychev polynomial, Coefficient	0	51.68264
	1	0.4023822
	2	0.1061073
	3	17.41088
	4	1.017197
	5	-5.837033

Instrument

Primary radius (mm)	217.5
Secondary radius (mm)	217.5

Corrections

Zero error	-0.05961568

Specimen displacement	10.07343
LP Factor	0

Miscellaneous

Start X	4

Structure 1

Phase name	refined 7XXX
R-Bragg	3.558
Spacegroup	P121/c1
Scale	3.80217761e-005
Cell Mass	698.695
Cell Volume (Å^3)	921.50462
Wt% - Rietveld	100.000
Crystallite Size	
Cry size Lorentzian (nm)	133.5
Crystal Linear Absorption Coeff. (1/cm)	31.848
Crystal Density (g/cm^3)	1.259
PVII peak type	
FWHM = a + b/Cos(Th) + c Tan(Th)	
a	0.3279577
b	0.3933629
c	1
Exponent m = 0.6+ma+mb/Cos(Th)+mc/Tan(Th)	
ma	0.0001
mb	0.0001
mc	4.999876
Lattice parameters	
a (Å)	11.4360533
b (Å)	10.0455773
c (Å)	8.8659273
beta (°)	115.2121

Site	Np	x	y	z	Atom	Occ	Beq
Cl1	4	0.25933	0.93049	0.09179	Cl	1	2.497
N1	4	1.07017	1.23886	0.76809	N	1	2.108
N3	4	1.31620	1.23743	0.91922	N	1	2.234
C2	4	1.18618	1.18274	0.88524	C	1	2.203
H2A	4	1.17680	1.11720	0.92900	H	1	2.369
C4	4	1.28205	1.33185	0.81932	C	1	2.4
H4A	4	1.35910	1.38210	0.82440	H	1	2.211
C5	4	1.12898	1.33249	0.72513	C	1	2.4
H5A	4	1.06240	1.37970	0.64300	H	1	2.606
C6	4	1.46890	1.20101	1.04160	C	1	2.985
H6A	4	1.45300	1.13160	1.09300	H	1	3.869
H6B	4	1.51600	1.26300	1.11500	H	1	3.79
H6C	4	1.53200	1.18170	0.99700	H	1	3.395
C7	4	0.90937	1.19944	0.68494	C	1	2.345
H7A	4	0.84950	1.26660	0.64200	H	1	2.685
H7B	4	0.88560	1.16560	0.75830	H	1	2.211
C8	4	0.88476	1.11324	0.55573	C	1	2.55
H8A	4	0.92310	1.14780	0.49000	H	1	2.921
H8B	4	0.94400	1.04370	0.60430	H	1	3
C9	4	0.71679	1.07988	0.45557	C	1	2.677
H9A	4	0.66020	1.14840	0.40420	H	1	2.685
H9B	4	0.67460	1.05250	0.52900	H	1	3

C10	4	0.69530	0.98570	0.33600	C	1	3.293
H10A	4	0.59100	0.96560	0.28000	H	1	4.974
H10B	4	0.75400	0.91500	0.39000	H	1	4.106
H10C	4	0.73700	1.01620	0.26300	H	1	3.869

Unconfined [BMIM][Cl] at 39 °C

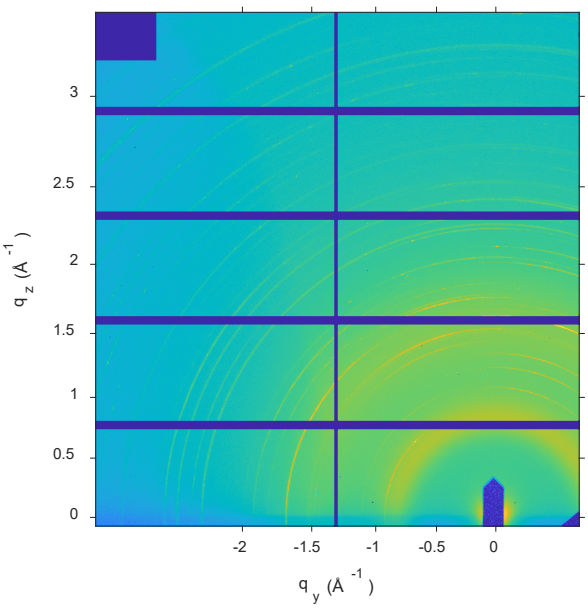

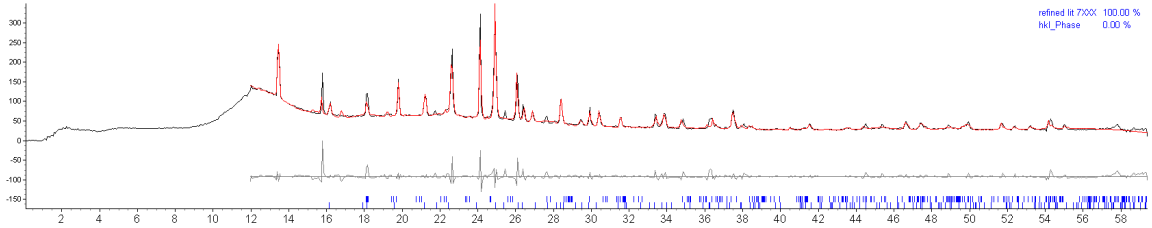

R-Values

Rexp : 11.28	Rwp : 10.02	Rp : 5.93	GOF : 0.89
Rexp`: 19.39	Rwp`: 17.23	Rp` : 11.76	DW : 1.51

Quantitative Analysis - Rietveld

Phase 1 : "refined lit 7XXX"	100.000 %
Phase 2 : hkl_Phase	0.000 %

Background

Chebychev polynomial, Coefficient	0	33.60476
	1	-21.46655
	2	22.57512
	3	-19.55366
	4	17.4492
	5	-13.76617

Instrument

Primary radius (mm)	217.5
Secondary radius (mm)	217.5

Corrections

Zero error	-0.1410659

Specimen displacement	10.26973
LP Factor	0

Miscellaneous

Start X	12

Structure 1

Phase name	refined lit 7XXX
R-Bragg	7.058
Spacegroup	P121/c1
Scale	1.17717394e-006
Cell Mass	698.695
Cell Volume (Å^3)	995.81316
Wt% - Rietveld	100.000
Crystallite Size	
Cry size Lorentzian (nm)	10000.0
Crystal Linear Absorption Coeff. (1/cm)	29.472
Crystal Density (g/cm^3)	1.165
PVII peak type	
FWHM = a + b/Cos(Th) + c Tan(Th)	
a	0.03372325
b	0.01503503
c	0.0001
Exponent m = 0.6+ma+mb/Cos(Th)+mc/Tan(Th)	
ma	20
mb	5
mc	5
Lattice parameters	
a (Å)	9.8734476
b (Å)	11.9506552
c (Å)	9.7346505
beta (°)	119.8932

Confined [BMIM][Cl] in 8 nm pores at -140 °C

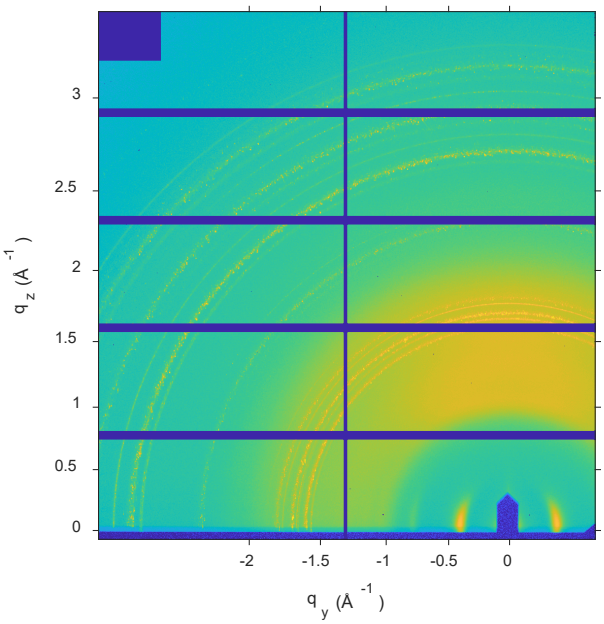

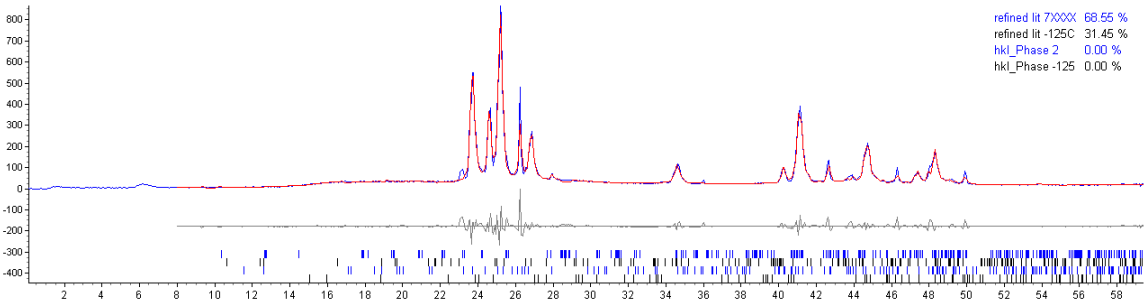

R-Values

```
Rexp : 11.51    Rwp : 13.07    Rp  : 9.28    GOF : 1.14
Rexp`: 16.02    Rwp`: 18.19    Rp` : 14.13   DW  : 1.29
```

Quantitative Analysis - Rietveld

```
   Phase 1  : "refined lit 7XXXX"          68.550 %
   Phase 2  : "hkl_Phase 2"                0.000 %
   Phase 3  : "refined lit -125C"          31.450 %
   Phase 4  : "hkl_Phase -125"             0.000 %
```

Background

```
   Chebychev polynomial, Coefficient  0     14.41823
                                      1     6.877887
                                      2     -7.418925
                                      3     4.886992
                                      4     3.021348
                                      5     -2.508542
```

Instrument

Primary radius (mm)	217.5
Secondary radius (mm)	217.5

Corrections

Zero error	-0.3487128
Specimen displacement	10.25972
LP Factor	0

Miscellaneous

Start X	8

Structure 1

Phase name	refined lit 7XXXX
R-Bragg	1.530
Spacegroup	P121/c1
Scale	9.48299318e-006
Cell Mass	698.695
Cell Volume (Å^3)	1017.08730
Wt% - Rietveld	68.550
Crystallite Size	
Cry size Lorentzian (nm)	21.0
Crystal Linear Absorption Coeff. (1/cm)	28.855
Crystal Density (g/cm^3)	1.141
PVII peak type	
FWHM = a + b/Cos(Th) + c Tan(Th)	
a	0.03486916
b	0.03423211
c	1
Exponent m = 0.6+ma+mb/Cos(Th)+mc/Tan(Th)	
ma	0.0001
mb	0.0001
mc	0.007677142
Lattice parameters	
a (Å)	9.8475827
b (Å)	12.2232233
c (Å)	9.7642267
beta (°)	120.0743

Structure 3

Phase name	refined lit -125C
R-Bragg	1.413
Spacegroup	C2
Scale	4.04575575e-006
Cell Mass	698.695
Cell Volume (Å^3)	1093.74127
Wt% - Rietveld	31.450
Crystallite Size	
Cry size Lorentzian (nm)	15.1
Crystal Linear Absorption Coeff. (1/cm)	26.833
Crystal Density (g/cm^3)	1.061
PVII peak type	
FWHM = a + b/Cos(Th) + c Tan(Th)	
a	0.02671795
b	0.0242638
c	0.5748069
Exponent m = 0.6+ma+mb/Cos(Th)+mc/Tan(Th)	
ma	0.0001

mb	0.0001
mc	0.003869578
Lattice parameters	
a (Å)	9.3938141
b (Å)	16.6190729
c (Å)	8.5140018
beta (°)	124.6267

Confined [BMIM][Cl] in 8 nm pores at -125 °C

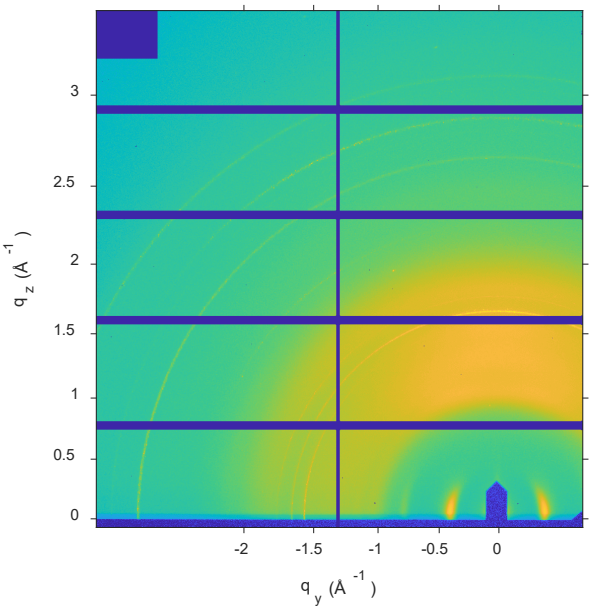

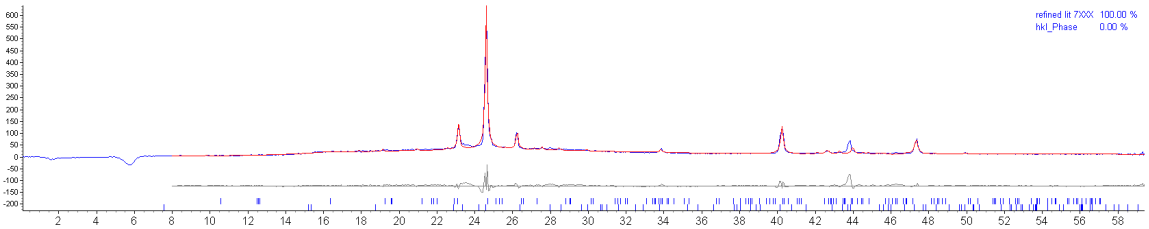

R-Values

Rexp : 19.56	Rwp : 15.19	Rp : 11.13	GOF : 0.78
Rexp`: 34.95	Rwp`: 27.14	Rp` : 23.32	DW : 0.80

Quantitative Analysis - Rietveld

Phase 1 : "refined lit 7XXX"	100.000 %
Phase 2 : hkl_Phase	0.000 %

Background

Chebychev polynomial, Coefficient	0	9.509502
	1	3.766029
	2	-7.25074
	3	5.770186
	4	-0.2623825
	5	-3.289541

Instrument

Primary radius (mm)	217.5
Secondary radius (mm)	217.5

Corrections

Zero error	-0.2855491

Specimen displacement	9.911472
LP Factor	0

Miscellaneous

Start X	8

Structure 1

Phase name	refined lit 7XXX
R-Bragg	1.377
Spacegroup	C2
Scale	1.24560616e-005
Cell Mass	698.695
Cell Volume (Å^3)	1093.74136
Wt% - Rietveld	100.000
Crystallite Size	
Cry size Lorentzian (nm)	9999.0
Crystal Linear Absorption Coeff. (1/cm)	26.833
Crystal Density (g/cm^3)	1.061
PVII peak type	
FWHM = a + b/Cos(Th) + c Tan(Th)	
a	0.843499
b	0.5763494
c	0.0001
Exponent m = 0.6+ma+mb/Cos(Th)+mc/Tan(Th)	
ma	0.0001
mb	0.0001
mc	0.0001
Lattice parameters	
a (Å)	9.3938141
b (Å)	16.6190729
c (Å)	8.5140018
beta (°)	124.6267

References

1. Chen, L.G., S.H. Strassburg, and H. Bermudez, *Characterization of Self-Assembled Amphiphiles in Ionic Liquids*, in *Ionic Liquid-Based Surfactant Science*. 2015, John Wiley & Sons, Inc. p. 23-46.
2. Welton, T., *Room-Temperature Ionic Liquids. Solvents for Synthesis and Catalysis.* Chemical Reviews, 1999. **99**(8): p. 2071-2084.
3. Bonhôte, P., et al., *Hydrophobic, Highly Conductive Ambient-Temperature Molten Salts.* Inorganic Chemistry, 1996. **35**(5): p. 1168-1178.
4. Peter, W. and W. Keim, *Ionic liquids—new "solutions" for transition metal catalysis.* Angewandte Chemie International Edition, 2000. **39**(21): p. 17.
5. Saha, B. and M.M. Abu-Omar, *Advances in 5-hydroxymethylfurfural production from biomass in biphasic solvents.* Green Chem., 2014. **16**(1): p. 24-38.
6. Dupont, J., R.F. de Souza, and P.A.Z. Suarez, *Ionic Liquid (Molten Salt) Phase Organometallic Catalysis.* Chemical Reviews, 2002. **102**(10): p. 3667-3692.
7. Dong, X., H.D. Shannon, and I.C. Escobar, *Investigation of PolarClean and Gamma-Valerolactone as Solvents for Polysulfone Membrane Fabrication*, in *Green Polymer Chemistry: New Products, Processes, and Applications*. 2018, American Chemical Society. p. 385-403.
8. Chen, S., et al., *Transition of Ionic Liquid [bmim][PF6] from Liquid to High-Melting-Point Crystal When Confined in Multiwalled Carbon Nanotubes.* Journal of the American Chemical Society, 2007. **129**(9): p. 2416-2417.
9. Iacob, C., et al., *Enhanced charge transport in nano-confined ionic liquids.* Soft Matter, 2012. **8**(2): p. 289-293.
10. Stefanopoulos, K.L., et al., *Investigation of confined ionic liquid in nanostructured materials by a combination of SANS, contrast-matching SANS, and nitrogen adsorption.* Langmuir, 2011. **27**(13): p. 7980-5.
11. Romanos, G.E., et al., *Investigation of Physically and Chemically Ionic Liquid Confinement in Nanoporous Materials by a Combination of SANS, Contrast-Matching SANS, XRD and Nitrogen Adsorption.* Journal of Physics: Conference Series, 2012. **340**: p. 012087.
12. Slowing, I.I., et al., *Mesoporous silica nanoparticles for drug delivery and biosensing applications.* Advanced Functional Materials, 2007. **17**(8): p. 1225-1236.
13. Torney, F., et al., *Mesoporous silica nanoparticles deliver DNA and chemicals into plants.* Nature nanotechnology, 2007. **2**(5): p. 295-300.
14. Clark Wooten, M.K., et al., *Synthesis and Nanofiltration Membrane Performance of Oriented Mesoporous Silica Thin Films on Macroporous Supports.* ACS applied materials & interfaces, 2016. **8**(33): p. 21806-21815.
15. Zhou, S., *PORE-CONFINED CARRIERS AND BIOMOLECULES IN MESOPOROUS SILICA FOR BIOMIMETIC SEPARATION AND TARGETING*, in *Chemical and Materials Engineering*. 2017, University of Kentucky.
16. Wang, T., J.A. Glasper, and B.H. Shanks, *Kinetics of glucose dehydration catalyzed by homogeneous Lewis acidic metal salts in water.* Applied Catalysis A: General, 2015. **498**: p. 214-221.
17. He, Y., et al., *In Situ Fourier Transform Infrared Study of the Effects of Silica Mesopore Confinement on Hydration of Ionic Liquid 1-Butyl-3-methylimidazolium Chloride.* Industrial & Engineering Chemistry Research, 2019.

18. Branco, L.C., et al., *Preparation and Characterization of New Room Temperature Ionic Liquids.* Chemistry - A European Journal, 2002. **8**(16): p. 3671-3677.
19. Choudhury, A.R., et al., *In situ Crystallization of Low-Melting Ionic Liquids.* Journal of the American Chemical Society, 2005. **127**(48): p. 16792-16793.
20. D. Holbrey, J. and K. R. Seddon, *The phase behaviour of 1-alkyl-3-methylimidazolium tetrafluoroborates; ionic liquids and ionic liquid crystals.* Journal of the Chemical Society, Dalton Transactions, 1999(13): p. 2133-2140.
21. Nordwald, E.M., et al., *Crystallographic Investigation of Imidazolium Ionic Liquid Effects on Enzyme Structure.* Chembiochem, 2015. **16**(17): p. 2456-9.
22. Binnemans, K., *Ionic liquid crystals.* Chemical Reviews, 2005. **105**(11): p. 4148-4204.
23. Lin, I.J.B. and C.S. Vasam, *Metal-containing ionic liquids and ionic liquid crystals based on imidazolium moiety.* Journal of Organometallic Chemistry, 2005. **690**(15): p. 3498-3512.
24. Chauvin, Y., B. Gilbert, and I. Guibard, *Catalytic dimerization of alkenes by nickel complexes in organochloroaluminate molten salts.* Journal of the Chemical Society, Chemical Communications, 1990(23): p. 1715-1716.
25. Fort, D.A., et al., *Can ionic liquids dissolve wood? Processing and analysis of lignocellulosic materials with 1-n-butyl-3-methylimidazolium chloride.* Green Chemistry, 2007. **9**(1): p. 63-69.
26. Saang'onyo, D.S., *CATALYTIC CONVERSION OF MONOSACCHARIDES INTO 5-(HYDROMETHYL)FURFURAL IN IONIC LIQUIDS USING ALUMINUM COMPLEXES BEARING BIDENTATE (AMINOMETHYL)PHENOLATE LIGANDS*, in *Chemistry*. 2018, University of Kentucky.
27. Saang'onyo, D., S. Parkin, and F.T. Ladipo, *Effect of ancillary (aminomethyl) phenolate ligand on efficacy of aluminum-catalyzed glucose dehydration to 5-hydroxymethylfurfural.* Polyhedron, 2018. **149**: p. 153-162.
28. Climent, M.J., A. Corma, and S. Iborra, *Converting carbohydrates to bulk chemicals and fine chemicals over heterogeneous catalysts.* Green Chemistry, 2011. **13**(3): p. 520.
29. Zhang, Y., E.A. Pidko, and E.J. Hensen, *Molecular aspects of glucose dehydration by chromium chlorides in ionic liquids.* Chemistry, 2011. **17**(19): p. 5281-8.
30. Bozell, J.J. and G.R. Petersen, *Technology development for the production of biobased products from biorefinery carbohydrates—the US Department of Energy's "Top 10" revisited.* Green Chemistry, 2010. **12**(4): p. 539.
31. Corma, A., S. Iborra, and A. Velty, *Chemical Routes for the Transformation of Biomass into Chemicals.* Chemical Reviews, 2007. **107**(6): p. 2411-2502.
32. Smith, E.F., et al., *Ionic liquids in vacuo; solution-phase X-ray photoelectron spectroscopy.* Chem Commun (Camb), 2005(45): p. 5633-5.
33. Gannon, T.J., et al., *First Observation of Molecular Composition and Orientation at the Surface of a Room-Temperature Ionic Liquid.* Langmuir, 1999. **15**(24): p. 8429-8434.
34. Zhao, H., et al., *Metal chlorides in ionic liquid solvents convert sugars to 5-hydroxymethylfurfural.* Science, 2007. **316**(5831): p. 1597-600.
35. Pidko, E.A., et al., *Coordination properties of ionic liquid-mediated chromium (II) and copper (II) chlorides and their complexes with glucose.* Inorganic chemistry, 2010. **49**(21): p. 10081-10091.
36. MacMillan, A.C., et al., *Effect of Alkyl Chain Length on Hygroscopicity of Nanoparticles and Thin Films of Imidazolium-Based Ionic Liquids.* The Journal of Physical Chemistry C, 2014. **118**(50): p. 29458-29466.
37. Conboy, J.C., M.C. Messmer, and G.L. Richmond, *Effect of alkyl chain length on the conformation and order of simple ionic surfactants adsorbed at the D2O/CCl4 interface*

as studied by sum-frequency vibrational spectroscopy. Langmuir, 1998. **14**(23): p. 6722-6727.
38. Jeon, Y., et al., *Structures of Ionic Liquids with Different Anions Studied by Infrared Vibration Spectroscopy.* The Journal of Physical Chemistry B, 2008. **112**(15): p. 4735-4740.
39. Takagaki, A., et al., *A one-pot reaction for biorefinery: combination of solid acid and base catalysts for direct production of 5-hydroxymethylfurfural from saccharides.* Chem Commun (Camb), 2009(41): p. 6276-8.
40. Eftekhari, A., Y. Liu, and P. Chen, *Different roles of ionic liquids in lithium batteries.* Journal of Power Sources, 2016. **334**: p. 221-239.
41. Balducci, A., *Ionic liquids in lithium-ion batteries*, in *Ionic Liquids II*. 2017, Springer. p. 1-27.
42. Guyomard-Lack, A., et al., *Enhancement of lithium transport by controlling the mesoporosity of silica monoliths filled by ionic liquids.* New Journal of Chemistry, 2016. **40**(5): p. 4269-4276.
43. Gupta, K.M. and J. Jiang, *Cellulose dissolution and regeneration in ionic liquids: A computational perspective.* Chemical Engineering Science, 2015. **121**: p. 180-189.
44. Tian, Z., S. Dai, and D.-e. Jiang, *Confined Ionic Liquid in an Ionic Porous Aromatic Framework for Gas Separation.* ACS Applied Polymer Materials, 2019. **1**(1): p. 95-102.
45. Triolo, A., et al., *Thermodynamics, Structure, and Dynamics in Room Temperature Ionic Liquids: The Case of 1-Butyl-3-methyl Imidazolium Hexafluorophosphate ([bmim][PF6]).* The Journal of Physical Chemistry B, 2006. **110**(42): p. 21357-21364.
46. Vafaeezadeh, M. and A. Fattahi, *Interaction of ionic liquids with the surface of silica gel using nanocluster approach: a combined density functional theory and experimental study.* Journal of Physical Organic Chemistry, 2014. **27**(2): p. 163-167.
47. Wang, Y., et al., *The influence of silica nanoparticles on ionic liquid behavior: a clear difference between adsorption and confinement.* Int J Mol Sci, 2013. **14**(10): p. 21045-52.
48. Coasne, B., L. Viau, and A. Vioux, *Loading-controlled stiffening in nanoconfined ionic liquids.* The journal of physical chemistry letters, 2011. **2**(10): p. 1150-1154.
49. Zhang, S., et al., *Nanoconfined Ionic Liquids.* Chemical Reviews, 2017. **117**(10): p. 6755-6833.
50. Néouze, M.-A., et al., *Ionogels, New Materials Arising from the Confinement of Ionic Liquids within Silica-Derived Networks.* Chemistry of Materials, 2006. **18**(17): p. 3931-3936.
51. Ivanchikova, I.D., et al., *User-friendly synthesis of highly selective and recyclable mesoporous titanium-silicate catalysts for the clean production of substituted p-benzoquinones.* Catalysis Science & Technology, 2014. **4**(1): p. 200-207.
52. Zhang, J., et al., *Nanocomposites of ionic liquids confined in mesoporous silica gels: preparation, characterization and performance.* Phys Chem Chem Phys, 2010. **12**(8): p. 1971-81.
53. Brunel, D., et al., *New trends in the design of supported catalysts on mesoporous silicas and their applications in fine chemicals.* Catalysis today, 2002. **73**: p. 152.
54. Marins, J.A. and B.G. Soares, *Ionic liquid-based organically modified silica for the development of new electrorheological fluids.* Colloids and Surfaces A: Physicochemical and Engineering Aspects, 2017. **529**: p. 311-319.

55. Xin, B. and J. Hao, *Imidazolium-based ionic liquids grafted on solid surfaces.* Chem Soc Rev, 2014. **43**(20): p. 7171-87.

56. Pu, J., et al., *Tribology study of dual-layer ultrathin ionic liquid films with bonded phase: Influences of the self-assembled underlayer.* Colloids and Surfaces A: Physicochemical and Engineering Aspects, 2010. **372**(1): p. 155-164.

57. Liu, J., et al., *Tribological Properties of Self-Assembled Monolayers of Catecholic Imidazolium and the Spin-Coated Films of Ionic Liquids.* Langmuir, 2011. **27**(18): p. 11324-11331.

58. Vangeli, O.C., et al., *Grafting of Imidazolium Based Ionic Liquid on the Pore Surface of Nanoporous Materials—Study of Physicochemical and Thermodynamic Properties.* The Journal of Physical Chemistry B, 2010. **114**(19): p. 6480-6491.

59. Perdikaki, A.V., et al., *Ionic Liquid-Modified Porous Materials for Gas Separation and Heterogeneous Catalysis.* The Journal of Physical Chemistry C, 2012. **116**(31): p. 16398-16411.

60. Kumar, P. and V.V. Guliants, *Periodic mesoporous organic–inorganic hybrid materials: Applications in membrane separations and adsorption.* Microporous and Mesoporous Materials, 2010. **132**(1): p. 1-14.

61. Ke, J., et al., *Electrodeposition of metals from supercritical fluids.* Proc Natl Acad Sci U S A, 2009. **106**(35): p. 14768-72.

62. Mehnert, C.P., *Supported ionic liquid catalysis.* Chemistry, 2004. **11**(1): p. 50-6.

63. Innocenzi, P., V.G. Kessler, and Y.L. Zub, *Sol-gel methods for materials processing: focusing on materials for pollution control, water purification, and soil remediation*. 2008: Springer.

64. Koganti, V.R. and S.E. Rankin, *Synthesis of Surfactant-Templated Silica Films with Orthogonally Aligned Hexagonal Mesophase.* The Journal of Physical Chemistry B, 2005. **109**(8): p. 3279-3283.

65. Islam, S.Z., *Synthesis and Energy Applications of Mesoporous Titania Thin Films*, in *Chemical and Materials Engineering*. 2017, University of Kentucky.

66. Hench, L.L. and J.K. West, *The sol-gel process.* Chemical Reviews, 1990. **90**(1): p. 33-72.

67. Raman, N.K., M.T. Anderson, and C.J. Brinker, *Template-Based Approaches to the Preparation of Amorphous, Nanoporous Silicas.* Chemistry of Materials, 1996. **8**(8): p. 1682-1701.

68. Wan, Y. and Zhao, *On the Controllable Soft-Templating Approach to Mesoporous Silicates.* Chemical Reviews, 2007. **107**(7): p. 2821-2860.

69. Brinker, C.J., et al., *Review of sol-gel thin film formation.* Journal of Non-Crystalline Solids, 1992. **147**: p. 424-436.

70. Brinker, C.J., et al., *Evaporation-induced self-assembly: nanostructures made easy.* Advanced materials, 1999. **11**(7): p. 579-585.

71. Lu, Y., et al., *Continuous formation of supported cubic and hexagonal mesoporous films by sol-gel dip-coating.* Nature, 1997. **389**(6649): p. 364.

72. Koganti, V.R., S. Das, and S.E. Rankin, *In Situ FTIR Investigation of the Kinetics of Silica Polycondensation in Surfactant Templated, Mesostructured Thin Films.* The Journal of Physical Chemistry C, 2014. **118**(33): p. 19450-19461.

73. Cao, L., T. Man, and M. Kruk, *Synthesis of Ultra-Large-Pore SBA-15 Silica with Two-Dimensional Hexagonal Structure Using Triisopropylbenzene As Micelle Expander.* Chemistry of Materials, 2009. **21**(6): p. 1144-1153.

74. Dunphy, D.R., et al., *Enlarged Pore Size in Mesoporous Silica Films Templated by Pluronic F127: Use of Poloxamer Mixtures and Increased Template/SiO2 Ratios in Materials Synthesized by Evaporation-Induced Self-Assembly.* Chemistry of Materials, 2014. **27**(1): p. 75-84.

75. Zhou, S., et al., *Lipid Pore-Filled Silica Thin-Film Membranes for Biomimetic Recovery of Dilute Carbohydrates.* Langmuir, 2017. **33**(49): p. 14156-14166.

76. Das, S., *Fundamental Studies of Surfactant Templeated Metal Oxied Materials Synthesis and Transformation for Adsoption and Energy Applications*, in *Theses and Dissertations--Chemical and Materials Engineering*. 2015.

77. Levchenko, T., Y. Plyuto, and N. Kovtyukhova, *Functionalisation of the template-free and template-structured silica films synthesised on glass substrates by sol–gel technique.* Journal of Sol-Gel Science and Technology, 2007. **43**(3): p. 269-274.

78. Smarsly, B., S. Polarz, and M. Antonietti, *Preparation of porous silica materials via sol–gel nanocasting of nonionic surfactants: A mechanistic study on the self-aggregation of amphiphiles for the precise prediction of the mesopore size.* The Journal of Physical Chemistry B, 2001. **105**(43): p. 10473-10483.

79. Naik, S.P., et al., *Studies on mesoporous silica films synthesized using F127, a triblock co-polymer.* Microporous and Mesoporous Materials, 2004. **75**(1-2): p. 51-59.

80. Brown, G. and A. Chakrabarti, *Ordering of block copolymer melts in confined geometry.* The Journal of chemical physics, 1995. **102**(3): p. 1440-1448.

81. Pickett, G.T. and A.C. Balazs, *Equilibrium orientation of confined diblock copolymer films.* Macromolecules, 1997. **30**(10): p. 3097-3103.

82. Matsen, M., *Thin films of block copolymer.* The Journal of chemical physics, 1997. **106**(18): p. 7781-7791.

83. Narayan, R., et al., *Mesoporous Silica Nanoparticles: A Comprehensive Review on Synthesis and Recent Advances.* Pharmaceutics, 2018. **10**(3): p. 118.

84. Zhao, D., et al., *Nonionic triblock and star diblock copolymer and oligomeric surfactant syntheses of highly ordered, hydrothermally stable, mesoporous silica structures.* Journal of the American Chemical Society, 1998. **120**(24): p. 6024-6036.

85. Rahman, M.S., et al., *Incorporation of isolated Ti sites into mesoporous silica thin films by sugar surfactant complexation.* Microporous and Mesoporous Materials, 2014. **190**: p. 74-83.

86. Alba, M.D., Z. Luan, and J. Klinowski, *Titanosilicate Mesoporous Molecular Sieve MCM-41: Synthesis and Characterization.* The Journal of Physical Chemistry, 1996. **100**(6): p. 2178-2182.

87. Griffiths, P.R. and J.A. De Haseth, *Fourier transform infrared spectrometry*. Vol. 171. 2007: John Wiley & Sons.

88. Nordhoff, E., et al., *Comparison of IR-and UV-matrix-assisted laser desorption/ionization mass spectrometry of oligodeoxynucleotides.* Nucleic acids research, 1994. **22**(13): p. 2460-2465.

89. Hagemann, H., et al., *Quantitative infrared methods for the measurement of crystallinity and its temperature dependence: polyethylene.* Macromolecules, 1989. **22**(9): p. 3600-3606.

90. Tait, S. and R.A. Osteryoung, *Infrared study of ambient-temperature chloroaluminates as a function of melt acidity.* Inorganic Chemistry, 1984. **23**(25): p. 4352-4360.

91. Chang, H.-C., T.-T. Tsai, and M.-H. Kuo, *Using High-Pressure Infrared Spectroscopy to Study the Interactions between Triblock Copolymers and Ionic Liquids.* Macromolecules, 2014. **47**(9): p. 3052-3058.

92. MacMillan, A.C., et al., *Interaction of water vapor with the surfaces of imidazolium-based ionic liquid nanoparticles and thin films.* J Phys Chem B, 2012. **116**(36): p. 11255-65.

93. Fazio, B., A. Triolo, and G. Di Marco, *Local organization of water and its effect on the structural heterogeneities in room-temperature ionic liquid/H2O mixtures.* Journal of Raman Spectroscopy, 2008. **39**(2): p. 233-237.

94. Gaffney, K., I. Piletic, and M. Fayer, *Hydrogen bond breaking and reformation in alcohol oligomers following vibrational relaxation of a non-hydrogen-bond donating hydroxyl stretch.* The Journal of Physical Chemistry A, 2002. **106**(41): p. 9428-9435.

95. Al-Abadleh, H.A. and V. Grassian, *FT-IR study of water adsorption on aluminum oxide surfaces.* Langmuir, 2003. **19**(2): p. 341-347.

96. Cammarata, L., et al., *Molecular states of water in room temperature ionic liquids.* Physical Chemistry Chemical Physics, 2001. **3**(23): p. 5192-5200.

97. Onori, G. and A. Santucci, *IR investigations of water structure in Aerosol OT reverse micellar aggregates.* The Journal of Physical Chemistry, 1993. **97**(20): p. 5430-5434.

98. Lee, C.M., et al., *Hydrogen-Bonding Network and OH Stretch Vibration of Cellulose: Comparison of Computational Modeling with Polarized IR and SFG Spectra.* J Phys Chem B, 2015. **119**(49): p. 15138-49.

99. Tainter, C.J., et al., *Hydrogen Bonding and OH-Stretch Spectroscopy in Water: Hexamer (Cage), Liquid Surface, Liquid, and Ice.* The Journal of Physical Chemistry Letters, 2013. **4**(1): p. 12-17.

100. Brubach, J.B., et al., *Dependence of Water Dynamics upon Confinement Size.* The Journal of Physical Chemistry B, 2001. **105**(2): p. 430-435.

101. González-Blanco, C., L. Rodriguez, and M. Velazquez, *Effect of the addition of water-soluble polymers on the structure of Aerosol OT water-in-oil microemulsions: a Fourier transform infrared spectroscopy study.* Langmuir, 1997. **13**(7): p. 1938-1945.

102. McDonough, L.A., et al., *Fourier transform infrared spectroscopy studies of water-polymer interactions in chemically amplified photoresists.* Journal of Vacuum Science & Technology B: Microelectronics and Nanometer Structures Processing, Measurement, and Phenomena, 2005. **23**(2): p. 344-348.

103. Zhang, Q.N., et al., *In situ observation on the dynamic process of evaporation and crystallization of sodium nitrate droplets on a ZnSe substrate by FTIR-ATR.* J Phys Chem A, 2014. **118**(15): p. 2728-37.

104. Müller-Buschbaum, P., *A basic introduction to grazing incidence small-angle X-ray scattering*, in *Applications of synchrotron light to scattering and diffraction in materials and life sciences*. 2009, Springer. p. 61-89.

105. Yamamoto, K., *Grazing-Incidence Small Angle X-Ray Scattering in Polymer Thin Films Utilizing Low-Energy X-Rays*, in *X-ray Scattering*. 2017.

106. Dourdain, S., et al., *Determination of porosity of mesoporous silica thin films by quantitative X-ray reflectivity analysis and GISAXS.* Thin Solid Films, 2006. **495**(1-2): p. 205-209.

107. Gibaud, A., et al., *Wall thickness and core radius determination in surfactant templated silica thin films using GISAXS and X-ray reflectivity.* Europhysics Letters (EPL), 2003. **63**(6): p. 833-839.

108. Jiang, Z., *GIXSGUI: a MATLAB toolbox for grazing-incidence X-ray scattering data visualization and reduction, and indexing of buried three-dimensional periodic nanostructured films.* Journal of Applied Crystallography, 2015. **48**(3): p. 917-926.

109. Tate, M.P., et al., *Simulation and interpretation of 2D diffraction patterns from self-assembled nanostructured films at arbitrary angles of incidence: From grazing incidence (above the critical angle) to transmission perpendicular to the substrate.* The Journal of Physical Chemistry B, 2006. **110**(20): p. 9882-9892.

110. Hexemer, A. and P. Muller-Buschbaum, *Advanced grazing-incidence techniques for modern soft-matter materials analysis.* IUCrJ, 2015. **2**(Pt 1): p. 106-25.

111. Hüsing, N., et al., *Silica-Titania Mesostructured Films.* Journal of Sol-Gel Science and Technology, 2003. **26**(1): p. 615-619.

112. Grosso, D., et al., *Highly Porous TiO2 Anatase Optical Thin Films with Cubic Mesostructure Stabilized at 700 °C.* Chemistry of Materials, 2003. **15**(24): p. 4562-4570.

113. Li, L., J. Groenewold, and S.J. Picken, *Transient Phase-Induced Nucleation in Ionic Liquid Crystals and Size-Frustrated Thickening.* Chemistry of Materials, 2005. **17**(2): p. 250-257.

114. *The Atomic Scattering Factor*. 1993, Berkeley Lab.

115. Scherrer, P., *Bestimmung der inneren Struktur und der Größe von Kolloidteilchen mittels Röntgenstrahlen*, in *Kolloidchemie Ein Lehrbuch*. 1912, Springer. p. 387-409.

116. Smilgies, D.M., *Scherrer grain-size analysis adapted to grazing-incidence scattering with area detectors.* J Appl Crystallogr, 2009. **42**(Pt 6): p. 1030-1034.

117. Cesiulis, H., et al., *The Study of Thin Films by Electrochemical Impedance Spectroscopy.* 2016: p. 3-42.

118. Lasia, A., *Electrochemical impedance spectroscopy and its applications*, in *Modern aspects of electrochemistry*. 2002, Springer. p. 143-248.

119. Orazem, M.E. and B. Tribollet, *Electrochemical impedance spectroscopy*. 2017: John Wiley & Sons.

120. Instruments, G. *Application Note: Basics of Electrochemical Impedance Spectroscopy*. 2010 [cited 2019.

121. Huang, J., et al., *Graphical analysis of electrochemical impedance spectroscopy data in Bode and Nyquist representations.* Journal of Power Sources, 2016. **309**: p. 82-98.

122. Wei, T.-C. and H.W. Hillhouse, *Mass Transport and Electrode Accessibility Through Periodic Self-Assembled Nanoporous Silica Thin Films.* Langmuir, 2007. **23**(10): p. 5689-5699.

123. Bason, S., Y. Oren, and V. Freger, *Characterization of ion transport in thin films using electrochemical impedance spectroscopyII: Examination of the polyamide layer of RO membranes.* Journal of Membrane Science, 2007. **302**(1-2): p. 10-19.

124. Freger, V. and S. Bason, *Characterization of ion transport in thin films using electrochemical impedance spectroscopyI. Principles and theory.* Journal of Membrane Science, 2007. **302**(1-2): p. 1-9.

125. Rouquerol, J., et al., *Recommendations for the characterization of porous solids (Technical Report).* Pure and Applied Chemistry, 1994. **66**(8): p. 1739-1758.

126. Alothman, Z., *A Review: Fundamental Aspects of Silicate Mesoporous Materials.* Materials, 2012. **5**(12): p. 2874-2902.

127. He, X., et al., *Heterogeneous nucleation from a supercooled ionic liquid on a carbon surface.* The Journal of Chemical Physics, 2016. **145**(21): p. 211919.

128. Murakata, T., et al., *Control of pore size distribution of silica gel through sol-gel process using inorganic salts and surfactants as additives.* Journal of Materials Science, 1992. **27**(6): p. 1567-1574.

129. Besson, S., et al., *Phase diagram for mesoporous CTAB–silica films prepared under dynamic conditions.* Journal of Materials Chemistry, 2003. **13**(2): p. 404-409.

130. Tolbert, S.H., et al., *Magnetic field alignment of ordered silicate-surfactant composites and mesoporous silica.* Science, 1997. **278**(5336): p. 264.

131. Robertson, C., et al., *Surface modification and porosimetry of vertically aligned hexagonal mesoporous silica films.* RSC Adv., 2016. **6**(114): p. 113432-113441.

132. Kibombo, H.S., et al., *Versatility of heterogeneous photocatalysis: synthetic methodologies epitomizing the role of silica support in TiO2 based mixed oxides.* Catalysis Science & Technology, 2012. **2**(9): p. 1737.

133. Zhang, X., F. Zhang, and K.-Y. Chan, *Synthesis of titania–silica mixed oxide mesoporous materials, characterization and photocatalytic properties.* Applied Catalysis A: General, 2005. **284**(1-2): p. 193-198.

134. Hüsing, N., et al., *Mesostructured Silica−Titania Mixed Oxide Thin Films.* Chemistry of Materials, 2002. **14**(6): p. 2429-2432.

135. Soler-Illia, G.J.A.A., et al., *Designed synthesis of large-pore mesoporous silica–zirconia thin films with high mixing degree and tunable cubic or 2D-hexagonal mesostructure.* J. Mater. Chem., 2004. **14**(12): p. 1879-1886.

136. Hao, J., et al., *Self-Assembly in Block Copolymer Thin Films upon Solvent Evaporation: A Simulation Study.* Macromolecules, 2017. **50**(11): p. 4384-4396.

137. Brendel, J.C., et al., *Macroscopic Vertical Alignment of Nanodomains in Thin Films of Semiconductor Amphiphilic Block Copolymers.* ACS Nano, 2013. **7**(7): p. 6069-6078.

138. Wang, H.S., K.H. Kim, and J. Bang, *Thermal Approaches to Perpendicular Block Copolymer Microdomains in Thin Films: A Review and Appraisal.* Macromol Rapid Commun, 2019. **40**(4): p. e1800728.

139. Choo, Y., et al., *Pathway-engineering for highly-aligned block copolymer arrays.* Nanoscale, 2017. **10**(1): p. 416-427.

140. Oveisi, H., et al., *Synthesis and characterization of highly ordered titania-alumina mixed oxide mesoporous films with high alumina content.* Microporous and Mesoporous Materials, 2010. **134**(1-3): p. 150-156.

141. Rahman, M.S., et al., *Incorporation of isolated Ti sites into mesoporous silica thin films by sugar surfactant complexation.* Microporous and Mesoporous Materials, 2014. **190**(Supplement C): p. 74-83.

142. Rahman, M.S. and S.E. Rankin, *Predictive synthesis of ordered mesoporous silica with maltoside and cationic surfactants based on aqueous lyotropic phase behavior.* Journal of Colloid and Interface Science, 2010. **342**(1): p. 33-42.

143. Nagpure, S., et al., *Layer-by-Layer Synthesis of Thick Mesoporous TiO_2 Films with Vertically Oriented Accessible Nanopores and Their Application for Lithium-Ion Battery Negative Electrodes.* Advanced Functional Materials, 2018. **28**(37): p. 1801849.

144. Matheron, M., et al., *Highly ordered CTAB-templated organosilicate films.* Journal of Materials Chemistry, 2005. **15**(44): p. 4741.

145. Hsu, C.-H., et al., *Thickness-Dependent Order-to-Order Transitions of Bolaform-like Giant Surfactant in Thin Films.* Macromolecules, 2017. **50**(18): p. 7282-7290.

146. Grosso, D., et al., *An in Situ Study of Mesostructured CTAB−Silica Film Formation during Dip Coating Using Time-Resolved SAXS and Interferometry Measurements.* Chemistry of Materials, 2002. **14**(2): p. 931-939.

147. Urade, V.N., et al., *Nanofabrication of Double-Gyroid Thin Films.* Chemistry of Materials, 2007. **19**(4): p. 768-777.

148. Ren, J., et al., *Silica–Titania mixed Oxides: Si–O–Ti Connectivity, Coordination of Titanium, and Surface Acidic Properties.* Catalysis Letters, 2008. **124**(3-4): p. 185-194.

149. Samantaray, S.K. and K. Parida, *Effect of phosphate ion on the textural and catalytic activity of titania–silica mixed oxide.* Applied Catalysis A: General, 2001. **220**(1-2): p. 9-20.

150. Joshi, S., *Mixed surfactant systems: Thermodynamics and applications in metal oxide imprinting*, S.E. Rankin, Editor. 2014, ProQuest Dissertations Publishing.

151. Kim, S.-S., T.R. Pauly, and T.J. Pinnavaia, *Non-ionic surfactant assembly of ordered, very large pore molecular sieve silicas from water soluble silicates.* Chemical Communications, 2000(17): p. 1661-1662.

152. Livage, J. and C. Sanchez, *Sol-gel chemistry.* Journal of Non-Crystalline Solids, 1992. **145**: p. 11-19.

153. Chen, L.G., S.H. Strassburg, and H. Bermudez, *Characterization of Self -Assembled Amphiphiles in Ionic Liquids*, in *Ionic Liquid-Based Surfactant Science: Formulation, Characterization, and Applications*, B.K. Paul and S.P. Moulik, Editors. 2015, Wiley: Hoboken, NJ. p. 23-46.

154. Shukla, M. and S. Saha, *A comparative study of piperidinium and imidazolium based ionic liquids: thermal, spectroscopic and theoretical studies*, in *Ionic Liquids-New Aspects for the Future*. 2013, InTech.

155. Wang, S.F., et al., *Direct electrochemistry and electrocatalysis of heme proteins entrapped in agarose hydrogel films in room-temperature ionic liquids.* Langmuir, 2005. **21**(20): p. 9260-6.

156. Zhao, H., et al., *Metal Chlorides in Ionic Liquid Solvents Convert Sugars to 5-Hydroxymethylfurfural.* Science, 2007. **316**(5831): p. 1600.

157. Lansalot-Matras, C. and C. Moreau, *Dehydration of fructose into 5-hydroxymethylfurfural in the presence of ionic liquids.* Catalysis Communications, 2003. **4**(10): p. 517-520.

158. Fayet, C. and J. Gelas, *Nouvelle méthode de préparation du 5-hydroxyméthyl-2-furaldéhyde par action de sels d'ammonium ou d'immonium sur les mono-, oligo- et poly-saccharides. Accès direct aux 5-halogénométhyl-2-furaldéhydes.* Carbohydrate Research, 1983. **122**(1): p. 59-68.

159. Karimi, B. and H.M. Mirzaei, *The influence of hydrophobic/hydrophilic balance of the mesoporous solid acid catalysts in the selective dehydration of fructose into HMF.* RSC Advances, 2013. **3**(43): p. 20655.

160. Mehnert, C.P., et al., *Supported ionic liquid catalysis− A new concept for homogeneous hydroformylation catalysis.* Journal of the American Chemical Society, 2002. **124**(44): p. 12932-12933.

161. Iacob, C., et al., *Charge transport and diffusion of ionic liquids in nanoporous silica membranes.* Phys Chem Chem Phys, 2010. **12**(41): p. 13798-803.

162. Maiti, A., A. Kumar, and R.D. Rogers, *Water-clustering in hygroscopic ionic liquids-an implicit solvent analysis.* Phys Chem Chem Phys, 2012. **14**(15): p. 5139-46.

163. Torrecilla, J.S., et al., *Effect of Relative Humidity of Air on Density, Apparent Molar Volume, Viscosity, Surface Tension, and Water Content of 1-Ethyl-3-methylimidazolium Ethylsulfate Ionic Liquid.* Journal of Chemical & Engineering Data, 2008. **53**(4): p. 923-928.

164. Cheng, H.-W., et al., *Characterizing the Influence of Water on Charging and Layering at Electrified Ionic-Liquid/Solid Interfaces.* Advanced Materials Interfaces, 2015. **2**(12): p. 1500159.

165. Gong, X., et al., *From Molecular Arrangement to Macroscopic Wetting of Ionic Liquids on the Mica Surface: Effect of Humidity.* Langmuir, 2018. **34**(40): p. 12167-12173.

166. Koganti, V.R., et al., *Generalized coating route to silica and titania films with orthogonally tilted cylindrical nanopore arrays.* Nano letters, 2006. **6**(11): p. 2567-2570.

167. Nagpure, S., et al., *In Situ GISAXS Investigation of Low-Temperature Aging in Oriented Surfactant-Mesostructured Titania Thin Films.* The Journal of Physical Chemistry C, 2015. **119**(40): p. 22970-22984.

168. Zhou, S., *Pore-confined Carriers and Biomolecules in Mesoporou Silica for Biomimetic Separation and Targeting*, in *Theses and Dissertations--Chemical and Materials Engineering*. 2017.

169. Dunn, B. and J.I. Zink, *Probes of Pore Environment and Molecule−Matrix Interactions in Sol−Gel Materials.* Chem. Mater., 1997. **9**(11): p. 11.

170. Gupta, A.K., R.K. Singh, and S. Chandra, *Crystallization kinetics behavior of ionic liquid [EMIM][BF4] confined in mesoporous silica matrices.* RSC Adv., 2014. **4**(42): p. 22277-22287.

171. Nusaibah Masri, A., A. Mutalib Mi, and J.M. Leveque, *A Review on Dicationic Ionic Liquids: Classification and Application.* Industrial Engineering & Management, 2016. **05**(04).

172. Fan, Z., et al., *In situ monitoring the moisture absorption of three ionic liquids with different halogen anions by ATR-FTIR spectroscopy.* Journal of Molecular Structure, 2018. **1164**: p. 297-302.

173. Bradley, M. *Curve Fitting in Raman and IR Spectroscopy: Basic Theory of Line Shapes and Applications*. 2007.

174. Landman, D.A., R. Roussel-Dupre, and G. Tanigawa, *On the Statistical Uncertainties Associated with Line Profile Fitting.* Astrophys. J., 1982. **261**: p. 732-735.

175. Yamada, T., et al., *Vibration Modes at Terahertz and Infrared Frequencies of Ionic Liquids Consisting of an Imidazolium Cation and a Halogen Anion.* Materials (Basel), 2014. **7**(11): p. 7409-7422.

176. Cha, S., et al., *Structures of ionic liquid-water mixtures investigated by IR and NMR spectroscopy.* Phys Chem Chem Phys, 2014. **16**(20): p. 9591-601.

177. Coates, J., *Interpretation of infrared spectra, a practical approach.* Encyclopedia of analytical chemistry, 2000.

178. Shukla, M., N. Srivastava, and S. Saha, *Theoretical and spectroscopic studies of 1-butyl-3-methylimidazolium iodide room temperature ionic liquid: Its differences with chloride and bromide derivatives.* Journal of Molecular Structure, 2010. **975**(1-3): p. 349-356.

179. Heimer, N.E., et al., *Vibrational spectra of imidazolium tetrafluoroborate ionic liquids.* Journal of Molecular Liquids, 2006. **124**(1-3): p. 84-95.

180. Cha, S. and D. Kim, *Anion exchange in ionic liquid mixtures.* Phys Chem Chem Phys, 2015. **17**(44): p. 29786-92.

181. Singh, M.P., R.K. Singh, and S. Chandra, *Thermal stability of ionic liquid in confined geometry.* Journal of Physics D: Applied Physics, 2010. **43**(9): p. 092001.

182. Singh, M.P., R.K. Singh, and S. Chandra, *Properties of ionic liquid confined in porous silica matrix.* Chemphyschem, 2010. **11**(9): p. 2036-43.

183. Chaplin, M. *Water Structure and Science*. The vibrational spectra of liquid water 2000 09-07-2017 [cited 2017 09-19].

184. Zhang, L., et al., *Prediction of the solvation and structural properties of ionic liquids in water by two-dimensional correlation spectroscopy.* The Journal of Physical Chemistry B, 2008. **112**(20): p. 6411-6419.

185. Kempter, V. and B. Kirchner, *The role of hydrogen atoms in interactions involving imidazolium-based ionic liquids.* Journal of Molecular Structure, 2010. **972**(1-3): p. 22-34.

186. Dieter, K.M., et al., *Ionic structure and interactions in 1-methyl-3-ethylimidazolium chloride-aluminum chloride molten salts.* Journal of the American Chemical Society, 1988. **110**(9): p. 2722-2726.

187. Roth, C., et al., *Hydrogen bonding in ionic liquids probed by linear and nonlinear vibrational spectroscopy.* New Journal of Physics, 2012. **14**(10): p. 105026.

188. Wernet, P., et al., *The structure of the first coordination shell in liquid water.* Science, 2004. **304**(5673): p. 995-999.

189. Zhang, F., C. Fang, and R. Qiao, *Effects of Water on Mica–Ionic Liquid Interfaces.* The Journal of Physical Chemistry C, 2018. **122**(16): p. 9035-9045.

190. Docampo-Álvarez, B., et al., *Molecular dynamics simulation of the behaviour of water in nano-confined ionic liquid–water mixtures.* Journal of Physics: Condensed Matter, 2016. **28**(46): p. 464001.

191. Saihara, K., et al., *Properties of Water Confined in Ionic Liquids.* Scientific Reports, 2015. **5**: p. 10619.

192. Dong, X., H.D. Shannon, and I.C. Escobar, *Investigation of PolarClean and Gamma-Valerolactone as Solvents for Polysulfone Membrane Fabrication.*

193. Castner, E.W. and J.F. Wishart, *Spotlight on ionic liquids.* J Chem Phys, 2010. **132**(12): p. 120901.

194. Zhang, Q., S. Zhang, and Y. Deng, *Recent advances in ionic liquid catalysis.* Green Chemistry, 2011. **13**(10): p. 2619.

195. Watanabe, M., et al., *Application of Ionic Liquids to Energy Storage and Conversion Materials and Devices.* Chem Rev, 2017. **117**(10): p. 7190-7239.

196. Schaltin, S., et al., *Towards an all-copper redox flow battery based on a copper-containing ionic liquid.* Chem Commun (Camb), 2016. **52**(2): p. 414-7.

197. Every, H.A., et al., *Transport properties in a family of dialkylimidazolium ionic liquids.* Phys. Chem. Chem. Phys., 2004. **6**(8): p. 1758-1765.

198. Guyomard-Lack, A., et al., *Destructuring ionic liquids in ionogels: enhanced fragility for solid devices.* Physical Chemistry Chemical Physics, 2014. **16**(43): p. 23639-23645.

199. Vatamanu, J., M. Vatamanu, and D. Bedrov, *Non-faradaic energy storage by room temperature ionic liquids in nanoporous electrodes.* Acs Nano, 2015. **9**(6): p. 5999-6017.

200. Singh, M.P., R.K. Singh, and S. Chandra, *Studies on Imidazolium-Based Ionic Liquids Having a Large Anion Confined in a Nanoporous Silica Gel Matrix.* The Journal of Physical Chemistry B, 2011. **115**(23): p. 7505-7514.

201. Gupta, A.K., et al., *Studies on an Ionic Liquid Confined in Silica Nanopores: Change in Tg and Evidence of Organic–Inorganic Linkage at the Pore Wall Surface.* The Journal of Physical Chemistry C, 2014. **118**(3): p. 1530-1539.

202. Xu, T., et al., *Gluing Ionic Liquids to Oxide Surfaces: Chemical Anchoring of Functionalized Ionic Liquids by Vapor Deposition onto Cobalt(II) Oxide.* Angew Chem Int Ed Engl, 2017. **56**(31): p. 9072-9076.

203. Vyas, R.N. and B. Wang, *Electrochemical analysis of conducting polymer thin films.* Int J Mol Sci, 2010. **11**(4): p. 1956-72.

204. Kumar, S. and S.L. Jain, *Non-symmetrical dialkyl carbonate synthesis promoted by 1-(3-trimethoxysilylpropyl)-3-methylimidazolium chloride.* New Journal of Chemistry, 2013. **37**(10).

205. Valizadeh, H., et al., *Ionic liquid 1-(3-trimethoxysilylpropyl)-3-methylimidazolium nitrite as a new reagent for the efficient diazotization of aniline derivatives and in situ synthesis of azo dyes.* Journal of the Iranian Chemical Society, 2011. **8**(2): p. 495-501.

206. Armarego, W.L. and D. Perrin, D., *Purification of laboratory chemicals*. 1997: Butterworth-Heinemann.

207. Bordoloi, A., et al., *Heteropoly acid-based supported ionic liquid-phase catalyst for the selective oxidation of alcohols.* Journal of Catalysis, 2008. **259**(2): p. 232-239.

208. Yu, B., et al., *Pdop layer exhibiting zwitterionicity: a simple electrochemical interface for governing ion permeability.* Chem Commun (Camb), 2010. **46**(32): p. 5900-2.

209. Zhou, S., et al., *Nanoconfinement Effects on Redox Probe Transport in Lipid Assemblies on and in Mesoporous Silica Thin Films.* Advanced Materials Interfaces. **n/a**(n/a): p. 1901787.

210. Coquil, T., et al., *Thermal conductivity of cubic and hexagonal mesoporous silica thin films.* Journal of Applied Physics, 2009. **106**(3).

211. Ryoo, R., et al., *Synthesis of Ordered and Disordered Silicas with Uniform Pores on the Border between Micropore and Mesopore Regions Using Short Double-Chain Surfactants.* Journal of the American Chemical Society, 2001. **123**(8): p. 1650-1657.

212. Kim, M.J. and R. Ryoo, *Synthesis and Pore Size Control of Cubic Mesoporous Silica SBA-1.* Chemistry of Materials, 1999. **11**(2): p. 487-491.

213. Etienne, M., et al., *Electrochemical approaches for the fabrication and/or characterization of pure and hybrid templated mesoporous oxide thin films: a review.* Anal Bioanal Chem, 2013. **405**(5): p. 1497-512.

214. Ulrich, C., *Electric Fields for Surface Design and Chemical Analysis*. 2008, Linköping University Electronic Press.

215. Hayes, R., G.G. Warr, and R. Atkin, *Physical chemistry of ionic liquids.* Phys Chem Chem Phys, 2010. **12**(8): p. 1648.

216. Sha, M., et al., *Double-Layer Formation of [Bmim][PF6] Ionic Liquid Triggered by Surface Negative Charge.* Langmuir, 2010. **26**(15): p. 12667-12672.

217. Shi, W. and D.C. Sorescu, *Molecular simulations of CO2 and H2 sorption into ionic liquid 1-n-hexyl-3-methylimidazolium bis (trifluoromethylsulfonyl) amide ([hmim][Tf2N]) confined in carbon nanotubes.* The Journal of Physical Chemistry B, 2010. **114**(46): p. 15029-15041.

218. Boon, J.A., et al., *Friedel-Crafts reactions in ambient-temperature molten salts.* The Journal of Organic Chemistry, 1986. **51**(4): p. 480-483.

219. Holbrey, J.D. and K.R. Seddon, *Ionic Liquids.* Clean Products and Processes, 1999. **1**(4): p. 223-236.

220. Zhu, J., et al., *Aqueous Grafting Ionic Liquid on Graphene Oxide for CO2 Cycloaddition.* Catalysis Letters, 2016. **147**(2): p. 335-344.

221. Steinrück, H.-P. and P. Wasserscheid, *Ionic Liquids in Catalysis.* Catalysis Letters, 2014. **145**(1): p. 380-397.

222. Riisager, A., et al., *Continuous fixed-bed gas-phase hydroformylation using supported ionic liquid-phase (SILP) Rh catalysts.* Journal of Catalysis, 2003. **219**(2): p. 452-455.

223. Werner, S., et al., *Screening of Supported Ionic Liquid Phase (SILP) catalysts for the very low temperature water–gas-shift reaction.* Applied Catalysis A: General, 2010. **377**(1-2): p. 70-75.

224. Bo, Z., et al., *Design of Supercapacitor Electrodes Using Molecular Dynamics Simulations.* Nano-Micro Letters, 2018. **10**(2): p. 33.

225. Feng, G. and P.T. Cummings, *Supercapacitor Capacitance Exhibits Oscillatory Behavior as a Function of Nanopore Size.* Journal of Physical Chemistry Letters, 2011. **2**(22): p. 2859-2864.

226. Yan, X.R., et al., *Ionic liquids combined with membrane separation processes: A review.* Separation and Purification Technology, 2019. **222**: p. 230-253.

227. Sasikumar, B., G. Arthanareeswaran, and A.F. Ismail, *Recent progress in ionic liquid membranes for gas separation.* Journal of Molecular Liquids, 2018. **266**: p. 330-341.

228. Liu, Y., et al., *Coexistence of Liquid and Solid Phases of Bmim-PF6 Ionic Liquid on Mica Surfaces at Room Temperature.* Journal of the American Chemical Society, 2006. **128**(23): p. 7456-7457.

229. Kotov, N., et al., *Structural Transitions of 1-Butyl-3-methylimidazolium Chloride/Water Mixtures Studied by Raman and FTIR Spectroscopy and WAXS.* Crystal Growth & Design, 2016. **16**(4): p. 1958-1967.

230. Holbrey, J.D., et al., *Crystal polymorphism in 1-butyl-3-methylimidazolium halides: supporting ionic liquid formation by inhibition of crystallizationElectronic supplementary information (ESI) available: packing diagrams for I and II; table of closest contacts for I, I-Br and II. See http://www.rsc.org/suppdata/cc/b3/b304543a.* Chemical Communications, 2003(14): p. 1636.

231. Saha, S., et al., *Crystal structure of 1-butyl-3-methylimidazolium chloride. A clue to the elucidation of the ionic liquid structure.* Chemistry letters, 2003. **32**(8): p. 740-741.

232. Hayashi, S., R. Ozawa, and H.-o. Hamaguchi, *Raman spectra, crystal polymorphism, and structure of a prototype ionic-liquid [bmim] Cl.* Chemistry letters, 2003. **32**(6): p. 498-499.

233. Dibrov, S.M. and J.K. Kochi, *Crystallographic view of fluidic structures for room-temperature ionic liquids: 1-butyl-3-methylimidazolium hexafluorophosphate.* Acta Crystallographica Section C, 2006. **62**(1): p. o19-o21.

234. Webber, J.B.W., *Studies of nano-structured liquids in confined geometry and at surfaces.* Progress in Nuclear Magnetic Resonance Spectroscopy, 2010. **56**(1): p. 78-93.

235. Verma, Y.L. and R.K. Singh, *Conformational States of Ionic Liquid 1-Ethyl-3-methylimidazolium Bis(trifluoromethylsulfonyl)imide in Bulk and Confined Silica*

Nanopores Probed by Crystallization Kinetics Study. The Journal of Physical Chemistry C, 2015. **119**(43): p. 24381-24392.

236. Tripathi, A.K., Y.L. Verma, and R.K. Singh, *Thermal, electrical and structural studies on ionic liquid confined in ordered mesoporous MCM-41.* Journal of Materials Chemistry A, 2015. **3**(47): p. 23809-23820.

237. Chen, S., et al., *Unravelling the Role of the Compressed Gas on Melting Point of Liquid Confined in Nanospace.* The Journal of Physical Chemistry Letters, 2012. **3**(8): p. 1052-1055.

238. Wang, Y., et al., *The Influence of Silica Nanoparticles on Ionic Liquid Behavior: A Clear Difference between Adsorption and Confinement.* International Journal of Molecular Sciences, 2013. **14**(10): p. 21045-21052.

239. Lu, Y., et al., *Continuous formation of supported cubic and hexagonal mesoporous films by sol–gel dip-coating.* Nature, 1997. **389**(6649): p. 364-368.

240. Zhao, D., et al., *Continuous Mesoporous Silica Films with Highly Ordered Large Pore Structures.* Advanced Materials, 1998. **10**(16): p. 1380-1385.

241. Mehnert, C.P., *Supported Ionic Liquid Catalysis.* Chemistry – A European Journal, 2005. **11**(1): p. 50-56.

242. Giacalone, F. and M. Gruttadauria, *Covalently Supported Ionic Liquid Phases: An Advanced Class of Recyclable Catalytic Systems.* Chemcatchem, 2016. **8**(4): p. 664-684.

243. Endo, T., T. Morita, and K. Nishikawa, *Crystal polymorphism of a room-temperature ionic liquid, 1,3-dimethylimidazolium hexafluorophosphate: Calorimetric and structural studies of two crystal phases having melting points of ~50K difference.* Chemical Physics Letters, 2011. **517**(4-6): p. 162-165.

244. Holbrey, J.D. and K.R. Seddon, *The phase behaviour of 1-alkyl-3-methylimidazolium tetrafluoroborates; ionic liquids and ionic liquid crystals.* Journal of the Chemical Society, Dalton Transactions, 1999(13): p. 2133-2140.

245. Gomes, M.F.C., J.C. Lopes, and A.A. Padua, *Thermodynamics and micro heterogeneity of ionic liquids*, in *Ionic Liquids.* 2009, Springer. p. 161-183.

246. Triolo, A., et al., *Thermodynamics, structure, and dynamics in room temperature ionic liquids: the case of 1-butyl-3-methyl imidazolium hexafluorophosphate ([bmim][PF6]).* The Journal of Physical Chemistry B, 2006. **110**(42): p. 21357-21364.

247. Huddleston, J.G., et al., *Characterization and comparison of hydrophilic and hydrophobic room temperature ionic liquids incorporating the imidazolium cation.* Green Chemistry, 2001. **3**(4): p. 156-164.

248. Endo, T., et al., *Phase Behaviors of Room Temperature Ionic Liquid Linked with Cation Conformational Changes: 1-Butyl-3-methylimidazolium Hexafluorophosphate.* The Journal of Physical Chemistry B, 2010. **114**(1): p. 407-411.

249. Wu, B., R. Reddy, and R. Rogers, *Novel ionic liquid thermal storage for solar thermal electric power systems.* Solar Engineering, 2001: p. 445-452.

250. Nockemann, P., K. Binnemans, and K. Driesen, *Purification of imidazolium ionic liquids for spectroscopic applications.* Chemical Physics Letters, 2005. **415**(1-3): p. 131-136.

251. Serra, P.B.P., et al., *Solid-liquid equilibrium and heat capacity trend in the alkylimidazolium PF6 series.* Journal of Molecular Liquids, 2017. **248**: p. 678-687.

252. Wang, Y. and G.A. Voth, *Unique Spatial Heterogeneity in Ionic Liquids.* Journal of the American Chemical Society, 2005. **127**(35): p. 12192-12193.

253. Hu, Z. and C.J. Margulis, *Heterogeneity in a room-temperature ionic liquid: persistent local environments and the red-edge effect.* Proc Natl Acad Sci U S A, 2006. **103**(4): p. 831-6.

254. Triolo, A., et al., *Nanoscale segregation in room temperature ionic liquids.* The Journal of Physical Chemistry B, 2007. **111**(18): p. 4641-4644.

255. Johnston, J.C. and V. Molinero, *Crystallization, melting, and structure of water nanoparticles at atmospherically relevant temperatures.* J Am Chem Soc, 2012. **134**(15): p. 6650-9.

256. Khan, M.A., et al., *Epitaxial Formation Mechanism of Multilayer TiO2 Films with Ordered Accessible Vertical Nanopores by Evaporation-Driven Assembly.* The Journal of Physical Chemistry C, 2019. **124**(3): p. 1958-1972.

257. Im, J., et al., *Anomalous thermal transition and crystallization of ionic liquids confined in graphene multilayers.* Chem Commun (Camb), 2012. **48**(14): p. 2015-7.

258. Hamaguchi, H.-O. and R. Ozawa, *Structure of Ionic Liquids and Ionic Liquid Compounds: Are Ionic Liquids Genuine Liquids in the Conventional Sense?*, in *Advances in Chemical Physics*. 2005.

259. Jiang, Q. and M.D. Ward, *Crystallization under nanoscale confinement.* Chem Soc Rev, 2014. **43**(7): p. 2066-79.

260. Endres, F., *Physical chemistry of ionic liquids.* Phys Chem Chem Phys, 2010. **12**(8): p. 1648.

261. Koel, M., *Ionic liquids in chemical analysis.* 2008: CRC press.

262. Dharaskar, S.A., et al., *Synthesis, characterization and application of 1-butyl-3 methylimidazolium chloride as green material for extractive desulfurization of liquid fuel.* The Scientific World Journal, 2013. **2013**.

263. Endo, T. and K. Nishikawa, *Thermal phase behavior of 1-butyl-3-methylimidazolium hexafluorophosphate: Simultaneous measurements of the melting of two polymorphic crystals by Raman spectroscopy and calorimetry.* Chemical Physics Letters, 2013. **584**: p. 79-82.

264. Khan, M.A., et al., *Adsorption and Recovery of Polyphenolic Flavonoids Using TiO2-Functionalized Mesoporous Silica Nanoparticles.* ACS Applied Materials & Interfaces, 2017. **9**(37): p. 32114-32125.

VITA

Educational institutions attended and degrees already awarded

Bachelor of Science in Chemical Engineering, Michigan State University, East Lansing, MI, 2015

Professional positions held (do not include job descriptions)

Graduate Research Assistant, Chemical and Material Engineering Department, University of Kentucky, Aug 2015-Present

Teaching Assistant, Chemical and Material Engineering Department, University of Kentucky, Aug 2015-May 2016

Undergraduate Research Assistant, Michigan State University, Sep 2012-Jan 2015

Scholastic and professional honors

Argonne National Laboratory APS/CNM Users Meeting Travel Award, 2019

University of Kentucky Graduate Student Congress (UK GSC) Research Award, 2018

UK GSC Pillar Award for Academic Success, 2018

EPSCoR Super Collider Outstanding Poster, 2017

Professional publications

He, Y., et al., (2019) " In-situ FTIR Study of the Effects of Silica Mesopore Confinement on Hydration of Ionic Liquid 1-Butyl-3-methylimidazolium Chloride ([BMIM][Cl]) " Ind. Eng. Chem. Res., 58(50),22609-22618

Khan M.A., He, Y., et al., (2020) “Epitaxial Formation Mechanism of Multilayer TiO2 Films with Ordered Accessible Vertical Nanopores by Evaporation-Driven Assembly” J. Phys. Chem. C., 124(3), 1958-1972

Zhou, S., He, Y., et al., (2019) “Nanoconfinement Effects on Redox Probe Transport in Lipid Assemblies on and in Mesoporous Silica Thin Films” Adv. Mater. Interfaces, 1901787

Jin, M., He, Y., et al. (2016). Toward lower cost cellulosic biofuel production using ammonia based pretreatment technologies. Green Chem., 18(4), 957-966.

Yuxin He

March 13, 2020